TiO_2 Nanomaterials: Photocatalysis and Multifunctional Water Treatment Applications

by

Robert Liang

A thesis
presented to the University of Waterloo
in fulfillment of the
thesis requirement for the degree of
Doctor of Philosophy
in
Mechanical and Mechatronics Engineering (Nanotechnology)

Waterloo, Ontario, Canada, 2017

Examining Committee Membership

The following served on the Examining Committee for this thesis. The decision of the Examining Committee is by majority vote.

External Examiner	NAME: Madjid Mohseni Title: Professor, Department of Chemical and Biological Engineering, University of British Columbia
Supervisor(s)	NAME: Norman Zhou Title: Professor, Department of Mechanical and Mechatronics Engineering, University of Waterloo
Internal Member	NAME: Mustafa Yavuz Title: Professor, Department of Mechanical and Mechatronics Engineering, University of Waterloo
Internal-external Member	NAME: Aiping Yu Title: Associate Professor, Department of Chemical Engineering, University of Waterloo
Other Member(s)	NAME: Mark Servos Title: Professor, Department of Biology, University of Waterloo

AUTHOR'S DECLARATION

This thesis consists of material all of which I authored or co-authored: see Statement of Contributions included in the thesis. This is a true copy of the thesis, including any required final revisions, as accepted by my examiners. I understand that my thesis may be made electronically available to the public.

Statement of Contributions

This thesis comprises of a literature review (Chapters 2) and a series of five data chapters each written in manuscript format (Chapters 4 – 8). At the time of submission two book chapters and two manuscripts were published, two manuscripts were submitted for review in refereed journals, and one manuscript was to be submitted. The manuscripts have been modified to fit the style of the thesis. I am the primary author in all my manuscripts. Dr. Norman Zhou is the anchor author and has reviewed each manuscript. There are several co-authors on these manuscripts that have contributed to the work and their contributions are described, below.

Chapter 2

R. Liang, A. Hu, M. Hatat-Fraile, and N. Zhou, "Fundamentals on Adsorption, Membrane Filtration, and Advanced Oxidation Processes for Water Treatment," in A. Hu, A. Apblett (Eds.), *Nanotechnology for Water Treatment and Purification*, 1, pp.1-45, Springer, 2014.
R. Liang, A. Hu, M. Hatat-Fraile, and N. Zhou, "Development of TiO_2 Nanowires for Membrane Filtration Applications," in A. Hu, A. Apblett (Eds.), *Nanotechnology for Water Treatment and Purification*, 2, pp. 47-77, Springer, 2014.

Mélisa Hatat-Fraile and Anming Hu provided editorial support. I wrote and revised both manuscripts.

Chapter 4

R. Liang, A. Hu, W. Li, and Y. N. Zhou, Enhanced degradation of persistent pharmaceuticals found in wastewater treatment effluents using TiO_2 nanobelt photocatalysts, *J. Nanoparticle Res.* 15 (10), ID 1990, 2013.

Anming Hu and Wenjuan Li provided editorial support and guidance. I synthesized the nanomaterials, characterized the nanomaterials, conducted photoelectrochemical and photochemical tests, and wrote the manuscript.

Chapter 5

R. Liang, L.C.M. Li Chun Fong, M. J. Arlos, J. C. Van Leeuwen, Emad Shahnam, P. Peng, M. R. Servos, and Y. N. Zhou, Photocatalytic degradation using one-dimensional TiO_2 and Ag-TiO_2 nanobelts under UV-LED controlled periodic illumination. Submitted to Env. Sci.: Nano (ID: EN-ART-04-2017-000324).

Lena Choon Moy Li Chun Fong and Jocelyn Van Leeuwen provided sampling and photocatalytic testing support. Emad Shahnam ran scanning electron microscopy tests. Maricor Arlos provided experimental support and developed the terephthalic acid testing protocol. Mark Servos and Peng Peng provided editorial support. I designed and conducted the majority of the materials

synthesis, materials characterization, and photocatalytic degradation tests. I wrote the entirety of the manuscript.

Chapter 6

R. Liang, J.C. Van Leeuwen, M. J. Arlos, L. C. M. Li Chun Fong, L. M. Bragg, P. Peng, M. R. Servos, and Y. N. Zhou, Utilizing UV-LED pulse width modulation on TiO_2 advanced oxidation processes to enhance the decomposition efficiency of pharmaceutical micropollutants.

Lena Choon Moy Li Chun Fong and Jocelyn Van Leeuwen provided sampling and photocatalytic testing support. Emad Shahnam ran scanning electron microscopy tests. Maricor Arlos and Leslie Bragg provided LC-MS/MS analysis and quantification support. Mark Servos and Peng Peng provided editorial support. I designed and conducted the majority of the materials synthesis, materials characterization, and photocatalytic degradation tests. I wrote the entirety of the manuscript.

Chapter 7

R. Liang*, M. Hatat-Fraile*, M. J. Arlos, R. X. He, P. Peng, M. R. Servos, and Y. N. Zhou, Concurrent photocatalytic and filtration processes using doped TiO_2/quartz fiber membranes in a photocatalytic membrane reactor. Submitted to Chem. Eng. J. (ID: CEJ-D-17-03230).

Rui Xiu (Horatio) He ran scanning electron microscopy tests. Mélisa Hatat-Fraile, Maricor Arlos, and Mark Servos provided editorial support. Mélisa Hatat-Fraile synthesized the nanomaterials using the sol-gel method, prepared membranes, and ran the filtration tests. I designed the photocatalytic membrane reactor, characterized the membranes, and wrote the manuscript.

Chapter 8

R. Liang, M. Hatat-Fraile, R. X. He, M. J. Arlos, M.R. Servos, Y.N. Zhou. TiO2 membranes for concurrent photocatalytic organic degradation and corrosion protection. In *SPIE Nanoscience+ Engineering*, pp. 95450M-95450M, 2015.

Rui Xiu (Horatio) He ran scanning electron microscopy tests. Mélisa Hatat-Fraile, Maricor Arlos, and Mark Servos provided editorial support. I synthesized the materials, characterized the nanomaterials, conducted photoelectrochemical tests, and wrote the manuscript.

Abstract

Globalization has increased the demand for clean water sources and has increased water pollution due to increased standards of consumption, urbanization and industrial activities. This has necessitated improvements in small-scale and large-scale water treatment processes in terms of improved energy efficiency for treatment and protocols and standards for unmonitored emerging contaminants.

One such treatment platform that can be improved is in the area of advanced oxidation processes (AOPs). AOPs are used to decompose organic pollutants into smaller constituents. However, they often use hazardous chemicals that need to be added on a continual basis. TiO_2 photocatalysis is an AOP that removes the need for consumable chemicals like hydrogen peroxide and ozone. This work focused on methods that improved the kinetics of TiO_2 photocatalysis and combined the application of TiO_2 photocatalytic AOP with other water applications, specifically filtration and corrosion protection, in order to increase its attractiveness for use in commercials applications by decreasing the energy required to operate and/or combining more than one application into one process.

Two methods were studied to improve the reaction kinetics and limit recombination in TiO_2 photocatalysis: (i) modifying physicochemical properties of TiO_2 and (ii) altering operational parameters. Physicochemical properties of TiO_2 were modified through the synthesis of various nanomaterials that limit recombination and/or increase the number reaction sites. One-dimensional TiO_2 (TiO_2 nanobelts) were synthesized and increased the electron lifetime compared to nanoparticles. Metal-semiconductor junctions (Ag-TiO_2) were also made and they were able to efficiently separate electron and hole via the Schottky barrier effect and limit recombination. This work also investigated the effect of varying operational parameters in order to study their effects on the reaction kinetics. Operational parameters such as pH, light intensity, temperature and catalyst configuration (slurry or membrane) were explored.

Of particular interest in this work was altering the light intensity intermittently, which is referred to as controlled periodic illumination (CPI). CPI was used as a means to increase reaction efficiency of TiO_2 photocatalysis. The amount of energy required to remove organic contaminants was decreased by lowering the duty cycle and increasing the pulse frequency. In addition, CPI was used to compare the performance of slurry reactors and immobilized TiO_2 membrane reactors, in which the latter suffered from mass transport limitations. CPI under mass transfer limitations revealed that the duty cycle may be reduced to 10% and this would not alter its reaction kinetics compared to continuous illumination.

Utilization of TiO_2 photocatalysis was studied in three other water treatment application areas – emerging contaminants, filtration and corrosion protection. Using immobilized TiO_2 under UV irradiation, emerging contaminants, specifically pharmaceuticals and personal care products were shown to be degraded based on their pharmaceutical properties (charge, molecular weight, and solubility). The compound charge had the greatest effect on the degradation performance. Another application that was explored was combining TiO_2 AOP with filtration using a photocatalytic membrane reactor (PMR). TiO_2 coated filters under PMR filtration were shown to increase flux under UV illumination and have higher removals than uncoated filters. Finally, the concurrent degradation of organic compounds and corrosion protection was demonstrated using TiO_2 photoanodes coupled with steel. This method reduced the mass loss due

to corrosion, while simultaneously degrading organic contaminants. It was shown that TiO_2 photocatalysis and the TiO_2 AOP process can be utilized in other pertinent areas in water treatment.

Overall, the research demonstrated that the efficiency of TiO_2 AOPs can be improved through the synthesis of nanomaterials that limit recombination, increasing material surface area, and effectively utilizing light using controlled periodic illumination. Furthermore, TiO_2 photocatalysis can be combined with filtration and corrosion protection processes to increase its attractiveness in other water treatment areas.

Acknowledgements

The proverb, “it takes a village to raise a [doctoral student],” is appropriate in describing the amount of help I have received in my long journey to get this stage of my life. I would like to acknowledge the contributions of all the people who have helped me throughout my doctoral studies.

I would like to thank my supervisor, Dr. Norman Zhou, and John Persic for their guidance, motivation, and opportunities they have given to me. I want to thank all of my research collaboration PIs for their guidance: Dr. Mark Servos and Dr. Susan Andrews, Dr. Anming Hu, Dr. Shine Xu, and Dr. Peng Peng. I would like to thank the wonderful labmates that have helped me throughout my doctoral studies in research and life (in no specific order): Maricor Arlos, Melisa Hatat Fraile, Stephanie Gora, Ola Sowolowski, Huda Oda, Leslie Bragg, Paola Russo, Ming Xiao, Foss Jiao, Nathan Lun, Riu Xiu (Horatio) He, Joanna Majarreis, Emad Shahnam, Boyd Panton, Andrew Michael, Andrew Pequegnat, Sashank Nayak, Dulal Saha, Neil Huang, Pavlo Penner, Ali Nasiri, Jeff Wang, Stephen Peterkin, Ehsan Marzbanrad, Siu Kei Tang, Gitanjali Shanbhag, and Joyce Koo. I would also like to thank my exceptional co-op students, Lena Li Chun Fong and Jocelyn Van Leeuwen, for their helping hand through the final stages of my doctoral studies.

I would like to thank all of my colleagues in the Centre for Advanced Materials Joining (CAMJ) who I have a pleasure spending my doctoral studies with. I would like to also thank Carmen Andrei at the Canadian Centre for Electron Microscopy (CCEM) for her support with transmission electron microscopy. I would like to thank Andrew Kacheff for conducting surface area analysis for my samples. I am also grateful for the advice of Bill Cairns at Trojan Technologies in the initial phase of our water project. I would like to thank the Natural Sciences and Engineering Research Council of Canada (NSERC) and Waterloo Institute of Nanotechnology (WIN), which help support my work.

Finally, I want to thank my family (mother, father, brother, and sister-in-law), relatives, and friends for their unwavering support throughout my time at the University of Waterloo.

Dedication

To my family

Table of Contents

List of Figures

List of Tables

List of Abbreviations

1-D	One-dimension(al)
AO7	Acid orange 7
AOP	Advance oxidation process
AST	Silver core-silica-titania shell
BET	Brunauer-Emmett-Teller
BPA	Bisphenol A
BTQFF	Boron-TiO_2 quartz fiber filter
CB	Conduction band
CC	Corrosion cell
CPC	Compound parabolic collector
CPE	Constant phase element
CPI	Controlled periodic illumination
CVD	Chemical vapor deposition
DBAA	Dibromoacetic acid
DBP	Disinfection by-products
DC	Direct current
DEF	Density of lattice defects
DI	Deionized
DLVO	Derjaguin, Landau, Vervey and Overbeek
DMP	Dimethyl phthalate
DRS	Diffuse reflectance spectroscopy
DSSC	Dye-sensitized solar cell
EC	Emerging contaminant
EDC	Endocrine disrupting compound
EDP	Electrodeposition
EDX	Energy dispersive x-ray
EE2	17α-Ethinylestradiol
EIS	Electroimpedance spectroscopy
FE-SEM	Field emission scanning electron miscroscopy
FTO	Fluoride tin oxide
GC-MS	Gas chromatography – Mass spectroscopy
GDP	Gross domestic product
HAA	Haloacetic acid
HMTA	Hexamethylenetetramine
HPLC-MS	High performance liquid chromatography – Mass spectroscopy
HRTEM	High Resolution Transmission Electron Microscopy
HTPA	2-Hydroxyterephthalic acid
IC	Inorganic carbon
IC dye	Indigo carmine dye
IEP	Isoelectric point
IPA	Isopropanol
IR	Infrared

LC	Liquid chromatography
LH	Langmuir-Hinshelwood
LSPR	Localized surface plasmon resonance
MG	Malachite green
MPM	Medium pressure mercury
MS	Mass spectroscopy
NHE	Normal hydrogen electrode
NOM	Natural organic matter
NP	Nanoparticle
NTQFF	Nitrogen-TiO_2 quartz fiber filter
OCP	Open circuit potential
OSPW	Oil sands process water
PAC	Photoanode cell
PEC	Photoelectrochemical
PMR	Photocatalytic membrane reactor
PPCP	Pharmaceutical and personal care product
PPS	Primary particle size
PTi	Porous titanium
PTT	Porous titanium-titanium dioxide
PVD	Physical vapor deposition
PWD	Pulse-width modulation
QFF	Quartz fiber filter
RPM	Rotations per minute
SAED	Selected area electron diffraction
SCE	Saturated calomel electrode
SEM	Scanning electron miscroscopy
SPE	Solid phase extraction
SPS	Secondary particle size
TOC	Total organic carbon
TCCB	Triclocarban
TCS	Triclosan
TEM	Transmission electron microscopy
$THAA^9$ FP	Total Haloacetic Acids Formation Potential
THM	Trihalomethane
TIC	Total inorganic carbon
TMP	Transmembrane pressure
TNB	Titanium dioxide nanobelts
TOC	Total organic carbon
TPA	Terephthalic acid
TQFF	TiO_2 quartz fiber filter
TTIP	Titanium tetraisopropoxide/Titanium (IV) isopropoxide
TTMHFP	Total trihalomethanes formation potential
UV	Ultraviolet
UV-Vis	UV-visible

VB	Valence band
WWTP	Wastewaster treatment plant
XPS	X-ray photoelectron spectroscopy
XRD	X-ray diffraction
STEM	Scanning transmission electron microscopy

Chemical Names

·OH	Hydroxyl radicals
2,4-DBP	Dibromophenol
22MNB5	Usibor^{TM} high strength steel
Ag	Silver
$AgNO_3$	Silver nitrate
Ag-TNB	Silver-TiO_2 nanobelts
Au	Gold
B	Boron
B-TiO_2	Boron TiO_2
$CHBr_3$	Bromoform
Cl^-	Chloride ions
H_2O_2	Hydrogen peroxide
HCl	Hydrochloric acid
HOO·	Perhydroxyl radical
i-PrOH/IPA	Isopropanol
KI	Potassium iodide
Mg	Magnesium
N	Nitrogen
Na_2S	Sodium sulfide
NaCl	Sodium chloride
NaOH	Sodium hydroxide
N-TiO_2	Nitrogen-doped TiO_2
$O_2{\cdot}^-$	Superoxide radical
Pd	Palladium
Pt	Platinum
S	Sulfur
Si	Silicon
SiO_2	Silicon dioxide
$Ti(OR)_4$	TiO_2 alkoxide
TiO_2	Titanium dioxide
Zn	Zinc

Symbols

ΔG	Gibbs free energy
Δp	Change in momentum
E	Energy

e^-	Electron
E_C	Conduction band energy
E_{corr}	Corrosion potential
E_{Eo}	Electrical energy per order
E_F	Fermi level energy
E_g	Band gap energy
E^o	Standard potential energy
E_{prot}	Repassivation potential
$F(R)$	Kubelka-Munk function
h	Planck's constant
h^+	Hole
I	Current
I_{corr}	Corrosion current
k	Rate constant
k_{app}	Apparent degradation rate constant
L_P	Hydraulic permeability
m_e^*	Effective mass of electrons
m_h^*	Effective mass of holes
n_i	Intrinsic carrier concentration
r	Pearson's coefficient
R^2	Sum of residual squares
r_R	Band to band recombination rate
T	Temperature
t	Time
t_{off}	Time off
t_{on}	Time on
V	Reduction potential
v	Frequency
V_{FB}	Flat band reduction potential
V_o	Standard reduction potential
V_{OC}	Open circuit potential
V_{SCE}	Saturated calomel electrode potential
wt %	Weight percent
α	Significance level
γ	Duty cycle
η	Overpotential
λ	Wavelength
λ_{ex}	Excitation wavelength
ρ	Spearman's coefficient
τ	Kendall's coefficient
ϕ	Radiant flux

1.0 Introduction

1.1 Background

The growing demand for clean water sources and increasing water pollution, from synthetic chemicals and products, requires improvements to conventional water treatment processes and maintenance applications in small and large-scale water treatment operations. Water treatment processes, such as advanced oxidation processes (AOPs), can be improved by (i) reducing energy costs for treatment and (ii) reducing the risk of exposure from contaminants that have not been monitored sufficiently, also known as emerging contaminants [1]–[3]. Maintenance applications can be improved by prolonging the lifetime of infrastructure.

AOPs are oxidation processes used in tertiary water treatment processes to degrade organic contaminants and disinfect water. These processes require an oxidant source, such as hydrogen peroxide (H_2O_2), ozone (O_3) and short-wave ultraviolet (UV-C) irradiation, which are consumable and need to constantly be inputted into the treatment process [4]. A non-consumable oxidant source would lower the energy cost for treatment substantially.

Photocatalytic materials, such as titanium dioxide (TiO_2), can be used as a non-consumable oxidant source to treat organic contaminants. There has been growing interest in titanium dioxide (TiO_2) primarily because of their photocatalytic properties that allows light energy to be converted into chemical energy, which is useful in many applications [5]–[7]. The chemical energy produced from UV light interacting with TiO_2 is the formation of radical species that are able to degrade organic compounds into their constituent parts.

TiO_2 photocatalysis has the following advantages compared to consumable chemical oxidation processes:

(1) The process avoids use of hazardous chemicals, such as chlorine, sodium hypochlorite, ozone, and hydrogen peroxide. The oxidants generated are hydroxyl radicals, which have short lifetime in solution and breaks down organic compounds into less toxic and more hydrophilic forms.

(2) The process can be more energy efficient than photolysis and sonolysis. Photolysis requires UV-C radiation to operate and sonolysis requires high power ultrasonic transducers, which requires more energy to operate. TiO_2 photocatalysis requires UV-A radiation, reducing the energy requirements from UV-C light sources.

TiO_2, however, is inefficient in the sense that it relies solely on UV radiation to generate radical species, it is dependent on the number of reaction sites on its surface, and recombination processes limit the efficiency of generating radical species to decompose organic contaminants. This presents an opportunity to overcome these disadvantages by using (i) nanomaterials and other materials to increase reaction rates and limit recombination processes and/or (ii) changing

the physical parameters, such as pH, temperature and light intensity, which contribute to the reactions taking place on the surface of TiO_2.

Nanomaterials are materials that are modified or synthesized in the nanoscale (1 – 100 nm) using a bottom-up (i.e. self-assembly techniques) or top-down (i.e. lithography techniques) approach and exhibit properties not observed in the macro-scale. TiO_2 nanomaterials, in particular, have high surface areas that allow for increased reaction rates that can be leveraged in TiO_2 photocatalysis [4].

TiO_2 nanomaterials have the benefit of other functionalities, such as photowetting, adsorption, and self-cleaning processes, which can be used in other water treatment and maintenance processes such as filtration, fouling control, and corrosion prevention (Table 1.1). The implementation of one or more of these functionalities into a conventional treatment process or maintenance application along with the optimization of oxidation kinetic reactions pertaining to these processes in TiO_2 nanomaterials are important areas of research that have not fully been explored.

Table 1.1: Water treatment applications using photocatalytic nanomaterials

FIELD	APPLICATION	USE OF TiO_2 NANOMATERIAL
Water Purification Applications	Advanced Oxidation Process – Semiconductor Photocatalysis	The inherent photocatalytic properties of TiO_2 are used to produce electron-hole pairs that participate in redox reactions which produce hydroxyl radicals that oxidize organic pollutants such as pharmaceuticals and personal care products.
	Adsorption	The high surface area of nanomaterials increases adsorption capacity.
	Filtration	TiO_2 nanomaterials are coated, grown, or incorporated into a filter demonstrating higher flux capacities under illumination.
Maintenance Applications	Fouling Control	The photocatalytic properties of TiO_2 are used to prevent organic pollutants to accumulate on the filter surface of a substrate in order to maintain the filter's functionality.
	Corrosion Prevention	The TiO_2 is incorporated onto an anode and acts as a photoanode in cathodic protection systems. It is a variant of an impressed current system except an external DC power supply is not required or required in a limited role. The system can be combined with TiO_2/UV AOP and other water purification applications.

1.2 Objectives

The aim of this research is to use TiO_2 nanomaterials to improve water treatment applications in filtration, advanced oxidation processes, and corrosion protection as seen in Figure 1.1. In order to improve these water treatment applications, two avenues were used: (i) improving the TiO_2 efficiency by limiting recombination and using intermittent light and (ii) incorporation of two separate water applications into one concurrent process. In addition, emerging contaminants were studied partially as a component in a larger collaboration project.

The effect of perturbation, via applying a continuous/pulsed potential or intermittent light using ultraviolet – light emitting diodes (UV-LEDs), on TiO_2 nanomaterials (nanoparticles and nanobelts) with its aqueous environment was investigated. Four topics were explored: the performance of slurry and membrane batch reactors, emerging contaminants, photocatalytic membrane filtration and concurrent organic degradation and cathodic corrosion protection processes. The main objectives of this research are listed, below:

1. Investigate the photoelectrochemical characteristics of titanium dioxide nanobelts (TNB).
2. Study the effects of continuous and controlled periodic illumination of UV light sources.
3. Test the degradation of emerging contaminants, specifically in membrane and slurry batch reactor setups.
4. Develop a photocatalytic membrane reactor (PMR) to test synthesized TiO_2 nano-membranes for their efficacy in the removal of dyes and pharmaceuticals.
5. Develop a galvanic cell for the concurrent degradation of organic contaminants and cathodic protection of steels.

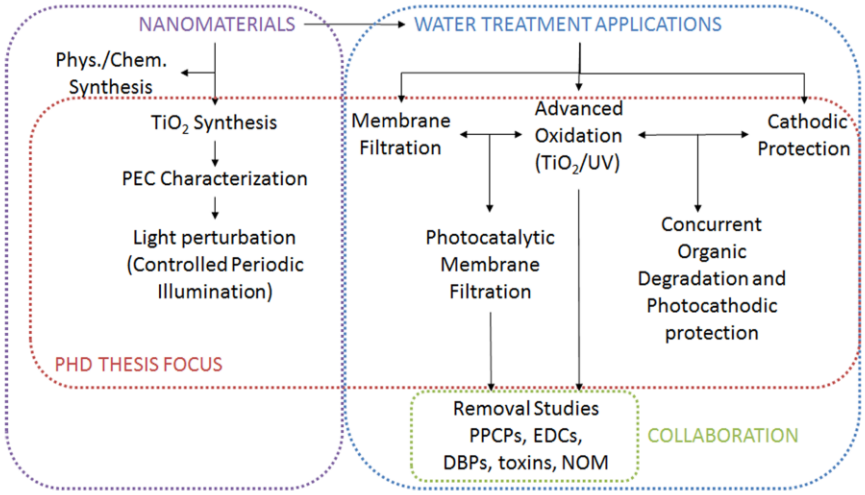

Figure 1.1: Research Overview

1.3 Thesis Organization

The thesis is focused on the understanding of the properties, synthesis, and applications of TiO_2 nanomaterials. The proposal is divided into ten chapters.

- **Chapter 1** is an introduction describing the objectives and motivation behind this work.
- **Chapter 2** contains a comprehensive literature review of semiconductor and TiO_2 properties, TiO_2 synthesis and membrane fabrication methods, and water treatment applications in advanced oxidation processes, membrane filtration, and corrosion protection.
- **Chapter 3** describes a general methodology in the experiments. The methods included are materials characterization, photoelectrocehmical testing, and photochemical testing methods.
- **Chapter 4** discusses the use of TiO_2 nanobelts and their material, photoelectrochemical, and photochemical properties.
- **Chapter 5** evaluates TiO_2 photocatalysts – P25, TiO_2 nanobelts, and Ag-TiO_2 nanobelts – and their degradation of terephthalic acid under controlled periodic illumination in a slurry batch reactor.
- **Chapter 6** evaluates the degradation of a cocktail of pharmaceuticals and personal care products using TiO_2 substrates and the effect of surface charge and mass transfer in determining which pharmaceuticals degrade under UV irradiation. The controlled periodic illumination of UV-LEDs was investigated on TiO_2 substrates. The duty cycle and frequency were changed to see the effect on kinetic decomposition rates.
- **Chapter 7** investigates the use of a photocatalytic membrane reactor combining filtration and photocatalytic processes in a dead-end filtration setup using undoped and doped TiO_2 nanomaterials.
- **Chapter 8** investigates the use of photocathodic protection of steels. Coupled TiO_2-composite and steel electrode pairs were investigated for their use in cathodic protection in salt solution in the presence and absence of organic or inorganic scavengers.
- **Chapter 9** reports the main conclusions and recommendations.
- **Chapter 10** lists the author's contributions to research.

2.0 Literature Review

Overview

The growing demand for clean, potable water sources has necessitated innovations in water treatment technologies and management. Current and emerging technologies that are of interest for industrial use are based on photocatalysis. Photocatalysis is the process whereby redox reactions are accelerated in the presence of a catalyst that is initiated by light of certain wavelengths. It relies on the catalyst to generate electron-hole pairs, which undergo a chain of redox reactions depending on its environmental conditions. Titanium dioxide (TiO_2) materials of different types and structures have shown to be effective photocatalysts because of their chemical stability, reactivity, and low toxicity [1, 2]. It has been used extensively as white pigments in food, personal care products, and coatings. The focus of this chapter is to summarize the properties of TiO_2 semiconductor (**Section 2.1** and **Section 2.2**), TiO_2 synthesis methods for powders (**Section 2.3**) and membranes (**Section 2.4**), photoelectrochemical characterization methods (**Section 2.5**), and TiO_2 based applications in water treatment based on literature and the contents of this study (**Section 2.6**). A portion of the literature review is a compilation of work done previously from written book chapters [3].

2.1 Properties of Semiconductors

2.1.1 General characteristics of semiconductors

2.1.1.1 Energy band gap

Semiconductors contain an energy band gap (E_g) between conduction band and the valence band and can be classified as either direct or indirect band gaps (Fig. 2.1). In direct band gap semiconductors, the energy of the valence band lies below the minimum energy of the conduction band without a change in momentum. On the other hand, in an indirect band gap semiconductor, the minimum energy in the conduction band is shifted by a change in momentum, Δp.

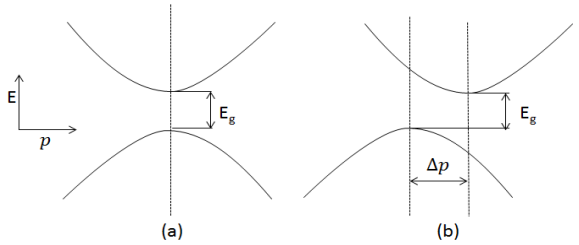

Figure 2.1: The band gap of (a) a direct semiconductor and (b) an indirect semiconductor. Reproduced with permission from [3a]

The probability that the energy level of a solid is occupied by electrons is determined by the Fermi-Dirac distribution function [4]:

$$f(E) = \frac{1}{1 + \frac{exp(E - E_F^o)}{k_B T}} \quad \text{Eqn. 2.1}$$

E is the energy (J),
E_F^o is the Fermi level (eV)
k_B is the Boltzmann constant (J K^{-1}), and
T is the temperature (K).

The Fermi level (E_F^o), represents the probability of finding 50 % of electrons in this level. For intrinsic semiconductors, E_F^o falls inside the bandgap and depends on the mass of electrons at the end of the conduction band (m_e^*), on the effective mass of electrons at the beginning of the valence band (m_h^*), and on the amplitude of the band gap (E_g). The equation of the Fermi level is as follows:

$$E_F^o = \frac{1}{2}E_g + \frac{3}{4}kTln\left(\frac{m_h^*}{m_e^*}\right) \quad \text{Eqn. 2.2}$$

where m_h^* is the effective mass of holes (kg), and
m_e^* is the effective mass of electrons (kg).

The value of E_F^o is equivalent to the electrochemical potential of an electron and is the work required to transport and electron from a large distance to the semiconductor.

2.1.1.2 *Semiconductor doping*

Some types of impurities and imperfections to the crystal lattice may drastically effect the electrical properties of a semiconductor [3, 5]. The conductivity of a semiconductor can be increased by doping, a technique that introduces foreign atoms into the lattice. For example, in the case of the Si lattice, with each Si atom having four covalent bonds with four nearby Si atoms, the addition of atoms – arsenic, phosphorous, or antimony – having one more valence electron compared to Si, will lead to an excess positive charge due to the electron transfer from the foreign atom to the conduction band. This is called donor doping and creates an n-type semiconductor, where the Fermi level will be close to the conduction band. The Fermi level changes for an n-type semiconductor are:

$$E_{Fn}^{o} = E_{F}^{o} + kTln\left(\frac{N_D}{n_i}\right) \quad \text{Eqn. 2.3}$$

where N_D is the concentration of donor atoms (mol L^{-1}) and
n_i is the intrinsic carrier concentration (mol L^{-1}).

On the other hand, if the foreign atom is boron, gallium, and indium, which have one valence electron less than Si, it can accept one electron from the valence band. This is called acceptor doping and creates a p-type semiconductor, where the Fermi level will reside closer to the valence band. The Fermi level changes for a p-type semiconductor are:

$$E_{Fp}^{o} = E_{F}^{o} - kTln\left(\frac{N_A}{n_i}\right) \quad \text{Eqn. 2.4}$$

where N_A is the concentration of acceptor atoms (mol L^{-1})

The Fermi levels of intrinsic, n-type, and p-type semiconductors are shown in Fig. 2.2.

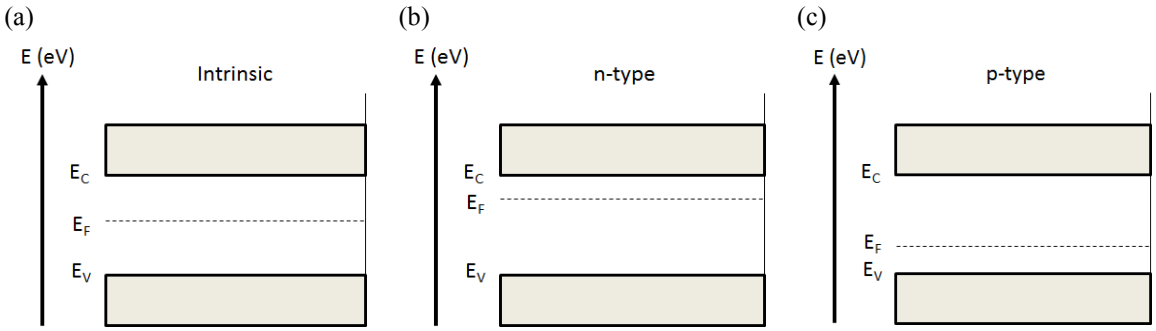

Figure 2.2: Three types of semiconductors: (a) intrinsic, (b) n-type, and (c) p-type. Reproduced with permission from [3a]

2.1.2 Semiconductor in electrolyte

The energy levels of electrons in solids can be extended to the case of an electrolyte solution containing a redox system [6]. The occupied electronic levels correspond to energetic states of reduced species, whereas unoccupied states correspond to energetic states of oxidized species. The Fermi level of the redox couple, $E_{F,\,redox}$, corresponds to the electrochemical potential of electrons in the redox system and is equivalent to the reduction potential V_o. To correlate energetic levels of the semiconductor and the redox couple in an electrolyte, two different scales are used (in eV and V). There are two scales because in solid-state physics, zero is the level of an electronic vacuum and in electrochemistry the reference is the potential of the normal hydrogen electron (NHE). The two scales are correlated using the potential of NHE, which is equal to -4.5 eV and is referred to as that of the electron in a vacuum [7].

If a semiconductor is placed in contact with a solution containing a redox couple, equilibrium is reached when the Fermi levels of both phases become equal. This occurs by means of an electron exchange from solid and electrolyte, which leads to the generation of charge inside the semiconductor. This charge is distributed in a spatial charge region near the surface, in which the value of holes and electron concentrations also differ considerably from those inside the semiconductor. Fig. 2.3a shows schematically the energy levels of an n-type semiconductor and a redox electrolyte before contact and after contact. In particular, as the energy of the Fermi level is higher than that of the electrolyte, equilibrium is reached by electron transfer from the semiconductor to the solution. An electric field is produced by this electron transfer, which is represented by upward band bending. Owing to the presence of the field, excess holes generated in the space-charge region move toward the semiconductor surface, whereas excess electrons migrate from the surface to the bulk of the solid [3]. Fig. 2.3b shows the contact between a redox electrolyte and a p-type semiconductor. In this case, electron transfer occurs from the electrolyte to the semiconductor and downward band bending occurs.

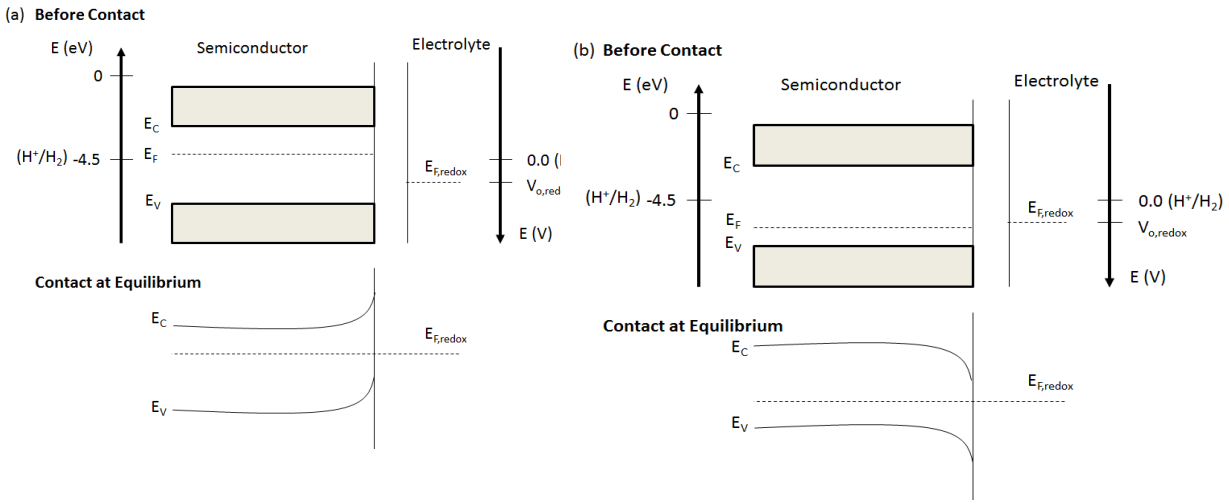

Figure 2.3: Formation of a junction between an (a) n-type semiconductor and (b) p-type semiconductor in an electrolyte solution before contact and at equilibrium after contact. Reproduced with permission from [3a]

Under anodic or cathodic polarization, a Fermi level shift of the n-type semiconductor with respect to that of the solution occurs with an opposite curvature of the bands as seen in Fig. 2.4. Under a certain electrode potential, the excess charge disappears and the bands become flat. The corresponding potential is called the flat band potential, V_{FB} [8].

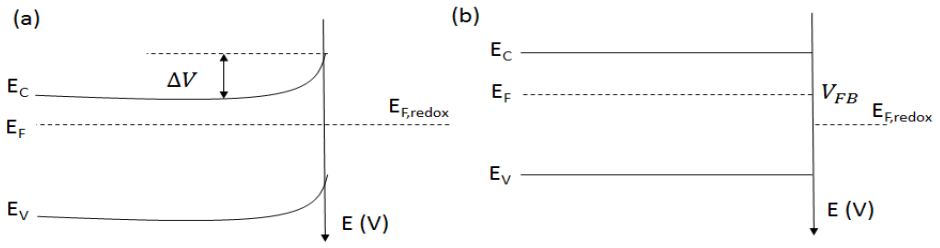

Figure 2.4: Scheme of the energetic levels at the interface semiconductor-electrolyte for an n-type semiconductor at (a) equilibrium and (b) flat band potential. Reproduced with permission from [3a]

When a semiconductor is irradiated by radiation of suitable energy, equal to or higher than that of the band gap, E_g, electrons can be promoted from the valence band to the conduction band. Fig. 2.5 shows the scheme of electron-hole pair formation due to the adsorption of a photon by a semiconductor.

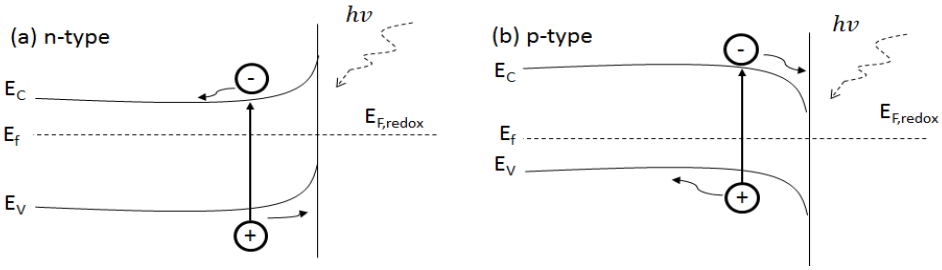

Figure 2.5: Generation of an electron-hole pair after irradiation of (a) n-type semiconductor and (b) p-type semiconductor. Reproduced with permission from [3a].

The existence of an electric field in the space-charge region allows for photogenerated electron-hole separation. In the case of n-type semiconductor, electrons migrate toward the bulk, whereas holes move to the surface (and vice-versa for p-type semiconductors). Photo-holes and photo-electrons, migrate in opposite directions and can either (i) recombine and dissipate their energy as radiation (photon emission) or heat, or (ii) react with electron-acceptor or electron-donor species present at the semiconductor electrolyte interface, thereby reducing or oxidizing them, respectively [3].

The energy of the conduction band (E_c), corresponds to the potential of the photo-electrons, whereas the energy of the valence band gap corresponds to the potential of the holes. If E_c is more negative than the potential of a species present in solution, electrons reaching the interface can reduce the oxidized form of the redox couple. Conversely, if the potential of E_v is more positive than that of the redox couple, photo-holes can oxidize the reduced form of the redox couple. Knowledge of the edge positions of the bands and of the energy levels of the redox

couples is essential to establish whether the thermodynamics allow for the oxidation/reduction of the species in solution [3]. The band gaps and the positions of the valence band and conduction band edges for various semiconductors are given in Fig. 2.6.

2.1.2.1 The case of the porous semiconductor in electrolyte

A porous semiconductor is defined as solid structures and pores that are in the 1 - 500 nm range and demonstrate remarkable charge-storage capabilities. In highly porous electrodes, the formation of a space-charge layer is improbable due to the small crystallite size and, if a space-charge layer exists, it is less than 100 nm [9]. In other words, the small TiO_2 crystals do not contain enough electrons to create an effective space-charge layer and there is no band bending compared to macroporous films.

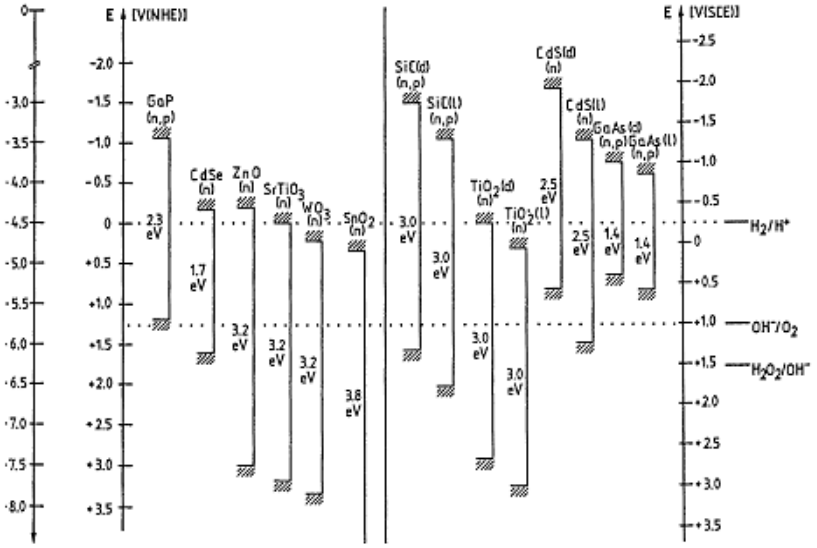

Figure 2.6: Positions of band edges for some semiconductors in contact with aqueous electrolyte at pH. Reproduced with permission from [10].

2.2 Properties of TiO_2

2.2.1 Lattice structure of TiO_2

TiO_2 occurs in three natural crystal forms – rutile, anatase, and brookite. The rutile and anatase have a tetragonal structure, whereas brookite has an orthorhombic structure; their lattice parameters are shown in Table 2.1. In nanostructured samples, the anatase and brookite transformed are dependent on the initial particle size, which determines the thermodynamic phase stability [3, 11, 12].

Table 2.1: The common TiO_2 crystal phases and their lattice parameters. Reproduced with permission from [3b].

Crystal Phase	Lattice parameter		
	a (Å)	b (Å)	c (Å)
Rutile*	4.5937	4.5937	2.9581
Brookite**	9.16	5.43	5.13
Anatase***	3.7842	3.7842	9.5146

* [13], ** [14], *** [15]

2.2.2 Photocatalytic mechanism of TiO_2

Photocatalysis occurs through the absorption of energy from a photon, hv_1, greater than or equal to the band gap energy of TiO_2 (3.2 eV for the anatase phase), producing an electron-hole pair on the surface of the TiO_2 nanomaterial as seen in Fig. 2.7. For pure TiO_2, a UV source is required for photoactivity. Under UV illumination, an electron from the valence band (VB) is promoted to the conduction band (CB), leaving an electron vacancy, or hole, in the valence band (VB). The excited electrons have the probability of the following processes occurring: (i) electron-hole recombination and dissipation, (ii) electron and hole trapping in metastable states, or (iii) reaction of electrons and holes with electron donors and acceptors adsorbed of the nanomaterial surface. Holes on the surface of the TiO_2 nanomaterials can cause oxidation reactions to occur that product hydroxyl radicals (·OH), which are powerful oxidations. Depending on the environmental conditions, oxidants produced in this process can play a significant role in the photocatalytic mechanism [1], [16]. The following scheme shows events that can occur using only a semiconductor-aqueous solution interface when TiO_2 is used as a photocatalyst [5] :

$$TiO_2 + hv \rightarrow TiO_2\,(e_{CB}^- + h_{VB}^+) \qquad \text{Eqn. 2.5}$$

$$OH^- + h_{VB}^+ \rightarrow \cdot OH \qquad \text{Eqn. 2.6}$$

$$O_2 + e_{CB}^- \rightarrow \cdot O_2^- \qquad \text{Eqn. 2.7}$$

$$\cdot O_2^- + H^+ \rightarrow \cdot HO_2 \qquad \text{Eqn. 2.8}$$

$$2 \cdot HO_2 \rightarrow O_2 + H_2O_2 \qquad \text{Eqn. 2.9}$$

$$H_2O_2 + \cdot O_2^- \rightarrow OH^- + \cdot OH + O_2 \qquad \text{Eqn. 2.10}$$

The photocatalytic process also allows for the elimination of inorganic ionic compounds present in water by reducing them to element form on the surface of the catalysis:

$$M_{(aq)}^{n+} + ne^- \rightarrow M_s \qquad \text{Eqn. 2.11}$$

The metal can be also be reduced and then converted to an oxide form with hydroxide. This reaction can also be advantageous to prevent corrosion in metals as will be shown in **Chapter 8**.

2.2.2.1 Effect of doping on the photocatalytic mechanism

The visible light photocatalytic activity of metal-doped TiO_2 is due to the metal nanoparticles deposited into the TiO_2 matrix. As shown in Fig. 2.7, electrons are excited from the defect state, imparted by the metal doping, to the CB by a photon with energy equals hv_2. Additionally, transition metal doping improves the trapping of electrons and decreases the occurrence of electron-hole recombination during irradiation, which results in enhanced photoactivity.

In non-metal doped TiO_2, there are various perspectives regarding the mechanism in which doping imparts visible light photoactivity, which include: (i) bandgap narrowing, (ii) impurity energy levels, and (iii) oxygen vacancies. Taking nitrogen doping as an example, in nitrogen doped anatase TiO_2 (N-TiO_2), the N 2p state overlaps O 2p state since their energies are very close, so the band gap energy of N-TiO_2 is narrowed allowing for visible light absorbance [17]. By introducing nitrogen atoms into the TiO_2 matrix, the oxygen sites in TiO_2 are substituted with nitrogen atoms in the form of impurity energy levels above the valence band. Under UV irradiation, electrons are excited in the VB and impurity energy levels, hv_3; but under visible irradiation, electrons are only excited from impurity energy levels [18]. Another perspective on the mechanism of TiO_2 visible light photoactivity is that oxygen vacancies or deficient sites are formed at grain boundaries and are important in imparting visible photoactivity in nitrogen doped TiO_2 as a blocker for re-oxidation [17].

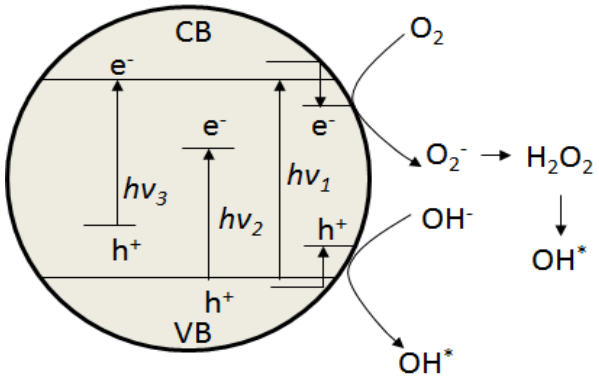

Figure 2.7: TiO_2 photocatalytic mechanisms: hv_1: pure TiO_2; hv_2: metal-doped TiO_2; hv_3: non-metal-doped TiO_2. Reproduced with permission from [3b].

2.2.3 Kinetics of photocatalysis

Heterogeneous catalysis involves systems in which reactants and catalyst are distinct physical phases. Photocatalysis in particular is a change in the rate of a chemical reaction or its generation when a semiconductor, the photocatalyst, absorbs ultraviolet-visible-infrared radiation. Photocatalysis taking place at the boundaries between two phases can be expressed as [3]:

$$A \xrightarrow{h\nu,\text{catalyst}} B \qquad \text{Eqn. 2.12}$$

where $A =$ reactant
$B =$ product

Photocatalysis of a heterogeneous system can be thought of as two steps: (i) photoadsorption/desorption processes and (ii) photoexcitation. Photosorption can be represented as:

$$A \xrightarrow{h\nu,\text{catalyst}} A_{ads} \qquad \text{Eqn. 2.13}$$

where $A =$ reactant
$A_{ads} =$ photoadsorbed species

It occurs at the TiO_2 surface that has been reported in earlier studies [19–23]. Photoadsorbed species can act as surface-hole trappings and photo-electrons can be trapped in the bulk of the solid or as surface electron trappings. It will depend on the chemical nature of the molecule adsorbed and on the type of the solid adsorbent. These changes are generally fast and reversible, such that once irradiation is stopped the surface recovers its previous features under equal initial conditions.

Photoexcitation of a semiconductor can be separated into four simplified types of electronic excitations induced by light adsorption. In a perfect crystal lattice absorption can produce only intrinsic photoexcitations with (i) the promotion of electrons from the valence band to the conduction band with formation of free electron-hole pairs; (ii) the formation of free bulk excitons (the combination of an electron and a positive hole that is free to move through a non-metallic crystal as a unit). In an imperfect lattice the presence of defects causes extrinsic absorption of light, in particular (iii) photon absorption by defects generating electronically excited defects and bound and /or self-trapped excitons; (iv) photon absorption generating ionization of defect transitions between localized and delocalized electron states [24, 25].

The effect of light absorption on the semiconductor and the adsorption of molecules in aqueous solution can be described by two mechanisms (Fig. 2.8): (i) Langmuir-Hinshelwood mechanism and (ii) Eley-Rideal mechanism. The Langmuir-Hinshelwood (LH) mechanism is

used to explain the interaction of surface charge carriers and excitons with adsorbed molecules that can promote surface chemical processes, whereas the Eley-Rideal mechanism is used to explain the interaction of molecules with surface active centers that can initiate surface chemical processes.

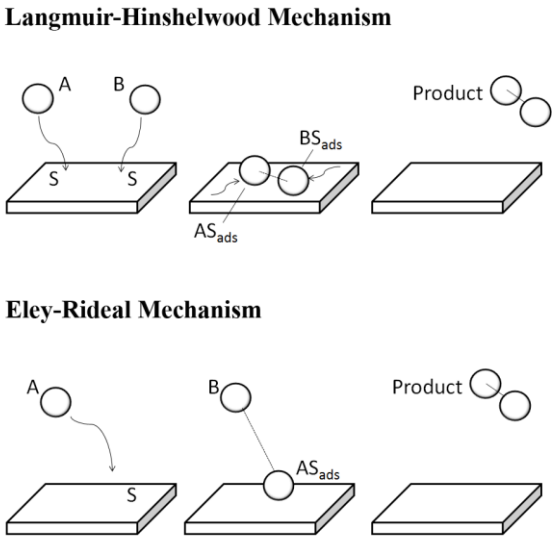

Figure 2.8: Langmuir-Hinshelwood Mechanism (top) and Eley-Rideal Mechanism (bottom). Reproduced with permission from [3a]

In the Eley-Rideal mechanism [5] proposed by Eley and Rideal in 1938, only one of the reactant molecules adsorbs and the other reacts with it directly from the gas phase, without adsorbing:

$$A_g + S_s \rightleftharpoons AS_{ads} \qquad \text{Eqn. 2.14}$$

$$AS_{ads} + B_g \rightleftharpoons \text{Product} \qquad \text{Eqn. 2.15}$$

In the LH mechanism both molecules adsorb and then undergo a bimolecular reaction:

$$A + S \rightleftharpoons AS_{ads} \qquad \text{Eqn. 2.16}$$

$$B + S \rightleftharpoons BS_{ads} \qquad \text{Eqn. 2.17}$$

$$AS_{ads} + BS_{ads} \rightleftharpoons \text{Product} \qquad \text{Eqn. 2.18}$$

The LH is widely applied to liquid and gas phase systems for the degradation of organic substrates on TiO_2 surfaces in the presence of oxygen [26–29]. It explains the kinetics of reactions that occur between two adsorbed species. The two main assumptions of the LH model are that (i) the adsorption equilibrium is established at all times and the reaction rate is less than the rate of adsorption or desorption and (ii) the reaction is assumed to occur between adsorbed species whose coverage, on the catalyst surface, is in equilibrium with the concentration of the species in the fluid phase, so that the rate-determining step of the photocatalytic process is a surface reaction.

The decrease in the amount of species in a liquid-solid phase photocatalytic system is the combination of photoadsorption and photoconversion processes. To describe this system, a molar balance can be applied to the species at any time [28]:

$$n_T = n_L + n_S \qquad \text{Eqn. 2.19}$$

where n_T = total number of moles present in a photoreactor (mol)
n_L = number of moles in the fluid phase (mol)
n_S = number of moles photoadsorbed by the solid (mol)

The molar balance can be rearranged in terms of the total concentration of the species (C_T), by dividing by the volume of the liquid phase (V), to obtain:

$$C_T = C_L + \frac{n_S}{V} \qquad \text{Eqn. 2.20}$$

where C_L = concentration in the liquid phase (mol L^{-1})

Both substrate and oxygen must be present for the occurrence of the photoreaction, then it is assumed that the total disappearance rate of substrate per unit surface area, r_T, relies on second-order kinetics (or a first order model with respect to the substrate coverage and oxygen coverage):

$$r_T = -\frac{1}{S}\frac{dn_T}{dt} = k''\theta_{Sub}\theta_{Ox} \qquad \text{Eqn. 2.21}$$

$$\theta_{Sub} = \frac{n_S}{WN_S^*} \qquad \text{Eqn. 2.22}$$

$$\theta_{Ox} = \frac{n_{S,Ox}}{WN_{S,Ox}^o} \qquad \text{Eqn. 2.23}$$

where S = catalyst surface area (mg g^{-1})
t = time (s)
k'' = second order rate constant
θ_{Sub} = substrate fractional coverage of the surface
θ_{Ox} = oxygen fractional coverage of the surface
$n_{S,Ox}$ = the number of moles of oxygen photoadsorbed on the solid on the

unit mass of irradiated solid (mol)
N_S^* = maximum capacity of photoadsorbed moles of substrate on the unit mass of irradiated solid (mol g^{-1})
$N_{S,Ox}^*$ = maximum capacity of photoadsorbed moles of oxygen (mol g^{-1})
W = the mass of catalyst (g)

If oxygen is continuously bubbled into the dispersion, its concentration in the liquid phase does not change and is always in excess. The θ_{Ox} term of Eq. 2.21 is then constant so we can define $k = k''\theta_{Ox}$ and Eq. 2.21 turns to a pseudo first order rate equation:

$$r_T = -\frac{1}{S}\frac{dn_T}{dt} = -\frac{1}{S_S W}V\frac{dC_T}{dt} = k\theta_{sub} \qquad \text{Eqn. 2.24}$$

where S_S = surface area per unit mass of catalyst
k = pseudo-first order rate constant

The kinetic information on a photoprocess consists of knowledge of substrate concentration values in the liquid phase, C_L, as a function of irradiation time. r_T and θ_{sub} can be formally written as a function of C_L, where θ_{sub} and C_L relations can be obtained from an appropriate isotherm:

$$r_T = -\frac{1}{S_S W}V\frac{dC_T(C_L)}{dt} = k\theta_{sub}(C_L) \qquad \text{Eqn. 2.25}$$

In a batch photocatalytic experiment, the substrate concentration values measured in the liquid phase represent the substrate concentration in equilibrium with an unknown substrate on the catalytic surface. This is apparent to all the measured values of substrate concentration except for the initial one. The substrate concentration measured at the start of a photodegradation experiment describes a system prior to light irradiation.

2.2.3.1 Physical factors that affect kinetics of photocatalysis

There are five physical parameters that affect kinetics: (i) mass of catalyst, (ii) wavelength, (iii) initial concentration of reactant, (iv) temperature, and (v) radiant flux. The reaction rate profiles as a function of these independent physical parameters are shown in Fig. 2.9. Optimizing these parameters is necessary to improve the reaction kinetics, however they come at

an additional cost and may not be feasible at large-scale, such as temperature and pH. Increasing the mass of catalyst, increases the reaction rate linearly until aggregation of particles and solution turbidity dominate. The wavelength of the photocatalyst can be modified through bandgap engineering using various synthesis methods. Increasing the radiant flux will lower photonic efficiency due to recombination from excess charge buildup and can be manipulated using controlled periodic illumination (CPI).

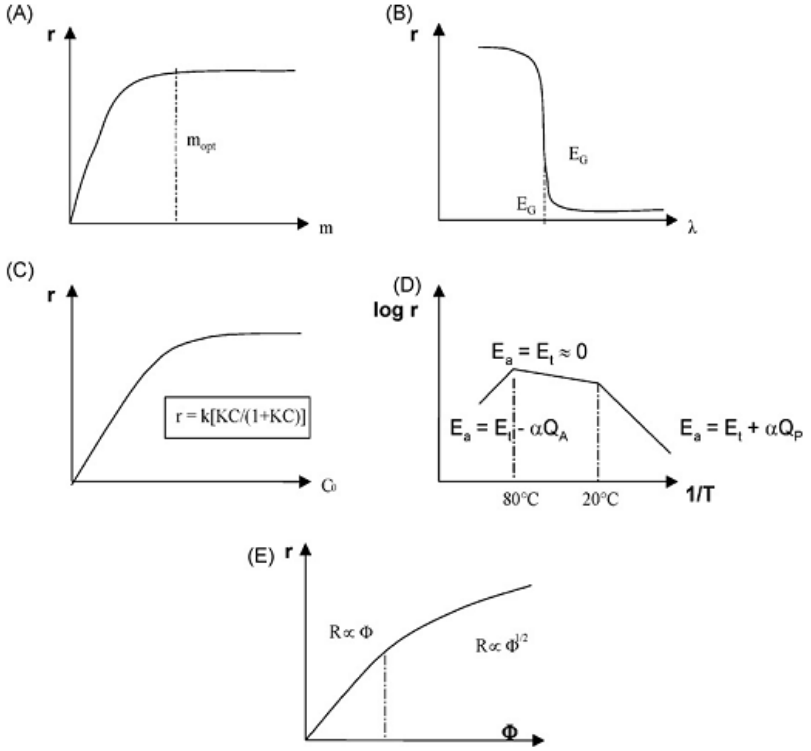

Figure 2.9: Influence of physical parameters that affect kinetics of photocatalysis: (A) mass of catalyst; (B) wavelength λ; (C) initial concentration of the reactant; (D) temperature; (E) radiant flux Φ. Reproduced with permission from [30]

Controlled periodic illumination

Fig. 2.9e illustrates the relationship between $r = f(\phi)$, where ϕ is the radiant flux (W m^{-2}) of the light source. At moderate radiant fluxes, r is proportional to ϕ below a maximum value; above this value, the rate declines from proportionality to follow a square root variation as $r \propto \phi^{\frac{1}{2}}$. High radiant fluxes greatly increase concentrations of photoelectrons and holes, which increases the recombination rate r_R parabolically:

$$e^- + h^+ \rightarrow N \qquad \text{Eqn. 2.26}$$

$$r_R = k_R[e^-][h^+] = k_R[e^-]^2 \qquad \text{Eqn. 2.27}$$

The increase in recombination generates losses in photonic efficiency, which can be mitigated using controlled periodic illumination (CPI). CPI is a technique that restores catalyst activity which is lost due to limitations in diffusion in large catalyst aggregates. In mass transport limited regimes, CPI provides a lower energy requirement to decompose organic pollutants. The immobilization of a photocatalyst adds a photonic penalty to a photocatalysis reaction. In contrast, use of a slurry reactor provides a homogeneous distribution of catalyst so mass transfer influences is negligible. CPI has been applied in other fields besides photocatalysis. It has been used to study photolysis and individual steps and mechanisms of chain reactions. It has also been applied to control chemical reaction-diffusion systems [31], photosynthesis [32], bacteria disinfection [33], and hydrogen production [34].

Correlation between physical properties and performance

It is difficult to ascertain how physical properties of the catalyst affect photocatalytic activity because controlling one property will change other properties using various synthesis methods. Finding a correlation between properties and photocatalytic activity is not straightforward due to the interrelatedness of all parameters. For example, the surface area depends on the density of lattice defects. Statistical analysis of photocatalytic activities of TiO_2 samples with different measured physical and structural properties can be analyzed. Ohtani's group conducted a study of 35 commercial titania powders to find the predominant properties determining photocatalytic activity [35]. Some of the physical and structural properties of photocatalysis that can be modelled are as follows: (i) specific surface area (via Brunauer-Emmett-Teller, BET), (ii) density of lattice defects (DEF), (iii) primary particle size (PPS), (iv) secondary particle size (SPS), and (v) percentage of anatase and rutile phases .

2.3 Synthesis Methods of TiO_2 Nanomaterials

There have been some commercial photocatalytic units for water treatment, but there are notable issues that prevent them to be fully utilized and this stems from the low photonic efficiency of unmodified TiO_2 [35]. There are three categories of controlling parameters of photocatalytic materials and reactor modules: (i) physicochemical properties (phase, size, energy level structure, surface morphology, etc.), (ii) design of photoreactors (falling film reactors vs.

stirred reactor, type of optics, supported vs. nonsupported photocatalysts, etc.) and (iii) operational parameters (contact time, pH, photon flux, and contaminant concentration). Operational parameters are not enough to overcome some of the problems in performance, and economically modifying the physicochemical properties of the TiO_2 photocatalyst via facile synthesis methods is necessary to commercialize photocatalytic TiO_2 into more applications.

There are several methods to produce TiO_2 nanomaterials, but some are more widely used than others. The most popular methods are (i) flame pyrolysis, (ii) hydrothermal synthesis, and (iii) sol-gel method, and will be discussed in this section. Furthermore, chemical doping methods will be discussed as they are often used to enhance the visible photoactivity of TiO_2. Other synthesis methods are extensions of the previous methods that have been mentioned; these include, but are not limited to, laser pyrolysis [36, 37], microwave synthesis [38–40], and solvothermal synthesis [41–43].

2.3.1 Flame pyrolysis

This process is used to prepare the most popular commercial sample used in photocatalytic studies, Degussa P25. Other researchers use this method to prepare TiO_2 agglomerates [44, 45]. An organometallic titanium source, such as titanium tetraisopropoxide (TTIP), is used as a precursor and diluted in an organic solvent and injected into a reactor through a capillary of the flame synthesis pyrolysis nozzle. Oxygen is fed through an annulus, dispersing the solution into droplets. The pressure drop at the nozzle is constant and a premixed combustible gas (ex. CH_4/O_2) flame surrounding the dispersion oxygen annulus is ignited, while stabilizing the spray flame. The extent of agglomeration or aggregation is dependent on the applied dispersion pressure.

2.3.2 Hydrothermal synthesis of 1-D TiO_2 nanostructures

One dimensional (1-D) nanomaterials (nanowires, nanobelts, and nanotubes) produced from hydrothermal synthesis [46]–[49] occur due to a phase transformation. All the 1-D nanostructures originate from an alkaline hydrothermal process. $Na_2Ti_3O_7$ nanobelts and nanotubes are synthesized through the following chemical reaction:

$$3\ TiO_2 + 2\ NaOH \rightarrow Na_2Ti_3O_7 + H_2O \qquad \text{Eqn. 2.28}$$

The TiO_2 precursor of anatase phase is a TiO_6 octahedral structure. During the hydrothermal process in Eq. 2.28, some of the Ti-O-Ti bonds break from the TiO_2 precursor and a

six-coordinated monomer, $[Ti(OH)_6]^{2-}$, is formed [49]. During the hydrothermal process, the alkaline solution is saturated and the $[Ti(OH)_6]^{2-}$ monomer is unstable and combines via oxolation or olation, forming a nuclei. As these nuclei grow, they become thermodynamically stable as the size of the nuclei exceeds the critical nuclei size. Thin nanosheets, composed of layer unit cells, can form during the growth process.

The growth of these nanosheets is anisotropic, with the growth along the b-axis being the fastest, leading to the formation of 1-D $Na_2Ti_3O_7$ nanostructures. The crystal structure of $Na_2Ti_3O_7$ is a monoclinic structure with layers of $[TiO_6]$ octahedral sites with shared edges and vertices. The Na^+ cations of these nanosheets are located between the $[TiO_6]$ layers.

Hydrogen deficiencies exist on the surface of the nanosheets, which increases surface tension and the tendency for the surface layer to bend. The surface strain energy becomes larger due to increasing hydrogen deficient sites causing layer separation. The morphologies of the nanostructures depend on various parameters. The synthesis of $Na_2Ti_3O_7$ nanotubes occurs at lower synthesis temperatures; this is due to the hydrogen deficiency in the surface layer. On the other hand, autoclaving at higher (180 ^oC) temperatures leads to an increased growth rate of nanosheets, which form long micron length nanobelts. This process may require larger strain energy than at lower temperatures, but the strain energy is not sufficient to overcome layer-by-layer coupling.

The $Na_2Ti_3O_7$ conversion to $H_2Ti_3O_7$, which is a related structure, requires an ion exchange process. When $Na_2Ti_3O_7$ is immersed and washed with dilute hydrochloric acid solution, the Na^+ ions in the TiO_2 matrix are replaced by H_3O^+ ions to form $H_2Ti_3O_7$:

$$Na_2Ti_3O_7 + 2\ HCl \rightarrow H_2Ti_3O_7 + 2\ NaCl \qquad \text{Eqn. 2.29}$$

Following, the conversion of $Na_2Ti_3O_7$ to H_2Ti3O7 in Eq. 2.29, anatase may be obtained by annealing the $H_2Ti_3O_7$ at 700 ^oC for 2 h [46] through crystal-lattice rearrangement as given by Eq. 2.30:

$$H_2Ti_3O_7 \rightarrow 3\ TiO_2 + H_2O \qquad \text{Eqn. 2.30}$$

Despite the heat treatment, anatase retains the 1-D structure of $H_2Ti_3O_7$. The lattice distortion during heat treatment is due to rotation and rearrangement of the $[TiO_6]$ octahedral and occurs during the $H_2Ti_3O_7$ to anatase conversion process.

2.3.3 Sol-gel method

The sol-gel method can be used to create colloidal suspensions called sols, which are obtained from solutions of organometallic or inorganic precursors, resulting in highly pure and homogeneous materials. The stability of the sol is dependent on van der Waals attraction and Coulombic repulsive forces among very small particles. The transformation of a sol into another phase (the gel) can be induced under various experimental conditions. The gel is a viscous solid that surrounds molecules of the chosen solvent. By drying the gel, it is possible to obtain porous solids and films.

In a typical sol-gel process to produce TiO_2, the sol is the result of hydrolysis and polymerization reactions of TiO_2 precursors, typically an organic titanium alkoxide (tetra-n-butoxide and TTIP). The precursor is dissolved in an alcohol solvent (ethanol, 2-propanol, 1-pentanol, etc.) and then added to water, in Eqn. 2.31, to induce hydrolysis to titanium hydroxide:

$$Ti(iso\text{-}OC_3H_7)_4 + 4H_2O \rightarrow Ti(OH)_4 + 4C_3H_7OH. \qquad \text{Eqn. 2.31}$$

The size for the TiO_2 particles depends on the experimental and process parameters used, such as the molar ratio between precursor and water, initial pH, reaction time, presence of external ionic species, and temperature. The polymerization reaction and the loss of solvent, transforms the liquid sol into a solid gel phase culminating in the formation of Ti-O-Ti chains. These chains are facilitated by the low content of water, low hydrolysis rate and excess of precursor in the reaction.

The sol-gel method is a versatile approach to preparing TiO_2 with certain morphological properties and removal of organics from TiO_2 gels play an important role in the preparation of TiO_2 samples on substrates, as residual organic moieties can affect photocatalytic efficiency [50], [51].The gelling process can be carried out by treating the reactant mixtures, including reducing pressure or adding various additives, such as chelating agents (HCl or $SnCl_2$) which allow one to control hydrolysis and condensation reaction rates [52].

2.3.4 Chemical doping methods

To increase the photocatalytic rate in the visible light region, there are many approaches proposed to dope impurities into TiO_2, including ion implantation, chemical vapour deposition, plasma deposition, and dopant incorporation in sol-gel synthesis methods. Table 2.2 gives a list of selected publications of metal and non-metal doping into the TiO_2 matrix.

The addition of noble metals via various methods such as solution-based processing and sputtering into the TiO_2 matrix can change the surface properties, thereby changing the efficiency

of photocatalysis. Metals (Ag, Au, Pt, Pd, and Fe) can enhance the rate of the photocatalytic reaction [53]–[57]; this was observed for the photo-conversion of H_2O to H_2 and O_2 using the Pt/TiO_2 system [58]. After excitation of the electron via visible light illumination, the electron travels to the metal where it is trapped, and thus electron-hole recombination is supressed [5]. When the semiconductor and metal come in contact, the Fermi levels of these two materials align causing electrons to flow from the semiconductor to the metal. The decrease in electron concentrations in the semiconductor increases the hydroxyl group acidity and affects the photocatalytic activity.

Additionally, TiO_2 can also be doped with non-metals to increase visible light photoactivity. Non-metals such as boron (B), carbon (C), phosphorus (P), nitrogen (N), and sulphur (S) have been shown to enhance the degradation rate compared to pure TiO_2 anatase under visible light irradiation due to impurity trapping and bandgap narrowing as discussed in **Section 2.2** [59–63]**.** These non-metals can be incorporated via solution-based processing, mechanical mixing, and chemical vapour deposition.

Table 2.2. Chemical doping of TiO_2 via non-metal and metal additions. Adapted from [3b]

Type of Dopant	Doped Element	Preparation Method	Reference
Metal	Ag	**Solution-based processing (sol-gel)** - Silver nitrate was mixed in sodium citrate tribasic dehydrate (reducing agent) at 353 K under continuous stirring. Titanium(IV) isopropoxide and nitric acid was added and the reaction maintained at 323 K for 24h. The prepared sol was dried at 378 K for 24 h and calcined at 573 K.	[53]
	Au	**Solution-based processing (sol-gel)** – Titanium (IV) butoxide in ethanol was added to a solution of tetrachloroauric acid, acetic acid, and ethanol. The resulting suspension was aged for 2 days and dried, ground, and calcined at 923 K.	[54]
	Fe	**Reactive Magnetiron Sputtering** – A titanium target and iron were placed in a reaction chamber where argon and oxygen were introduced into the chamber during discharge.	[55]
	Pt	**Photoreduction processing** – TiO_2 was suspended in methanol containing hexachloroplatinic acid. The suspension was irradiated with a mercury lamp (125 W) for an hour. $Pt\text{-}TiO_2$ was separated via filtration, washed with distilled water, and dried at 373 K for 24 h.	[56]
	Pd	**Reduction reaction –** Pd nanoparticles were grown on TiO_2 nanobelts in solution using sodium tetrachloropalladate as a Pd source and $NaBH_4$ as a reducing agent.	[57]

	B	**Mechanical mixing** - Anatase TiO_2 powder with boric acid triethyl ester was grounded and calcined in air at 723 K.	[59]
	C	**Solution-based processing (sol-gel)** – Titanium (IV) isopropoxide was dissolved in alcohol and hydrochloric acid solution. The sol gel was aged for several days and calcined in air for 3 h at 338 K and 3 h at 523 K and grounded.	[60]
Non Metal	P	**Solution-based processing (sol-gel)** – Titanium (IV) isopropoxide was hydrolyzed with isopropanol and water. Phosphoric acid was added after hydrolysis and the dispersion was stirred for 2 h, centrifuged, and dried at 373 K. The powder was calcined at 573 K.	[61]
	N	**Chemical vapour deposition** – Anatase TiO_2 powder was treated in ammonia (67 %) in argon at a temperature of 873 K for 3 h.	[62]
	S	**Thermal process** – Oxidation annealing of titanium disulphide at 573 K – 873 K.	[63]

2.4 TiO_2 Membrane Fabrication Methods

2.4.1 Self-Standing TiO_2 nanowire membranes

TiO_2 nanowire membranes can be fabricated through filtration and hot-press method [64]. To obtain these membranes, a $H_2Ti_3O_7$ nanowire suspension is deposited on filter paper using vacuum filtration. The deposited $H_2Ti_3O_7$ nanowire cake is sandwiched between alumina disks and pressed under uniaxial pressure at a temperature of 200^oC. The resulting TiO_2 filter cakes are fired at 700^oC for 1 h to anneal the $H_2Ti_3O_7$ monoclinic phase to a TiO_2 anatase phase. These membranes can only withstand very low pressures and supports are required for high pressure use.

2.4.2 Deposition of TiO_2 onto porous substrates

2.4.2.1 Dip Coating

Dip-coating is carried out by immersing a support in a liquid in which the precursor of a material of interest is present, and then withdrawing the porous or solid support at a controlled speed and temperature under atmospheric conditions. The process has generally been developed for small surface for lab bench and research purposes. The process has been used to coat TiO_2 nanomaterials for plate glass, solar energy systems, anti-reflecting coatings on windows, and photocatalytic films [5].

The process of dip-coating can be used to coat substrates with TiO_2 films, which are a few nm to 1 μm in thickness. The thickness can be obtained with high precision by selecting a suitable viscosity of the coating liquid and withdrawal rate according to the Landau-Levich equation [65]:

$$t = \frac{0.94(\mu \cdot U)^{\frac{2}{3}}}{\gamma_{LV}^{\frac{1}{6}}(\rho g)^{\frac{1}{2}}} \qquad \text{Eqn. 2.32}$$

where t is the coating thickness ,
μ is the viscosity,
γ_{LV} is the liquid-vapor surface tension,
ρ is the solution density, and
U is the withdrawal rate

Eqn. 2.32 can be applied under the following conditions: (i) The withdrawal rate must be greater than 1 mm s^{-1} and (ii) particles cannot repel each other. Additionally, the ambient environment controls the evaporation of both the solvent and the subsequent transformation of the sol into the film. The thickness of the layer also depends on the dipping angle between the support and the liquid surface and different thickness can be produced at the top and bottom sides of the surface that is coated.

2.4.2.2 Electrospinning

Electrospinning is a production technique to produce continuous ultrafine fibers (with diameters of 10 μm to 10 nm) based on forcing a polymer melt or organic based solution through a spinneret with an electrical driving force. The technique is comprised of three components: a high voltage source, a metallic collecting plate, and a capillary tube equipped with a needle of small diameter. In this process, an electrically charged jet of the spinning solution is produced out of the nozzle or needle when a high voltage is applied between two electrodes connected to the outlet. The spinning solution is ejected from the nozzle forming a charged jet that continually deposits onto the collector electrode until no spinning solution, supplied from an infusion pump, remains.

Electrospinning can be used to create TiO_2 nanofibers for physical separation applications. It is possible to create nanofibrous membranes using this technique in order to generate higher porosities and interconnected porous structures that are more water permeable than conventional counterparts [66, 67]. Nanofibers have a much higher surface-to-volume ratio than conventional microfibers, providing efficient separation of particulates in a solution. Electrospinning also offers opportunities to fine tune surface functionality through polymer chemistry. Electrospun nanofibers can be tailored for many applications where the diameter, composition, morphology, and spatial alignment can be changed [67]. Even though this technique

is a simple method, the design of functional nanofibers for filter membranes requires specific and controlled parameters for reproducible and controlled electrospinning.

Although nanofiber membranes have been previously used for air filtration applications, there is potential in using these membranes in water treatment for the removal of micro-sized particles from the liquid phase at a high rejection rate without substantial fouling [68]. These nanofiber membranes have been proposed to be used as pre-treatment step prior to ultrafiltration and reverse osmosis. Functional nanomaterials can be created from spinning solutions with dopants to produce impregnated nanofibers or formed *in situ*. The tunable process allows electrospun nanofibers to be an effective research and development platform for constructing multifunctional membrane filters by either using multifunctional materials, such as TiO_2, or by introducing functional materials onto the nanofibers network through a deposition process. For instance, by incorporating specific chelating agents on a TiO_2 nanofiber matrix, TiO_2 nanofiber membranes can be designed to selectively remove, or have an affinity towards, heavy metals and organic pollutants during filtration.

2.4.2.3 Electrophoretic deposition

Electrophoretic deposition (EDP) can be used to deposit TiO_2 nanomaterials on a porous conductive substrate [69]–[72]. The EDP process takes place in two steps: (i) charged particles suspended in a liquid migrate towards an electrode under the effect of an electric field and (ii) the particles deposit on the electrode form a homogeneous compact or film depending on its thickness. The post-EPD processing step includes heat treatment in order to improve the adhesion of the coating to the substrate.

There are several factors that affect the quality of coating and can be optimized by optimizing suspension parameters, including suspension stability, particle size, conductivity, viscosity, solvent and zeta potential. Furthermore, the physical parameters of the process can also be improved by increasing the conductivity of electrodes, voltage, deposition time, and concentration of TiO_2 particles.

2.4.2.4 Physical vapour deposition

In physical vapour deposition (PVD), deposition of films or coatings are conducted by condensation of a vaporized form of a TiO_2 precursor onto porous substrates. There are several PVD techniques [5] used. These include vacuum evaporation-deposition [73], electron beam vapour deposition [74], sputtering deposition [75], plasma deposition [76], and pulsed-laser deposition [77].

2.4.2.5 Chemical vapour deposition

In chemical vapour deposition (CVD), one or more volatile Ti precursors (i.e. TTIP) react and/or decompose on the surface of the substrate where a desired TiO_2 film or coating is formed [5, 78, 79]. Thin layers of TiO_2 can be achieve and the volatile by-products of CVD can be removed by gas flow.

2.4.3 Oxidation of Ti porous substrates

Ti porous or non-porous substrates can be oxidized to form TiO_2 porous membranes by chemical [80] or anodic oxidation [81–83]. In chemical oxidation, oxidative chemical species such as H_2O_2, HF, or NaF are used to oxidize Ti and elevating temperatures increases the rate of reaction of the oxidation reaction [80]. In anodic oxidation, similar chemical species are used as in chemical oxidation. An anodic potential is applied between Ti substrate serving as the anode and a Pt electrode as the cathode. This anodic oxidation can form high aspect-rate TiO_2 nanotubes on the surface of the Ti substrate [81–83].

2.5 Photoelectrochemical Characterization of TiO_2 Nanomaterials

For research purposes, the photoelectrode is the working electrode in a three-electrode electrochemical cell. The system can be investigated by perturbing the photoelectrode in various ways and recording the system's response, including include current, voltage, and frequency tests in dark and illuminated conditions [9].

2.5.1 Current density – potential tests

Most applications of photoelectrochemical systems refer to transfer of electrons across an interface and current density-potential techniques are commonly used. The difference in electrochemical potential of electrons across the interface of interest (accessible via the working electrode – reference electrode potential difference) and the current density through this interface are used as the perturbation and the response (or vice versa) [9]. Under an applied potential, the dark current and photocurrent are analyzed for photon-to-current efficiency. Under an applied current, the photovoltage is measured. In particular, when the current is zero (open-circuit), the flat-band potential and conductivity type of the electrode can be determined.

2.5.2 Electrochemical impedance spectroscopy

An alternative strategy to investigate electrochemical and photoelectrochemical reactions at the interface is to work in the frequency domain. It is useful to study the interfacial properties, internal resistances, and charge-transfer characteristics of TiO_2 films. In impedance spectroscopy a sinusoidal potential with small amplitude is applied to the surface, and the resulting response of the current is measured. The signal is given as [84]:

$$V(t) = V_o e^{-i\omega t} \qquad \text{Eqn. 2.33}$$

where V_o is the amplitude of the applied potential (V).

When V_o is sufficiently small ($V_o << kT\ e_o^{-1}$), the response of the interface is linear and the current I takes the form:

$$I(t) = I_o e^{i\omega t} \qquad \text{Eqn. 2.34}$$

where I_o is the amplitude the current that is sufficiently small.

The amplitude I_o can be written in phase notation:

$$I_o = |I_o| e^{-i\phi} \qquad \text{Eqn. 2.35}$$

where ϕ is the phase shift

The impedance is given as the ratio of the voltage over current:

$$Z = \frac{V_o}{I_o} = |Z| e^{i\phi} \qquad \text{Eqn. 2.36}$$

The frequency of the modulation is varied over a range and the impedance spectrum $Z(\omega)$ is recorded and various electrode processes make a contribution to the impedance. A Nyqvist plot is retrieved from the real and imaginary contributions to the impedance. In many cases, it is useful to model the impedance with an equivalent circuit consisting of electrical elements such as resistors and capacitors, arranged in parallel and/or in series. Table 2.3 shows a list of circuit elements that can be used in an equivalent circuit and their contribution to impedance. In

complex systems more than one equivalent circuit with the same overall impedance may exist and interpretation is difficult.

Table 2.3: Circuit Elements in Equivalent Circuit Model

Circuit Element	Symbol	Impedance
Resistance	R	R
Capacitance	C	$\frac{1}{i\omega C}$
Inductor	L	$I\omega L$
Constant Phase Element (CPE)	Q_n(CPE)	$\frac{1}{Y_o}(i\omega)^a$
Warburg Impedance	W	$\frac{1}{Y_o}\sqrt{iw}$

Note: Y_o = C = capacitance; $0 \leq a \leq 1$, where $a = 1$ is an ideal capacitor

2.6 Applications in Water Treatment

Photocatalytic treatment of water is dependent on the arrival of photons at the photocatalyst surface. In many waters, the solution absorbance may be high, and preclude economic use of photocatalysis. However, the method can be effective in low concentration polluted waters such as tertiary treatment options in drinking water treatment plants, semiconductor, food and beverage, and pharmaceutical industries, in which uncontaminated water is necessary. One particular application of TiO_2 photocatalysis is in the decomposition of emerging contaminants, compounds which include many small molecules and their interactions with other compounds, that have not been regulated and the health risks are unknown. Other applications are combining TiO_2 photocatalysis in other applications such as membrane filtration and corrosion protection.

2.6.1 Emerging organic contaminants and the TiO_2 AOP

2.6.1.1 Emerging contaminants

Globalization has led to an increase in production and consumption of material goods. These products eventually end up as either solid or liquid wastes in influent streams and must be removed before release to the environment. Of concern are emerging contaminants, chemicals or microorganisms that are not commonly monitored in the environment, that come from products such as pharmaceuticals and personal care products (PPCPs) [47, 85, 86] as they pose adverse health effects to humans and the ecosystem.

Recent research has found evidence of low concentrations of these PPCPs, such as endocrine disrupting compounds (EDCs), in source waters in many developed communities [47, 85, 86]. PPCPs, including medical products, cosmetics and pesticides, enter the wastewater system via human excreta or urine, washing, improper disposal, lawn care, and other means. They have potential effects and consequences for human life and water ecosystems. Many of these chemicals may disrupt the human endocrine system, which controls metabolic processes.

Another cause for concern is disinfection by-products (DBPs). These are by-products of oxidation processes and natural organic matter (NOM). DBPs have undergone significant scrutiny due to their carcinogenetic nature and the fact that these emerging contaminants can be difficult to remove or avoid using current infrastructure. Techniques such as coagulation/flocculation are commonly used in water treatment plants for the removal of particulates found within wastewater. However, these technologies are unable to completely remove small molecular weight NOM. These small molecular weight NOMs (i.e. fulvic acids and humic acids) have been shown to react with the major disinfectants found in conventional oxidation processes – chlorine, chlorine dioxide, chloramines, and ozone – to produce DBPs, including trihalomethanes (THMs), haloacetic acids (HAAs), bromoform ($CHBr_3$), dibromoacetic acid (DBAA), and dibromophenol (2,4-DBP), and others [87].

Addressing these current and future problems requires technologies of purifying water at lower cost, energy, and environmental impact than current methods. TiO_2/UV may offer a solution to the problem of emerging contaminants as shown in the research in the next section.

2.6.1.2 TiO_2 nanomaterials in the removal of pesticides, PPCPs, DBPs, and NOM

Pesticides

TiO_2 coatings under solar illumination have been used as an advanced oxidation processes in commercial water treatment plants in Spain under the SOLARDETOX project. The TiO_2 was coated on glass using a sol-gel technique. The photocatalytic detoxification of water containing pesticides was conducted using compound parabolic solar collectors (CPCs) and TiO_2 photocatalysis. Photocatalysis and photo-Fenton methods were coupled to ensure 80% mineralization of pesticides based on total organic carbon (TOC) [88, 89].

Pharmaceuticals and Personal Care Products

Hu et al. performed a comprehensive study on 13 different pharmaceuticals using 1-D TiO_2 nanowires and UV illumination sourced from a medium mercury pressure lamp [90]. The photodegradation profiles of the PPCPs with an initial concentration of 100 μg L^{-1}, using first-order kinetics, are listed in Table 2.4. A low degradation rate was observed for carbamazepine and ibuprofen, which are often, passed through wastewater treatment plants near surface waters of urban centres [91, 92]. Despite the low performance of carbamazepine and ibuprofens, the photocatalytic degradation associated with TiO_2 nanowires still effectively removed many other PPCP pollutants from water.

Table 2.4: Photocatalytic degradation using TiO_2 nanowires analyzed by pseudo-first order kinetics for individual pharmaceuticals with an initial concentration of 100 ppb. Reproduced with permission from [90].

Compound	k_{app} (min^{-1})	r^2
Norfluoxetine	0.1239	0.999
Atorvastatin	0.0688	0.999
Lincomycin	0.043	0.999
Fluoxetine	0.0408	0.995
Venlafaxin	0.0319	0.997
Sulfamethoxazole	0.0422	0.989
Diclofenac	0.0398	0.999
Trimethoprim	0.0269	0.997
Bisphenol A	0.0227	0.988
Gemfibrozil	0.0159	0.993
Atrazine	0.0155	0.999
Carbamazepine	0.0008	0.971
Ibuprofen	0.0005	0.945

Endocrine Disrupting Compounds

Arlos *et al*. studied TiO_2 immobilized on TiO2 photocatalysis and were able to remove both the biological activity (total estrogenicity) of estrogenic mixtures using the yeast estrogen assay and decompose parent estrogen compounds, a class of endocrine disrupting compounds [93]. Studies have also seen removal using an array of UV sources (mercury lamp, UV-LED, and xenon lamp) and TiO_2 substrates (titanium, zeolite, glass beads, and polymer) under their associated experimental conditions (Table 2.4).

Disinfection Byproducts

Different classes of DBP precursors have varying degrees of removal through UV/TiO_2 processes [94]. In a study by Kent *et al.*, trihalomethanes (TMH) were difficult to remove even with UV irradiation of TiO_2; however haloacetic acid removal from this process is substantial. Fig. 2.10 shows the Total Trihalomethanes Formation Potential (TTMHFP) and Total Haloacetic Acids Formation Potential ($THAA^9$ FP) values for the raw water and the degree of formation potential changes after three different UV/TiO_2 treatments were applied. The three UV/TiO_2 treatments exhibited less than 20 % removal of the formation potential of THM compounds [94]. Studies conducted by other researchers using higher TiO_2 doses have shown a higher removal rate of THM precursor compounds [95, 96]. In contrast, the $THAA^9$FP was reduced by 88 % with UV/TiO_2 treatment despite the low concentration of TiO_2 (1 mg L^{-1}).

Table 2.5: Removal kinetics by other TiO_2 immobilized studies of estrogen compounds under varying experimental conditions. Reproduced with permission from [93]

Compound	Use	Conc. (mg L^{-1})	Substrate	UV conditions	k_{app} (min^{-1})	Ref.
EE2	birth control pill	0.010	Titanium Alloy (Ti-4V-6Al)	HP mercury lamp, 125 W	0.086	[97]
		0.004	Porous titanium	UV-LED, 1.67 mW	0.020	[93]
		10	Zeolite	LP mercury, 8 W	0.045	[98]
E2	primary female sex hormone	0.010	Titanium Alloy (Ti-4V-6Al)	HP mercury lamp, 125 W	0.106	[97]
		272.38	Glass beads	Fluorescent lamp, 4 W	0.017	[99]
		0.250	PTFE sheet	fluorescent lamp 15 W	0.15	[100]
		0.004	Porous titanium	UV-LED, 1.67 mW		[93]
E1	female sex hormone	0.010	Titanium alloy	HP mercury lamp, 125 W	0.086	[97]
		270.36	Glass beads	fluorescent lamp, 4 W	0.015	[99]
		0.250	PTFE sheet	fluorescent lamp, 15 W	0.12	[100]
		0.004	Porous titanium	UV-LED, 1.67 mW	0.015	[93]
BPA	plasticizer	10	Porous PF foam cube	LP mercury lamp, 25 W	0.0025	[101]
		0.004	Porous titania	UV-LED, 1.67 mW	0.011	[93]
		0.6	Titanium	Xenon, 150 W	0.36	[102]

PTFE = polytetrafluorethylene; PF = phenol formaldehyde; LP = low pressure; HP = high pressure

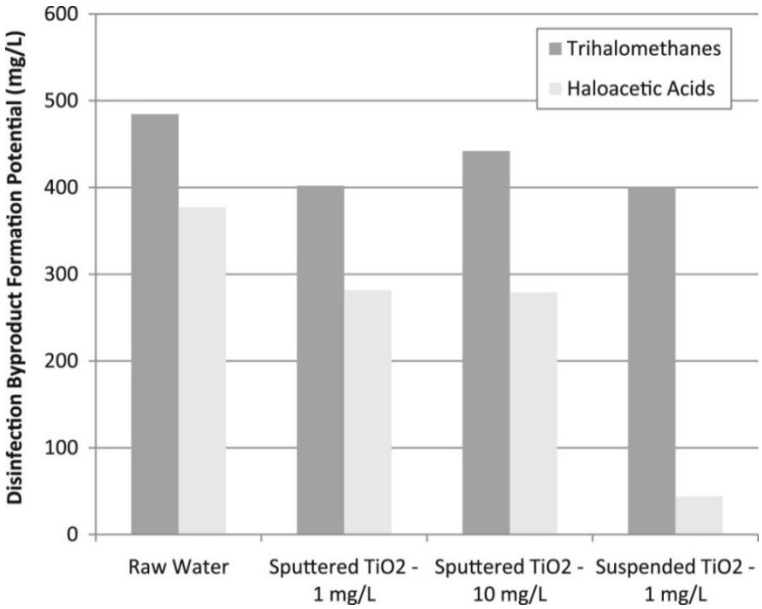

Figure 2.10: DBP formation potential of raw and treated wastewaters. Reproduced with permission from [94].

2.6.2 Membrane filtration using TiO_2 nano-membranes

2.6.2.1 Basics of membrane filtration

A membrane is a physical interface which separates two phases, forming a barrier to the transport of matter. Membranes have microscopic openings, or pores, that allow water molecules to pass, but not compounds that are larger than the pore diameter. Membrane filtration can be operated either as dead-end filtration or cross-flow filtration as shown in Fig. 2.11. In dead-end filtration, the feed water flows perpendicular to the membrane surface and all solids amass onto the membrane surface during filtration and are removed via backwashing processes. The accumulation of solids often results in a lower flux compared to cross-flow filtration. In cross-flow filtration, the feed water is parallel to the membrane surface. The flow velocity parallel to the surface of the membrane generates a shear force that reduces the growth of the filter cake. Since the majority of solids pass with the retentate, instead of collecting on the membrane surface, the system can function at a higher flux [3].

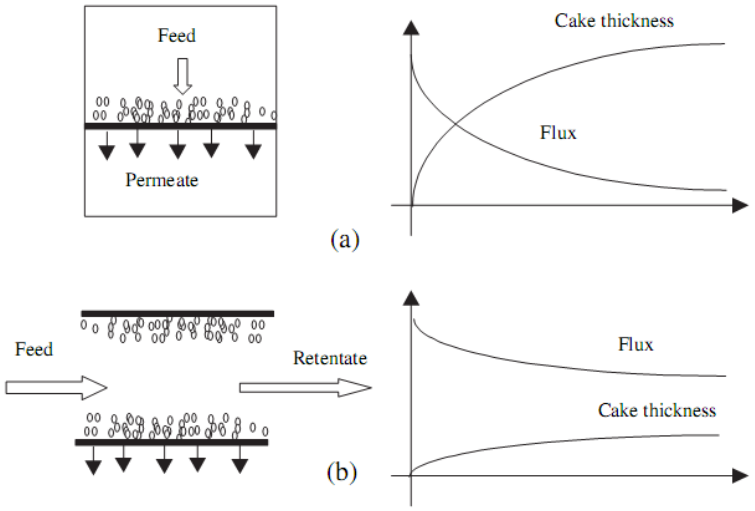

Figure 2.11: Schematic of (a) dead-end and (b) cross-flow filtration. Reproduced from [103]

2.6.2.2 Use of TiO_2 nanomaterials in membrane filtration

TiO_2 nanopowders in suspension can be utilized to increase the probability of contact between TiO_2 particles and target pollutants in water, and hence improve photocatalytic efficiency. However, the separation of these powders from treated wastewater prior to discharge requires additional time and resources, thus limiting the application of TiO_2 photocatalysis in water treatment. This drawback can be avoided by immobilizing TiO_2 on a substrate. However, immobilization can result in decreased photocatalytic ability, as immobilized TiO_2 are no longer dispersed in water, reducing contact with target pollutants. Immobilized TiO_2 also has mass transport limitations. Instead of focusing on the degradation performance of immobilized TiO_2, one can use immobilized TiO_2 as a membrane which can be used as a filtration apparatus, with a photocatalytic self-cleaning ability. This self-cleaning property increases the lifespan of the membrane that would otherwise be ineffective due to organic and biofouling [3]. The advantages and disadvantages of slurry and immobilized systems are listed in Table 2.6.

Table 2.6: Summary of main advantages and disadvantages of slurry and immobilized photocatalysis.

	Slurry photocatalyst	**Immobilized photocatalyst**
Advantages	• High surface to volume ratio • Homogeneous catalyst distribution	• Catalyst separation not required, lowering operational costs • Polluted water can be treated in continuous mode
Disadvantages	• Slow and expensive catalyst separation processes • Aggregation of suspended particles at high concentrations • Difficulties in continuous flow systems	• Low catalyst accessibilities to photons • Significant external mass transfer limitations at low fluid flow rate • Increasing role of internal mass transfer with catalyst film thickness • Possible catalyst detachment from the support

There are many TiO_2 membrane substrates used in filtration applications and are classified as (i) non-adsorbent and (ii) adsorbent substrates. Non-adsorbent substrates, such as glass [104], have been used in the past. Additionally, adsorbent substrates with large surface area, such as silica [105], zeolite [106], activated carbon [107], and activated carbon fibers [108] are increasingly being researched because the adsorption of unwanted contaminants on substrates can rectify some of the loss of photocatalytic ability caused by lower surface area to volume caused by immobilization.

In a study by Liu *et al*. [109], the flux performance of an Ag/TiO_2 nanofiber membrane, pure TiO_2 nanofiber membrane and P25 membrane were investigated using a dead-end membrane setup. The permeate flux was calculated by dividing the permeate mass by the filtration time and the effective surface area (L m^{-2} min^{-1}). As seen in Fig. 2.12, the trends for both the pure TiO_2 nanofiber membrane and Ag/TiO_2 nanofiber membrane follow a linear regression ($R^2 > 0.99$), suggesting that TiO_2 nanofiber and Ag/TiO_2 nanofiber membrane behave well in terms of permeate flux. On the other hand, the permeate flux as a function of transmembrane pressure (TMP) did not fit a linear regression ($R^2 = 0.77$) for commercial P25 deposited on a glass filter membrane. At the same TMP, the P25 deposited membrane showed a decrease in flux compared to the TiO_2 nanofiber membrane and Ag/TiO_2 nanofiber membrane. These results indicate that (i) 1-D TiO_2 nanomaterials are favourable to maintain membrane flux compared to commercial P25 and (ii) the Ag/TiO_2 nanofiber membrane demonstrates a slight

decrease of flux compared with pure TiO_2 nanofiber membrane due to the addition of Ag deposited on the membrane.

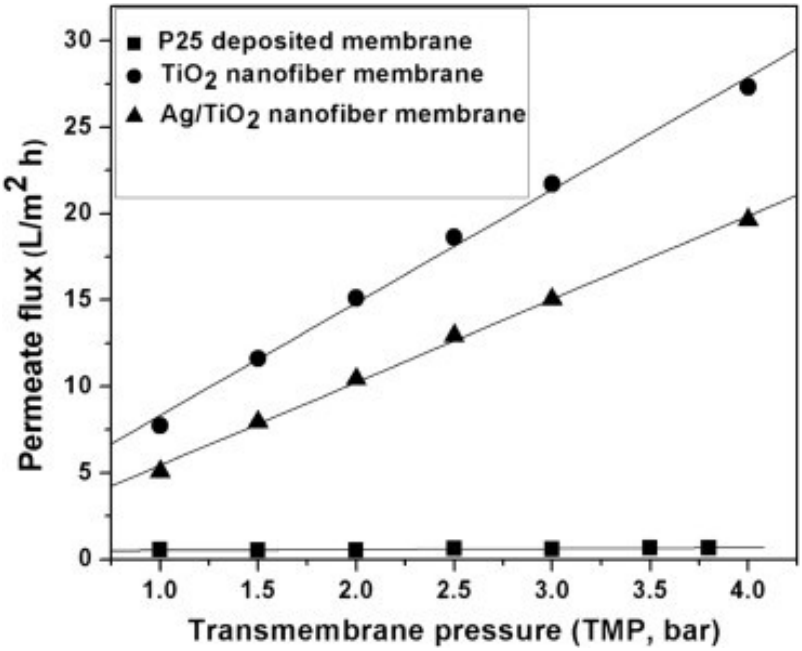

Figure 2.12: Change in permeate flux of P25, TiO_2 nanofiber and Ag-TiO_2 nanofiber membranes under different TMP. Reproduced with permission from [109]

In another study by Zhang *et al*. [110], the TMP as a function of time was measured for their nanowire membranes with and without UV irradiation to evaluate the existence of fouling. Fig. 2.13 exhibits the outcome of TMP changes during filtration, monitored via a pressure sensor, with UV irradiation and without UV irradiation. The TMP of the TiO_2 nanowire membrane as a function of filtration time increases rapidly after 7 h without UV irradiation. However, the TMP of the TiO_2 nanowire membrane under UV irradiation stays constant after 30 h of filtration time, after accounting for the initial resistance of the membrane in the initial stage of the experiment. A constant TMP throughout the duration experimental filtration time (30 h) implicitly reveals that fouling of TiO_2 nanowire membrane does not occur in this case because the formation of a fouling cake, which would increase the TMP, is inhibited.

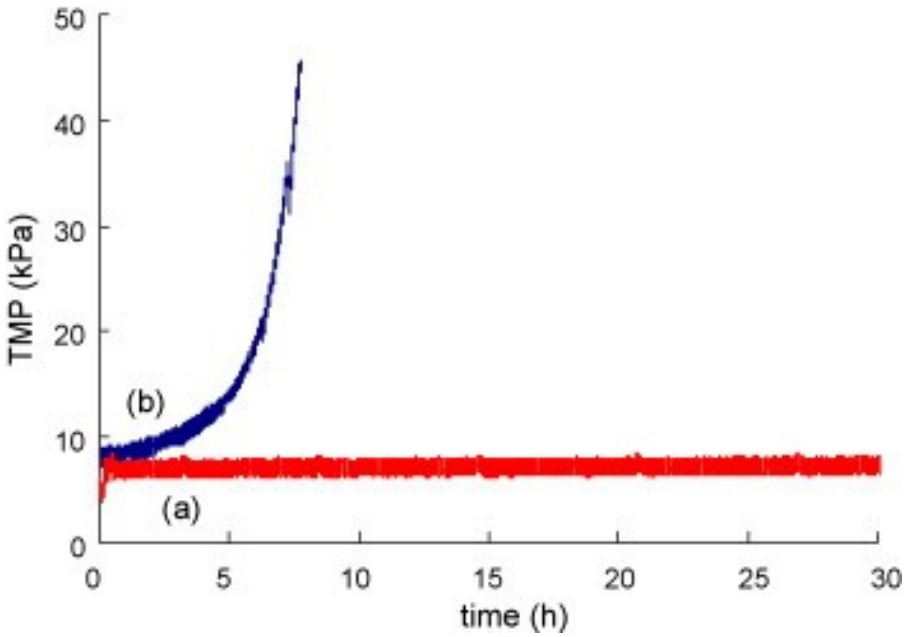

Figure 2.13: TMP changes of the TiO_2 nanowire membrane during filtration (a) with UV irradiation (b) without UV irradiation. Reproduced with permission from [110].

2.6.3 Corrosion protection using TiO_2 photoanodes

2.6.3.1 Basics of corrosion

Corrosion is the degradation of metals due to environmental factors. The direct costs of corrosion – the costs of replacing or fixing damaged equipment – are a significant fraction of a country's gross domestic product. The indirect costs of corrosion – the costs associated with reduced efficiency of equipment, contamination, leakage, and over-design – are estimated to be equivalent to the costs of the direct cost [111, 112]. A significant portion of a country's GDP can be reduced if corrosion reduction measures are taken.

Most metals will corrode when exposed to water, especially when oxidants are present such as chlorine ions or dissolved oxygen. The thermodynamics of a corrosion reaction is based on Gibb's free energy [112]:

$$\Delta G = -nFE \qquad \text{Eqn. 2.37}$$

where n is the number of electrons transferred,
F is the Faraday constant (C mol^{-1}), and
E is the electrical potential (V).

If the free energy of the reaction is positive, then corrosion does not occur; and if the free energy of the reaction is negative, corrosion may occur. This means that although thermodynamics can favour corrosion, kinetics – the rate of reaction – may be too slow for corrosion to occur. The

kinetics is influenced not only by thermodynamic conditions, but also by the metal surface quality, mass transport, and other factors.

A corrosion cell contains four key elements: (i) cathode, (ii) anode, (iii) conductor, and (iv) conducting electrolyte; this is depicted in a simplified iron corrosion cell containing NaCl as shown in Fig. 2.14. At the anode, the following reaction occurs [113]:

$$Fe \rightarrow \mathrm{Fe}^{2+} + 2\mathrm{e}^{-} \,. \qquad \text{Eqn. 2.38}$$

At the cathode, the following reaction occurs:

$$2H^{+} + 2e^{-} \rightarrow H_2. \qquad \text{Eqn. 2.39}$$

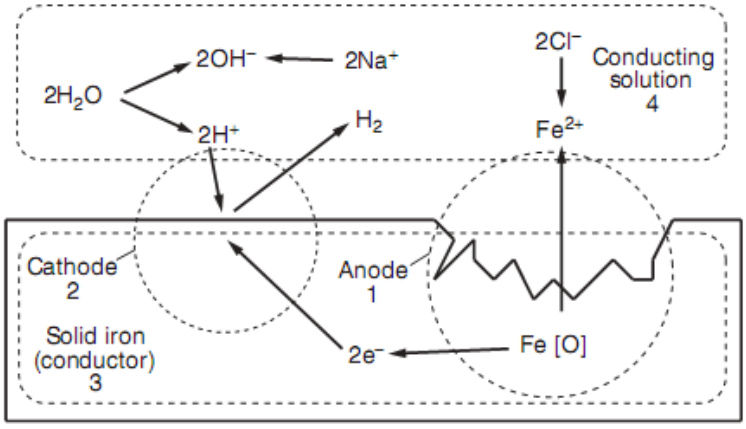

Figure 2.14: A corrosion cell of iron in NaCl conducting solution. Reproduced with permission from [113].

2.6.3.2 Corrosion protection

Corrosion prevention frequently focuses upon the electrochemical nature of the corrosion reaction. If the corrosion cell can be altered or broken, corrosion rates can be eliminated or at least reduced to insignificant levels. The simplest way to break the corrosion cell is to apply one or more electrically resistant coatings, which can successfully mitigate the corrosion when applied correctly. Defects in coatings, however, may occur and cathodic protection is frequently used in conjunction with coatings.

Cathodic protection is a thermodynamic means of corrosion, and there are two methods to apply it: (i) electrically coupling the metal to a more reactive metal that corrodes or (ii) applying an impressed or rectified direct current [112].

From a thermodynamic point of view, the cathodic protection process can be illustrated in a Pourbaix diagram for iron seen in Fig 2.15. There are two ways cathodic protection can be initiated. The first way is via a thermodynamic effect, whereby the iron metal can be shifted into the immune region (native iron) of the diagram via a negative potential change. The negative potential change (E) makes the Gibb's free energy increasingly positive, thus suggesting that corrosion does not occur. The second effect is related to the pH of the solution at the surface of the iron. Increasing the pH, results in the imbalance caused by shifting the anodic reaction to remotely located anodes, in other words, the protected metal is cathodic. However, the increase in pH at the site of the protected metal is highly localized, and the effect on the surrounding water is miniscule. The cathodic protection process be applied to other metals as well as long as its protection potential can be ascertained using the half-cell Nernst equation of the dissolution reaction [113]:

Eqn. 2.40

$$E = E_{Red}{}^{o} + \frac{RT}{nF} ln(a_{Ox}/a_{Red})$$

where $E_{red}{}^{o}$ os the standard half-cell reduction potential (V);
R is the universal gas constant (8.314 J K mol^{-1});
T is the absolute temperature (K);
a is the chemical activity or ion concentration, where a_{Red} is the reductant and a_{Ox} is the oxidant; and
F is the Faraday constant (9.648 x10^{4} C mol^{-1}).

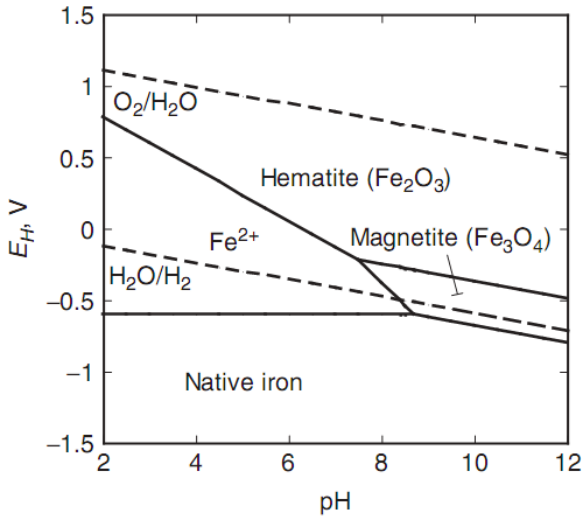

Figure 2.15: Pourbaix diagram of iron. Reproduced with permission from [113]

2.6.3.3 TiO_2 photoanodes and cathodic protection of metals

A few studies have proposed that using the photo-induced charge-transfer processes at the TiO_2/electrolyte interface can be applied to corrosion prevention [114–118]. This technique was found by chance in an article discussing a pre-oxidized stainless steel plate being reduced and bleached by a UV illumination TiO_2 film coated on the surface of the steel [115]; and indicated that photogenerated electrons from the conduction band (CB) of the TiO_2 migrated to the bulk of the pre-oxidized stainless steel and induced a cathodic (reduction) reaction. Various other groups have investigated this phenomenon in TiO_2-copper and TiO_2-coated steel [116], [117]. Other types of setups of this same process have been explored, in which the TiO_2 photoanode and a metal cathode are connected to each other physically in a galvanic cell under illumination at the TiO_2 photoanode side [118]; this eliminates the effects of TiO_2 behaving as a physical barrier between the metal and electrolyte solution.

2.7 Summary and Areas to Study

There are many functions of TiO_2 that can be exploited in applications in environmental applications. Nanostructures of TiO_2 have higher surface areas and different electron transport mechanisms compared to bulk TiO_2; these TiO_2 nanomaterials can be synthesized using relatively simple methods, including hydro-solvothermal, sol-gel, and pyrolysis. Furthermore, these nanomaterials can be applied to membranes or substrates via self-assembled growth on titanium (Ti)-based supports or deposited using a top-down approach. These TiO_2 membranes or TiO_2 coated substrates can be used in PMR for to remove particulates and reduce fouling of the membrane. Furthermore, TiO_2 coated on conductive substrates can serve as a photoanode for the corrosion protection. The literature of TiO_2 photocatalysis nanomaterials and water applications is vast, but there are still areas in emerging in contaminants, membrane filtration, and corrosion protection that require to be explored. The following areas have been identified to be addressed in the study:

1) An in-depth study on the photochemical and photoelectrochemical properties of TiO_2 nanobelts (Chapter 4 and 5).
2) The effect of CPI on 1-D TiO_2 and metal-semiconductor (Ag-TiO_2) nanobelts in slurry batch reactors (Chapter 5). There has been no prior study on CPI of one-dimensional and metal-semiconductor photocatalysts.
3) There is no literature on the effect of CPI in the photocatalytic degradation of pharmaceutical mixtures. Chapter 6 presents the first study on the degradation of a

pharmaceutical mixture using CPI-controlled TiO_2 photocatalysis in immobilized batch reactors.

4) Chapter 6 explains the effect of pharmaceutical parameters on the degradation kinetics of various compounds. There is no prior literature on using a multi linear regression method to understand the correlation of individual pharmaceutical degradation profiles with parameters (charge, molecular weight, and solubility) of pharmaceutical compounds.
5) The effect of doping on TiO_2 membranes has been investigated, but not many have used them in photocatalytic membrane reactors (PMR). Chapter 7 investigates the use of N-doped and B-doped TiO_2 nanomaterials in a PMR dead-end filtration setup. Very few studies have been conducted using dead-end PMR.
6) Photocathodic protection has been studied previously [119–122], however the protection of welded metals have not been explored and the coupling of contaminant degradation and corrosion protection has not been studied. Chapter 8 investigates the use of hole scavengers in conjunction with photocathodic protection of welded and unwelded steel.

3.0 General Methodologies

Overview

The project is setup to take synthesized TiO_2 nanomaterials, analyze their material and photoelectrochemical properties, and compare them with other synthesized samples and commercial benchmarks. The TiO_2 nanomaterials are also used in various applications in water treatment such as absorption, photocatalytic advanced oxidation, filtration processes, and corrosion protection. These applications have their own sets of characterization methods. The common methods in the proposal and in subsequent chapters are outlined in this chapter in Table 3.1. Any changes to the methods or chapter-specific information for any individual test or analysis are mentioned in subsequent chapters.

Table 3.1: Common characterization and experimental methods

General	Type of Test	Instrument(s) Used
Materials characterization	Crystal Phase	XRD, Raman, TEM
	Morphology	TEM, SEM
	Surface elemental composition	XPS
	Absorbance measurements and bandgap energy determination	UV-Vis spectroscopy equipped with integrating sphere
	Isoelectric Point and surface charge	Zeta Potential Analyzer
Photoelectrochemical characterization	Photocurrent density test	Potentiostat-Chronoamperometry
	Photovoltage test	Potentiostat-Chronopotentiometry
	Electroimpedance spectroscopy	Potentionstat - EIS
UV-Solar-Visible/TiO_2 Experiments	Slurry batch test	TOC, UV-Vis spectroscopy, LC-MS/MS
	Membrane batch test	UV-Vis spectroscopy, LC-MS/MS
	Photocatalytic filtration test	UV-Vis spectroscopy, LC-MS/MS, flux measurement tools

3.1 Materials Characterization

3.1.1 Crystal phase and morphology

The crystal phase and morphology of fabricated TiO_2 nanomaterials were examined by X-ray diffraction (XRD), Raman spectroscopy, Scanning Electron Microscopy (SEM), and High Resolution Transmission Electron Microscopy (HRTEM). Powder XRD measurements were performed on a Rigaku SA-HF3 X-ray diffractometer using Cu Kα radiation (1.54 Å) X-ray source equipped with an 800 μm collimator, operating at an excitation voltage of 50 kV. The obtained diffraction patterns were collected from 10^o to 90^o at a scanning rate of 1.5^o per minute. Raman spectroscopy was conducted using a Raman microscope (Renishaw inVia microscope equipped with 488 nm Ar ion laser). The morphology of the as-synthesized TiO_2 nanobelts was evaluated using a ZEISS LEO 1550 FE-SEM at an accelerating voltage of 10 kV. HRTEM observation was conducted using a JEOL 2010F at the Canadian Centre for Electron Microscopy (Hamilton, Ontario, Canada). The TEM samples were prepared by suspending TiO_2 nanomaterials in ethanol and drop casting the solution onto lacey carbon grids. The images were processed using Gatan Microscopy Suite: Digital Micrograph^{TM} (Ver. 2.11.1404.0), CrysTBox – diffractGUI, and ImageJ.

3.1.2 Surface elemental composition

X-ray photoelectron spectroscopy (XPS) was conducted to determine the chemical composition and chemical bonds. A Thermo ESCALAB 250 instrument configured with an $Al_{K\alpha}$ X-ray source (1486.6 eV, 150W), a hemispherical analyzer (150 mm radius), and an analysis chamber was used. Data was collected with pass energy of 20 eV for the core-shell spectra and 50 eV for the survey spectrum. The takeoff angle, defined as the angle between the substrate normal and the detector, was fixed at 0^o. Non-monochromated $Al_{K\alpha}$ twin anode was used to reduce charging in some samples.. Regional spectra downs were obtained and their peaks were deconvoluted using CasaXPS software.

3.1.3 Diffuse reflectance and bandgap determination

The band gap energy of a semiconductor can be calculated from Tauc plots [1] of $(\alpha h\nu)^n$ vs photon energy ($h\nu$), where α is the absorption coefficient, h is the Planck constant, ν is the light frequency and n depends on the characteristic of the transition in the semiconductor, where n = 2 for direct transitions and n = 0.5 for indirect transitions. The absorption coefficient is estimated from Eq. 3.1:

$$\alpha = F(R_\infty) = \frac{(1-R_\infty)^{\frac{1}{n}}}{2R_\infty} \qquad \text{Eqn. 3.1}$$

where R_∞ is the reflectance of an infinitely thick sample with respect to a reference at each wavelength.

TiO_2 semiconductors have bandgaps that are indirect (n = 0.5). The bandgap energy (E_g) can be estimated from the Tauc plot by determining the intercept of the tangent at the inflection point. The band gap energy is obtained from a diffuse reflectance spectrum (DRS) using a Shimdazu UV-2501 PC spectrophotometer equipped with an integrating sphere, with $BaSO_4$ as reference scatter. The diffuse reflectance spectrum was scanned from 200 nm – 800 nm and Tauc plots were generated to determine bandgap energy.

3.2 Photoelectrochemical Properties of Synthesized TiO_2 Nanobelts

3.2.1 Photoelectrochemical setup

Photoelectrochemical measurements were performed with a Gamry potentiostat (Series 300) using a three electrode setup immersed in an electrolyte contained in a quartz vessel as shown in Fig. 3.1. A quartz vessel was used so that short-wave UV light is able to maximally transmit through the material, unlike with common borosilicate glass vessels. In the three-electrode setup, the working electrode, counter electrode, and reference electrode are connected to the potentiostat. TiO_2 nanomaterials on fluoride tin oxide (FTO) glass served as the working electrode when testing the photoelectrochemical properties of the material. A Pt mesh was used as the counter electrode. Two types of reference electrodes were used in this work: saturated calomel electrodes (SCE) and silver-silver chloride (Ag/AgCl) electrodes. A Xenon lamp (Newport, Research Solar Simulator) was used to illuminate the TiO_2 deposited FTO glass and equipped with several filters depending on the tests (i.e. 400 nm cutoff filter and A.M. 1.5G filter). Controlling and recording of the tests was done using Gamry Framework v4.35 software.

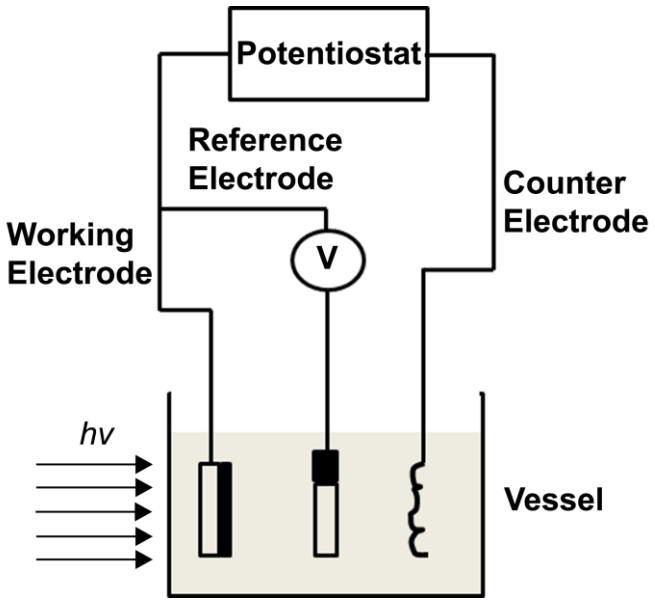

Figure 3.1: Three-electrode setup for photoelectrochemical tests

3.2.2 Photoelectrochemical measurements

The photoelectrochemical setup was used to measure the photocurrent density, photovoltage, and electroimpedance of TiO_2 working electrode samples to determine electrical and semiconductor properties of a synthesized or standardized sample.

3.2.2.1 Photocurrent density

Photocurrent density tests were conducted using chronoamperometry mode in the Gamry Framework software. Under this mode, a constant applied potential was applied to the working electrode with respect to the reference electrode. Light sources was switched on and off at specified intervals.

3.2.2.2 Photovoltage

Photovoltage tests were conducted using chronopotentiometry at open circuit potential (no current) to test the potential changes under illumination and the photovoltage decay over time. The dopant type of the semiconductor can be determined from this test based on the direction of the potential change upon illumination. If the potential change is positive (negative), then the semiconductor is p-type (n-type). Furthermore, the voltage decay rate after the illumination source is turned off can be used to determine the electron lifetime.

3.2.2.3 *Electrochemical imepedance spectroscopy*

Electrochemical impedance spectroscopy was conducted under an AC sinusoidal wave of 5 mV with and without DC bias. The frequency examined was 100 kHz to 0.1 Hz at 10 points per decade. Nyquist and Bode plots were acquired from the impedance data. The Nyquist plots were fitted with an equivalent circuit model to determine the values of elements in the model, which are helpful in determining the photoelectrochemical behavior at the material/electrolyte interface under various conditions and environments.

3.3 UV/TiO_2 AOP Experiments

3.3.1 Experimental setups

Three types of experiments were conducted to analyze the absorption and photocatalytic degradation performance of TiO_2 nanomaterials in powder or membrane forms: (i) slurry, (ii) membrane batch test, and (iii) the photocatalytic filtration reactor tests (Fig. 3.2). The TiO_2 powders were analyzed solely using the slurry batch test. TiO_2 membranes were characterized under the membrane batch photocatalytic filtration reactor test. For the purposes of the subsequent chapters, photocatalytic tests were performed with a medium pressure mercury lamp with a peak wavelength (100 W, 365 nm peak), UV-LEDs (max: 4.1 W, 365 nm peak), and a Xenon arc lamp (max: 150 W, 400 nm cutoff filter).

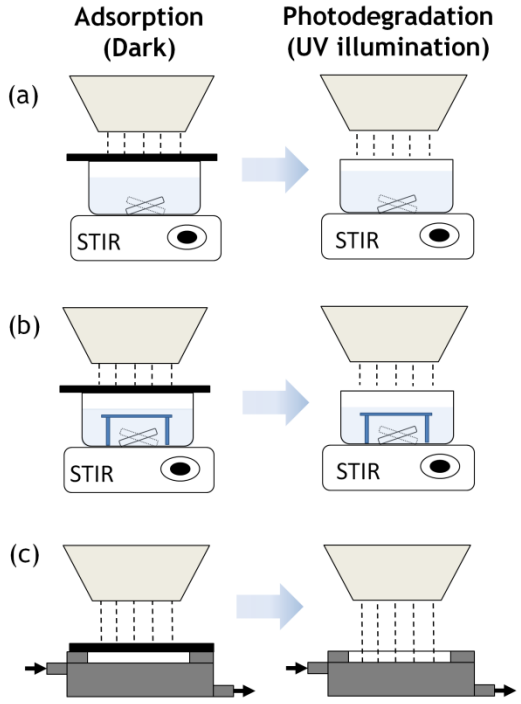

Figure 3.2: A (a) slurry, (b) membrane batch, and (c) photocatalytic filtration test setup

3.3.1.1 UV-LED slurry and membrane batch reactor setup

The setup consisted of multi-position stir plate and a UV-LED setup with a collimating column as mentioned in Arlos et al. [2]. The UV-LED was controlled using a microcontroller (Arduino) coupled with a LED Current Driver (LEDSEEDUINO) and PWM script was programmed into the controller. The average power output of the UV-LED lamps was measured using a Thorlabs power and energy meter (PM100-USB). The pulse frequency and duty cycle was calculated as:

$$Pulse\ frequency = v = \frac{1}{t_{on} + t_{off}} \quad \text{Eqn. 3.2}$$

$$Duty\ cycle = \gamma = \frac{t_{on}}{t_{on} + t_{off}} \quad \text{Eqn. 3.3}$$

where t_{on} and t_{off} were the length of time that the UV-LED was on and off, respectively.

3.3.2 Measurements and analysis

3.3.2.1 UV-Vis absorbance measurements

Photocatalytic degradation of compounds was monitored by the extent of parent compound degradation using UV-Vis spectroscopy for compounds have distinct absorbance peaks in the UV-visible range. A UV-Visible-Near IR spectrometer (Shimadzu UV-2501PC) was used to analyze these compounds from a spectral range of 200 nm to 800 nm, with a detector path length of 10 cm. Serial dilutions of standards were used to determine integrated peak areas of each standard and create calibration curves, which were employed to establish concentrations for samples. Peak area integration and analysis was conducted on the UV Probe (Shimadzu Corporation, ver. 2.10).

3.3.2.2 Total organic carbon

The extent of degradation calculated from UV adsorption does not indicate the degree of mineralization or total organic carbon content (TOC), only the parent compound degradation. Oxidative mineralization of organic compounds was measured by using TOC analyzer. TOC measurement was used as a secondary analysis tool for compound degradation analysis.

Two types of carbon are present in water: organic and inorganic carbon. Organic carbon (OC or TOC) contains hydrogen atoms bonded to the carbon backbone. Inorganic carbon (IC or TIC) is the fully oxidized form of carbon compounds and is structural basis for inorganic

compounds such as carbonates and carbonate ions. Collectively the two forms of carbon are referred to as total carbon (TC). The total organic carbon is:

$$TOC = TC - IC. \quad \text{Eqn. 3.4}$$

TOC was measured using an Aurora 1030c TOC Analyzer. The TOC concentration of a sample was determined by converting the organically bound carbon into CO_2 based on Standard Method 531- D: Wet Oxidation method [3]. In short, the sample is acidified to pH 2 or less to convert inorganic carbon species to CO_2, purged to remove the inorganic carbon, then oxidized with persulfate in an autoclave at temperatures from 116 ^oC to 130 ^oC. The CO_2 produced from the sample is then quantified by non-dispersive infrared spectrometry and converted to TOC.

3.3.2.3 Sample analysis using tandem mass spectroscopy

The analysis of the compounds were completed using liquid chromatography and tandem mass spectroscopy (LC-MS/MS) using the Agilent 1200 HPLC coupled to an Applied Biosystems 3200 QTRAP mass spectrometer. The analysis of target pharmaceuticals is described elsewhere [4, 5].

3.3.2.4 Pseudo-first order kinetic equation

Langmuir-Hinshelwood kinetics may be simplified to pseudo-first order equation at low concentration of pollutants to determined kinetic rate coefficients [6], The equation is as follows:

$$-r = \frac{dC}{dt} = -k_{app}C \quad \text{Eqn. 3.5}$$

and rearranged to its integrated form:

$$\ln\left(\frac{C}{C_o}\right) = k_{app}t. \quad \text{Eqn. 3.6}$$

where k_{app} (min^{-1}) is the apparent first-order reaction rate,
C is the concentration (mg L^{-1}) at time t, and
C_0 is the initial concentration (mg L^{-1}).

The apparent kinetic constant, k_{app}, and was obtained by taking the slope of the *$ln(C/C_0)$ vs. t* plot.

4.0 TiO_2 Nanobelts: Material, Photoelectrochemical, and Photochemical Properties

Overview

TiO_2 nanobelts (TNB) were prepared from a facile hydrothermal synthesis. The crystal phase and growth direction were determined by electron microscopy. The photoelectrochemical properties (photocurrent density, electron lifetime, and electrical characteristics) of the TiO_2 film were measured using photoelectrochemical tests. These tests helped determine electron-hole separation and redox processes that enable the improvement of photocatalytic processes in synthesized TiO_2 nanomaterials. TNB was tested under photochemical slurry batch reactors exposed to 365 nm UV illumination from a medium pressure mercury lamp and the measured photocatalytic degradation rates for single pollutant were explored using kinetic models. The degree of degradation as a function of physical parameters, such as temperature, pH, and pollutant concentration, was also investigated. The role of active radical species involved in the photocatalytic mechanism was explored.

4.1 Introduction

Early TiO_2 photocatalytic research efforts focused on single crystal samples [1, 2] carried mostly on easily available rutile phases and some work on anatase phase. After the importance of nanoscale morphology was recognized in TiO_2-based photocatalysis and dye sensitized solar cells [3], research efforts were dedicated to synthesizing different powders of varying size, crystallinity, and structures [4–7]. Different approaches were used such as hydrothermal synthesis and sol-gel methods (see **Section 2.3**). Among various nanostructures, one-dimensional (1-D) TiO_2 nanomaterials – nanorods [8], nanowires [9–11], nanobelts [12, 13], and nanotubes [14] – offer direct pathways for photogenerated electron transfer, possessing advantages such as increased charge transport and reducing electron-hole pair recombination compared to conventional nanoparticles of the same phase [15, 16].

In this study, a facile method of fabricating one type of 1-D TiO_2 nanomaterial, TiO_2 nanobelts (TNB), was reported and the material characteristics and photoelectrochemical properties were determined. Material characteristics were evaluated using UV-vis spectroscopy, XRD, Raman, and BET isotherm. TNB were electrophoretically deposited onto fluoride tin oxide (FTO) glass to perform photoelectrochemical tests, namely photovoltage, photocurrent density, and EIS measurements. The electron lifetime was determined from photovoltage decay tests. Electrical characteristics such as resistances and capacitances from electrolyte/TNB and TNB/FTO interfaces were modelled using an equivalent circuit based on data from EIS obtained

Nyquist plots. Photochemical studies were conducted using a slurry batch reactor. Single pollutant degradation was tested using theophylline as a compound of choice because of its high solubility in water and non-sensitization reactions, which are problematic with dye compounds such as malachite green and methylene blue.

4.2 Experimental Methods

4.2.1 Synthesis of TiO_2 nanobelts

TNB were synthesized from a previous study [12, 13]. In a 125 mL Teflon-lined stainless steel autoclave (Parr-Instruments), $Na_2Ti_3O_7$ nanobelts were grown for 72 h in 60 mL NaOH (10 M) alkaline solution at 190 ^oC using 2 g of P25 Aeroxide^{TM} (P25, Evoniks). After cooling the reactor, the suspended nanobelts were transferred and centrifuged 5 times using Millipore water. Subsequently, the sodium titanate ($Na_2Ti_3O_7$) nanobelts were immersed in 0.1 M HCl solution, and through an ion exchange process, hydrogen titanate ($H_2Ti_3O_7$) was obtained. Afterward, $H_2Ti_3O_7$ nanobelts were dried in a furnace for 80 ^oC for 8 hours to obtain a powder. The fabricated nanobelts were annealed at 700 ^oC for 1 h to form TNB.

4.2.2 Materials and photoelectrochemical characterization

The crystal phase and morphology of TNB were determined by XRD, Raman, SEM, and HRTEM. The specific surface area of TNB was determined by BET and the bandgap energy was determined by UV–Vis spectroscopy– Diffuse Reflectance Spectroscopy. The general method for the use of the each of the aforementioned instruments is mentioned in **Section 3.1**. A photoelectrochemical setup and its related tests were described in **Section 3.2** and used to determine the photovoltage, photocurrent density, and EIS characteristics of TNB. A xenon lamp was switched on and off at 5 min intervals to determine dark current and photocurrent densities.

4.2.3 Surface adsorption using a slurry batch reactor

The general method of this test was referred to in **Section 3.3.1.1**. Surface adsorption experiments were carried out by dispersing 40 mg of TiO_2 nanomaterial into a Pyrex beaker containing 200 mL of naproxen, carbamazpine, and theophylline solutions of varying concentrations in the dark, at room temperature, with adsorption accelerated by magnetic stirring for 90 min at 300 rpm.

4.2.4 Photocatalytic degradation tests using a slurry batch reactor

Photocatalytic degradation was assessed under the same conditions as surface adsorption experiments, but in the presence of UV illumination using a 100 W middle pressure mercury lamp (UVP, Blak-Ray® Model B 100AP) at 365 nm. The distance between the UV lamp surface (quartz) and surface of the water matrix was 5 cm with an intensity of 2.1 mW cm^{-2}. To saturate the surface sites of TNB before photocatalytic degradation, each solution was first stirred in the dark for 30 min. Subsequently, the UV lamp was turned on and the photocatalytic degradation experiment was conducted for 90 min. In order to determine the active radical species in the TiO_2-pharmaceutical solution, potassium iodide (KI) and isopropanol (i-PrOH) were used as selective radical scavengers during degradation. The concentration of KI and i-PrOH in the initial reaction solution were both 1 mM [13].

4.2.5 Analyte preparation and analysis

All samples were centrifuged at 3200 rpm for 30 min, after the aforementioned experiments, to remove TiO_2 for analysis. The procedure in **Section 3.3.2.1** was followed. The experiments were reproducible with errors less than 5 % (3 trials).

4.2.6 Kinetic modelling

4.2.6.1 Adsorption model

A pseudo-second-order equation was used to evaluate the adsorption and is given by [15]:

$$\frac{t}{q_t} = \frac{1}{kq_e^2} + \frac{1}{q_e}t \qquad \text{Eqn. 4.1}$$

$$q_t = \frac{(C_o - C_t)}{C_o} \qquad \text{Eqn. 4.2}$$

where q_t and q_e are adsorption capacities at time, t, and at equilibrium (g g^{-1}),
t is the time (min),
k is the initial adsorption rate constant,
C_o is the initial concentration (g L^{-1}), and
C_t is the concentration at time t (g L^{-1}).

The values of k and q_e are obtained from the linear plot of $\frac{t}{q_t}$ vs. t, and if the fit of the data is linear, it suggests that chemisorption takes places [16], [17].

4.2.6.2 Intraparticle diffusion model

The Weber-Morris Model was used to evaluate intra-particle diffusion from mass transfer processes and is given by [18]:

$$q_t = k_i t^{\frac{1}{2}} + c \qquad \text{Eqn. 4.3}$$

where k_i is the intra-particle diffusion rate constant ($min^{-1/2}$)
t is the time (min), and
c is a constant .

The intra-particle diffusion rate, k_i, may be separated into diffusion stages based on macro-, meso- and micro-pore- structures of the adsorbent [19], [20]. Plotting q_t vs. $t^{1/2}$ gives two linear sections of the curve demonstrating a transition from macro-pore diffusion to micro-pore diffusion. The slopes of the two diffusion regions give the intra-particle diffusion rate for that region.

4.2.6.3 Photocatalytic degradation model

The photocatalytic degradation can be described using a pseudo first-order kinetic model (Eqn. 3.5) and its integrated form (Eqn. 3.6) in **Section 3.3.2.4**.

4.3 Results and Discussion

4.3.1 TiO_2 nanobelt material analysis

Fig. 4.1a shows XRD patterns of TNB and P25. There are several characteristic anatase peaks that are seen in both samples, which come from {101}, {004}, {200}, {105}, {211}, {204}, {116}, {220}, and {215} planes. However, P25 does contain a minor amount of rutile, indicated by the presence of {110}, {101}, and {111} rutile diffraction peaks. Peak broadening of the TNB is observed indicating a decrease of crystalline grain sizes. The XRD results are confirmed by Raman analysis in Fig. 4.1b. The typical Raman modes of anatase – 395 cm^{-1}, 515 cm^{-1}, and 637 cm^{-1} – are clearly observed [16, 17], but the lower modes at 144 cm^{-1} and 197 cm^{-1} are out of the range of the device. There is also a small peak at 247 cm^{-1} in TNB , which is possibly due to a minor content of amorphous TiO_2 [18, 19].

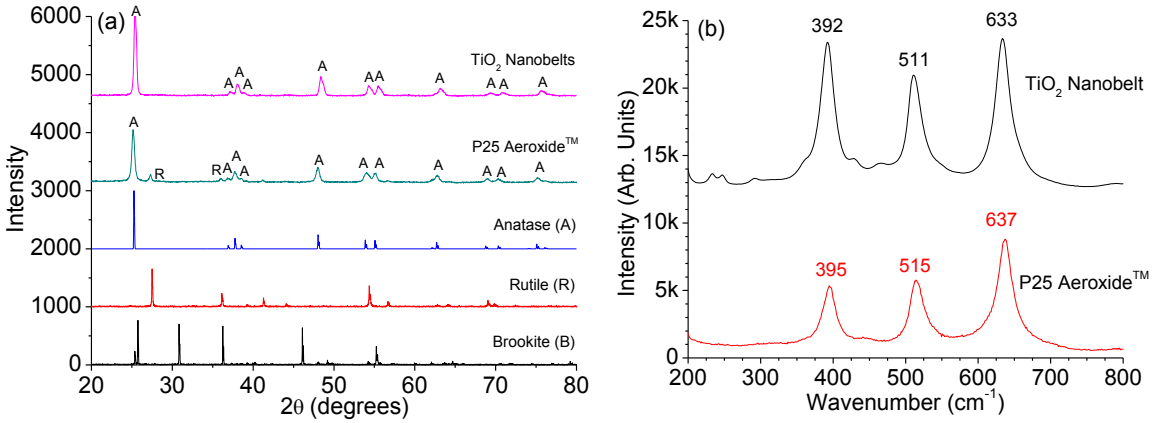

Figure 4.1: (a) X-ray diffraction patterns of synthesized TNB and P25; and (b) Raman spectra of TNB. Reproduced with permission from [13]

The field electron scanning electron microscopy (FESEM) images (Fig. 4.2) depict hierarchical TNB with widths ranging from 30-100 nm and lengths in the range of tens of μm. In addition, the specific surface area of the nanobelts obtained is 21.52 m^2 g^{-1}. It is also apparent that these hierarchical structures are not only composed of nanobelts, but also a small amount of truncated rods fused on the nanobelt surface (Fig. 4.2b).

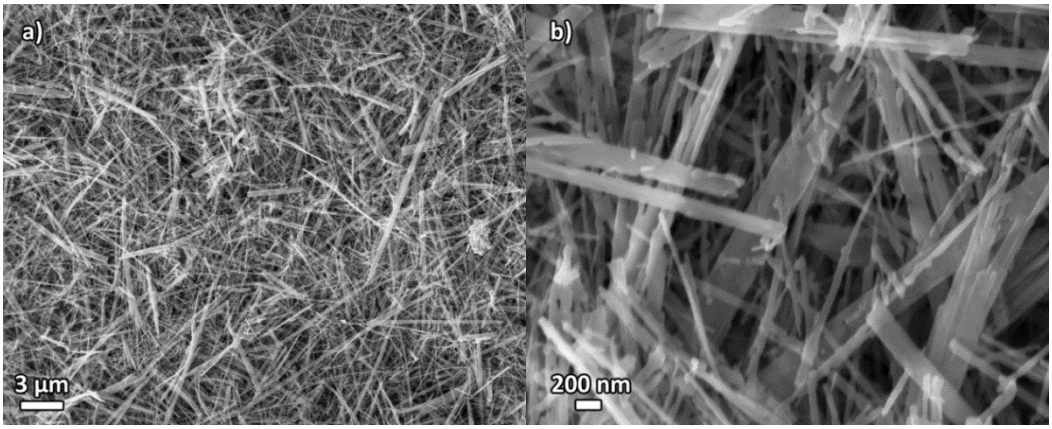

Figure 4.2: FESEM images of hierarchal TNB: (a) low magnification and (b) high magnification. Reproduced with permission from [13]

Using HRTEM, the detailed lattice structure of TNB shown in Fig. 4.3. A nanobelt with indexed selected area electron diffraction (SAED) was obtained in the highlighted area using a zone axis of [001] (Fig. 4.3b). The indexed SAED pattern indicates that the crystal structure is anatase, which is a tetragonal structure, in agreement with XRD and Raman results. Furthermore, the growth direction of the nanobelts is in the <100> direction, which is consistent with another

study [20]. Fig. 4.3b reveals the crystal lattice structure of the anatase TNB and the dominant crystal planes in the observed nanobelts from the d-spacing of the lattice, which is 3.8 Å, corresponding to the {100} family of planes.

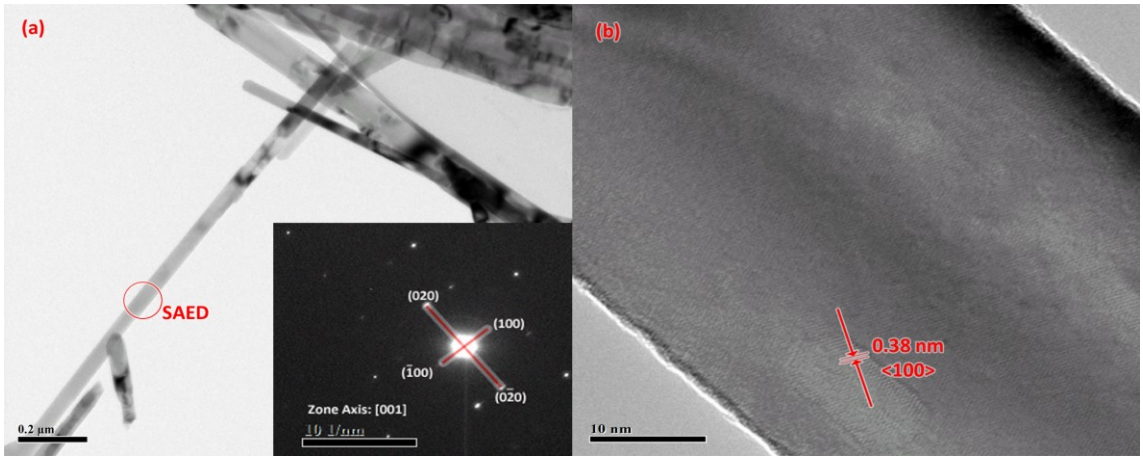

Figure 4.3: HRTEM images of hierarchical TNB: single nanobelt with indexed SAED pattern and (b) high resolution of nanobelts with crystal d-spacing of 0.38 nm. Reproduced with permission from [21]

The bandgap of TNB was determined by UV-Vis DRS and applying Tauc method (see **Section 3.1.3**). Using the Tauc method, the optical bandgap for TNB and P25 precursor were 3.23 eV and 3.06 eV, respectively. The P25 has lower bandgap energy than TNB because it is a mixture of anatase and rutile phases, whereas TNB are predominantly anatase. The rutile phase has a lower bandgap energy than the anatase phase [22]. The wide band gap is of importance to yield strong oxidizing hydroxyl radicals through photocatalytic degradation.

The TiO_2 nanobelt synthesis was typically conducted at 190 ^oC for 72 h in previous articles, and the time was reduced to 24 h at 250^oC. The synthesis method is capable of producing the TiO_2(B) phase, which can be transformed to anatase. TiO_2(B) attracts increasing interest due to its monoclinic structure with low-density crystal framework with larger channels and pores as compared to other titania polymorphs. However it is not as photoactive as the anatase phase [23]. The BET surface area of hydrothermal synthesized $H_2Ti_3O_7$ heat treated at 550 ^oC had a surface area of 88 $m^2\ g^{-1}$. Increasing the heat treatment to 700 ^oC reduced to surface area to 20 $m^2\ g^{-1}$. The sample treated at 550 ^oC is a combination of anatase and TiO_2(B), whereas the sample treated at 700 ^oC is anatase.

In Fig. 4.4a, the SAED image of 550 ^oC is indexed as predominantly anatase, however the HRTEM image indicates that TiO_2(B) crystalline grains are also present. The HRTEM image shows the interface between anatase and TiO_2(B). The (101) planes in anatase and (011) planes in

TiO_2(B) closely match and have similar lattice parameters. Increasing the calcination temperature from 550 ^oC to 700 ^oC converts TiO_2(B) into anatase. The d-spacings for TNB heat treatment at 700 ^oC were 0.35 nm and 0.45 nm, which match the (101) and (002) planes of anatase. The higher heat-treatment steps lower the defects and decreases the number of crystalline grain boundaries. Generally, higher surface area samples will have a greater number of lattice defects than low surface area samples [24].

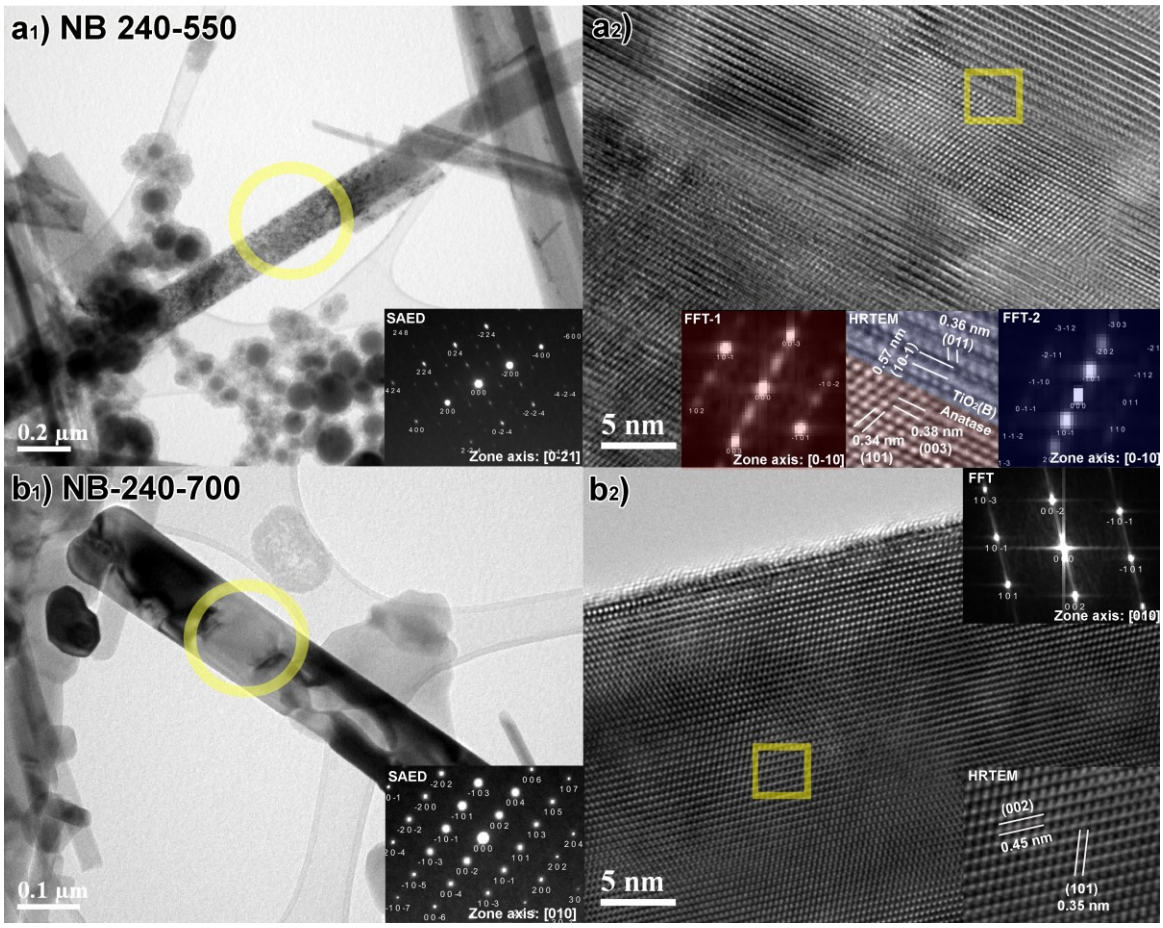

Figure 4.4: (1) TEM images with SAED indexed regions (yellow) and (2) HRTEM images corresponding to TNB samples heat treated at (a) 550 ^oC and (b) 700 ^oC

4.3.2 Photoelectrochemical properties of TiO_2 nanobelts

4.3.2.1 Intermittent photocurrent density

Fig. 4.5 shows that the photocurrent density of TNB under unfiltered and filtered (400 nm cutoff filter) xenon lamp irradiation in (a) 1M KOH and (b) 1M KOH + 100 mM glucose. In Fig. 4.5a, the photocurrent under unfiltered light is 4.0 µA cm^{-2}, whereas under filtered light (> 400 nm) it is less than 0.2 µA cm^{-2}. This demonstrates that photogenerated electrons are mostly

produced under UV irradiation of the TiO_2 nanomaterial. Adding glucose minimizes the direct charge carrier recombination in the film (Fig. 4.5b). The current density with glucose under unfiltered and filtered illumination is around 20 μA cm^{-2} and 1.0 μA cm^{-1}, respectively which is a 5-fold increase from the solution without glucose. The reduction of recombination processes can be seen during the 5 min interval under illumination where the current density increases after the onset of illumination to a threshold value, most probably due to photoadsorption of glucose onto the TiO_2 surface.

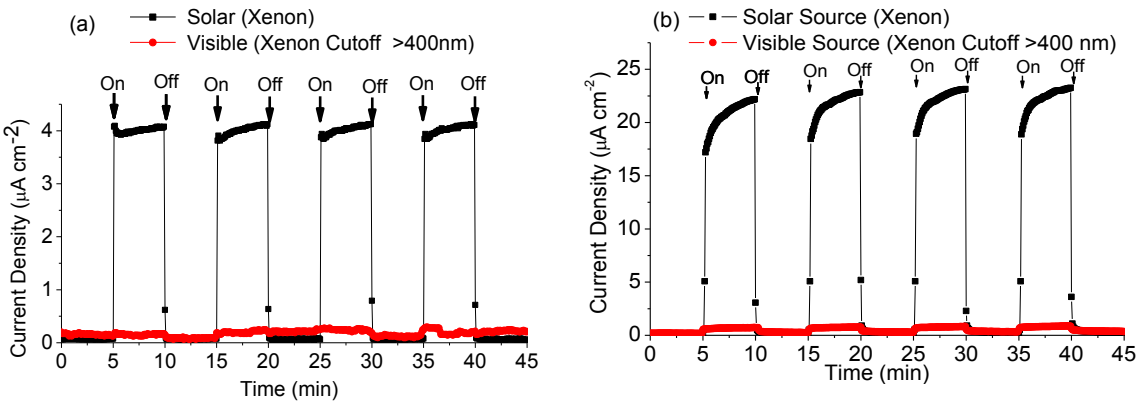

Figure 4.5: Photocurrent density of TiO_2 NW at - 0.3 $V_{Ag/AgCl}$ in 1 M KOH solution under unfiltered and filtered (400 nm cutoff) irradiation with (a) no glucose and (b) 100 mM glucose. Reproduced with permission from [25]

4.3.2.2 Open-circuit potential decay and electron lifetime

The TNB were investigated for electron recombination kinetics by monitoring the transient open circuit potential, V_{oc}, as a function of time after turning off the illumination source. Under open circuit conditions, electrons will accumulate within the semiconductor nanostructure film following solar light irradiation and shifting the apparent Fermi level to negative potentials. Once illumination has stopped, the accumulated electrons are slowly discharged because they are scavenged by redox species in the electrolyte [25]. The electron density in the conduction band decays sharply due to charge recombination, with the V_{oc} decay rate determined by the recombination rate. Fig. 4.6a shows the V_{oc} decay as a function of time after illumination has stopped based on the base solutions containing 100 mM glucose or no glucose. It is evident that the V_{oc} decay rate is slower in when glucose is added because glucose acts a hole scavenger thereby reducing electron recombination. From the V_{oc} decay rate, the lifetime of the

photogenerated electrons, the average time that the photogenerated electrons exist before they recombine, can be calculated using the following expression [26]:

$$\tau = -\left(\frac{k_B T}{e}\right)\left(\frac{dV_{oc}}{dt}\right)^{-1} \qquad \text{Eqn. 4.4}$$

where k_B is Boltzmann's constant (J K^{-1}),
T is the temperature (K), and
e is the elementary charge (C).

The calculated τ is plotted as a function of V_{oc} as seen in Fig. 4.6b. It is observed that the electron lifetime increases when glucose is added to the 1 M KOH base solution over the entire V_{oc} range.

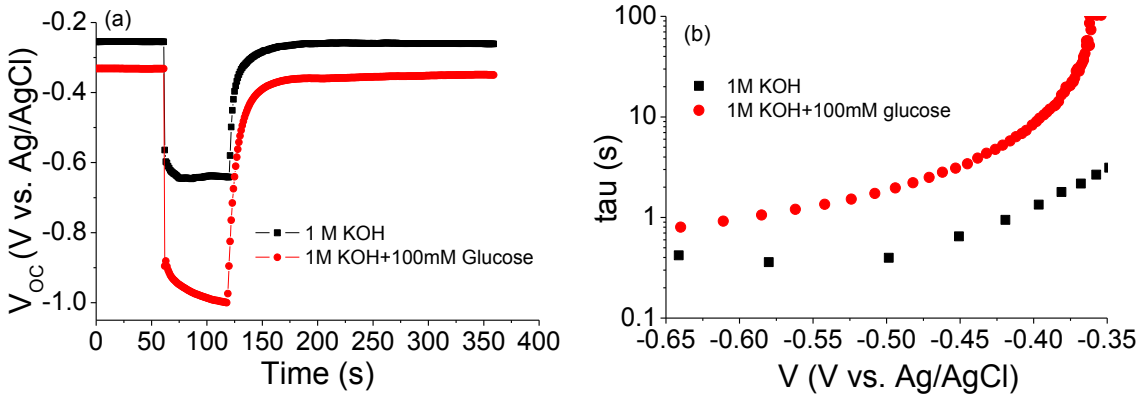

Figure 4.6: (a) Open-circuit potential of TNB under 150 W xenon lamp irradiation and (b) the corresponding electron lifetime as a function of the open circuit potential with respect to Ag/AgCl reference electrode using 1 M KOH and 1 M KOH + 100 mM glucose solutions. Reproduced with permission from [25].

4.3.2.3 Electrical characteristics of TNB/FTO under dark and illumination

It is well established that EIS Nyquist plots are associated with the charge transfer resistance and the separation efficiency of photogenerated electron-hole pairs at the semiconductor-electrolyte interface [27]. Fig. 4.7 depicts Nyquist plots of TNB under dark and under xenon lamp illumination. An equivalent circuit model was used to model the results from the Nyquist plot (Fig. 4.8). Circuit element parameters based on the electrical response from the Nyquist plot can be extracted and is effective in simulating coated samples [27]. In the circuit, R_s is the solution resistance; R_f and CPE_f are the resistance and capacitance of the film; R_{ct} is the electron charge transfer resistance; and CPE_{dl} is the double-layer capacitance. The elements C_f

and C_{dl} were replaced with constant phase elements (CPE) due to non-ideal capacitance response of the porous surface structure. The impedance of CPE is given by:

$$Z_{CPE} = \frac{1}{C_0(j\omega)^m} \qquad \text{Eqn. 4.5}$$

where C_o is the admittance magnitude of CPE (F) and
m is an exponential term (m = 1 represents ideal capacitance behavior).

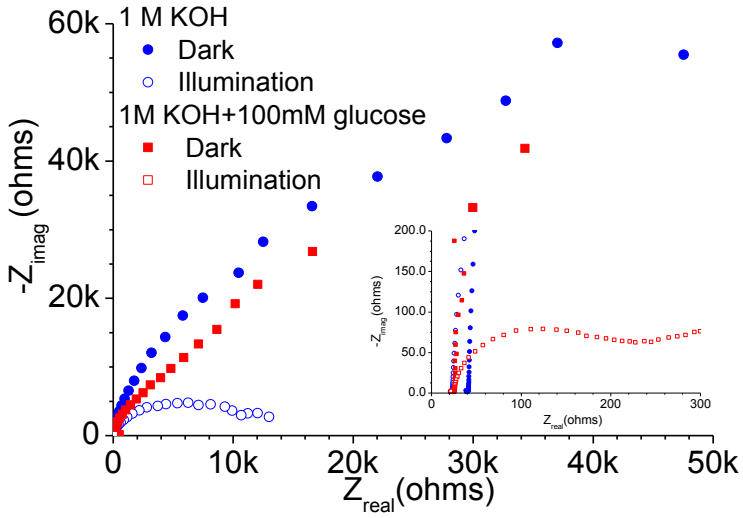

Figure 4.7: Nyquist plots of TNB in 1 M KOH (base) and base + 100 mM glucose solution under dark and xenon lamp conditions

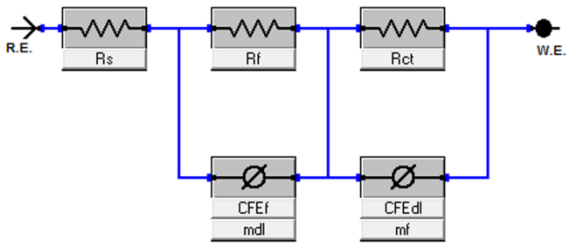

Figure 4.8: Equivalent circuit of TiO_2 film/FTO substrates. R_s is the electrolyte resistance; R_f and CPE_f are resistance and capacitance of the film; R_{ct} is the charge transfer resistance; and C_{dl} is double layer capacitance

The EIS was conducted in the absence and presence of UV illumination using two types of electrolytes – 1 M KOH and 1 M KOH + 100 mM glucose. Table 4.1 lists the parameters

obtained from Nyquist plots with the equivalent circuit shown in Fig. 4.8. The values of R_f under solar illumination in both electrolyte are smaller than those in the dark. The difference in R_f in the dark and under xenon lamp illumination is a 30-fold difference under 1 M KOH + 100 mM glucose and only 1.47-fold difference in 1 M KOH. The 30-fold difference is that glucose is an effective hole scavenger [28–30] and the holes produced from photocatalysis undergo an oxidation reaction with glucose, resulting in a decrease in the resistance of the film and more efficient separation of electrons and holes [27, 31]. The transfer of photogenerated electrons is expected to cause non-ideality in the film capacitance during xenon lamp illumination; this is evident in the decrease of m_f in both electrolyte solutions. In 1 M KOH solution, m_f decreased from 0.946 to 0.913. The addition of 100 mM glucose in 1 M KOH solution decreased m_f from 0.949 to 0.498.

Table 4.1: TNB EIS models of Nyquist plots under no potential bias conditions in 1 M KOH and 1 M KOH + 100 mM glucose

EIS model parameters	**TNB in 1 M KOH**		**TNB in 1 M KOH + 100 mM glucose**	
	Dark	**Illumination**	**Dark**	**Illumination**
R_s (Ω)	34.0	22.1	24.6	22.3
R_f (kΩ)	12.5	8.47	4.51	0.148
C_f (μF)	132	91.0	162	111
m_f	0.946	0.913	0.940	0.498
R_{ct} (kΩ)	11.3	5.40	72.5	0.491
C_{dl} (mF)	17.6	1.02	15.9	4.98
m_{dl}	0.970	0.955	0.990	0.952
χ^2	0.0116	0.00137	0.00709	0.00130

4.3.2.4 Effect of potential bias

A potential bias was applied to the TNB/FTO electrode and was swept from 0 to 1.0 $V_{Ag/AgCl}$ in dark and illuminated conditions as seen in Fig.4.9. The potential is increased to more oxidative values. Under dark conditions (Fig. 4.9a), the onset of glucose oxidation occurs at 0.28 $V_{Ag/AgCl}$ based on the increase in current density due to glucose acting as a hole scavenger. Electron-hole pairs are increasingly separated when the anodization potential is increased and recombination is decreased [32–34]. The addition of xenon light increases the current density

and oxidation reactions occurring as seen in Fig. 4.9b. At sufficiently high anodic potentials, larger than band gap of TNB, Schottky barrier breakdown occurs and holes are generated that react with the aqueous environment [32]. This anodic radical generation approach may be useful in environments where UV light cannot be used. The photocurrent become constant above a certain applied potential known as the saturation point, in which interfacial kinetics are fast and due to limitations of the hole capture [35].

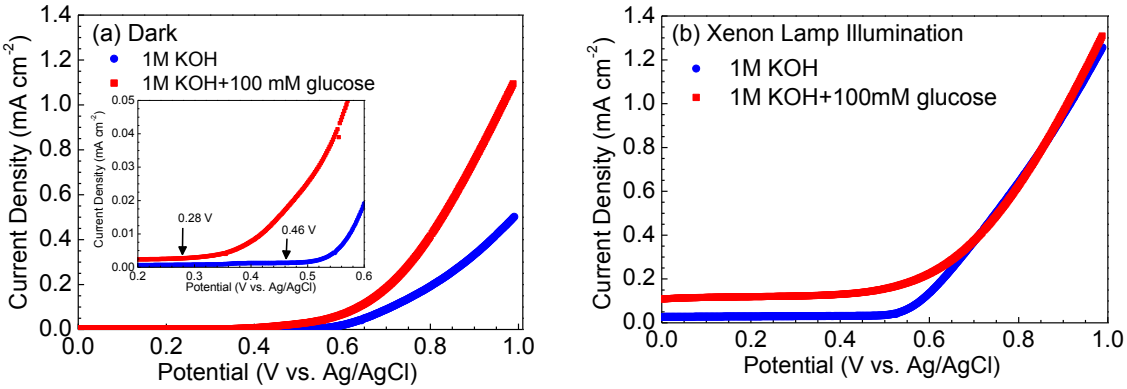

Figure 4.9: Linear sweep voltammograms of TNB/FTO substrates under (a) dark and (b) 150 W xenon lamp illumination in 1 M KOH and 1 M KOH + 100 mM glucose

4.3.3 Photochemical studies - single compound degradation

Synthesized TNB were used in a series on known persistent PPCPs and the photocatalytic degradation rates of their parent compounds in a slurry batch reactor were evaluated. High concentrations of PPCPs, compared to those found in drinking water effluents, were used because of detection limitations using UV-Vis spectroscopy. The photocatalytic degradation of theophylline was chosen due to conduct temperature, pH, radical generation, and concentration dependence studies. Typical dye studies contain contribution from non-catalytic side-reactions or artifact. Dye decolorization can occur from UV-irradiate titania, and can be degraded under visible light in some instances, such as indigo carmine dye. The decolorization of indigo carmine was complete by visible light, but the total organic carbon remained intact via photolysis. The loss of colour corresponds to electron transfer, which destroys the regular distribution of conjugated bonds within the dye molecule and causes its decolourization. Once transferred to TiO_2, the electron will participate to an additional ion-sorption of molecular oxygen as O_2:

$$S + h\nu \rightarrow S^* \qquad \text{Eqn. 4.6}$$

$$S^* + O_2 \rightarrow S^{\cdot+} + O_2{}^{\cdot-} \quad \text{Eqn. 4.7}$$

Free radicals form from homolytic scission processes and these radicals can react with dissolved oxygen generating peroxide radicals. The formation of reactive oxygen species and radicals lead to degradation of the parent compound.

4.4.3.1 Adsorption and photocatalytic degradation of single pollutants

Although, the BET surface area, and adsorption capacity of the TNB is lower (21.52 m^2 g^{-1}) than that of commercial P25 nanoparticles (50.69 m^2 g^{-1}), a greater photocatalytic degradation rate compared to P25 was reported in our earlier study for some pharmaceuticals, such as venlafaxine, fluoxetine, and sulfamethoxazole, but not others [36]. The photocatalytic degradation may be enhanced in some reactions using TNB due to differing charge transfer reactions and a decrease of grain boundary defects and size in one dimensional nanostructures [37]–[39].

The adsorption and photocatalytic degradation of theophylline was evaluated using kinetic models – pseudo-first-order, pseudo-second-order, and Weber-Morris – in Table 4.2. The pharmaceuticals were subjected to adsorption and photocatalytic degradation experiments using an initial concentration of 15 ppm without adjusting the pH. The adsorption for all pharmaceuticals follows a pseudo-second-order model and its intraparticle diffusion parameters may be found using a Weber-Morris plot; whereas the photocatalytic degradation follows a pseudo-first order model.

Table 4.2: Values obtained from pseudo-first-order, pseudo-second-order, and Weber-Morris models for dark adsorption and UV illumination. Reproduced with permission from [21]

Compound	Dark Adsorption					UV Illumination	
	Pseudo Second-Order Model			Weber-Morris Model		Pseudo-first-order Model	
	Initial Sorption Rate (kq_e^2, min^{-1})	Equilibrium Adsorption Capacity (q_e, mg g^{-1})	R^2	Intraparticle Diffusion Rate Constant 1 (k_1, min^{-1})	Intraparticle Diffusion Rate Constant 2 (k_2, min^{-1})	Apparent Photocatalytic Degradation Rate Constant (k_{ap}, min^{-1})	R^2
NPX	1.56×10^{-1}	4.51	0.962	3.10×10^{-3}	-2.00×10^{-3}	6.16×10^{-2}	0.957
THYP	7.58×10^{-2}	21.59	0.997	7.27×10^{-3}	-1.49×10^{-4}	9.12×10^{-2}	0.996
CBZ	3.66×10^{-2}	16.48	0.993	5.34×10^{-3}	-1.61×10^{-3}	2.91×10^{-2}	0.989

NPX – naproxen, THYP – theophylline, and CBZ - carbmazepine

The kinetic rates obtained from Table 4.3 indicated that theophylline is easily degraded compared to naproxen and carbamazepine using a UV/TiO_2 process from their apparent

photocatalytic degradation rate constants, k_{app} (See Fig. A1 and Fig. A2 in **Appendix A** for fitted curves). This is possibly due to a greater adsorption capacity (21.59 mg g^{-1}) than naproxen (4.51 mg g^{-1}) and carbamazepine (16.48 mg g^{-1}). In addition, the macropore diffusion rate, k_1, of theophylline onto the surface of TiO_2 is much higher than the other two pharmaceuticals suggesting that theophylline molecules are able to occupy available surface sites on TiO_2 quicker than the other two pharmaceuticals, thereby allowing radicals to oxidize this molecule sooner. However, the negative values of the intraparticle rate constant, k_2, seems to suggest that desorption rate increases in theophylline, carbamazepine, and naproxen after a certain period of time, where all macropore sites are occupied by the pharmaceutical adsorbents.

Giri et al. conducted a vast analysis of various AOP processes, including UV/TiO_2 anatase nanoparticles and UV/H_2O_2, with various pharmaceuticals at a concentration of 1 ppm [40]. From their data, naproxen has a k_{app} value of 6.23 x 10^{-2} min^{-1} and 7.51 x 10^{-2} min^{-1} under UV/TiO_2 nanoparticles and UV/H_2O_2, respectively. On the other hand, carbamazepine had a rate constant of 2.17 x 10^{-3} min^{-1} and 2.17 x 10^{-2} min^{-1} under UV/TiO_2 nanoparticles and UV/H_2O_2, respectively. These values are lower than our UV/TNB due to different nanostructures used, despite having an initial concentration in the order of magnitude less than the one reported here (15 ppm) and using a shorter wavelength UV source that is conducive to producing ·OH via photolysis.

When comparing the theophylline degradation under UV/H_2O_2 and UV/TNB processes (Fig. A3 in **Appendix A**), theophylline slowly degrades under 10 mM H_2O_2 (standard experimental concentration) with UV illumination (k_{app} = 3.65 x 10^{-3} min^{-1}), whereas the degradation performance using 0.25 mM TiO_2 under UV illumination is an order of magnitude greater (k_{app} = 5.68 x 10^{-2} min^{-1}). Theophylline degrades extremely slowly using only UV illumination at wavelengths of 365 nm and 254 nm is consistent with the research conducted by Kim et al. [41].

The pH of the TiO_2 suspension was altered by either adding dilute HCl or NaOH to acidify or alkalinize the solution. The pH of the TiO_2 slurry containing theophylline influences the surface ionization state of TiO_2 because it is amphoteric in nature in the following reactions:

$$TiOH + H^+ \rightleftharpoons TiOH_2^+ \qquad \text{Eqn. 4.8}$$

$$TiOH + OH^- \rightleftharpoons TiO^- \qquad \text{Eqn. 4.9}$$

The flatband potential of the TNB is a function of pH. When OH^- and H^+ ions are chemisorbed from aqueous solutions, at a certain pH value, the overall charge of the adsorbed ions will be at zero, or the isoelectric point (IEP). When the pH in the solution is close to the IEP of TiO_2, particles and other nanostructures tend to agglomerate. The TNB have positive charges on the surface in neutral water, according to another study, where TNB had a positive zeta potential of +9.65 mV at pH 7.0 [42].

The pH is also influenced by the adsorption and desorption of the reactants and intermediates of theophylline on the surface of TiO_2 because the increase in adsorption capacities in Table 4.3 suggests that the pH increases adsorption of theophylline onto surface sites of TiO_2 [43]–[45]. The adsorption capacity of TiO_2 roughly increases 4-fold from pH 4.0 (10.04 mg g^{-1}) to pH 10.0 (36.79 mg g^{-1}). Consequently, the apparent photocatalytic rate constants obtained in Table 5.2 indicate that the photocatalytic degradation increases with pH, and this observation has also been confirmed in other studies [46]–[48]. Furthermore, the increase in photocatalytic degradation may also be partially attributed to alkaline solutions tending to favour ·OH formation because they are formed between the reaction between OH^- ions, available from dissociated NaOH, and hole (h^+). HCl was used to acidify the TiO_2 solution, and the Cl^- ions from HCl are ·OH scavengers, thereby reducing the degradation rate of theophylline.

Table 4.3: Pseudo-second-order model values – photocatalytic degradation of theophylline at pH values of 4.0, 6.8, and 10.0. Reproduced with permission from [21]

pH	Dark Adsorption Pseudo-second-order Model			UV Illumination Pseudo-first-order Model	
	Initial Sorption Rate (kq_e^2, min^{-1})	Equilibrium Adsorption Capacity (q_e, mg g^{-1})	R^2	Apparent Photocatalytic Degradation Rate Constant (k_{app}, min^{-1})	R^2
4.0	1.93 x 10^{-1}	10.04	0.975	5.44 x 10^{-2}	0.953
6.8	7.60 x 10^{-2}	21.59	0.993	5.68 x 10^{-2}	0.984
10.0	4.97 x 10^{-2}	36.79	0.999	7.63 x 10^{-2}	0.847

4.3.3.2 Reactive oxygen species in theophylline

The reactive oxygen species has been studied previously in TiO_2 nanoparticles, where ·OH , h^+, and H_2O_2 are identified as dominant oxygen species [49, 50]. Table 4.4 lists the photocatalytic degradation rates when potassium iodide and isopropanol quenchers were added to the TiO_2-theophylline slurry. Potassium iodide is used to scavenge valence band holes and hydroxyl radicals, whereas isopropanol is selective to hydroxyl radials [50]. From the photodegradation rates, the ·OH contribution to the reaction was 75 % and the h^+ concentration was determined to be 20 %. The contribution of other reactive oxygen species, which include

H_2O_2, $HO_{2\cdot}$, and O_2^- is around 5 %. Surface hydroxyls scavenge valence holes to eventually produce ·OH , which are the primary oxidizing species in photocatalytic reactions [51–53]. Although, theophylline's effect on the results [54] was mitigated by increasing the isopropanol concentration to 1 mM, from 0.1 mM, as established in previous studies [50, 55].

Table 4.4: Apparent rate constants of theophylline and composition of reactive oxidative species determined using isopropanol (1 mM) and potassium iodide (1 mM) quenchers. Reproduced with permission from [21]

Conditions	Rate constant (x 10^{-2} min^{-1})	R^2
No quencher	5.69	0.984
Potassium iodide (1 mM)	0.29	0.958
Isopropanol (1 mM)	1.42	0.981

4.3.3.3 Temperature effects

Photocatalytic systems generally do not require heating and are able to operate at room temperature. However, the apparent activation energy is often a small value at a certain temperature range [56]. The apparent activation energy, k_A, can be measured using the Arrhenius equation (Eq. 4.10):

$$k_A = Ae^{-\left(\frac{E_a}{k_b T}\right)} \qquad \text{Eqn. 4.10}$$

where E_a is the apparent activation energy (J),
k_b is the Boltzmann constant (J K^{-1})
A is the pre-exponential factor, and
T is the temperature (K).

The apparent activation energy, E_a, is obtained from the slope of the $\ln(k)$ vs. $1/T$ plot (Fig. 4.10). The obtained apparent activation energy from the temperature range of 4 ^oC to 60 ^oC is 0.35 kJ mol^{-1}, which is similar to the dye compound degradation using Degussa P25 nanoparticles obtained in other studies [57, 58]. The true activation energy depends on other parameters, which include light flux and oxygen concentration [57].

The photocatalytic degradation rate increases as a function of temperature at a range of 4 ^oC to 60 ^oC as seen in Table 4.5 (See Fig. A4 in Appendix A for temporal degradation curve). In other words, the diffusion of theophylline onto the TNB surface is temperature dependent.

Increasing the temperature increases the diffusion rate of theophylline onto TNB surface, and hence the photocatalytic degradation rate of the adsorbed pharmaceutical. An increase in temperature also helps the photocatalytic reaction to complete much more efficiently with electron-hole recombination [57].

Table 4.5: Apparent rate constants of theophylline at temperatures of 4 ^{o}C, 20 ^{o}C, 40 ^{o}C, and 60 ^{o}C. Reproduce and modified with permission from [21]

Temperature (^{o}C)	**Rate constant (x 10^{-2} min^{-1})**	**R^2**
4	1.70	0.974
20	5.70	0.984
40	6.70	0.984
60	10.2	0.983

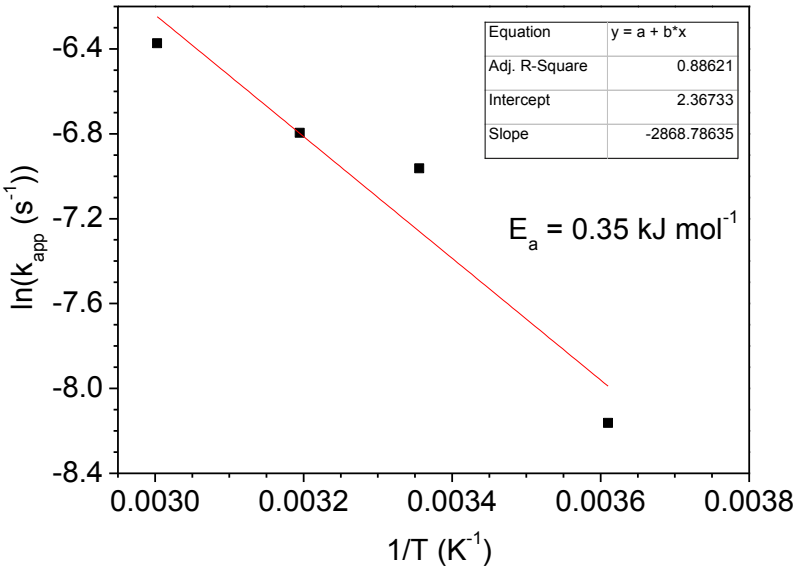

Figure 4.10: Activation energy from temperature range of 4 ^{o}C – 60 ^{o}C is 56.2 J mol^{-1}. Reproduce and modified with permission from [21]

4.3.3.4 Concentration effects

The effect of pharmaceutical concentration on UV/TiO_2 photocatalytic degradation was evaluated in Table 4.6 (See Fig. A5 in Appendix A for temporal degradation curve). At 3.0 ppm, 30 ppm, and 300 ppm the apparent degradation rates of theophylline were 1.46 x 10^{-1} min^{-1}, 5.67

x 10^{-2} min^{-1}, and 8.20 x 10^{-3} min^{-1}, respectively. For every magnitude increase in concentration of theophylline, the apparent degradation rate of theophylline would decrease at a rate of 0.0688 per ppm per min for concentrations from 3 ppm to 300 ppm. At 30 min, the removal ratio of theophylline is 99 %, 68 %, and 11 % for an initial concentration of 3 ppm, 30 ppm, and 300 ppm, respectively. Additionally, the total mass degraded over a span of 90 min was 15 mg, 100 mg, and 165 mg for an initial concentration of 3.0 ppm, 30 ppm, and 300 ppm.

Table 4.6: Photocatalytic degradation of theophylline at concentrations of 3 ppm, 30 ppm, and 300 ppm. Reproduced with permission from [21]

Compound Concentration (ppm)	**Rate constant (x 10^{-2} min^{-1})**	**R^2**
3	14.56	0.982
30	5.67	0.991
300	0.81	0.975

4.4 Summary

In this chapter, TNB were characterized and its photoelectrochemical properties using TiO_2 photoanodes were assessed. The photochemical properties under slurry batch reactor using a model pollutants. The following major conclusions from this work are listed below:

(1) A facile hydrothermal method was used to synthesize TNB that were grown in the {100} family of planes and of anatase phase and calcination lowered the number of lattice defects.

(2) The photocatalytic efficiency of TNB/FTO electrode can be improved, through the prevention of electron-hole recombination, with the use of h^+ scavengers and increasing the anodization potential of the electrode with respect to the reference electrode.

(3) The charge transfer and film resistances of the TiO_2/FTO electrode decreases under xenon lamp illumination and high anodization potential, therefore increasing efficiencies for redox reactions to occur on the electrode.

(4) TNB suspensions under UV illumination were able to degrade the model compound theophylline – through the generation of holes, hydroxyl radicals, and other oxidizing radical species - of which the reaction with holes was the major contributor to the degradation rate.

(5) TNB photochemical experiments show that a high reaction temperature, alkaline (high pH) conditions, and low pollutant concentration increase the photodegradation of theophylline.

5.0 Photocatalytic Degradation using Ag-TiO_2 Nanobelts under UV-LED Controlled Periodic Illumination

Overview

In this chapter, three methods were used to investigate and improve the efficiency of UV/TiO_2 slurry systems: (i) synthesizing one-dimensional TiO_2, (ii) forming Schottky junctions, and (ii) UV-LED controlled periodic illumination (CPI). These parameters were monitored using the formation of 2-hydroxyterephthalic acid (HTPA) as a probe molecule. In order to improve charge separation in TiO_2, one-dimensional TiO_2 nanobelts (TNB) were synthesized using a hydrothermal method (**Chapter 4**) and Ag nanoparticles were deposited on these nanobelts (Ag-TNB) to form metal-semiconductor junctions. Ag-TNB was found to have HTPA formation rate greater than 1.33 and 2.59 times than that of P25 and TNB, respectively, under continuous illumination. UV-LED CPI was explored to control low photonic efficiencies so the HTPA formation rate was normalized by illumination period and compared at various duty cycles from 10% to 100%. At a duty cycle of 10%, normalized HTPA formation rate was 1.75, 1.40, and 0.70 times the HTPA formation rate at continuous illumination for commercial TiO_2 (P25), TNB, and Ag-TNB nanomaterials, respectively. The pulse frequency was increased by orders of magnitude from 0.05 Hz to 25 Hz and it was found that generally the HTPA formation rate was greater under higher frequencies for Ag-TNB and P25 samples. It was found that Ag-TNB was an effective photocatalyst using CPI by demonstrating photon-limiting behaviour when lowering the duty cycle.

5.1 Introduction

Photocatalysis has applications in environmental remediation such as air pollution control and water treatment [1]. The limitations of conventional TiO_2 photocatalysis prevents it from being fully utilized in advanced oxidation processes in water treatment because it relies solely on UV radiation or higher energy wavelengths to generate electron-hole pairs. In addition, recombination losses are inherent in semiconductors which subsequently reduces their overall efficiency [2].

There have been attempts to increase the photonic efficiency and visible light absorption by optimizing material properties and/or physical operational parameters. The photonic efficiency may be improved by changing the material properties of TiO_2 . For instance, decreasing the bandgap energy of TiO_2 via metal [3, 4]and non-metal doping [5–8] have been increasingly used

as this allows TiO_2 to absorb visible light and generate electron-hole pairs from lower energy wavelengths in the visible range. Other studies have attempted to reduce recombination losses by creating metal-semiconductor (Schottky) junctions [9–12] or synthesizing 1-D TiO_2 nanomaterials (nanowires, nanorods, and nanotubes) that have greater electron transport than nanoparticles [13–16].

Operational parameters of TiO_2 photocatalytic processes such as catalyst concentration, light intensity, pH, temperature, and adding additional oxidant sources have been explored to optimize photonic efficiencies [17]. Addition of pH adjusting chemicals and adjusting temperature adds costs. Advanced oxidation processes combining TiO_2 photocatalysis with chemical oxidants such as hydrogen peroxide and ozone have been attempted and have shown improvement in removal, but also comes at additional cost [18–22].

Increasing the light irradiance will lower the photonic efficiency [17]. The photocatalytic reaction order is dependent on the irradiance and may be described in three regimes: (i) low, (ii) intermediate, and (3) high irradiance. At the low irradiance regime, the reaction rate is linearly proportional to the irradiance. At intermediate intensity, the reaction rate varies by the square root of the irradiance. At high intensity, the reaction rate is independent of the irradiance [23]. Because of the latter two irradiance regimes, photocatalysis suffers in efficiency at higher intensities. UV-LEDs are more favourable at lower power compared to mercury lamps, especially under low pollutant concentrations [24].

Most photocatalytic studies until recently were conducted using low and medium pressure mercury lamps as UV light sources [25, 26]. However, they suffer from warm-up time, reliability, durability, and efficiency [27, 28]. Other studies have focused on using solar radiation in TiO_2 applications [29, 30] but are only feasible in locations where solar radiation is abundant. The advent of high power LEDs has increased the widespread adoption of LEDs for general lighting and other applications. LEDs are more efficient because the quantum yields are close to unity. LEDs also have higher lifetimes than mercury lamps [31]. Furthermore, mercury lamps cannot be alternatively turned on and off effectively in the millisecond time-scale. Based on previous studies, LEDs under controlled periodic illumination (CPI) was more effective for photocatalysis using xenon lamp illumination and a mechanical shuttering system [28, 32].

One way to reduce recombination is to introduce noble metals such as gold [33], platinum [3], [34], palladium [35], and silver [36, 37] to serve as electron sinks for photogenerated electrons, facilitating electron transfer to electron acceptors, such as dioxygen. Recombination is controlled by the formation of a Schottky barrier between surface metal particles and semiconductor photocatalyst [38]. Besides the reduction of recombination, the use

of silver is beneficial due to being a: (i) relatively inexpensive noble metal compared to other noble metals, (ii) an effective and known disinfectant [39], and (iii) thermal catalysis from localized surface plasmon resonance (LSPR) effect to prevent deactivation of photocatalysts [40] .

The objective of this study was to explore the effect of CPI on the photonic efficiency of UV-LED irradiation TiO_2 process in a batch slurry reactor by using the temporal decomposition of terepthlatic acid as molecular probe. The decomposition of malachite green was also assessed under continuous illumination. In this study, three procedures were used to decrease recombination processes: (i) conversion of nanoparticles into a one dimensional TiO_2 nanobelt, (ii) addition of silver nanoparticles onto TiO_2, and (iii) the utilization UV-LED controlled CPI processes. The effects of UV-LEDs under various duty cycles were explored. Ag-TiO_2 nanobelts and TiO_2 nanobelts were compared with commercial P25 nanoparticles under controlled periodic illumination to increase kinetic rates by preventing charge carrier recombination.

5.2 Experimental Methods

5.2.1 Reagents and chemicals

Titanium Dioxide (P25 Aeroxide^{TM}), silver nitrate ($AgNO_3$), hexamethylenetetramine (HMTA), hydrochloric acid (HCl), and sodium hydroxide (NaOH) were used in TiO_2 synthesis procedures. Terephthalic acid (TPA) and malachite green (MG) were used as model pollutant compounds for photocatalytic experiments. All materials were purchased from Sigma-Aldrich. Ultrapure water was obtained from a MilliQ water purification system which was operated at 18.2 MΩ·cm resistivity and <5 µg/L total organic carbon (TOC) at 25 ^oC (EMD Millipore).

5.2.2 TiO_2 synthesis methods

5.2.2.1 TiO_2 nanobelt synthesis

TiO_2 nanobelts (TNB) were synthesized using a modified hydrothermal method [41] developed in **Chapter 4**. The following changes were made to the method: (i) $Na_2Ti_3O_7$ nanobelts were grown for 24h in 60 mL NaOH (10 M) alakaline solution at 250 ^oC and (ii) $H_2Ti_3O_7$ nanobelts were annealed at 700 ^oC for 2h.

5.2.2.2 Ag-TiO_2 nanobelt synthesis

$H_2Ti_3O_7$ nanobelts from the TNB synthesis were used in the preparation of Ag-TNB. In a solution containing 60 mL of 0.02 M H_2SO_4, 1 g of the precursor was added in the acid digester and kept at 100 ^oC for 12 h. The products were centrifuged, washed with ultrapure water several

times, and dried at 70 ^{o}C overnight. The hydrogen titanate, $H_2Ti_3O_7$, obtained by acid treatment was heated at 700 ^{o}C for 2 h to for TiO_2 nanobelts. A hydrothermal method was used to create nano-heterostructures of Ag nanoparticles on TiO_2 nanobelts [37]. 1 g of treated TiO_2 nanobelts were put into a 125 mL acid digested containing 60 mL of 1 mM $AgNO_3$ and 2 mM HMTA. The acid digester was heat treated for 4 h at 100^{o}C. Silver ions in solution were removed my washing with ultrapure water, centrifuging samples, and decanting the supernatant. This process was repeated three times. The Ag-TNB was dried in the furnace at 80^{o}C for 8h.

5.2.3 Nanomaterial characterization

The crystal phase and morphology of TNB were determined by XRD, Raman, and SEM. The specific surface area of TNB was determined by BET and the bandgap energy was determined by UV–Vis spectroscopy–Diffuse Reflectance Spectroscopy. Details on the use of the aforementioned instruments are mentioned in **Section 3.1**.

The isoelectric point (IEP) of engineered nanomaterials was obtained measuring the zeta potential of the nanomaterial at pH values ranging from 3 to 10. Zeta potential measurements were conducted with 0.1 g L^{-1} in ultrapure water and adjusted to various pH values using NaOH or HCl. No salt, such as NaCl, was added as is the case with methods used by others to measure zeta potential in order to simulate experimental conditions [42]. The zeta potential analyzer was programmed to six measurements for each sample.

5.2.4 Standardization and setup

A schematic of the UV-LED/TiO_2 process under pulsed-width modulation (PWM) is shown in Fig. 5.1. More details on the setup is mentioned in **Section 3.3.1.1**. A PWM script (See Section B1 in Appendix B) was programmed into the controller. The light pulse frequency,v, and duty cycle, γ, of UV-LEDs was controlled with various illumination and dark periods listed in Table 5.1.

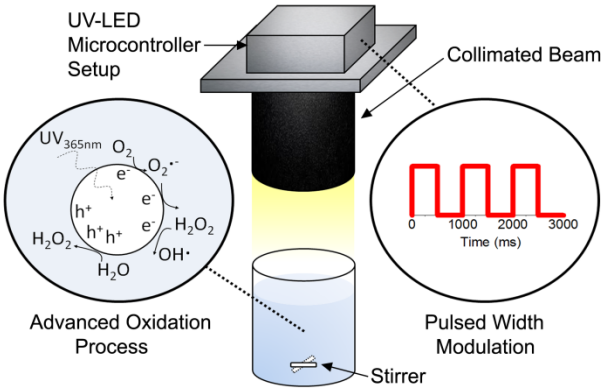

Figure 5.1: Schematic of UV-LED/TiO_2 advanced oxidation under pulsed width modulation

Table 5.1: Light profiles for continuous and periodic illumination showing duty cycle and frequency of pulsing

Duty Cycle (γ)	**Average UV intensity ($mW\ cm^{-2}$)**	**t_{on} (ms)**	**t_{off} (ms)**	**Period (ms)**
Duty cycle experiments at constant frequency				
10%	0.217	100	900	1000 (1 Hz)
25%	0.544	250	750	
50%	1.080	500	500	
75%	1.632	750	250	
100%	2.177	Continuous illumination		
Frequency experiments at constant duty cycle				
50%	1.080	10000	10000	20000 (0.05 Hz)
50%	1.080	1000	1000	2000 (0.5 Hz)
50%	1.080	100	100	200 (5 Hz)
50%	1.080	20	20	40 (25 Hz)

5.2.5 Photocatalytic degradation

5.2.5.1 Malachite green degradation and pseudo-first kinetics model

A stock solution containing 60 ppm MG was prepared by dissolving MG (60 mg) in 1 L of ultrapure water. Three replicates of MG solution (300, 10 ppm) were made by mixing 60 ppm MG stock (50 mL) and 250 mL of ultrapure water. P25, TNB, and Ag-TNB were TiO_2 nanomaterials that were tested. In each test, TiO_2 nanomaterials were added to each replicate for a

final concentration of 0.1 g L^{-1}. The beakers were placed in the multi-position stir plate and the solutions were stirred at 600 rpm for the duration of the experiment.

A 60 min equilibration period for adsorption of MG solution onto TiO_2 nanomaterials was allowed prior to UV exposure. Aliquots were sampled throughout the 300 min time span of the experiment. The samples were centrifuged at 5000 rpm for 5 minutes to remove TiO_2 nanomaterials from solution. The supernatant was then transferred to a 96 well-plate for MG degradation analysis. The endpoint adsorption of MG was measured at a wavelength of 615 nm against a calibration curve. The photocatalytic degradation of MG was evaluated using pseudo-first order kinetics (**Section 3.3.2.4** in **Chapter 3**) derived from Langmuir-Hinshelwood kinetics [43]. The experiments were conducted in triplicates and the standard deviation was calculated.

5.2.5.2 TPA degradation and HTPA formation kinetic model

A similar TPA degradation and HTPA fluorescence method was used from work conducted previously [44]. In a beaker, 0.3 L of 0.5 mM TPA was dissolved in 6 mM NaOH solution. TiO_2 nanomaterials were added to the solution with a TiO_2 concentration of 0.1 g L^{-1}. The experiments were conducted under illumination for 240 min and aliquots (1 mL) were taken at several time points.

TPA undergoes a reaction with a hydroxyl radical, producing 2-hydroxyterephthalic acid (HTPA)[44], [45]. The HTPA concentration was monitored using a fluorescence plate reader (SpectraMax M3, Molecular Devices). Under excitation mode (λ_{ex} = 315 nm), a emission spectra from 350 – 550 nm was used. A HTPA standard curve was included in the plate to quantify the amount of HTPA formed during TPA degradation. The standard curve was generated from the intensity of the peak emission wavelength of each spectrum.

The formation constant rate, k_1, of HTPA, which is the first degradation product of TPA, was studied. In the first minutes of the experiment, there is an excess of TPA and the concentration of HTPA rapidly increases (first reaction step – formation of HTPA) due to the oxidation of TPA by holes and/or hydroxyl radicals formed on the surface of the TiO_2 nanomaterial. As the HTPA concentration increased over time, its degradation rate also increases (second reaction step). An equilibrium concentration is reached, in which the rates of formation and degradation of HTPA are equal. A simplified kinetic model for HTPA was proposed by Černigoj et al. [45]:

$$\frac{dC_{HTPA}}{dt} = k_1 - k_2 C_{HTPA} \quad \text{Eqn. 5.1}$$

where C_{HTPA} represents the molar concentration of HTPA (mol L^{-1}),
k_1 represents the zero-order HTPA formation rate (min^{-1}), and
k_2 represents the pseudo-first order kinetic degradation rate (min^{-1}).

The fitting function was represented by the equation [45]:

$$C_{HTPA} = \frac{k_1}{k_2}\left(1 - e^{-k_2 t}\right) \quad \text{Eqn. 5.2}$$

In order to compare the photocatalysts used in the study, only the initial rate constant k_1 (first reaction step) was considered. The experiments were conducted in triplicates and the standard deviation was calculated.

5.3 Results and Discussions

5.3.1 Materials characterization

Three types of TiO_2 nanomaterials were investigated: P25, TNB, Ag-TNB and their material characteristics are given in Table 5.2 (See Fig. B1 in Appendix B for (a) Tauc plot, (b) Raman spectra, and (c) zeta potential). The SEM images of the nanomaterials are shown in Figure 1. P25 has clustered particles that range from 10 – 30 nm, which is in the range of the 21 nm average particle size reported from the manufacturer. TNB images show nanobelts that range from 20 to 100 nm in width and μm lengths. This size distribution is consistent with previous studies [46, 47]. The TNB samples are also composed of nanoparticles and truncated rods fused on the surface of the nanobelt. Ag-TNB images are similar in morphology to TNB samples and show no obvious Ag nanoparticles on the TNB. However a purple tinge can be seen by observation in Fig. B1d. Because of the growth along one dimension and large structure than P25, the synthesized one dimensional TiO_2 nanomaterials settled faster in aqueous solution. The zeta potential can describe the stability of the dispersion and the average values obtained for P25, TNB, and Ag-TNB were -12.15 mV, -6.45 mV, and -8.6 mV, respectively, at the experimental pH of 11 used in this study. P25 is more stable than the synthesized nanomaterials in solution, however all the nanomaterials will settle over time under a zeta potential magnitude of less than 30 mV under no external agitation.

All three nanomaterials are of anatase phase as confirmed through Raman spectroscopy with characteristic peaks as referenced through the RRUFF online database (R060277 and R050417). This is also confirmed through diffuse reflectance spectroscopy in which the bandgap energy is between 2.95 – 3.2 eV, characteristic for TiO_2 anatase and indicates that only radiation below 400 nm is capable of generating electron-hole pairs in all samples.

The surface area can impact adsorption capacity and photocatalytic activity, though the latter does not a correlate linearly to surface area; it depends on the other factors such as the contents of the water matrix used. The BET surface area of P25, TNB, and Ag-TNB were and 57 20, and 87 $m^2 g^{-1}$, respectively. TNB has a lower surface area due to fusing of P25 nanoparticles during the hydrothermal process, reducing the overall surface area compared to P25. Ag-TNB has a higher surface area due to the acid corrosion step preceding Ag deposition than increases porosity.

Table 5.2: Material Characterization of TiO_2 nanomaterials

Material Measurement	P25	TNB	Ag-TNB
BET Surface Area ($m^2 g^{-1}$)	57	20	87
DFT Pore Volume ($cm^3 g^{-1}$)	0.12	0.03	0.24
Zeta potential at TPA (mV)	-12.15	-6.45	-8.6
Bandgap energy (eV)	3.02	2.95	3.20
Crystal phase (Raman)	Anatase/Rutile	Anatase	Anatase

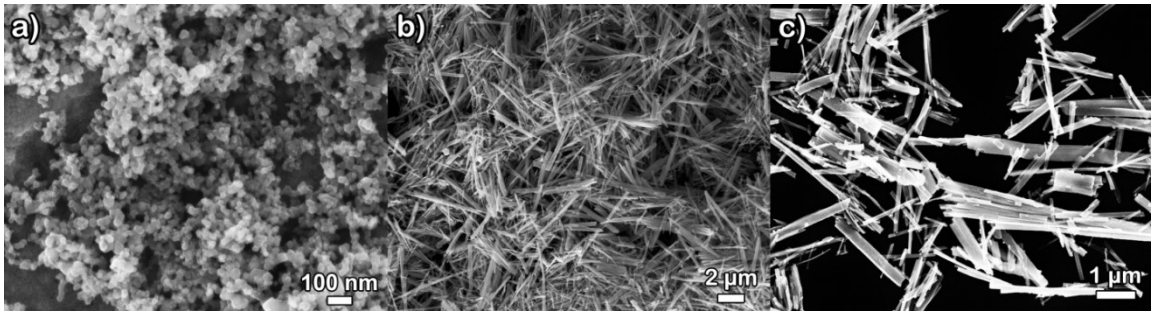

Figure 5.2: FESEM images of (a) P25, (b) TNB, and (c) Ag-TNB

5.3.2 Photocatalytic performance under continuous illumination

HTPA formation rate from TPA degradation and MG apparent removal rate coefficients were determined using P25, TNB, and Ag-TNB (Fig. 5.3). MG was used as a model dye pollutant similar to many studies that use dye pollutants to compare various catalysts and is not as

susceptible to dye decolourization under UVA radiation compared to visible light irradiation [24]. There was no statistical difference between the absolute kinetic rate coefficients of P25 and TNB, however there was a difference with Ag-TNB ($p < 0.017$) for both MG removal and HTPA formation rates (Table B2-A for one-way ANOVA test). . Even though the P25 and TNB have similar TPA formation rates, the recombination rate of one-dimensional TiO_2 is generally lower when compared to nanoparticles due to a decrease of grain boundary defects when joining nanoparticles into a one-dimensional structure, which decreases charge transfer resistance [48], [49].

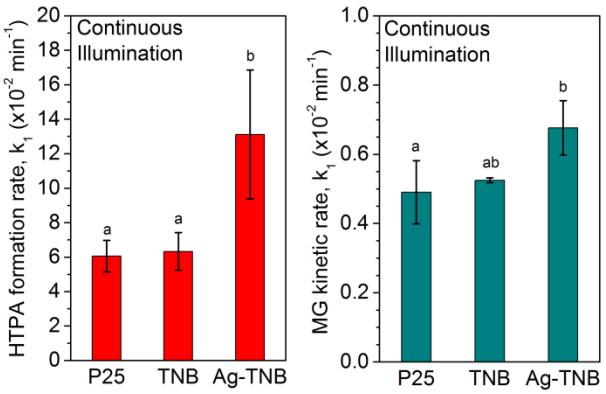

Figure 5.3: HTPA and MG kinetic rates for P25, TNB, and Ag-TNB nanomaterials. Bars that do not share a common letter are significantly different at $\alpha = 0.05$ significance level as determined by one-way ANOVA using the Holm-Sidak post-hoc test.

5.3.2.1 *Electron lifetime of TiO_2 nanoparticles compared to nanobelts*

To test that nanobelts have a lower recombination rate than nanoparticles, the electron lifetime of the nanomaterials were compared. P25 nanoparticles and TNB were cast on fluorine-tin oxide (FTO) glass using an electrodeposition method and tested using a photoelectrochemical setup (See Section B2 and B3 in Appendix B). Under open circuit conditions, the photogenerated electrons accumulate within TiO_2 photoanode and react with is aqueous environment. At steady state conditions, the rate of electron accumulation reaches equilibrium with the rate of electron loss [50, 51]. The electron lifetime of the photoelectrode can be found from the change in open circuit potential, V_{OC}, upon termination of UV illumination. Electron recombination kinetics at the semiconductor interface can be analyzed from the decay rate. The decay rate can be calculated via the following equation [50–52]:

$$\tau = -\left(\frac{k_B T}{e}\right)\left(\frac{dV_{OC}}{dt}\right)^{-1} \qquad \text{Eqn. 5.3}$$

where k_B is Boltzmann constant (J K^{-1}),
T is the temperature (K), and
e is the elementary charge (C).

The TNB film has an electron lifetime approximately one order of magnitude longer than the P25 NP film (Fig. 5.4b). This suggests that TNB supresses the recombination pathways at the photoanode interface better than TiO_2 nanoparticles. Even though the electron lifetime is greater using nanobelts compared to nanoparticles, there is no statistical significant difference between the P25 and TNB in HTPA formation rate or MG removal rate (Table B2-A). However, this may be attributed to the higher surface area in P25 (57 m^2 g^{-1}) compared to TNB (20 m^2 g^{-1}). TNB is also more prone to aggregation when dispersed in solution due to increased size in one dimension (μm range) compared to nanoparticles.

Generally, it is the case that the higher the surface area of the TiO_2 nanomaterial, the higher the apparent reaction rate. The zeta potential magnitude of nanobelts is lower than P25, which indicates that TNB will aggregate faster compared to P25 nanoparticles due to lower repulsion forces. The addition of Ag on TNB improved the electron-hole pair generation as shown by the increased HTPA formation rate and MG degradation rate via hole and hydroxyl radical in Fig. 5.3.

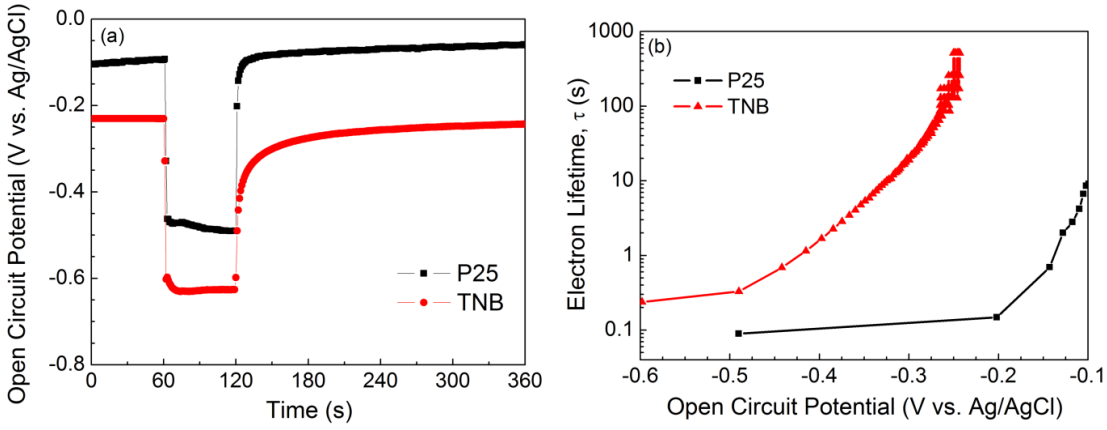

Figure 5.4: (a) Open circuit potential and (b) electron life of P25 and TNB

5.3.3 TPA degradation under varied duty cycles

To determine the effect of duty cycle on TiO_2 photocatalysis, the duty cycle was tested at 10%, 25%, 50%, 75%, and 100% at a constant pulse frequency (ν= 1 Hz. Absolute and

normalized rates of HTPA under the various duty cycles were tabulated (Table B1 in Appendix B). The normalized rate was given as:

$$Normalized\ k_1 = \frac{k_1}{\gamma(\%)\ x\ 0.01} \qquad \text{Eqn. 5.4}$$

The absolute and normalized rates of formation of HTPA (Fig. 5.5a) and the ratio of the normalized rate of HTPA formation at a specific duty cycle γ to the HTPA formation rate at continuous illumination (duty cycle γ = 100%), $k_{1,DC}$:$k_{1,DC=100\%}$, were plotted for P25, TNB, and Ag-TNB (Fig. 5.5b). Under continuous illumination, Ag-TNB has an increased HTPA formation rate compared to P25 and TNB by a factor of 1.33 and 2.59, respectively.

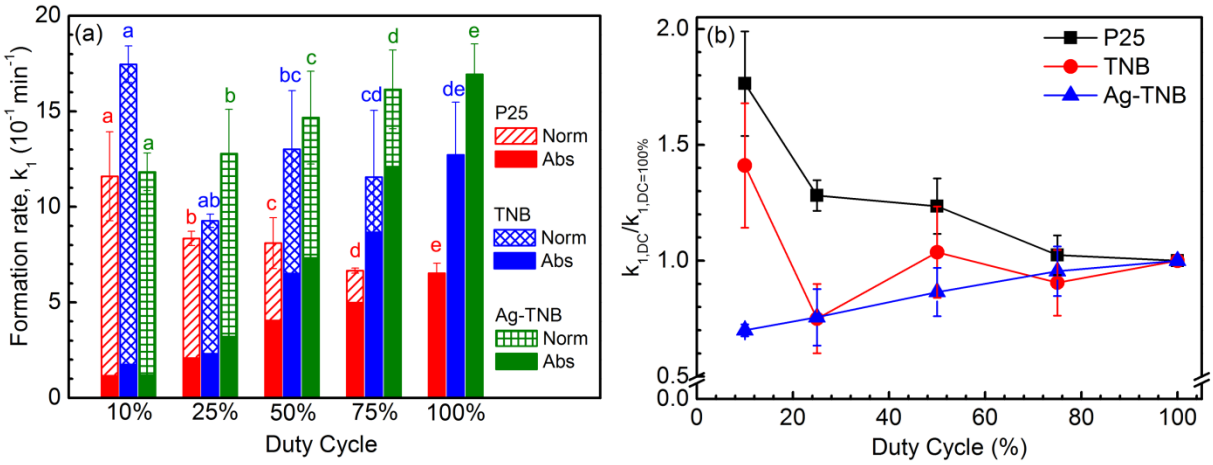

Figure 5.5: (a) Absolute (filled) and normalized (patterned) formation rate of TPA, k_1, at various duty cycles using P25, TNB, and Ag-TNB nanomaterials; (b) $k_{1,DC}/k_{1,DC=100\%}$ ratio vs. duty cycle. Bars that do not share a common letter are significantly different at α = 0.05 significance level as determined by one-way ANOVA using the Holm-Sidak post-hoc test to compare the formation rates at various duty cycles.

The continuous introduction of photons results in a build-up of charges (e_{cb}^-/h_{vb}^+) that can favour undesirable recombination processes [53, 54]. This effect can be shown through the reaction order of photocatalysis at various intensities. There is an initial linear dependency of the photocatalytic reaction rate on radiant flux (ϕ) that eventually changes into a square-root dependency ($\phi^{1/2}$) above a threshold radiant flux value. As the radiant flux increases, the concentrations of photo-electrons and holes increases, which exponentially increases the band-to-band recombination rate r_R, defined as[17]:

$$r_R = k_R[e^-][h^+] = k_R[e^-]^2 \qquad \text{Eqn. 5.5}$$

where k_R is the recombination rate coefficient,
$[e^-]$ is the electron concentration, and
$[h^+]$ is the hole concentration.

It was found that the lowest duty cycle tested (γ=10%) had a significant increase in the normalized HTPA formation rate compared to continuous illumination for P25 and TNB experiments (P25: p<0.000; TNB: p<0.000). At γ=10%, the normalized HTPA rate was 1.75, 1.40, and 0.70 times the HTPA formation rate at continuous illumination for P25, TNB, and Ag-TNB nanomaterials, respectively. In the case of P25 and, to a lesser extent, TNB, there was an improved normalized HTPA formation rate at low duty cycles (γ=10%). This improvement is due to the introduction of a dark period that is beneficial in limiting the number of excess charges on the surface that do not undergo recombination and tend to recombine [28, 54].

In the case of Ag-TNB, the duty cycle confirms that the recombination losses are not of the same magnitude to P25 and TNB. Lower the duty cycle was detrimental to the photonic efficiency for Ag-TNB (Fig. 5.5). Ag nanoparticles on TNB form a metal-semiconductor and the Ag serves as an "electron sink" that collect electrons, while holes are left on the TiO_2 surface. The enhanced charge separation at the metal-TiO_2 interface has been attributed to the formation of a Schottky energy barrier that prevents recombination in the depletion region [55]. Because of lower recombination, a dark period is not necessary compared to other nanomaterials. Therefore, higher light intensities can be used for Ag-TNB without suffering from photonic losses. Because the normalized HTPA formation rate was detrimental when lowering the duty cycle indicates that other processes are occurring under continuous UV irradiation that increases the normalized reaction rate such as localized surface plasmon resonance (LSPR) [33, 56–58].

5.3.4 TPA degradation under varied frequency

The HTPA formation rate was measured under various pulse frequencies (v =25Hz, 5 Hz, 0.5 Hz, and 0.05 Hz) at a constant duty cycle of γ = 50% for P25, TNB, and Ag-TNB in Fig. 5.6 (See Table B2-C for one-way ANOVA test). As the frequency increases, the UV irradiation approaches continuous illumination [54, 59]. There was a statistical difference using P25 at a pulse frequency of 0.05 Hz compared to all other frequencies tested (25 Hz: p=0.0006; 5 Hz: p=0.0002; 0.5 Hz: p=0.0018, $\alpha = 0.05$). There was no statistical difference in HTPA formation for TNB when increasing the pulse frequency. There was a statistical difference in HTPA

formation rate at a pulse frequency of 25 Hz compared to 0.05 Hz for Ag-TNB samples (α=0.10). Because high frequency CPI mimics continuous illumination, the results confirm the observations in the duty cycle experiments, in which Ag-TNB produced higher formation rates when UV light exposure was increased.

P25 experiments indicate an improvement in HTPA formation at higher frequencies tested compared to 0.05 Hz as shown in Fig.5.6 (See Table B2-B for one-way ANOVA test), which may be due to two possible mechanisms: (i) the excess charge under longer illumination periods and (ii) fragmentation processes in TiO_2 particle networks that generate new adsorption sites from aggregates from illumination [54, 60, 61]. Under 0.05 Hz pulse frequency, HTPA formation kinetics for P25 reach steady-state due to the long UV exposure time of 10 seconds follow by a dark period of 10 seconds. This increased period permits excess charge build-up that increases recombination. Increasing the frequency from 0.05 Hz to a higher pulse frequency reduces the steady-state time and increases the HTPA formation rate, which was found to occur in the study by Bahnemann et al. [62]. Under aqueous conditions, TiO_2 nanoparticles can attract other nanoparticles and aggregate due to electrostatic and van der Waals interactions. The concept of photoinduced disaggregation was proposed by Bahnemann's group as explanation for higher oxidation using intermittent pulsing [60, 63]. Their group attributed the increase in the quantum yield of formic acid oxidation under repetitive laser-pulses to disaggregation of nanoparticles and fragmentation of networks that promote additional adsorption sites for reactants. Irradiation of sufficient energy can partially disaggregate nanoparticles from their aggregates, increasing diffusion. This has been demonstrated through dynamic light scattering studies and membrane filtration comparisons under dark and light conditions in other studies, where the hydrodynamic diameter of TiO_2 aggregates can be reduced via light exposure [42], [64]. Agglomerated TiO_2 particles not only increase in catalyst surface area upon disaggregation, but also acts as an antenna for transferring photon energy from the site of absorption to the site of reaction through a network effect [60].

Derjaguin, Landau, Vervey, and Overbeek (DLVO) theory was used to ascertain if UV-LEDs have sufficient energy to dislodge nanoparticles from aggregates. Electrostatic repulsion forces and van der Waals attraction forces are taken into consideration determining how these forces interact with particles. There exists a deep energy well, called the primary minimum, that traps particles that are below the energy well and coalesce. At larger separation distances, the energy profile passes through a shallow energy well, referred to as the secondary minimum [42]. The force-separation distance profile for TiO_2 nanoparticles was calculated (See Section B4 in Appendix B). The calculation indicates that 3.9×10^{-21} J ($0.95\ k_bT$) are needed for a particle to

escape the secondary minimum well. When irradiated with UV-LED, each particle can absorb up to 1.7 x 10^{-17} J s^{-1}. This energy from UV-LEDs is sufficient to dislodge a particle in the secondary minimum from agglomerates.

In the case of TNB experiments, there was no significant change in the HTPA formation rate when increasing the pulse frequency as indicated in Fig. 6 (See Table B2-C for one-way ANOVA test). This may be due to TNB having lower surface area and greater dimensions compared to nanoparticles, which increases the energy required for a particle to dislodge from the secondary minimum. Anisometric particles, such as nanorods and nanowires, are also likely to aggregate under the secondary minimum [65]. The degree of aggregation is dependent on shape and is most favourable for platelets, less favourable for rods and cylinders, and the least favourable for spherical nanoparticles [65].

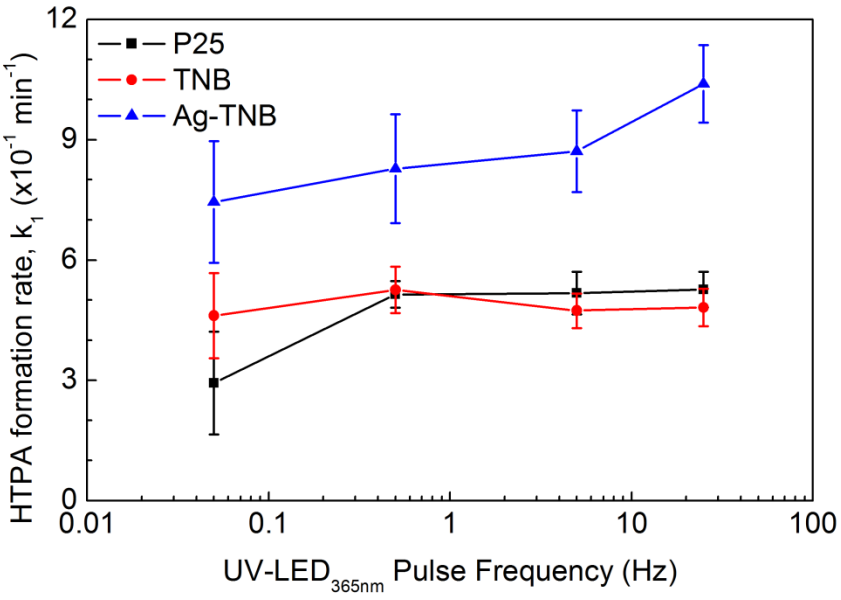

Figure 5.6: HTPA formation rate as a function of frequency

5.3.4.1 Implications of CPI in photocatalyst application

CPI has the benefit in reducing energy costs for TiO_2 photocatalysts and the evaluation of the treatment maintenance costs, specifically energy, is one aspect that requires attention. Since the UV/TIO_2 process requires electrical energy and can represent a significant amount of operating cost when it is scaled, figures-of-merit based on electrical energy consumption may be informative. In this case, electrical energy per order (E_{EO}), defined as the number of kilowatt hours of electrical energy required to degrade HTPA by one order of magnitude in a unit volume containing TPA as the starting compound. The E_{EO} (kWh m^{-3} $order^{-1}$) can be calculated [66, 67]:

$$E_{EO} = \frac{38.4\ P_{el}}{V\ \times k_2} \qquad \text{Eqn. 5.6}$$

where P_{el} is the input power (kW) to the UV-LED system,
V is the volume of water (L) in the reactor,
k_2 is the degradation constant of HTPA (min^{-1}), and
the constant multiplier accounts for conversions to kWh m^{-3} $order^{-1}$.

The addition of CPI can reduce the energy required to operate a batch reactor and under UV treatment options. The E_{EO} of HTPA degradation under UV-LED CPI-controlled TiO_2 photocatalysis (P25, TNB, and Ag-TNB) was determined under a favourable CPI condition (v = 25 Hz, γ = 50%) and continuous illumination (Fig. 5.7). Ag-TNB under the CPI condition requires only 50% to 55% of the E_{EO} required by P25 and TNB. Additionally, under the chosen CPI condition, Ag-TNB and P25 require 27% and 39% less E_{EO} than under continuous illumination. The use of TNB did not change significantly under both light conditions. It may be beneficial of investigating catalysts under operational parameters such as CPI in terms of E_{EO} and compare other batch reactor setups with similar chemical compounds of interest [66], [67] as kinetic rates alone do not take into account the reactor parameters.

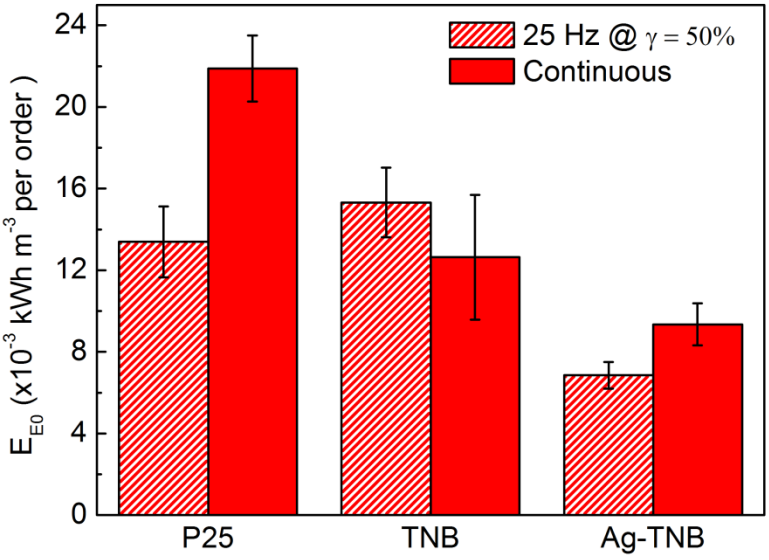

Figure 5.7: Energy per order magnitude of UV-LED/TiO_2 process under CPI and continuous illumination.

5.4 Conclusions

TNB and Ag-TNB nanomaterials were synthesized using a hydrothermal synthesis method. The following conclusions from the work are listed below:

(1) The formation of P25 to TNB nanomaterials decreased the grain boundary defects that increase recombination reactions. Using open-circuit photovoltage study, one-dimensional TiO_2 provides a greater charge-separation than P25 nanoparticles.

(2) P25 and TNB have a greater photonic efficiency at the lowest duty cycle (γ = 10%) tested due to excess charge build-up under continuous illumination which leads to recombination losses. Ag hydrothermal deposition onto TNB reduces the recombination and increases the HTPA formation rate due to the formation of metal-semiconductor junctions.

(3) The Ag-TNB experiments demonstrate detrimental performance when lowering the duty cycle, which may be due to the effective charge separation under a photon-limited regime and/or the LSPR effects that enhance reaction rates under illumination.

(4) P25 shows a slight increase in HTPA formation rate when the frequency is increased from 0.05 Hz, whereas TNB shows no change in formation rate when frequency is increased because of the shape in aggregation and increased energy required from UV-LEDs to dislodge TiO_2 particles from the secondary minimum of TNB.

(5) The energy per order of magnitude was lowest for Ag-TNB under a high frequency CPI condition compared to the catalysts tested and continuous illumination.

6.0 Degradation of pharmaceuticals using UV-LED/TiO_2 pulse width modulation

Overview

The presence of pharmaceutical and personal care products (PPCPs) in aquatic systems has been a growing cause for concern. Advanced oxidation processes such as UV/TiO_2 can breakdown PPCPs into smaller constituents, reducing the pharmaceutical activity. However, this process is limited by low photonic efficiency under UV systems. Controlled periodic illumination (CPI) is a promising solution to overcome the issues concerning low photonic efficiencies. Using a CPI controlled UV-LED/TiO_2 process, a mixture of twenty-one PPCP compounds were analyzed for their degradation removal on porous titanium – titanium dioxide (PTT) substrates. Immobilization of TiO_2 removes the need to recover TiO_2 nanomaterials in slurry batch reactors, which were used in **Chapter 4 and Chapter 5**. The kinetic rates of PPCPs may be analyzed using multiple regression analysis with parameters such as net charge at experimental pH, solubility, and molecular weight. Negatively charged PPCP compounds were found to have the highest removal compared to neutral and positively charged compounds due to electrostatic attraction forces. Decreasing the duty cycle under CPI did not significantly change the individual and cumulative PPCP compound removal, suggesting that the CPI controlled UV-LED/TiO_2 processes using PTT substrates were effective in reducing energy requirements, without sacrificing removal performance.

6.1 Introduction

Advanced oxidation processes (AOPs), such as ozone (O_3) and hydrogen peroxide (H_2O_2) are effective in treating organic contaminants but require a constant supply of chemical oxidants [1–5]. More recent technologies such as TiO_2 photocatalysis are of interest. TiO_2 can be used as a renewable oxidant source generated from the interaction between a radiation source (artificial or natural) of enough energy to generate electron-hole pairs that can participate in redox reactions. These redox reactions can decompose small molecules [6–10].

Conventional TiO_2 photocatalysis suffers from low photonic efficiencies, which prevents application of photocatalytic technology for large scale water treatment operations [11]. Increasing the photonic efficiency and degradation rate of photocatalysis is an ongoing goal and is primarily focused on optimizing operational conditions such as catalyst type, catalyst concentration, light intensity, pH, and temperature [12]. A simple approach is to optimize the

light intensity or using a doped catalyst [13–16]that increases light adsorption and/or lowers carrier recombination [16, 17] .

Generally, light intensity is linearly proportional to the kinetic reaction rate at low intensities and the square root of light intensity is proportional to kinetic reaction rate at high light intensities [12, 18, 19]. This drawback limits the photonic efficiency at high light intensities. However Sczechowski et al. suggested that intermittently turning on and off a UV source, known as controlled periodic illumination (CPI), can increase the photonic efficiency of TiO_2 while reducing light exposure times [20]. The practical application of CPI was limited to mercury lamps due to the warm up time required to output light and the tendency of filament failure if the lamp is turned on and off too quickly and frequently. A potential solution is to design systems with mechanical shutters, such as a rotating disk reactor with a pneumatic shutter [21]. However, the mechanical shutter system cannot be scaled up without increasing cost and energy substantially. With the advent of UV-LED technology, it was possible to pulse UV-LEDs using microcontrollers and pulsed width modulation (PWM), increasing the lifespan of the light source and lowering energy expenditure [11]. Additionally, the workable wavelength of undoped TiO_2 photocatalysis is below 400 nm and mercury lamps possess some emission peaks above the wavelength for undoped TiO_2 photocatalysis, thereby limiting efficiency using these light sources. UV-LEDs can utilize much of the light energy that is emitted because of its single, narrow Gaussian distribution [22–24].

An analog of CPI employs the concept of Parrondo's paradox, which may provide insight into developing chemical systems in which forced oscillating conditions may bring unexpected outcomes [25]. Parrondo's paradox is the unexpected outcome in which two "losing" strategies can, by alternative them, produce a favourable outcome. Parrondo's paradox applied to photocatalytic processes may generate a higher yield of a measured product of interest when switching between UV light and dark conditions, compared to the steady-state condition alone, even though the total irradiation period is lower than under steady-state illumination. There have been some examples of this paradoxical behaviour under TiO_2 photocatalysis. Tada et al. showed that by using Pt-shell/Ag-core particles loaded on TiO_2 and applying light on-off cycles on thiol (2-mercaptopyridine), the H_2 production rate was greater than steady-state illumination or dark adsorption which produced no H_2 [26]. Additionally, microorganisms and organic compounds under high frequency UV light on-off cycles showed higher removal compared to continuous illumination using similar UV intensities [27, 28].

All of the current CPI studies observed photochemical reactions using a single pollutant source [11, 21, 27–30]. However, natural water matrices contain many pollutants and components

that compete for adsorption sites in photocatalysts, thereby affecting the kinetic rates of pollutant removal [9]. Understanding the CPI conditions in complex matrices is of interest because cycling conditions may influence interactions within this system that result in unexpected outcomes compared to single pollutant sources and under steady-state conditions [25].

This study investigates the removal rates of 21 pharmaceuticals and personal care products (PPCPs) using synthesized porous titanium – titanium dioxide substrates under CPI conditions using UV-LEDs. PPCPs are emerging contaminants (ECs) that are of major concern in source waters and have been investigated in recent years due elevatedconcentrations in wastewater treatment plant (WWTP) discharges [4, 31–34].The apparent kinetic rate constants from the removal of PPCPs were correlated to the net charge, molecular weight, and solubility. The UV-LED pulse profile was controlled by duty cycle at a constant pulse frequency and the decomposition of a pharmaceutical cocktail containing twenty-one pharmaceuticals was observed over time. The study also investigates the electric energy consumption of the CPI-controlled UV-LED/TiO_2 processes compared to steady-state conditions.

6.2. Materials and Methods

6.2.1 Reagents and chemicals

All solvents and chemicals for synthesis methods were purchased from Sigma Aldrich at >99% purity. Ultrapure water ((18.2 mΩ·cm resistivity at 25^{o}C) was obtained from a Milli-Q® Integral Water Purification System EMD Millipore. The suppliers for all the reagents and chemicals for running experiments (parent compounds, metabolites, and deuterated standards) sample preparation, and LC-MS/MS analysis are described in previous work [9].

6.2.2 PTT substrate synthesis

The PTT substrate synthesis was similar to prior work [9, 10]. Briefly, the porous titanium (PTi) sheets (0.254 mm thickness, Accumet Materials, Ossining, NY, USA) were cut into 50 mm diameter substrates and cleaned with ethanol and water. PTi substrates were immersed in 50 mL of 30% H_2O_2 solution in a jar (500 mL) at 80^{o}C for 2 h. After the reaction, oxidized PTi substrates were washed in water, dried at 80^{o}C for 8 h, and calcined at 600^{o}C for 2 h. The resultant substrates have an oxidized TiO_2 surface on porous titanium (PTT).

6.2.3 Materials characterization

The morphology and features of PTi and PTT substrates was characterized using scanning electron microscopy (FE-SEM LEO 1550, Carl Zeiss Microscopy). Micro-Raman spectroscopy (Renishaw, He-Ne laser: λ = 632.8 nm) and X-ray diffraction (XRD, XPERT-PRO) was used to determine the crystal structure.

6.2.4 CPI UV-LED/TiO_2 setup and experimental methods

6.2.4.1 PPCPs and pharmaceutical metabolites

Twenty-one PPCPs and metabolites were selected and analyzed for the experiments based on previous studies and their prevalence in the environment in Table 6.1 [9, 10, 35, 36]. Stock solutions of PPCPs (1 g L^{-1}) in methanol were prepared and stored at 20^{o}C when not in use and the appropriate amount was pipetted into the experiment when need [9]. Methanol was used to dissolve all pharmaceuticals at some expense to the degradation performance on photocatalysis due to scavenging of holes and hydroxyl radical species as discovered in previous studies [9], [10]. The methanol concentration was adjusted to 0.02 % v/v before degradation experiments.

Table 6.1: Physical and chemical properties of target compounds

Compound	Abbr.	Mol. Weight (g mol^{-1})	pKa_1, pKa_2[a]	pIEP[a]	Net Charge Distribution Value at pH=5[a]	Solubility (logS) at pH=5[a]
Atenolol	ATEN	266.34	9.60	11.87	1(POS)	0.43
Atorvastatin	ATOR	558.64	4.33	0.98	-0.83(NEG)	-6.28
o-hydroxy atorvastatin	o-ATOR	573.65	4.33	0.98	-0.83(NEG)	-6.68
p-hydroxy atorvastatin	p-ATOR	573.65	4.33	0.98	-0.83(NEG)	-6.68
Atrazine	ATZ	214.68	1.6	8.74	0 (NEUT)	-3.8
Bisphenol-A	BPA	228.29	9.78	N/A	0 (NEUT)	-3.18
Caffeine	CAF	194.19	-1.16	N/A	0 (NEUT)	-0.44
Carbamazepine	CBZ	309.33	13.9	6.10	0 (NEUT)	-3.79
Carbamazepine-10,11-epoxide	e-CBZ	252.27	3.65, 5.13	9.39	0.46 (POS)	-3.11
Diclofenac	DCF	296.15	4.51	0.96	-0.91(NEG)	-3.25
17-a-	EE2	296.41	-1.66,	4.33	0.00 (NEUT)	-4.83

Ethinylestradiol			10.33			
Fluoxetine	FLX	309.33	9.80	11.90	1.00(POS)	0.00
Norfluoxetine	NFLX	295.00	9.80	N/A	1.00 (POS)	0.00
Gemfibrozil	GFZ	250.33	4.42	N/A	-0.79 (NEG)	-2.63
Ibuprofen	IBU	206.28	4.80	4.90	-0.58 (NEG)	-3.16
Naproxen	NPX	230.60	4.12	N/A	-0.87(NEG)	-2.58
Sulfamethoxazole	SULF	253.28	1.6, 5.7	4.06	-0.06(NEG)	-2.17
Triclosan	TCS	289.54	7.60	1.96	0 (NEUT)	-5.27
Triclocarban	TCB	315.58	12.70	3.40	0 (NEUT)	-5.67
Trimethoprim	TRIM	290.32	7.16	12.24	0.99 (POS)	-0.64
Venlafaxine	VEN	277.40	9.8	11.66	1.00 (POS)	0.0

pKa= acid dissociation constant, IEP = isoelectric point, S = solubility (g mol^{-1})
[a] Properties were taken from http://chemicalize.org
N/A – Not Available

6.2.4.2 UV-LED CPI standardized setup

The experimental setup consisted of stir plate, collimated UV-LED column, and microcontroller setup as seen in Fig. 6.1. The details of the setup is described in **Section 3.3.1.1**. The microcontroller was programmed using a Arduino script (see Section C1 in Appendix C).

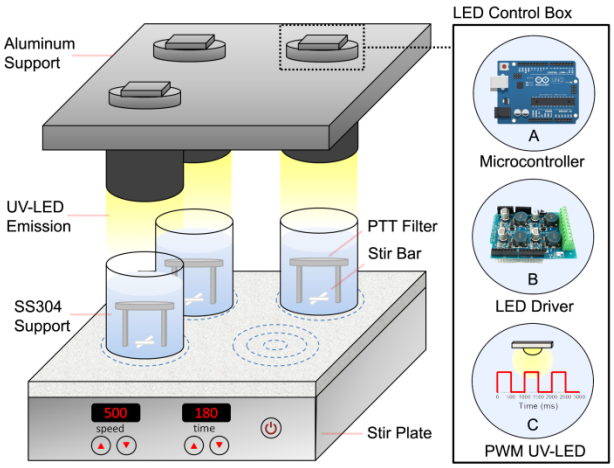

Figure 6.1: Experimental photocatalytic batch reactor with pulse width modulation (PWM) control unit containing a (a) microcontroller, (b) LED driver, and (c) UV-LED

The pharmaceutical stock solution was spiked into a beaker containing 300 mL of ultrapure water (2 ug L^{-1}). . The methanol concentration of the solution was 5 x 10^{-3} mM (0.02 %

v/v). The PTT substrates were placed on stainless steel holders inside the beakers. The beakers were placed in a digital magnetic stir plate (four-position, Talboys), three of which contain a UV-LED (λ= 365 nm) collimating column with a beam size of 4 cm. The UV-LEDs were situated 10.5 cm from the starting water level of the reactor; the PTT filter (sitting on the holder) was 1.5 cm under the water level.

The PTT batch reactor was illuminated under steady and intermittent UV light regimes using five duty cycles at a constant pulse frequency of 1 Hz and two frequencies at a constant duty cycle of 50% with varying light and dark times (t_{on} and t_{off}) as shown in Table 6.2. The cycle is defined as the period of illumination for a complete light and dark cycle and is the sum of the time on (t_{on}) and the time off (t_{off}), whereas the duty cycle, γ, and pulse frequency, v, are defined in Eqn. 3.2 and Eqn. 3.3 in **Section 3.3.1.1**. The power output of the UV intensity estimated at 10.5 cm from the UV-LED source is also shown in Table 6.2. The pH conditions (around pH ~ 5) were not adjusted.

Table 6.2: Light profiles for dark, continuous, and periodic illumination under various duty cycles (γ)

Duty Cycle (γ)	**Average UV power intensity ($mW\ cm^{-2}$)**	**T_{on} (ms)**	**T_{off} (ms)**	**Period (ms)**
Duty cycle experiments at constant frequency				
10%	0.22	100	900	
25%	0.54	250	750	1000 (1 Hz)
50%	1.08	500	500	
75%	1.63	750	250	
100%	2.18	----------Continuous illumination----------		
Frequency experiments at constant duty cycle				
50%	1.08	10000	10000	20000 (0.05 Hz)
50%	1.08	20	20	40 (25 Hz)

T_{on} – Time light source is on; T_{off} – Time light source is off; Period – time of one exposure cycle

6.2.4.3 Sample preparation and analysis

Sample preparation and analysis was similar to previous work by Arlos et al. [9, 10]. Aliquoted samples (4 mL) were spiked with deuterated standard stock solution to a final concentration of 20 µg L^{-1}. Solid phase extraction (SPE) was not used as in previous publications

because an ultrapure water matrix was used and no natural organic matter or other sources that could clog the liquid chromatography column were present [9, 10]. Two 4 mL samples of ultrapure water were spiked with both 32 μL of 100 μg L^{-1} regular and deuterated standard solution. A negative control consisting of 4 mL of ultrapure water was added to serve as a blank. Samples were evaporated completely using a solvent evaporator (Dionex SE 500, Thermo Scientific, Mississauga, ON). The dried samples were reconstituted with 160 μL of methanol. The samples were transferred into 2 mL amber glass vials with plastic inserts, capped, and stored at -20^{o}C until analysis.

The analysis of the compounds was completed using Agilent 1200 HPLC (Agilent Technologies) coupled to a mass spectrometer (3200 QTRAP, ABSciex, Concord, ON). The optimized parameter values, including chromatographic and ionization parameters, data acquisition, and quantitation are detailed in Tables C1-C3 in Appendix C.

6.2.4.4 Multiple regression and correlation analysis

OriginLab (Version 8.0) was used to plot data and perform statistical analyses. Measured removal rate constants were fitted using pseudo first-order models. Multiple regression and correlation analyses were conducted on experimental sets. A multiple regression model was selected based on the relationship between the dependent variable, kinetic rate, and three independent variables – net charge at experimental pH, molecular weight, and solubility – obtained from an online chemical database (Chemicalize, ChemAxon Ltd.). The best model was chosen based on minimizing the residual sum of squares, maximizing R^2, and testing for the significance of the variables. Correlation analysis was performed on the dependent and independent variables. Three correlation coefficients (Pearson's r, Spearman's ρ, Kendall's τ) that measure monotonic relationships were used. These correlation coefficients help discern whether the relationship is linear or non-linear (e.g. exponential, piecewise linear, and power functions). Spearman and Kendall's coefficients are resistant to the effect of outliers, whereas Pearson's r measures linear correlations, a specific type of monotonic relationship, and is affected by outliers [37].

6.3. Results and Discussions

6.3.1 PTT membrane characterization

TiO_2 was synthesized on porous titanium (PTi) substrates as shown in Fig. 6.2. The unprocessed PTi substrate has an average pore size of 10 μm using a thermal sintering process (Fig. 6.2a). The porosity of the substrate was 50% according to the manufacturer. Although the

increase in porosity is proportional to the surface area and the number of adsorption sites will increase as a result, there is a tradeoff to the mechanical strength of the substrate or adsorbent. When the porosity of absorbents exceeds 50%, they are more brittle and have lower mechanical strength [38]. The thermal-chemical oxidation of PTi occurred under 30% H_2O_2 and produced an oxidized TiO_2 surface containing a TiO_2 complex. Upon drying, the PTi-TiO_2 complex was heat treated at 600^oC to form porous titanium – titanium dioxide (PTT) substrate as seen in difference in contrast between Fig. 6.2b and Fig. 6.2a. TiO_2 hierarchical nano-structures assembled on the surface of Fig. 6.2b were generated through the thermal oxidation process.

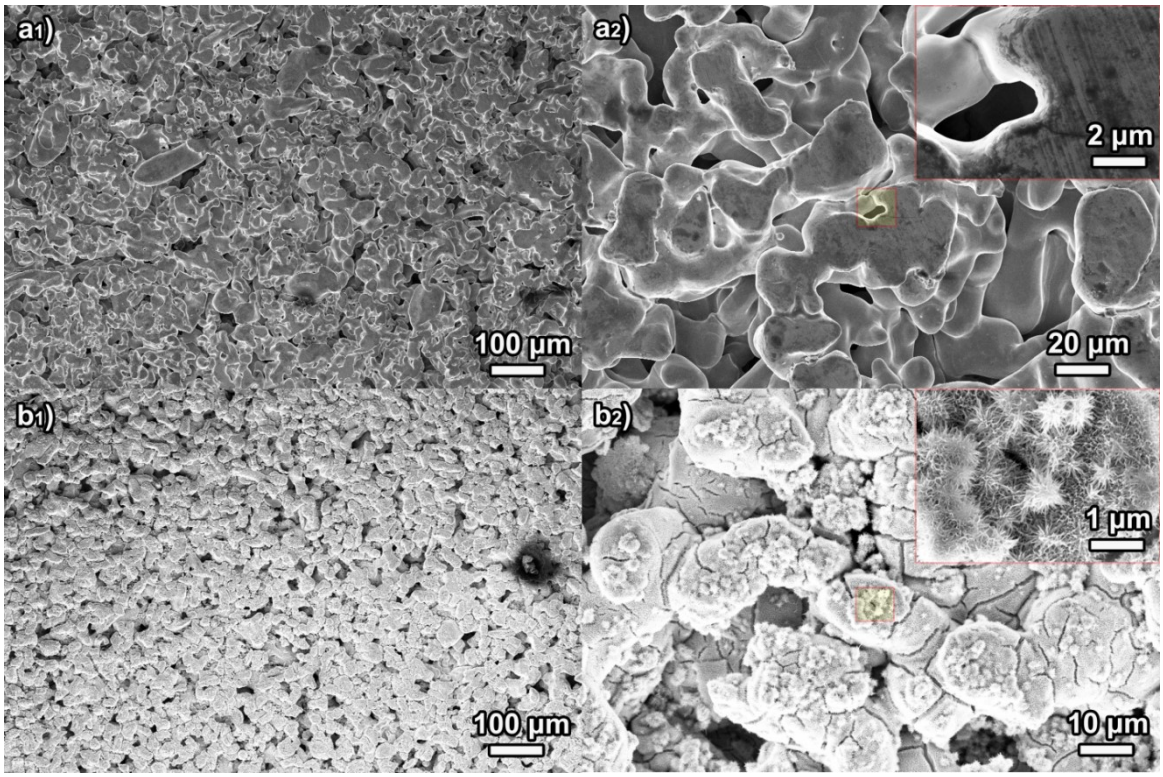

Figure 6.2: SEM images of (a) PTi substrate and (b) PTT substrate at low magnification (1) and high magnification (2)

The material characterization methods and values of the PTT substrate are given in Table 6.3. The PTT substrates weigh 1.33 ± 0.08 g and have an average surface roughness determined to be 5-10 μm [10]. The Raman spectra indicates that the TiO_2 surface is of anatase phase for PTT substrate and PTi support showed no Raman peaks indicative of TiO_2 crystalline phases (Fig. 6.3a). XRD confirms that there is also rutile and titanium crystalline phases in the PTT sample

along with the anatase phase (Fig. 6.3b). The bandgap energy of PTT was estimated to be at 3.0 eV derived from the Tauc plot in previous work [9], and corresponds to crystalline TiO_2. The isoelectric point was 6.0 based on previous work [9].

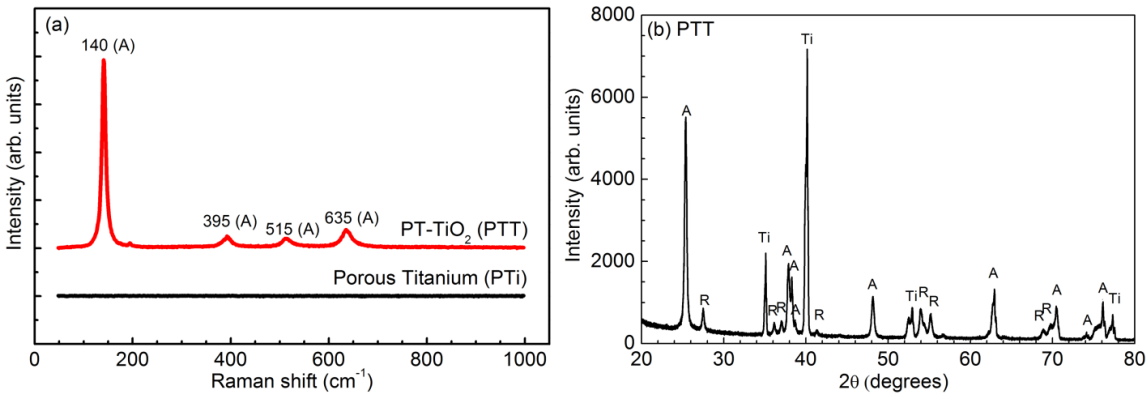

Figure 6.3: (a) Raman and (b) XRD spectra of PTT substrates

Table 6.3: Material Characteristics of PTT substrate

Material Characterization	Value	Method of Determination
Crystal Phase	Anatase	Raman Spectroscopy
Bandgap Energy	3.0 eV	Diffuse-Reflectance Spectroscopy
Surface Roughness	5-10 um	Optical Scanning
Pore size	~10 um	Scanning Electron Microscopy
Isoelectric Point	6.0	Zeta Potential
Mass of substrate	1.33 +/- 0.08 g	Weight Measurements

6.3.2 UV-LED/TiO_2 process against dark and photolysis controls

The normalized parent compound concentration was used to determine the total cumulative pharmaceutical removal after the 60 min equilibration period, which is defined as:

$$Normalized\ Parent\ Compound\ Concentration = \frac{\sum_1^i C_{i_t}}{\sum_1^i C_{i_0}} \qquad \text{Eqn. 6.1}$$

where i is the number of compounds tested,
C_{i_t} is the concentration (μg L^{-1}) of the i^{th} compound at time t, and
C_{i_0} is the initial concentration (μg L^{-1}) of the i^{th} compound.

The photocatalytic degradation of the individual or cumulative organic compounds can be modelled using Langmuir-Hinshelwood kinetics [39]. The L-H kinetics was simplified to Eqn. 3.5 and 3.6 (See **Section 3.3.2.4** for details). Individual compound and total parent compound kinetic rates were obtained.

Under continuous illumination, the magnitude of the pharmaceutical removal rate was 2.6 x 10^{-3} min^{-1} and was lower compared to previous studies due to higher total pharmaceutical concentration and substrate compound adsorption selectivity [9, 10]. The surface charge of PTT is negative at the experimental pH. The low removal rate is attributed to surface charge effects of pharmaceuticals that do not easily adsorb on the surface of the PTT substrate, such as positively charged compounds (venlafaxine, atenolol, norfluoxetine, fluoxetine, and caffeine) [9]. The individual compound kinetic rates are found in Table C4 in Appendix C and confirm that cationic compounds were not removed. The cumulative pharmaceutical removal profile (Fig. 6.4) depicts the changes in concentration over the 300 minute UV exposure time. The continuous UV illumination of the PTT substrate shows a statistically significant removal compared to pure photolysis (p<0.001) and dark (p<0.001) conditions in which little to no reductions in concentrations were observed. There was no significant difference between dark and photolysis conditions (p=1).

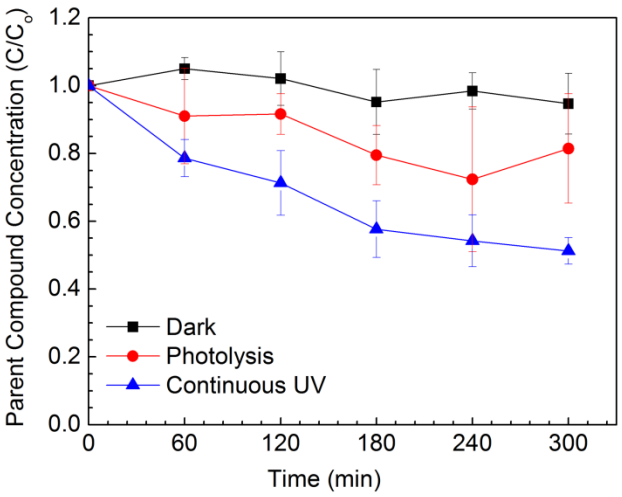

Figure 6.4: Cumulative pharmaceutical removal profile under dark and UV illumination conditions (with PTT substrate) and under photolysis (without PTT substrate)

6.3.3 Effect of net charge, molecular weight, and solubility on kinetics

The decomposition rates of pharmaceuticals can be attributed to many physical and chemical characteristics of the PPCPs used in the study. The dark and photo- adsorption processes inherent in the TiO_2/UV advanced oxidation process are dictated by the summation of interactions and forces in three interfaces: (1) the adsorbate-adsorbent, (2) the adsorbate and water, and (3) the water and adsorbent [38]. These forces cannot be readily measured. They can, however, be related to measurable parameters such as pH, net surface charge, solubility, and size [38]. Adsorption is also driven by pH as the pH affects both the charge of the PTT substrate which has an isoelectric point of 6.0, and the charge of ionizable polar species in PPCP compounds.

Different multiple regression models in Table 6.4 was used to relate the apparent kinetic rate degradation of PPCPs using TiO_2/UV under continuous illumination with three variables: net charge at the experimental pH, molecular weight, and solubility. The 21 compounds is a mixture of PPCPs that are negatively charged (n = 8), neutral (n= 7), and positively charged (n = 6). Regression analysis was first conducted on net charge alone (R^2 = 0.61), followed by the sequential addition of molecular weight (R^2 = 0.82) and solubility (R^2 = 0.87). Each added variable improved the model based on higher adjusted R^2 and lower residual sum of squares when compared to one or two explanatory variables alone. All of the independent variables inputted were significant using t-tests at α = 0.05. The overall model using ANOVA (Table C5 in Appendix C) was also significant ($p < 0.000$).

Table 6.4: Multiple regression analysis (forward approach)

Forwards		Model 1	Model 2	Model 3
Constant	**Slope**	0.566	-0.392	-0.328
	Std. Err.	0.010	0.205	0.177
	t	5.666	-1.907	-1.848
	p	<0.000	0.073	0.082
Net Charge	**Slope**	-0.823	-0.633	-0.855
	Std. Err.	0.146	0.105	0.121
	t	-5.633	-6.022	-7.064
	p	<0.000	<0.000	<0.000
Molecular Weight	**Slope**		0.003	0.0041
	Std. Err.		<0.000	<0.000
	t		4.930	6.324
	p		<0.000	<0.000
Solubility	**Slope**			0.118
	Std. Err.			0.043
	t			2.742
	p			0.014
Adjusted R^2		0.605	0.823	0.870
Residual Sum of Squares		3.97	1.69	1.17

Correlation analysis was used to measure relationships with the apparent kinetic rate, the dependent variable, and the three independent variables: net charge, molecular weight, and solubility. The kinetic rate was monotonically correlated with the net charge of pharmaceuticals. The experimental pH of this study was set at 5which indicates that the PTT substrate has a net positive charge and would attract and preferentially adsorb ionizable PPCP species that have a net negative charge. This behaviour was consistent in the removal of anionic compounds and lack of removal of cationic compounds as shown in Fig. 6.5a. The monotonic relationship between the kinetic rate and charge may not be linearly correlated. Pearson's coefficient (r = 0.79) is sufficient to assume linearity, however Spearman's coefficient (ρ = 0.88) is higher than r, suggesting that the relationship is non-linear. A power law, also known as Pareto Principle or the 80/20 rule, may be feasible to model this relationship. The most negative pharmaceutical compounds at the experimental pH tend to degrade the fastest and represent much of the removal

during the first 60 min under illumination, whereas less negative, neutral, and positive compounds are degraded much slower, or not at all. For instance, the five compounds with the highest negative net charge – diclofenac, atorvastatin, *o*-hydroxy atorvastatin, *p*-hydroxy atorvastatin, and naproxen – represent close to 23 % of the total pharmaceuticals in the water matrix tested, but account for 74.0 $\pm$ 5.0 % of the total compound removal after 60 min of illumination.

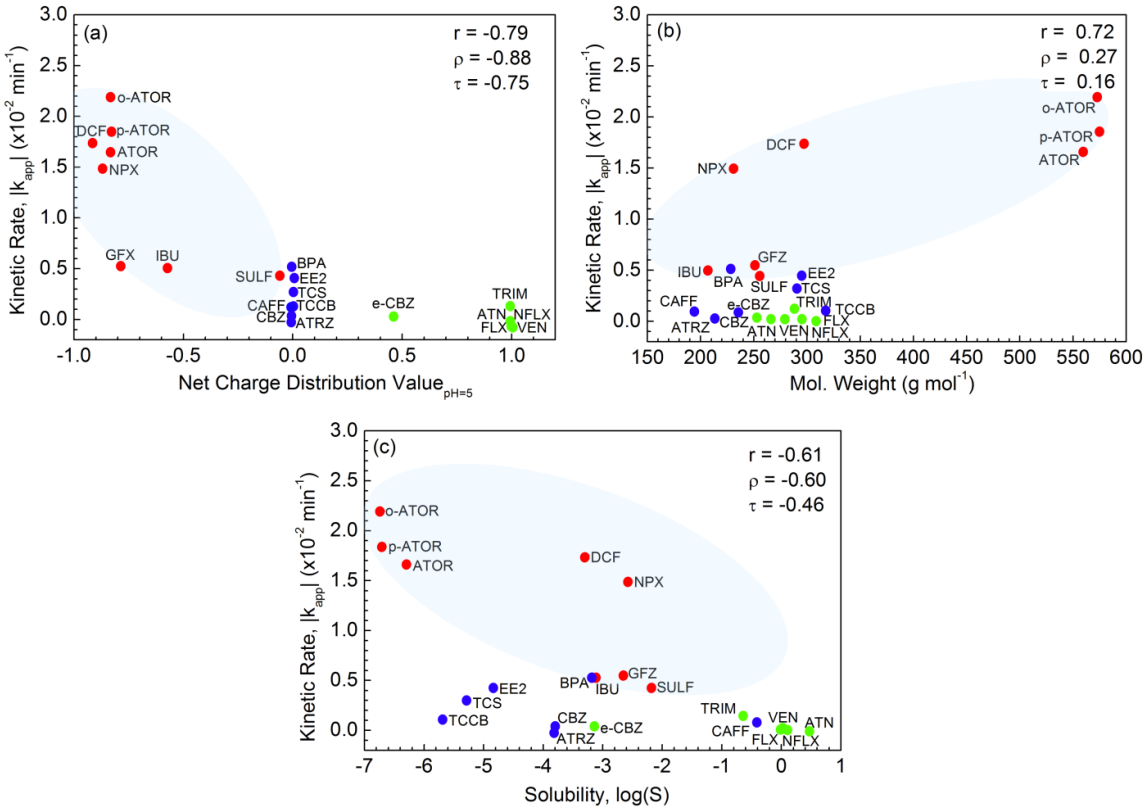

Figure 6.5: Multiple regression analysis of kinetic rate as a function of (a) net charge, (b)molecular weight, and (c) solubility at experimental pH (pH=5). Negative (red), neutral (blue), and positive (green) compounds at experimental pH were distinguished. Highlighted region (light blue) represents region of interest for negative compounds only

There is also a weak, significant correlation between the apparent kinetic rate and solubility (p = 0.04), and a weak, non-significant relationship with molecular weight (p = 0.25) when all twenty-one compounds are considered in Fig. 6.5b and Fig. 6.5c. The correlation coefficients are stronger only when compounds with negative net charge are considered. The relationship is monotonic and significant between kinetic rate of negative compounds and

molecular weight using Pearson's coefficient (r = -0.76, p = 0.030) and Spearman's coefficient (ρ = -0.80, p = 0.017). There is an even stronger monotonic relationship between the kinetic rate solubility of negatively charged PPCPs using Pearson's coefficient (r = -0.75, p_r = 0.030) and Spearman's coefficient (ρ = 0.87, p = 0.005). Kendall's coefficient, τ, is usually smaller than both r and ρ, but are above $|\tau|$ = 0.70, suggesting that there are good monotonic relationships between apparent kinetic rate and the independent variables, molecular weight and solubility .

6.3.4 The effect of duty cycle on the UV/TiO_2 process

To determine the effect of duty cycle on the apparent kinetic rates, the duty cycles of γ = 0% (Dark), 10%, 25%, 50%, 75%, and 100% (Continuous) at a constant pulse frequency of 1 Hz were tested (Fig. 6.6a) and the significance was calculated using ANOVA (Table C6-A in Appendix C). At 0% (Dark), there is little to no cumulative removal ($k_{app} < 1x10^{-4}$ min^{-1}) which is significant compared to all duty cycles tested (p<0.024). This indicates that dark adsorption has no effect after the initial 60 min equilibrium time. There is also no significant difference in cumulative removal between any two γ above 0% at the = 0.05 significance level (See Table C6-A in Appendix C). However there was a significant difference in the kinetic rate at γ = 25% compared to γ = 100% at the α = 0.1 significance level. Overall, changing the duty cycle from a range between 10% to 100% has no bearing on the overall apparent kinetic rate and reveals that the photocatalytic reaction of PPCP cocktail on the PTT substrate is much more efficient under longer t_{off} periods and that the reaction is not photon-limited.

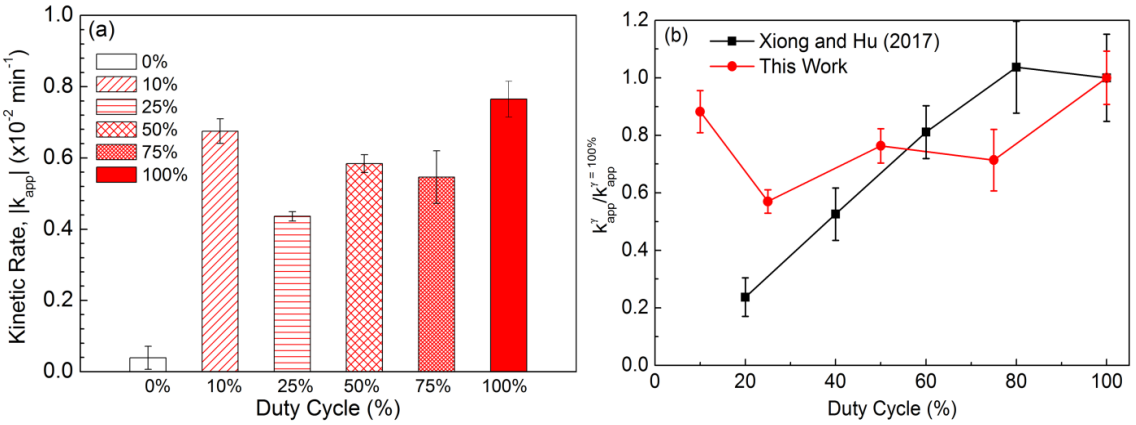

Figure 6.6: (a) Cumulative kinetic rates of PPCPs at various duty cycles at a pulse frequency of 1 Hz and (b) a comparison of normalized kinetic rates. Our work: $[Total_{PPCP}]$ = 42 ppb, PTT substrate, light intensity = 2.2 mW cm^{-2}, pH=5, pulse frequency = 1 Hz. Xiong and Hu: $[Ace]_0$=200 ppb, $[TiO_2]$=10 ppm, light intensity = 5.0 mW cm^{-2}, pH=5.6, pulse frequency = 10 Hz.

In a study by Xiong and Hu [27] ,CPI-controlled UV/TiO_2 was used to decompose acetaminophen at relevant treatment concentrations in the parts per billion range. The kinetic rate results were adjusted by normalizing with the kinetic rate γ = 100% and plotted as a function of duty cycle. The results were compared to the results in this work (Fig. 6.6b). Both experiments were conducted at a similar pH and light intensity, however, in Xiong and Hu's experiment, the pulse frequency time is an order of magnitude higher and TiO_2 slurry was used rather than an immobilized TiO_2 substrate. Their results showed that the kinetic rate decreases linearly as γ decreases from γ = 20% to γ = 80%, even though the photonic efficiency increases. In the current work, there was no significant difference in kinetic rate at the lowest duty cycle tested (γ = 10%) and under continuous irradiation (γ = 100%). In the case of Xiong and Hu, the decrease in kinetic rate when decreasing γ was due to less photon generation because the dark time, t_{off}, increases and would be considered a rate-limiting step. In our work, mass transfer was the rate-limiting step due to three possible factors: (i) the lack of adsorption of positively charged and neutral pharmaceuticals, (ii) the relative difficulty in transferring micropollutants to a substrate compared to a slurry batch reactor, and (iii) less adsorption sites in TiO_2 substrate compared to a TiO_2 particle-based slurry batch reactor [18]. Under a mass-transfer limited regime, the dependency of the reaction rate to light intensity is negligible (0^{th} order) because of saturated surface sites, low adsorption/desorption rates, and desorption products that may promote recombination [18].

As in the case of photocatalysis under continuous illumination (γ = 100%), only negative compounds and select neutral compounds showed removal no matter what γ was chosen. Lowering the duty cycle from 100% did not affect removal characteristics in that the most negatively charged compounds degraded first, select neutral compounds showed low removal rates, and positive compounds showed no removal. Fig. 6.7a depicts the negatively charged compounds that were capable of being removed at all duty cycles from 10% to 100% above the threshold of $|k_{app}| = 0.1x10^{-2}$ min^{-1}. All other compounds did not show removal above the threshold, except neutral compounds such as BPA, TCS, TCCB, and EE2 (Fig. 6.7b). There was no significant difference in removal rates between γ for any individual compound, which matches the results obtained from the cumulative pharmaceutical removal rates at α = 0.05 (Table C6B in Appendix C).

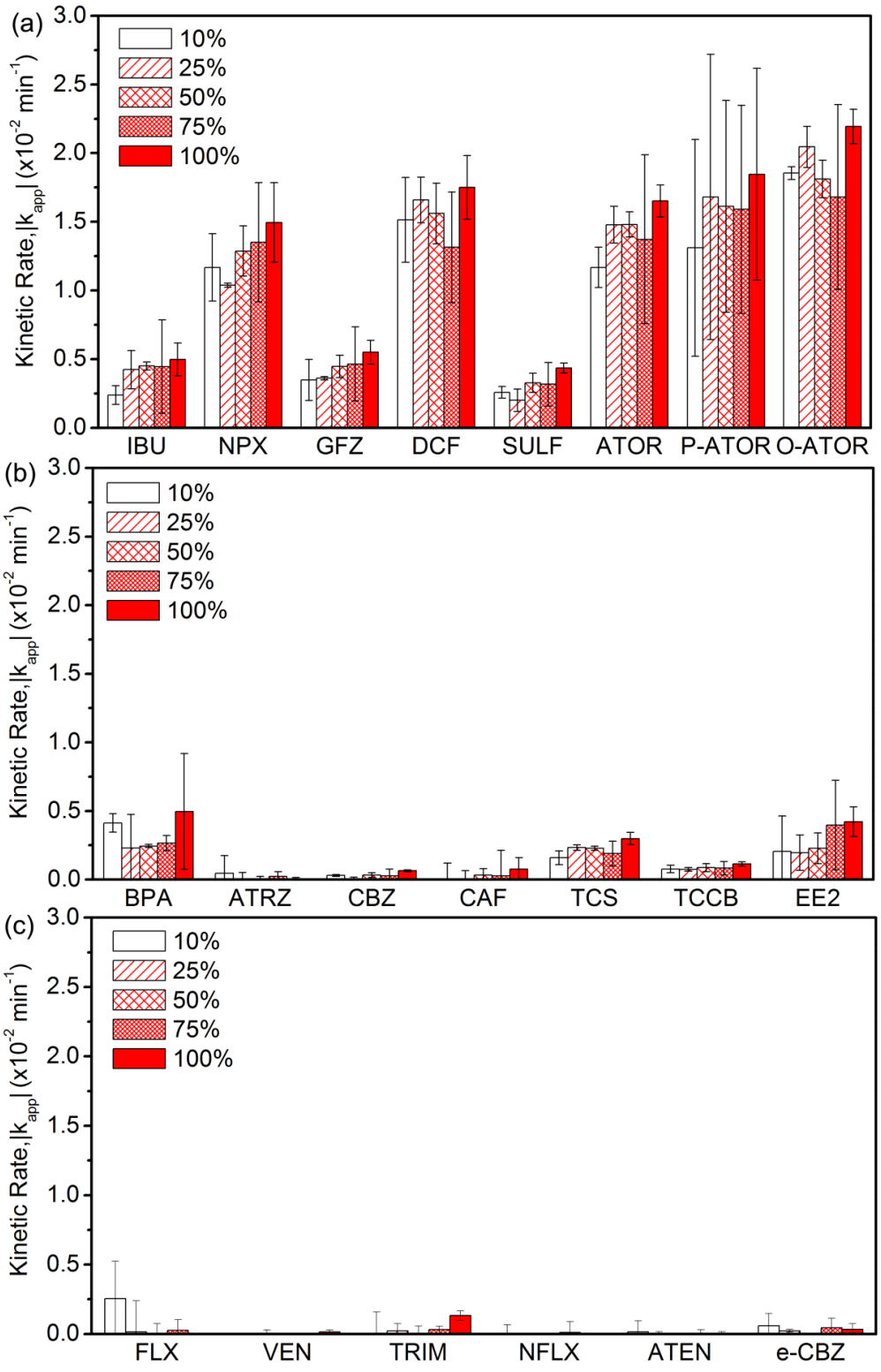

Figure 6.7: Kinetic rate of (a) negative, (b) neutral, and (c) positive compounds at various duty cycles

6.3.5 The effect of pulse frequency on the UV/TiO_2 process

The effect of pulse frequency was determined under three pulse frequency profiles: (a) 0.05 Hz, (b) 25 Hz, and (c) alternating between 25 Hz for 500 cycles and 1 cycle at 0.05 Hz (dual frequency) at γ = 50% (Fig. 6.8). There was statistically significant removal rates (Table C7A in Appendix C) under continuous irradiation compared to 0.05 Hz pulse profile (p = 0.013) and dual frequency compared to the 0.05 Hz profile (p = 0.050). All other comparisons were not significant at the α = 0.05 significance level, however there is a significant difference between continuous illumination and the 25 Hz profile (p = 0.062) at the α = 0.1 significance level.

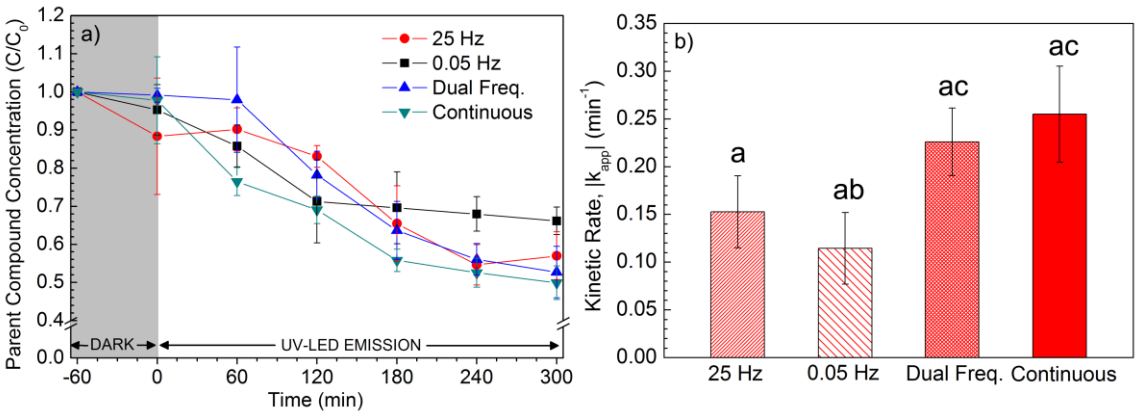

Figure 6.8: The (a) Concentration vs. Time Profile and (b) Kinetic Rates of total compound degradation at different frequencies (0.05 Hz, 25 Hz, Dual Frequency., and Continuous). Bars that do not share a common letter are significantly different at α = 0.05 significance level as determined by one-way ANOVA using the Tukey post-hoc test.

Under the dual frequency profile, the total pharmaceutical parent compound kinetic rate was greater than the 25 Hz and 0.05 Hz profiles alone. This suggests that switching between a high frequency and low frequency profiles can generate higher kinetic removal rates due to interactions between pharmaceuticals and PTT substrate in the water matrix (Fig. 6.9). There are no statistical differences between 25 Hz and 0.05 Hz frequency profiles of individual compounds (Table C7B in Appendix C). However under 0.05 Hz, the average kinetic rates of more negatively charged compounds were higher than 25 Hz profile but lower with more neutral compounds. The dual frequency profile has a synergetic effect that takes advantage of both single frequency profiles and has higher average degradation rates than individual 0.05 Hz and 25 Hz profiles. One compound, gemfibrozil, had a higher average kinetic rate under the dual frequency regime than at 0.05 Hz (p = 0.021, α = 0.05) and at 25 Hz (p = 0.096, α = 0.10). The difference

between continuous and dual frequencies is not significant, even though the kinetic rate is slightly higher compared to dual frequency than in the continuous regime k_{app}=-(5.51 $\pm$ 0.86) x 10^{-3} min^{-1}.

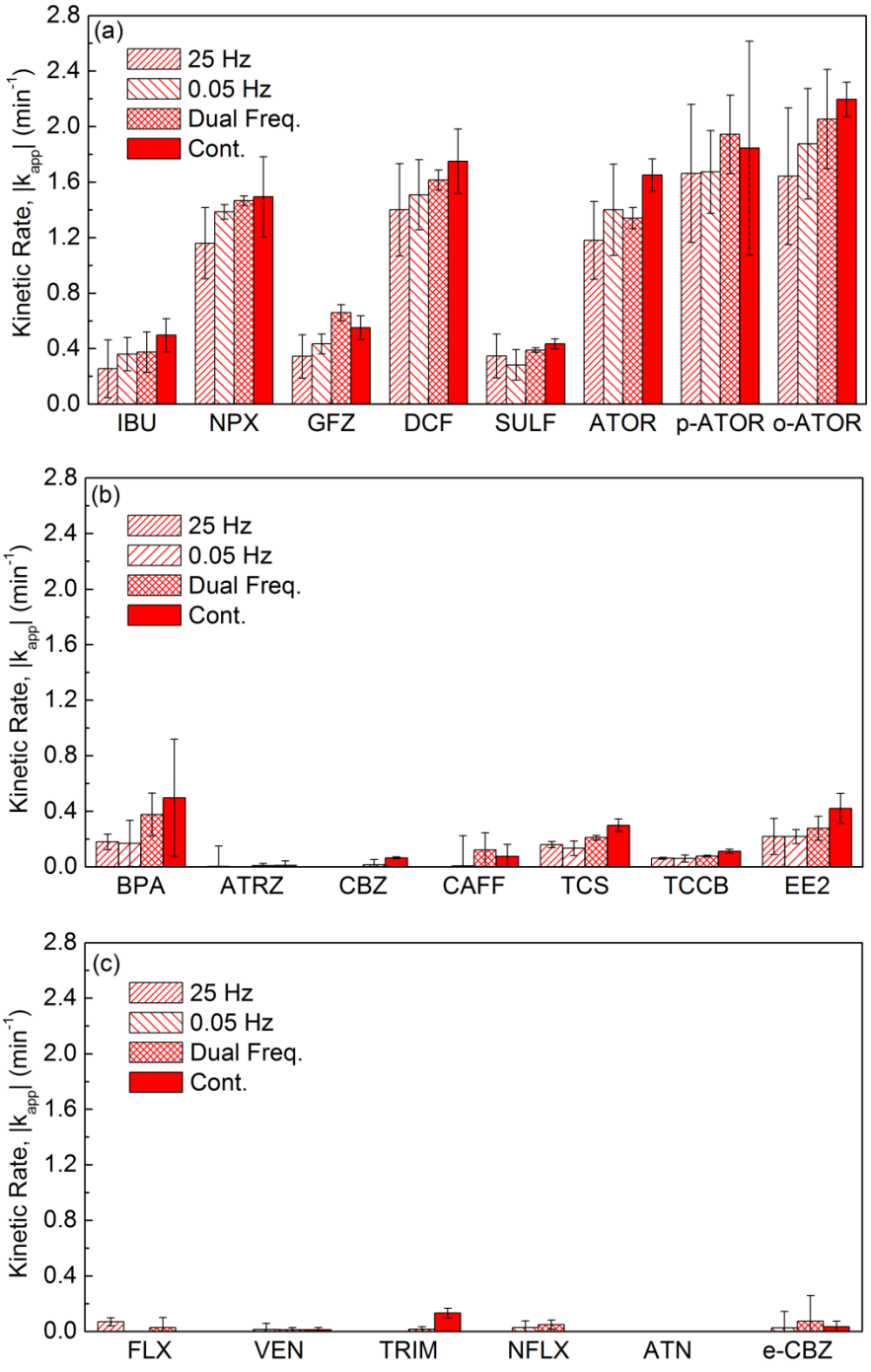

Figure 6.9: Kinetic rate of (a) negative, (b) neutral, and (c) positive compounds at different frequencies (0.05 Hz, 25 Hz, Dual Frequency, and Continuous)

6.3.6 Implications and energy analysis of the CPI controlled TiO_2/UV process

The photocatalytic process is initiated by UV light when irradiation energy is greater than the TiO_2 band gap energy. The generation of electrons and holes is in the order of femtoseconds. Slower reaction processes that do not require UV illumination and occur at the nanosecond to millisecond range, which are rate-limiting steps for TiO_2 photocatalysis [11, 40]. These slower reaction processes include charge-carrier trapping, recombination, and interfacial charge transfer [11]. The incident photons that initiate charge separation are not efficiently used due to charge carrier recombination, which occurs from 0.1 ns (shallow trap states) to 10 ns (deep trap states). Recombination is faster than interfacial charge transfer processes so it limits charge transfer processes that are necessary for redox reactions [11, 29]. Sczechowski et al. proposed that under continuous illumination, photocatalytic reactions will build-up electron-hole (e^-/h^+) charges and photogenerated species ($OH^*/O_2{}^{*-}$) that lead to undesirable reactions result in low photonic efficiency [20, 41]. The introduction of CPI and alternating the t_{on} and t_{off} UV-LED profiles can limit these undesirable reactions.

Ku et al. modelled the interfacial charge transfer processes under CPI by establishing transient and steady-state balances of holes and electrons and generating a profile for the surface coverage profile for the adsorbate, dimethyl phthalate (DMP), OH^-, O_2, and $O_2{}^{*-}$. It was assumed that DMP molecules were adsorbed onto TiO_2 surface, while electron-hole pair was generated during the illumination period. DMP was oxidized into smaller constituents by radical species generating from interfacial charge transfer (OH*, $O_2{}^{*-}$, and h^+) and were then desorbed from the TiO_2 surface. During the dark period, adsorption and desorption of reacting species and products occur as they do under illumination. The model showed that the carrier recombination of photo-induced electrons and holes is enhanced with decreasing surface coverage of OH^- or the DMP due to charge build-up when illumination time is increased. The dark period allows $O_2{}^{\bullet-}$ to react with DMP, which may increase the surface coverage due to desorption oxidation of DMP molecules [29]. Once the surface coverage is replenished, DMP molecules, OH-, and O_2 molecules can be adsorbed under illumination. The overall process improves the utilization efficiency of photons.

Because of increased utilization of photons using CPI, it is expected that energy consumption for photocatalytic systems can be improved through periodic illumination. The evaluation of the unit treatment costs is one aspect that requires attention. Since the UV/TIO_2 process requires electrical energy and can represent a significant amount of operating cost when it is scaled, figures-of-merit based on electrical energy consumption may be informative. Electrical energy per order removal (E_{EO}, Wh m^{-3} $order^{-1}$) for low pollutant concentrations was determined for a batch-type reactor [29, 42]:

$$E_{EO} = \frac{38.4 P_{el}}{V \times k_{app}} \qquad \text{Eqn. 6.2}$$

where P_{el} is the input power (W) to the UV-LED system,
V is the volume of water (L) in the reactor, and
k_{app} is the apparent rate constant (min^{-1}).

In Fig. 6.10a, the E_{EO} of the UV-LED source increases linearly with increasing illumination time (duty cycle) at a constant irradiation pulse frequency of 1 Hz. Under the same experimental time of 5 h, the electric energy per order was decreased by a factor of ten from τ=100% to τ=10%. The decrease in energy required to remove an order of magnitude of pollutants is much lower using CPI at low τ for the PTT substrate and may represent significant cost savings in energy if implemented in a larger scale for photocatalytic operations. Similarly, the implementation of alternating single frequency profiles (dual frequency) also lowers energy consumption compared to single frequency profiles alone without changing the duty cycle (Fig. 6.10b). The dual frequency profile lowers the E_{E0} by around 35 to 45% compared to continuous illumination.

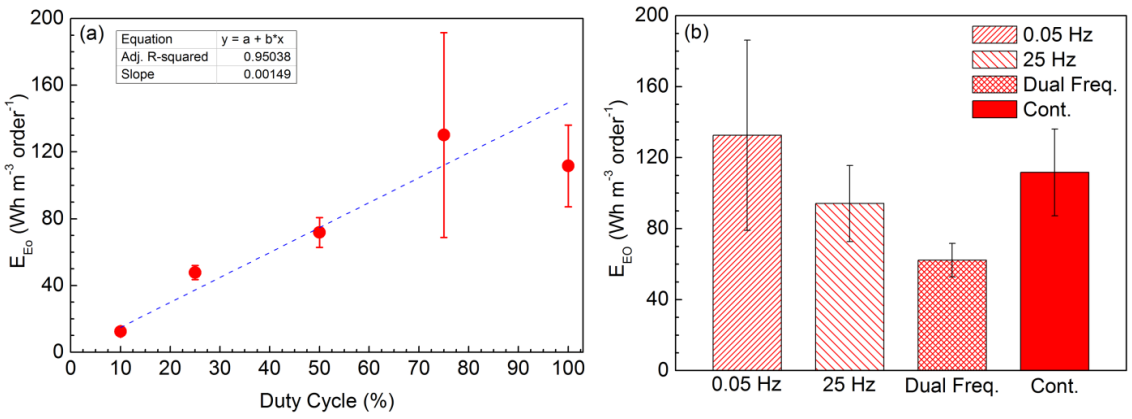

Figure 6.10: Energy per order magnitude of UV-LED/TiO_2 process under various (a) duty cycles and (b) frequencies.

6.4. Conclusions

In this chapter, UV-LED/TiO_2 experiments were conducted under continuous and CPI conditions using PTT substrates. The following conclusions from this work are listed below:

(1) PPCP kinetic rates were affected by the water matrix containing 21 pharmaceuticals varying in net charge, solubility, and molecular weight. The net charge at the experimental pH was the main factor in determining the kinetic rate of a specific PPCP compound, in which negatively charge compounds degrade first and positive compounds do not degrade during the time span of the experiment. Other factors such as solubility and molecular weight also explain the variations in kinetic rate using a multiple regression model.

(2) Programming UV-LEDs to operate under CPI and applying the process in TiO_2 photocatalysis is an effective treatment option when TiO_2 is immobilized on a substrate. The electrical energy that is required to reduce the concentration per order of magnitude,E_{E0}, is lower at lower duty cycles (τ <50%) than under continuous illumination. These results occur because of mass-transfer limitations as there was no significant difference between using τ=10% and τ=100%. Additionally, τ=10% requires a tenth of the light source energy required to reduce the PPCP compound mixture by an order of magnitude compared to τ=100%.

(3) Alternating frequency profiles lowered the E_{E0} compared to continuous illumination without changing the duty cycle. Under a mass-transfer limited regime, the dependency of the reaction rate to light intensity is negligible. This could be mitigated by using TiO_2 particle based suspensions and increasing fluid turbulence, which would increase the energy costs of operation, including particle separation steps

Overall, CPI is a feasible method from an operational standpoint to lower energy costs of light sources using immobilized TiO_2. Using CPI UV/TiO_2 process with complex water matrices, containing microorganisms or natural organic matter, may be studied to understand its effects and varying treatment outcomes compared to continuous illumination.

7.0 Doped TiO_2-quartz fiber membranes in a photocatalytic membrane reactor

Overview

Immobilized TiO_2 batch reactors suffer from mass transfer limitations as seen in **Chapter 6**. A solution to this problem is to increase mass transfer through fluid flow via filtration processes. Instead of relying solely on adsorption and photocatalytic oxidation processes; using a filtration apparatus reduces the requirement of decomposition. The self-cleaning property of immobilized TiO_2 can reduce organic fouling and increase the lifespan of the membrane. This chapter investigates the use of TiO_2 membranes in a photocatalytic membrane reactor (PMR).

The TiO_2 membranes were prepared by means of sol-gel dip coating methods and were subsequently tested in a PMR experiment that incorporated two pollutant removal processes: dead-end filtration and photocatalytic degradation.. Quartz fiber filters were immediately dip coated with undoped and doped TiO_2 suspensions producing three types of membranes: undoped, nitrogen-doped, and boron-doped TiO_2. The synthesized composite filters were analyzed for their (i) morphology using scanning electron microscopy (SEM) and (ii) crystal structure using Raman spectroscopy and X-ray diffraction (XRD). Chemical composition and chemical bonding of the membranes were determined using X-ray photoelectron spectroscopy (XPS). The permeability performance of the membranes was analyzed by measuring the flux using deionized water and acid orange 7 (AO7). The experiments were conducted in the PMR under dark and ultraviolet (UV) illumination. The removal of AO7 was improved when undoped and doped TiO_2 filters were used in place of a bare quartz fiber filter, except in the case when boron was used at a low doping concentration The removal of A07 was due to four processes occurring concurrently: adsorption, filtration, photocatalysis, and photowetting. The study demonstrates that optimization of doping parameters, such as the type of dopant (N or B) and concentration, on TiO_2 filter can improve the removal rates of AO7 using solely UVA irradiation without contribution of visible light irradiation. Overall, the experiments demonstrated the potential of PMR using undoped and doped TiO_2 materials for the removal of organic pollutants.

7.1 Introduction

Water pollution caused by refractory organic compounds – pharmaceuticals, pesticides, and organic dyes – is a prevalent problem. These compounds are difficult to remove using conventional water treatment methods, such as adsorption, flocculation, and biological treatments

[1, 2]. Membrane filtration and advanced oxidation processes (AOPs) have been shown to remove these compounds effectively, but have drawbacks regarding secondary costs associated with their implementation. Membrane filtration can be used to remove organic compounds, particulates, and microorganisms [3, 4], but these same pollutants can limit the lifetime of the membrane via fouling. Fouling limits the operation due to a reduction of filtration performance from the accumulation of particles on the surface. Chemical disinfection can be used to mitigate fouling, but it requires high dosages to be effective and can be costly [5].

For several decades, advanced oxidation processes (AOPs) have been used to remove refractory organic pollutants through the generation of highly oxidative radical species, including hydroxyl (·OH), superoxide ($O_2^{\cdot-}$), and perhydroxyl (HOO·) radicals [6]. These radicals oxidize organic compounds and may lead to their mineralization into CO_2, H_2O, or mineral acids provided sufficient exposure and reaction time [7, 8]. Semiconductor photocatalysis, a passive AOP, uses a photocatalyst, often TiO_2, in conjunction with a light source that is capable of exciting electrons from the valence band to the conduction band. The main advantage of semiconductor photocatalysis is that a renewable oxidant source is used compared to other AOPs which uses a consumable oxidant source, such as hydrogen peroxide (H_2O_2) with UV, or ozonation. TiO_2 is often used as a photocatalyst due to its chemical and thermal stability, non-toxicity, and relative cost compared to other photocatalysts. It is often used in slurry batch setups, which offer high organic degradation rates [9–11]. The major drawback of heterogenous photocatalysis in slurry reactors is the need for separation of TiO_2 particulates from the liquid phase to prevent secondary contamination of treated water effluents, which introduces a secondary cost for its implementation. Current methods of separation, such as gravity settling and centrifugation, are not feasible and cost-effective due to the low density and nano-scale size of TiO_2 [12]. Immobilized TiO_2 nanoparticles on a substrate offer a solution to this limitation and have been explored previously [13]–[18]. Some of the types of substrates that have been used to immobilize TiO_2 include glass [19], metals [20] , activated carbon [21], polymers [22], inorganic membranes [23], alumina [24], and silica paper [25].

TiO_2 thin films can be adhered onto a substrate using reactive Ti precursors, or sol-gels, which allow for chemical bonding with various substrates [15, 19, 26]. A catalyst film is formed at the induction period of the sol-gel process and the reaction takes place in an alcoholic solution containing TiO_2 alkoxide ($Ti(OR)_4$) and water as precursors. The chemistry of the process is a combination of hydrolysis and condensation reactions [27, 28] which are as follows:

$$Ti(OR)_4 + H_2O \leftrightarrow Ti(OR)_3OH + ROH \quad \text{Eqn. 7.1}$$

$$(RO)_3Ti\text{-}OH + OH\text{-}Ti(OR)_3 \leftrightarrow (RO)_3Ti\text{-}O\text{-}Ti(OR)_3 + H_2O \quad \text{Eqn. 7.2}$$

$$(RO)_3Ti\text{-}OH + RO\text{-}Ti(OR)_3 \leftrightarrow (RO)_3Ti\text{-}O\text{-}Ti(OR)_3 + R\text{-}OH. \quad \text{Eqn. 7.3}$$

TiO_2 photocatalysis is limited by the maximum wavelength that electron-hole pairs can be produced. It can only be used under UV irradiation under λ = 385 nm, if no modification is made. This restricts the viability of TiO_2 under solar light, in which less than 5 % of the power output comes from UV light [29, 30]. In order to extend the photoactivity into the visible light regime, its bandgap should be modified. These modification of TiO_2 includes doping with metals [31], non-metals [32–34], or coupling TiO_2 with other narrow bandgap semiconductors. *Choi et al.* studied the photoactivity of metal doped TiO_2 using 21 different dopants, including ruthenium (Ru), molybdenum (Mo), osmium (Os), rhenium (Re), vanadium (V), and rhodium (Rh) [35] . Other metal dopants have been investigated as well, such as copper (Cu) [36], zinc (Zn) [37], iron (Fe) [38].

Doping with non-metal atoms, such as nitrogen (N) [39], boron (B) [40], and sulfur (S) [41], has been shown to increase the photocatalytic removal efficiency of organic compounds using TiO_2 photocatalysts under visible light irradiation, and also change the morphology of the photocatalysts. N-doped TiO_2 synthesized using hydrothermal methods have been reported to generate high surface area and demonstrate increased photoactivities under visible light radiation [42, 43]. Certain nitrogen containing compounds have been demonstrated as good precursors for N-doping on TiO_2, including urea [44], ammonia [45], and ethyl methylamine [46].

The present study is focused on combining filtration and photocatalytic processes in a dead-end PMR setup using immobilized undoped TiO_2, N-TiO_2, and B-TiO_2 onto quartz fiber filters (QFF). Undoped and doped TiO_2 QFF was synthesized by dip coating deposition of sol-gel TiO_2 using an optimized T-mixer setup. Material characterization and hydraulic properties were carried out to determine the influence of undoped and doped TiO_2 coatings on permeate flux using deionized (DI) water and acid orange 7 (AO7). The photowetting process in DI water was investigated in the absence of AO7. The filter performance was evaluated using the removal efficiency and cumulative removal of A07 using a medium mercury pressure lamp. The study highlights the optimization of doping parameters, such as the type of dopant (N or B) and

concentration, on TiO_2 filter using solely UVA irradiation to assess improvements in removal compared to undoped TiO_2.

7.2 Experimental Procedures

7.2.1 Materials

Titanium isopropoxide (TTIP, 97%), urea, boric acid, and isopropanol (IPA, HPLC grade) were used as synthesis materials and obtained from Sigma-Aldrich. Acid orange 7 (AO7, >85%) was also obtained from Sigma-Aldrich and used as a model pollutant for filtration experiments. Commercial α-Al_2O_3 porous ceramic discs (diameter: 50 mm, thickness: 6 mm) with a pore size of 1.4 μm were purchased from Coors Tek, Inc. Quartz fiber filters (Type A/G, particle retention = 1.0 μm) were obtained from Pall Corporation and were used as substrates for TiO_2 sol-gel deposition.

7.2.2 Preparation of membranes

TiO_2 quartz fiber filters (TQFF) were prepared using a sol-gel method using a T-mixer setup (See Fig. D1 in Appendix D). Undoped TiO_2 nanoparticles were synthesized by mixing two solutions: (A) MilliQ water/IPA and (B) TTIP/IPA (C_{Ti}=0.126 M) at 293 K. Equal volumes of reactant solutions (100 mL) at 293 K were pumped into a static T-mixer using two peristaltic pumps at a flow rate of 0.6 L min^{-1} [29]. The hydrolysis ratio was C_w/C_{Ti} = 2.1. Doped nanoparticles were prepared using the aforementioned procedure with the addition of different amounts of urea (N/Ti = 3, 5, and $7x10^{-2}$) and boric acid (B/Ti=3, 5, and $7x10^{-2}$) for N-doped and B-doped nanoparticles, respectively. The dopant compounds were added to solution (A) prior to injection with solution (B) into the T-mixer.

The particles were immobilized during their period of relative stability, $t<t_{induction}$ [47]. QFF were washed with sulphuric acid (98%) for one hour and then rinsed with ultrapure water, followed by drying at 70°C overnight. The supports were submerged for 90 s in the TiO_2 nanoparticle suspension at a withdrawal speed of 2 mm min^{-1} using a dip-coating apparatus (MTI Corpoaration, PTL-MMBO1); this process was repeated 6 times for adequate coating thickness and subsequently dried at 70 °C overnight. After drying, calcination was conducted using a ramp rate of 2 °C min^{-1} to a final temperature of 450 °C. The coated filters were washed in MilliQ water to remove any excess non-reacted and loose nanoparticles from the filter.

For N-TiO_2/QFF (NTQFF), the following abbreviations are used to denote samples at N/Ti concentration ratios of 3, 5, and $7x10^{-2}$, respectively: $NTQFF_3$, $NTQFF_5$, and $NTQFF_7$. Similarly, for B-TiO_2/QF (BTQFF), the following abbreviations were used to denote samples at B/Ti concentration ratios of 3, 5, and $7x10^{-2}$, respectively: $BTQFF_3$, $BTQFF_5$, and $BTQFF_7$.

7.2.3 Analytical Procedures

7.2.3.1 Materials characterization

SEM, Raman Spectroscopy, and XRD were conducted as described in **Section 3.1.1**.XPS measurements were conducted as in **Section 3.1.2**. Ti_{2p}, O_{1s}, N_{1s}, and B_{1s} peaks were analyzed and their peaks were deconvoluted.

7.2.3.2 Photocatalytic membrane reactor setup and experiments

The photocatalytic membrane reactor (PMR) test setup is shown in Fig. 7.1. The permeate flux, transmembrane pressures and analyte concentration were measured. The setup (Fig. 7.1) is comprised of a compressed air line, pressurized feed tank, pressure gauge, UV irradiation source, and PMR module. The designed PMR module was made out of stainless steel and contains an inlet and outlet with a quartz window to transmit a light source through the enclosure and onto the membrane. Polyethylene tubing (outer diameter of 5/16" and inner diameter of 3/16") was used as connections. Medium pressure mercury lamp (MPM, UVP Blak-Ray B-100SP, 100W) was used as the UV irradiation source and the beam was collimated using an accessory funnel with a height of 10.2 cm (4"). The effective quartz window and membrane illumination area was 38.1 cm (1.5"). A porous support disc was used in conjunction with the photocatalytic membrane to add enough resistance for an optimum flow rate for testing. A silicon (Si) photodiode (Thorlabs, PM-100USB) was used to measure the power density at a reference point 2 cm from the collimating funnel of the MPM lamp; the power density was adjusted to 12.0 mW cm^{-2} at λ=365 nm at this reference point.

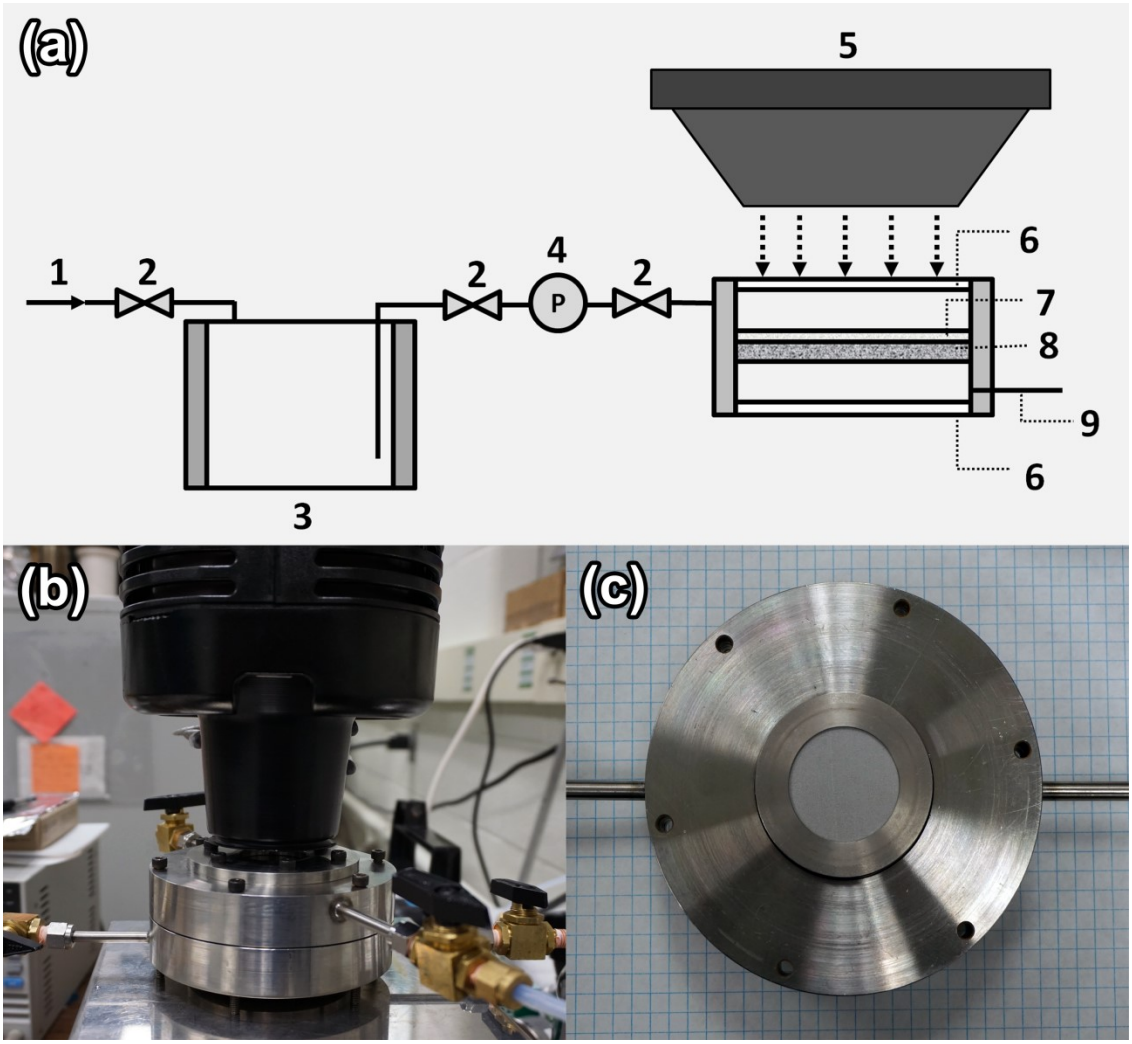

Figure 7.1: (a) Schematic of photocatalytic membrane reactor (PMR) setup containing (1) compressed air line, (2) valve, (3) pressurized feed tank, (4) pressure gauge, (5) UV irradiation source, (6) quartz window, (7) membrane, (8) α-Al_2O_3 porous support, (9) permeate outlet; (b) UV light emission from medium-pressure mercury lamp with collimating funnel targeting PMR quartz window; and (c) TiO_2 membrane on porous support in a stainless steel housing

In order to evaluate the membrane permeate properties, the water permeability and flux under dark and UV conditions were tested. The performance of various undoped and doped membranes were evaluated using AO7 azo dye (See Table D1 for properties of the dye in Appendix D). Dead-end filtration was carried out to evaluate the combined photocatalytic and separation performance using a test solution of 2 mg L^{-1} AO7 in a 5 L feed tank. Membranes and porous alumina supports were immersed in AO7 solution for 1 hour prior to the experiment to eliminate the adsorption effects of AO7 dye. During the experiment, the MPM lamp was

switched on for 1 hour, followed by 1 hour of filtration in the dark. The transmembrane pressure was fixed at 0.5 bar. After single pass filtration, the treated water was collected in the bottom chamber where it could be analyzed. The concentration of AO7 was determined using a UV-Vis spectrometer (Shimadzu UV-2501 PC) from a range of 200 nm to 800 nm. The peak height of the AO7 molecule at the 485 nm peak was used to determine the concentration from prepared calibration curves in the linear range. Adsorption tests were replicated in triplicates.

7.3 Results and Discussions

7.3.1 Membrane Material Characteristics

Pure and doped TiO_2 were immobilized onto a QFF during the induction period of the sol-gel reaction. These TiO_2/QF filters were characterized using SEM, XRD, and Raman spectroscopy. Uncoated QFF (Fig. 7.2a) consisted of fibers less than 2 µm in diameter, with lengths ranging from 10 - 100 µm. The coated QFF consisted of thin layers of TiO_2 as seen in Fig. 7.2. The TiO_2 agglomerates are deposited directly on the QF, allowing for a porous network structure and high surface area. Pristine TiO_2 sol-gel and B-TiO_2 appeared homogeneous (Fig. 2b and 2d) compared to N-TiO_2 in which nanoparticles agglomerated and formed clusters (Fig. 2c). These agglomerates were also observed by Kadam et al. [48] when they doped TiO_2 nanoparticles with nitrogen.

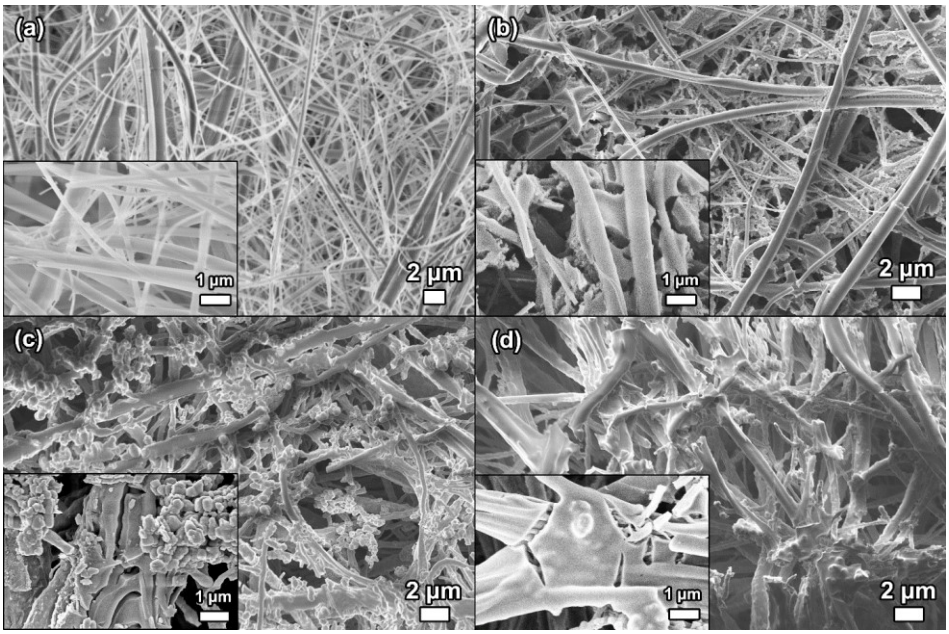

Figure 7.2: SEM images of the following filters: (a) QFF (b) TQFF, (c) $NTQFF_5$, and (d) $BTQFF_5$

The bandgap energy - the minimum energy for the generation of electron-hole pairs - was determined from diffuse reflectance spectra of the membranes. The diffuse reflectance spectra was converted into a Tauc plot, $[hvF(R)]^{1/n}$ vs. hv, where h is the Planck's constant, v is the frequency, R is the reflectance, n is a constant related to the nature of the sample transition, and $F(R)$ is the Kubelk-Munk function, given by:

$$F(R) = \frac{(1-R)^2}{2R}. \qquad \text{Eqn.7.4}$$

The value of n is 2 because TiO_2 is an indirect bandgap semiconductor [49], [50]. The bandgap was estimated as the intercept between x-axis and the tangent line of the inflection point (See Fig. D2 in Appendix D). The optical bandgap of pure TiO_2 and B-TiO_2 was 3.20 eV; there is no significant difference in the bandgap energy of these two materials, which is in agreement with the reported results [51]. The bandgap of N-TiO_2 was narrowed to 3.15 eV, which is consistent with literature [44–46], and there exists a wavelength range that can excite electrons in N-TiO_2 that are not permissible in undoped TiO_2 or B-TiO_2.

The X-ray diffraction patterns of TiO_2, B-TiO_2, and N-TiO_2 produced by the sol-gel process and heat treated at 400^{o}C are shown in comparison with commercial P25 Aeroxide™ (Figure 3). The doped and undoped TiO_2 diffraction patterns show characteristic anatase peaks of (101), (004), (200), (105), (211), (204), (116), (220), and (215) planes. The P25 Aeroxide™ contains anatase and a minor amount of rutile, represented by the (110), (101), and (111) diffraction peaks. N and B doping conducted from a range of $3x10^{-2}$ to $7x10^{-2}$ dopant/Ti concentration ratio did not affect the crystal phase of the samples, nor produced other crystalline diffraction peaks. This is either because dopants are highly dispersed into the TiO_2 structure, or the XRD is not sensitive enough to detect crystalline peaks containing these dopants [52–55].

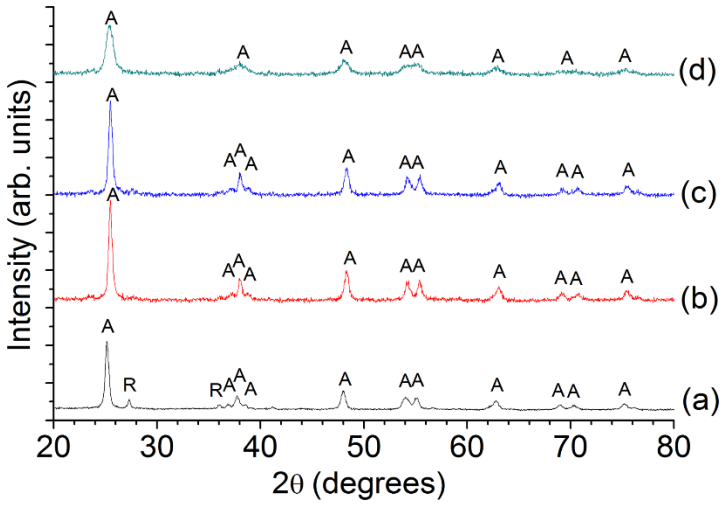

Figure 7.3: X-ray diffraction patterns of (a) P25 Aeroxide^{TM}, (b) TiO_2 sol-gel, (c) N-doped TiO_2 and (d) B-doped TiO_2 powders. Anatase (A) and rutile (R) phases are labelled

X-ray photoelectron spectroscopy was used to determine the presence of nitrogen or boron incorporated into the TiO_2 photocatalyst. Table 7.1 lists the binding energies of peaks found in Ti_{2p}, O_{1s}, N_{1s}, and B_{1s} regions which were deconvoluted (See Fig. D3 in Appendix D). All of the TiO_2 samples exhibited $Ti_{2p3/2}$ and $Ti_{2p1/2}$ peaks at 459.5 eV and 465.2 eV, respectively, which are consistent with values reported in literature [15,30]. The O_{1s} peaks of undoped, N-doped, and B-doped TiO_2 possessed of an asymmetric peak that was deconvoluted into two peaks with binding energy values of 530.6 eV and 532 eV. N-doped TiO_2 exhibited a 400.62 eV peak in the N_{1s} spectra, signifying the presence of interstitial nitrogen, N-O bonds in the photocatalyst matrix, or NH_4^+ species [51, 57]. It was found that interstitial nitrogen has no significant shift in conduction or valence bands of TiO_2, but the anti-bonding π^* N-O orbital between the TiO_2 valence and conduction bands facilitating visible light absorption which benefits increases efficiency at the visible light range and hence the reaction rate for treatment processes using solar energy[31] . B-doped TiO_2 exhibited a peak at 192.9 eV associated with the B-O-B bonds in B_2O_3 [54, 58]. The addition of boron by interstitial B-doping or formation of B_2O_3 on TiO_2 particle have unclear effects in photocatalytic activity in the treatment of various compounds [54, 58] .

Table 7.1: XPS peaks for undoped, N-doped, and B-doped TiO_2 powders

Sample	Binding Energy (eV) and Percentage of Integrated XPS region spectra					
	Ti_{2p} region		O_{1s} region		N_{1s} region	B_{1s} region
	$Ti_{2p1/2}$	$Ti_{2p3/2}$	O_{1s}	O_{1s}	N_{1s}	B_{1s}
Undoped TiO_2	465.19 (32.03%)	459.49 (67.97%)	530.72 (85.52%)	532.2 (14.48%)		
N-doped TiO_2	465.16 (32.74%)	459.46 (67.26%)	530.71 (86.06%)	532.1 (13.94%)	400.62 (100%)	
B-doped TiO_2	465.21 (31.42%)	459.55 (68.58%)	530.77 (60.45%)	531.52 (39.55%)		192.9 (100%)

7.3.2 Water permeability experiments

The permeate flux was obtained from the measurements of flow rate at the outlet of the PMR module as shown in Fig.7.1a). The permeate flux is defined by Darcy's law [59]:

$$J_P = \frac{Q}{A} = \frac{L_P}{\mu}\Delta P = \frac{\Delta P}{\mu R_m} \qquad \text{Eqn. 7.5}$$

where J_p is the flux density (m s^{-1}),
Q is the flow rate (m^3 s^{-1}),
A is the filtration area (m^2),
L_p is the hydraulic permeability of the membrane (m),
μ is the dynamic viscosity of the solvent used (Pa s),
ΔP is the transmembrane pressure (Pa), and
R_m is the hydraulic resistance of the membrane (m^{-2}).

The hydraulic permeability (L_p) of the fiber filters depend on intrinsic characteristics of the membrane such as size distribution, thickness and hydrophilic nature. The permeability of all membranes was obtained from flux *vs.* transmembrane pressure plots (See Fig. D4 in Appendix D). The total membrane resistance can be determined by the sum of the contributions of each component in the membrane stack, given by:

$$R_m = R_p + R_f + R_c \qquad \text{Eqn. 7.6}$$

where R_p is membrane resistance of the porous support (m^{-1}),
R_f is membrane resistance of the quartz fiber filter (m^{-1}), and
R_c is the membrane resistance of the TiO_2 coating (m^{-1}).

The undoped, N-doped, and B-doped TiO_2 membrane resistances are shown in Fig. 7.4). The addition of TiO_2 coating decreases the water permeability and increases resistance. In the case of TQFF and $NTQFF_5$, there is a 9% and 29% decrease, respectively in water permeability. This phenomenon was also observed elsewhere [24, 27] and is due to increased thickness and pore size reduction after TiO_2 deposition. Doped TiO_2 samples have higher hydraulic resistances due to increased deposition of N-doped and B-doped TiO_2 onto the surface of the QFF, albeit different surface morphologies, as seen in the SEM images (Fig.7.2).

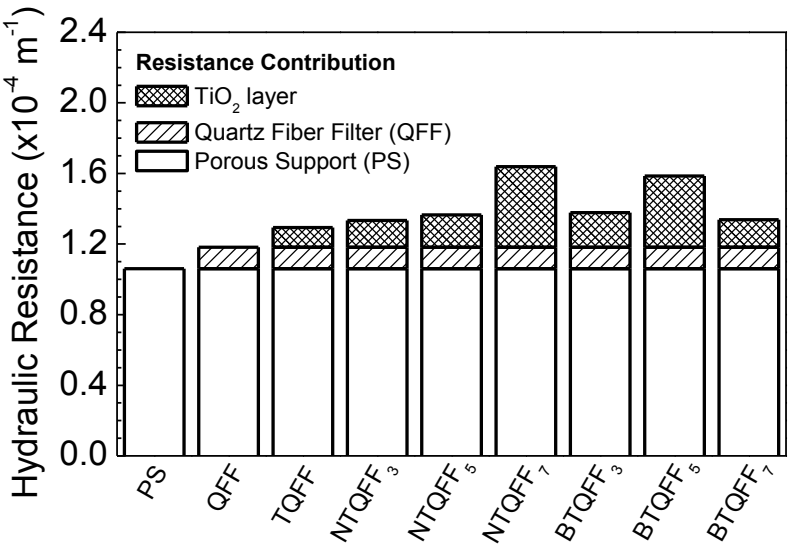

Figure 7.4: Hydraulic resistances of QFF, TQFF, NTQFF, and BTQFF membranes

7.3.3 Photowetting processes of TiO_2 filters

The addition of a TiO_2 layer introduces an effect called photowetting, in which the surface wettability of a substrate can be changed by light stimuli. *Wang et al.* observed amphiphilic surfaces when conducting contact angle measurements, in which a TiO_2 surface under dark formed water droplets that varied from 15^o to 72^o, increasing in hydrophobicity as a function of time in darkness. Upon UV illumination, the contact angle changed to 0^o .The contact angle of a TiO_2 film under aqueous conditions generally decreases after UV exposure. This can be modelled using an exponential function [60]:

$$\theta = \theta_0 e^{-k_{UV} t} \qquad \text{Eqn. 7.7}$$

where k_{UV} is the rate constant (min^{-1}) and
t is the time (min)

The k_{UV} value from other sources that use TiO_2 films was around 0.15 – 0.16 min^{-1} [60, 61]. The function was plotted in Fig. 7.5a to visualize contact angle decrease of TiO_2 on a relatively flat surface. As in the case of water, it has been proven that the same process can be applied to organic solvents and is independent of photocatalytic activities [34, 62, 63].

The normalized permeate flux of TQFF using DI water was compared to QFF under two conditions (Fig. 7.5b): (i) 2 h dark and (ii) 1 h dark with 1 h UV. In the case of 2 h dark condition, the flux steadily decreased by around 15% of its initial value for both QFF and TQFF towards equilibrium conditions. When UV light was introduced, the flux increased by about 12% initially using TQFF, and did not change when using naked QFF. The increased flux under illumination and decrease in flux in dark conditions using TQFF demonstrates the photowetting effect in TiO_2 because the increase in hydrophillicity decreases the membrane resistance and water passes through the membrane easily in comparison to more hydrophobic materials resulting in increased flux [58, 59]. QFF also did not show a sudden increase in flux after illumination indicating that it is not irradiation of UV light alone that contributes to increased flux, but rather a material property of TiO_2 in TQFF as depicted in Fig. 7.5a.

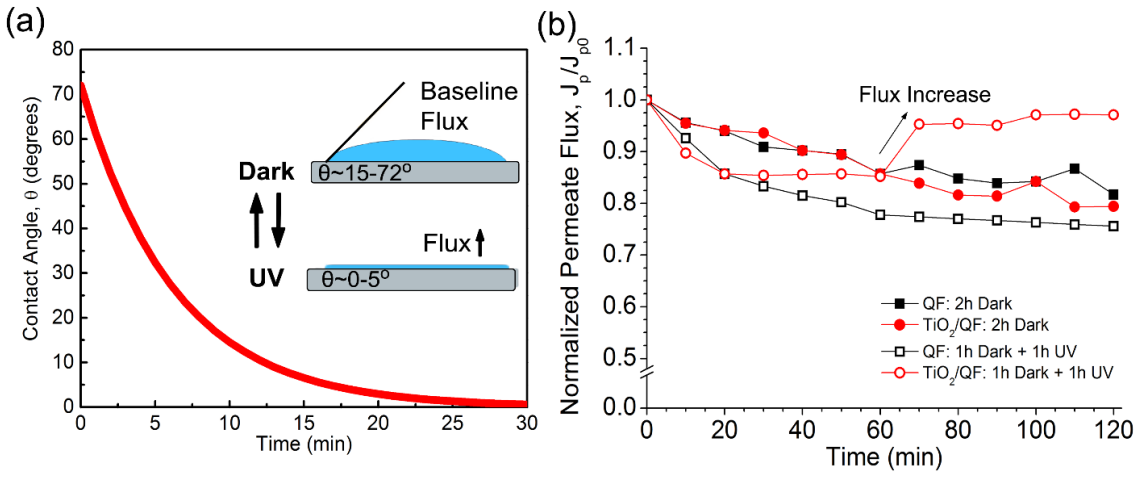

Figure 7.5: (a) Schematic of photowetting effect on TiO_2 surface; and (b) Normalized Permeate QFF and TQFF membranes

The flux measurements were further carried out under dark and UV illumination conditions as a function of time for NTQFF and BTQFF samples (Fig. 7.6). Filtration was carried out in the dark for one hour, followed by UV illumination in the next hour. Fig. 7.6 depicts the

normalized flux of TQFF, NTQFF, and BTQFF. Under UV illumination for 10 min and 60 min, there was an increase of 12% and 14% increase in flux for the TQFF compared to its baseline under dark conditions (at time point 60 min). This may be due to TiO_2 photowetting effect. In the case of NTQFF samples (Fig. 7.6a), the flux increased under UV illumination initially (at time point 70 min) by 0%, 13%, and 7%, respectively. After 1h of UV illumination, the flux decreased by 7% for $NTQFF_3$ and increased by 20% and 7% for $NTQFF_5$ and $NTQFF_7$, respectively. TQFF, $NTQFF_5$, and $NTQFF_7$ all demonstrated an increase in DI water flux when using a UVA radiation source. In the case of BTQFF samples (Figure 6b), at doping concentration ratios of B/Ti = 3, 5, and $7x10^{-2}$, the flux did not increase under UVA illumination at any point.

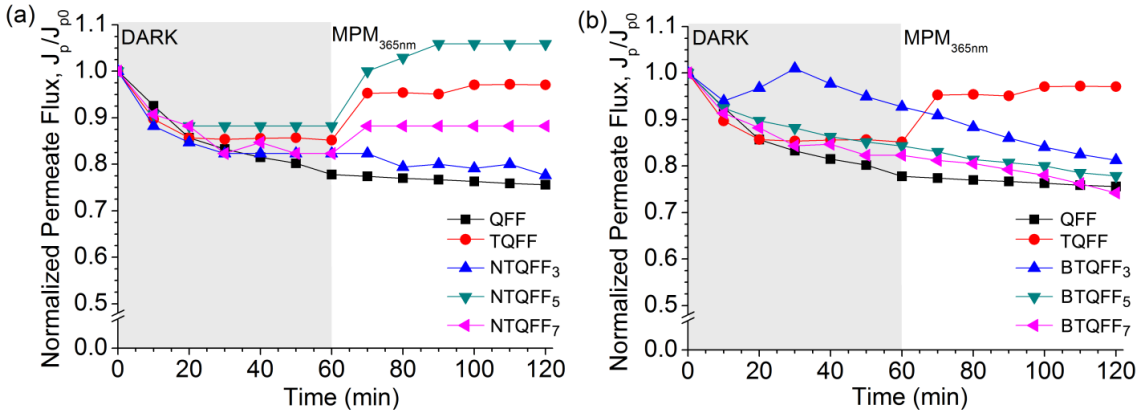

Figure 7.6: Permeate flux of (a) NTQFF and (b) BTQFF using DI water under dark and UV illumination period

7.3.4 Removal of AO7 using photocatalytic membrane filtration

AO7 was chosen as a compound of interest for the filtration through PMR because it is a non-biodegradable dye and any direct biological treatments are ineffective in removing this organic compound; however it can be removed through oxidation processes using TiO_2 in conjunction with a UV source or through filtration. In this study, the adsorption, permeate flux, and removal efficiency were measured and analyzed for QFF, TQFF, NTQFF, and BTQFF. The water purification experiments were performed using photocatalytic filtration treatment of AO7 solutions with concentration of 2 mg L^{-1} ($5.7x10^{-6}$ mol L^{-1}).

7.3.4.1 AO7 Adsorption on filters

All undoped and doped TQFFs and α-alumina porous supports were immersed in 50 mL of the solution of AO7 at 2 mg L^{-1} for one hour under darkness and stirring in order to reach the

adsorption equilibrium. The following equation was used to calculate the percentage of the initial concentration of dye adsorbed on the membrane:

$$\%\ adsorption = \frac{(C_o - C_{eq})}{C_o} \qquad \text{Eqn. 7.8}$$

where C_o is the AO7 concentration at the initial state (mg L^{-1}) and
C_{eq} is the AO7 concentration at the equilibrium state (mg L^{-1}).

The AO7 adsorption of the membranes was quantified and shown in Fig. 7.7. Using nitrogen as a dopant, the adsorption of AO7 was higher than with undoped TiO_2. This may be due to the film morphology in which N-TiO_2 sol-gel nanoparticles deposited a greater number of TiO_2 agglomerates on the NTQFF than TQFF, increasing the surface area and thus the total adsorption of AO7. Increased B-doping of BTQFF reduced the adsorption because of its "smooth" film morphology (Figure 2d), in comparison to the high surface agglomeration of TiO_2 particulates on NTQFF (Figure 2c), which results in a lower surface area for adsorption.

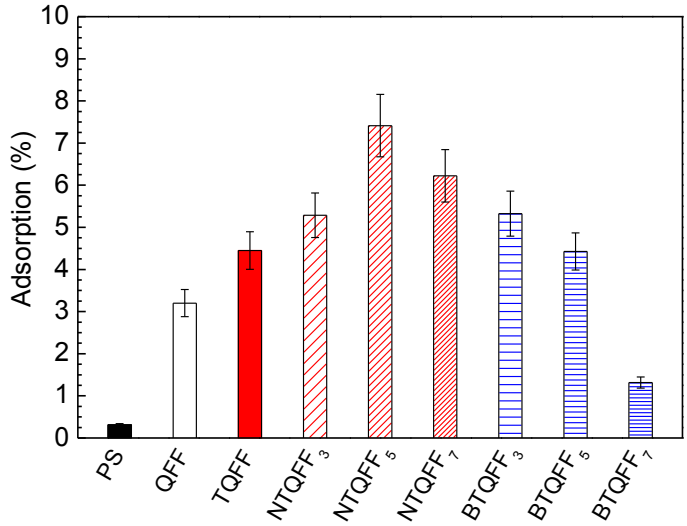

Figure 7.7: Percentage of initial concentration of dye adsorbed on the surface of the porous support, bare quartz fiber filter (QFF), and doped and undoped TiO_2/QFF. Error bars represent the standard deviation.

7.3.4.2 Permeate flux using AO7 under UV and dark conditions

After equilibrium was achieved, filtration of dye solution was carried out using the PMR setup (Fig. 7.1). A solution of AO7 (2 mg L^{-1}) was fed into the PMR module for 2 hours, 1 h

under UV followed by 1 h in the dark, and the permeate flux was measured in Fig. 7.8. The flux through the filters in AO7 solution was lower than DI water, which is attributed to dye molecules accumulating on the membrane surface forming a cake layer and increasing the membrane resistance [23].

The permeate flux of the uncoated membranes decreased continuously to 32% of its initial value through 2 hours of the experiment and UV irradiation had no effect on the permeate flux. The permeate flux decreased less using TQFF and NTQFF than QFF under UV irradiation. The minimal decrease in flux for TQFF and NTQFF samples compared to QFF is due to an increase in wettability as mentioned and antifouling properties of TiO_2 caused by photocatalytic degradation on the membrane surface [14, 23, 26]. The contribution of photocatalysis and photowetting processes is not easily understood as they both occur under light processes and quantifying the contribution of each is not in the scope of this study.

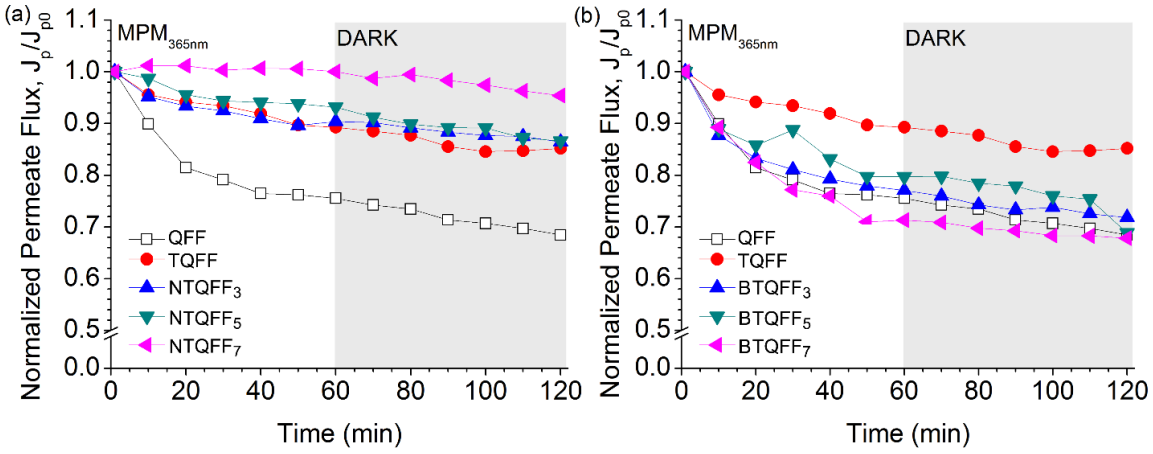

Figure 7.8: Permeate flux of (a) NTQFF and (b) BTQFF membranes using AO7 (2 mg L^{-1}) in water under UV and dark conditions

The flux of all membranes decreased slightly after switching to dark conditions after 1 h of UV irradiation. The contact angle does not change rapidly after UV irradiation is removed so the hydrophilicity and flux would not significantly changed over 1 h in the dark [66]. This phenomenon was shown by Lee et al. in which they found that when switching from the hydrophobic to hydrophilic state (turning the UV source on) the contact angle change occurs in the order of minutes; whereas switching from the hydrophilic state to the hydrophobic state (turning the UV source off), occurs in the order of days [66]. In the case of BTQFF, there were no significant changes in normalized permeate flux compared to QFF.

7.3.4.3 Removal of AO7 under UV and dark conditions

The percentage (Fig. 7.9a and b) and cumulative (Fig. 7.9c and d) removal of AO7 were conducted under 1 hour irradiation, followed by 1 hour dark condition using undoped and doped filters. The percentage removal and cumulative removal are defined as:

$$\text{Percentage Removal} = \frac{C_o - C_t}{C_t} \times 100\ (\%) \qquad \text{Eqn. 7.9}$$

$$\text{Cumulative Removal} = \frac{\sum_t (C_o - C_t) \cdot V_t}{M \cdot A}\ (\text{mol m}^{-2}) \qquad \text{Eqn. 7.10}$$

where C_o is the initial concentration (mol L^{-1}),
C_t is the concentration at time t (mol L^{-1}),
V_t is the total volume filtered (L),
M is the molar mass (g mol^{-1}), and
A is the filtration area (m^2).

The percentage removal does not take into account the hydraulic resistance of the membranes, and only gives the permeate concentration at specific time with respect to the inlet concentration. However, the cumulative removal considers the permeate flux, or the volume the membrane has filtered, and area of the membrane.

The percentage removal of $NTQFF_3$ and $NTQFF_7$ was compared to TQFF and QFF. The results indicated that the removal of AO7 using NTQFF was higher than QFF and was dependent on the concentration of the dopant. After 1 h of UV irradiation, $NTQFF_5$ and $NTQFF_7$ removed 10% and 55%, respectively, more on a percentage basis than TQFF. However $NTQFF_3$ removed 45% less than the TQFF. Under dark conditions, the removal percentage lowers as a function of time, whereas TQFF stays constant over 1 h. This is caused by the greater photocatalytic activity in NTQFF than TQFF. There is also an increased hydraulic resistance in doped TiO_2 filters (Fig. 7.8). This observation suggests that because of the lowered flux, the volume filtered and the cumulative removal are generally lower compared to undoped TiO_2 filters. The $NTQFF_7$ had a greater cumulative removal under UV conditions than TQFF, but the removal rate over time decreased under dark conditions. The decrease in removal rate was also apparent for $NTQFF_3$ and $NTQFF_5$ when switching from UV conditions to dark conditions. The change in rate may be due to the wetting properties in which the contact angle decreases exponentially as in Eqn. 7.7.

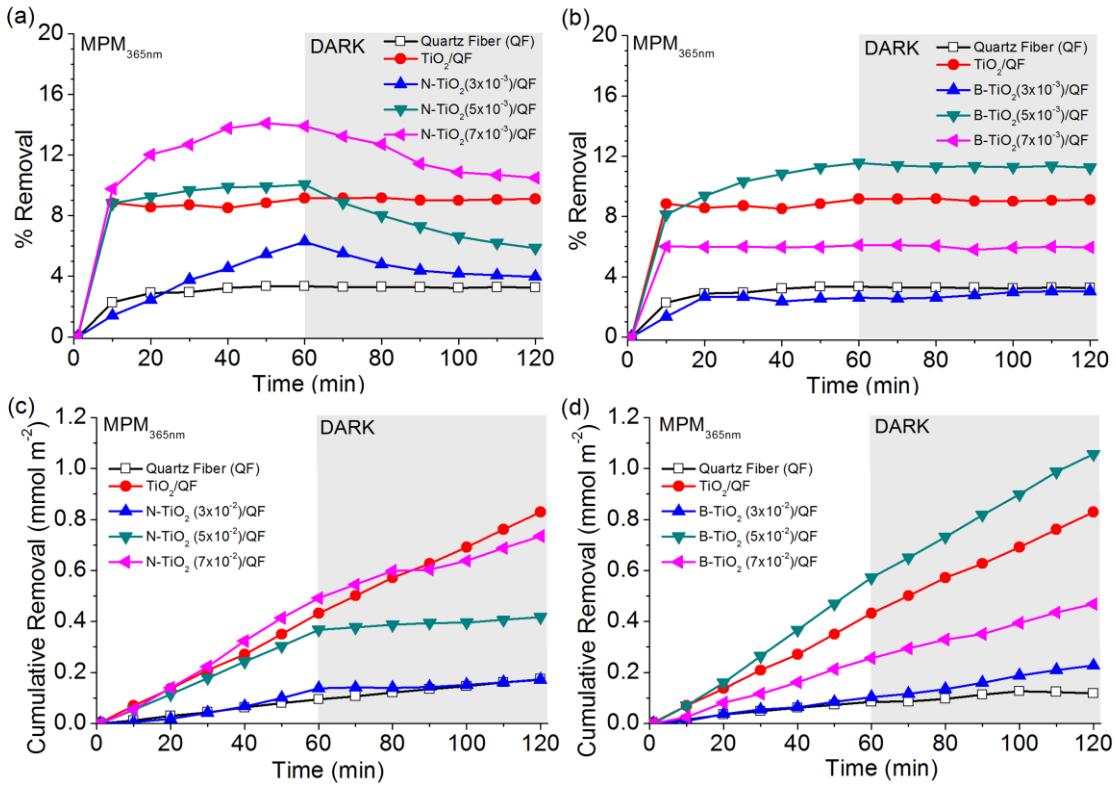

Figure 7.9: Percentage (a, b) and cumulative removal (c, d) of AO7 in (a, c) NTQFF and (b, d) BTQFF samples

$BTQFF_3$, and $BTQFF_7$ had a 70% and 45% lower A07 percent removal compared to TQFF, respectively. However, $BTQFF_5$ demonstrated a 20% increase in percent removal compared to TQFF. There was no difference in dye removal when comparing under UV irradiation and dark conditions as revealed by the water flux measurements in Fig. 7.8b, in which no apparent changes in flux were observed. Boron was shown to be a poor dopant for TiO_2 photocatalysis compared to undoped TiO_2 sources under UVA radiation sources [65, 66]. Additionally, the cumulative removal of A07 using $BTQFF_3$ and $BTQFF_7$ was lower than that of TQFF. The lower cumulative removal was due to higher hydraulic resistance as in the NTQFF samples except for $BTQFF_7$, which demonstrated higher cumulative removal than other B-doped filters.

The NTQFF membranes may be further improved using solar sources as the medium pressure mercury lamp has a peak wavelength of 365 nm and this does not extend to the visible light region. The application of solar light in the form of natural sunlight or xenon illumination may be used to improve $N\text{-}TiO_2$, however, this is out of scope for this study. Doping with

nitrogen has been shown in literature to improve the photoactivity under visible light conditions (400-500 nm)

7.4 Conclusions

Photocatalytic quartz fiber filters were synthesized using sol-gel processes. The pore size and TiO_2 deposits were controlled by the sol properties, immersion time, and thermal treatment temperature and duration. TiO_2 coatings on quartz filters were determined to be anatase for both undoped and doped TiO_2 filters via XRD and Raman analysis. The following conclusions were made:

(1) Coupling adsorption, photowetting, photocatalysis, and membrane filtration into a PMR by adding TiO_2 sol-gel coating on QFF increased the flux and improved the removal rate of dissolved organic matter compared to uncoated QFF

(2) It was discovered that the flux did not drop immediately after UVA radiation was removed during the AO7 filtration process due to the photowetting effect. NTQFF and TQFF demonstrated increased permeate flux using DI water and AO7 under dark and UV illumination; whereas the flux in BTQFF and QFF did not improve after UV irradiation was introduced.

(3) Higher doping concentrations generally produced higher membrane removal than the lowest dopant concentration used. For example, the percentage and cumulative removal of AO7 was favourable using $NTQFF_7$ and $BTQFF_5$ compared to TQFF.

(4) The percentage removal of AO7 exposed to 1 h UV irradiation followed by dark conditions was greater in UV conditions than in dark conditions for NTQFF samples, but not for TQFF and BTQFF.

Additional studies on the effect of sunlight or a visible light source is useful in further determining the efficacy of doped-membranes in PMR.

8.0 Concurrent Photocatalytic Degradation of Organic Contaminants and Photocathodic Protection of Steel

Overview

The treatment of water is only one aspect of maintaining water quality. The maintenance of infrastructure is another necessity. Corrosion is of concern in water treatment plants and distribution systems, which require expensive steel infrastructure. Corrosion products from the oxidation of steel causes water quality problems, including health risks, discoloration, and taste-and-odour issues [1–5].

In **Chapter 4**, the application of UV illumination of an n-type TiO_2 decreases the open circuit potential. When a metal coated with an n-type semiconductor (i.e. TiO_2) is in contact with its aqueous environment, electrons will be transferred across the semiconductor-solution interface until the chemical potentials of electrons in the solid and solution is in equilibrium. A Schottky barrier is formed analogous to the synthesized Ag-TNB in **Chapter 5**. Upon illumination, the electrode potential of the metal could be made sufficiently negative by injecting photo-electrons from the photoanode and preventing anodic reactions from occurring.

In this chapter, coupled TiO_2-composite and steel electrode pairs were investigated for their use in cathodic protection under illuminated and dark conditions. A series of photoelectrochemical tests were used to determine the properties of the photoanode and identify the cathodic protection behaviour in the presence and absence of organic/inorganic contaminants. Additionally, corrosion-prone steel (martensitic 22MNB5) was used to test the principle of photocathodic protection in reducing oxide formation and mass loss under base metal and welded materials.

8.1 Introduction

Stainless steel is an important material in industrial applications due to its mechanical properties and corrosion resistance. It is widely used in materials of construction because of the protective passive film layer that forms spontaneously on the surface. However passive film breakdown and localized corrosion in chloride-containing aqueous environments is a concern. Various surface treatments and coatings have been used to improve the corrosion resistance of stainless steels and other metals by providing a physical barrier between the environment and the metal surface [1–4]. However, these coatings can be easily scratched, so cathodic protection systems are often used.

Cathodic protection is used to supply metal to be protected with electrons to shift its potential to a region where it is immune based on the Pourbaix diagram of the metal. The source of electrons could be supplied via sacrificial anode or impressed current using an external power supply (see **Section 2.6.3**). Sacrificial anodes, such as Mg and Zn, can be used to protect metals by having a greater negative reduction potential compared to the metal being protected. The sacrificial anode, however, is consumed and needs to be replaced periodically [5].

The photocathodic protection method is a solution to replace sacrificial anodes with a semiconductor photoanode that generates photo-electrons under illumination. TiO_2 photoanodes that are connected to metals can drastically shift to negative potentials under illumination and such approach is effective to protect the cathode [6–8]. However, a plain TiO_2 coating usually suffers from charge recombination problems and is non-active under visible light illumination and in the dark.

The photoresponse of TiO_2 can be vastly improved. Many efforts have been made to enhance the performance of TiO_2 under UV and visible light illumination. It has been shown that metal nanoparticles (NPs), such as gold (Au), silver (Ag), platinum (Pt), and palladium (Pd), can be embedded in TiO_2 and enhance the photocatalytic activity of TiO_2 in visible light [9–12]. Ag NPs is often used as it is cheaper than noble metal elements [13]. However, Ag is chemically reactive and will form an oxide layer [14, 15], but it can be coated with a thin, transparent passive layer material (i.e. SiO_2) to prevent oxidation under dark conditions.

In this work, silver core – silica and titania shell ($Ag@SiO_2$-TiO_2, AST) NP were mixed into a commercial TiO_2 powder and deposited on fluoride tin oxide (FTO) conductive glass substrates via electrophoretic deposition and served as photoanodes. The morphology and elemental map of the composite thin films were characterized and the effects of AST on the photoelectrochemical (PEC) properties were examined. Photocathodic protection of SS304 was conducted in (i) inorganic and (ii) organic (glucose) hole scavenger solution under solar illumination. Additionally, corrosion sensitive steel (22MNB5) was used to inspect corrosion product formation at a short timescale through mass loss analysis and oxide peak identification.

8.2 Methods

8.2.1 Materials

Fluoride tin oxide coated glass (FTO, surface resistivity, 15 ohm cm^{-2}), iodine, and acetylacetone was purchased for Sigma-Aldrich. Ti metal sheet (grade 2) and stainless steel (SS304) were purchased from McMaster Carr. 22MNB5 sheets were obtained from Dofasco.

8.2.2 Sample preparation

8.2.2.1 Preparation of photoanodes

1 % Ag@SiO_2-TiO_2/P25 composites (AST-P25) were made by mixing 990 mg of P25 and 10 mg of synthesized Ag@SiO_2-TiO_2 NP (see Section E1 in Appendix E for synthesis protocol) in a 20 mL scintillation vial. 10 mL of ethanol was pipetted into the vial and the mixture was sonicated for 30 min. The AST-P25 solution was then placed in a beaker containing an electrophoretic solution mixture (140 mL ethanol, 100 mL methanol, 4 mL acetylacetone, 2 mL water, and 27 mg iodine).

An electrophoretic setup (similar to the one used in **Chapter 4**) was used to deposit the charged particles in the electrophoretic solution mixture. FTO glass was used as the cathode and Ti metal sheet (grade 2) was used as the anode. A DC power supply was used to supply a constant voltage of 30 V for 20 s. An average of 4.0 mg $\pm$ 0.2 mg of the AST-P25 was deposited onto the FTO substrates. The FTO substrates were heat treated at 450 ^{o}C to improve adhesion of the particles and remove organic impurities.

8.2.2.2 Preparation of SS304 working electrodes

SS304 sheet metal was cut into 9 x 9 mm squares using a hydraulic shear. The samples were progressively ground with 600, 800, and 1200 fine grit silicon carbide paper then polished for a mirror-like finish on a polishing pad using 1 μm diamond spray under 250 rpm rotation. Cleaned SS304 samples were placed in a working electrode cell when required for PEC studies.

8.2.2.3 Preparation of base and welded 22MNB5 working electrodes

A 200 x 100 mm coupon of galvanneal coated 22MNB5 (See Table E1 in Appendix E for steel chemistry) was heated in a baffle furnace at 900 ºC for 6 minutes then transferred to a press containing flat dies for press hardening. The cooling rate of the coupon during press hardening was in excess of 30 ^{o}C s^{-1} in order to achieve a fully martensitic microstructure. The samples were progressively ground to 600 grit size using silicon carbide paper. Laser welding was performed using a fiber laser (IPG Photonics: YLS-6000) mounted on a 6-axis welding robot. The press hardened coupon was clamped in a welding fixture to prevent movement during the welding process. A single linear laser weld was performed at a laser power and welding speed of 4 kW and 12 m min^{-1}, respectively. Welded specimens of 9 x 9 mm with the weld bead in the center were sheared from the coupon. The weld bead is approximately 1 mm in diameter. The MM2NB5 samples were placed in a working electrode cell when required for PEC studies and stored in a vacuum desiccator.

8.2.3 Material characterization

SEM, HRTEM, and XRD were conducted as described in **Section 3.1.1**. For HRTEM, EDS maps were collected for AST NPs and the Ag, Si, and Ti locations were superimposed on one image.

8.2.4 Photoelectrochemical and corrosion testing

Two PEC setups were used for the (i) PEC properties of photoanodes and (ii) corrosion performance of SS304 using photoanode assisted cathodic protection. For both setups, a xenon solar simulator (Newport, Research Solar Simulator) and a Gamry Potentiostat (Series 300) were used. All potentials were reported with respect to the saturated calomel electrode (V_{SCE}). This setup was chosen to separate physical barrier effects in TiO_2 coated metals and the photocathodic effect when determining corrosion performance. The coupled components form an electrochemical circuit using conductive solutions.

The PEC tests for only photoanodes are described in **Section 3.2**. The corrosion performance of SS304 using photoanodes was determined using a galvanic cell consisting of a photoanode cell (PAC) and a corrosion cell (CC), as seen in Fig. 8.1. The AST-P25 in the PAC is connected with the stainless steel (SS304) in the CC. A salt bridge containing 1 M KCl is connected between the cells. The CC consists of SS304 working electrode, Pt counter electrode, and SCE as reference in 0.5 M NaCl. The PAC consists of FTO glass with TiO_2 in 0.2 M KOH + hole scavenger solution. Nitrogen gas bubbling was used in the corrosion cell.

The PEC setup was used to evaluate the open circuit potential (OCP) and cyclic potentiodynamic polarization tests. The OCP test was carried out under open circuit (no current) mode for 10 h under intermittent light and continuous illumination. Cyclic potentiodynamic polarization tests were conducted from -0.8 V_{SCE} to 0.8 V_{SCE} with a maximum current density of 20 mA cm^{-2}, in which polarization will reverse above this value. The test was performed at a scan rate of 0.167 mV s^{-1}.

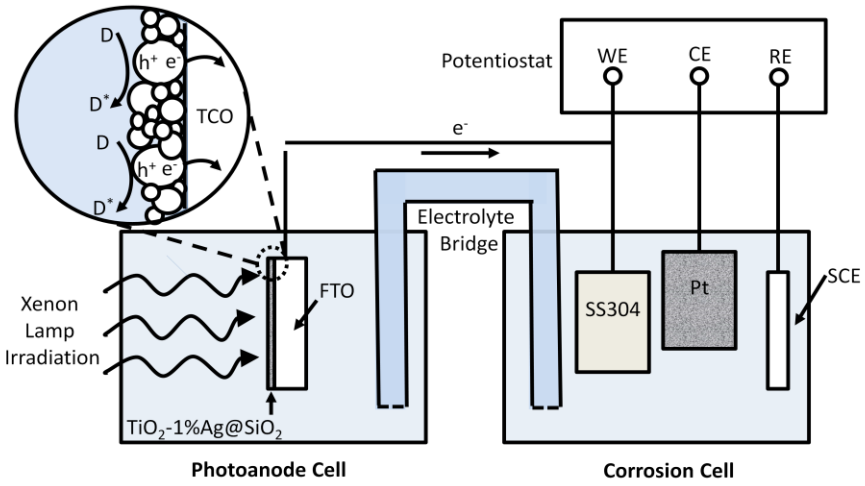

Figure 8.1: Schematic diagram of an electrochemical cell containing two compartments: (i) photoanode cell and (ii) corrosion cell. The photoanode cell, electrolytic bridge, and corrosion cell contain 0.2 M KOH + hole scavenger (D), 1 M KCl, and 0.5 M NaCl, respectively.

The OCP testing of 22MNB5 samples was similar to SS304 except that the CC was in 5 wt % NaCl (0.86 M) in order to accelerate corrosion, whereas as the photoanode cell contained 0.1 M Na_2S. The test was maintained for 48 h. After the experiment, the solution was sonicated to remove loosely bound oxides on the surface of the sample formed during corrosion and the electrolyte solution was kept in 50 mL conical tubes. The samples were centrifuged and washed three times to remove salts at 3500 rpm. The conical tubes containing corrosion products were dried under furnace at 100 ^{o}C overnight and weighed. Subsequently, the corrosion products were removed through washing and sonication step under 0.1 M HCl M. The sample was then rinsed with ultrapure water, dried under furnace overnight, and weighed. The difference between the masses with and without the corrosion products was used to calculate the mass loss.

8.3 Results and Discussions

8.3.1 Materials analysis

TEM images of as synthesized Ag@SiO_2-TiO_2 (AST) compounds and an SEM image of AST-P25 composite are shown in Fig. 8.2 and Fig. 8.3a, respectively. The Ag NPs developed using the polyol methods are on average 64.6 $\pm$ 12.3 nm (Fig. E1). There is a thin layer of SiO_2 and TiO_2 around 10 - 15 nm Fig. 7.2b. The existence of Si (red) and Ti (green) elements in the superimposed STEM-EDX images (Fig. 7.2d) shows that there is evidence of a SiO_2-TiO_2 shell layer even though XRD was not sensitive enough to detect the shell layer containing SiO_2-TiO_2 (Fig. 8.3b). The AST compound was mixed in P25 via sonication in ethanol solution. The

resulting SEM image is shown in Fig. 8.3a where the P25 and AST NPs are clustered together after mixing.

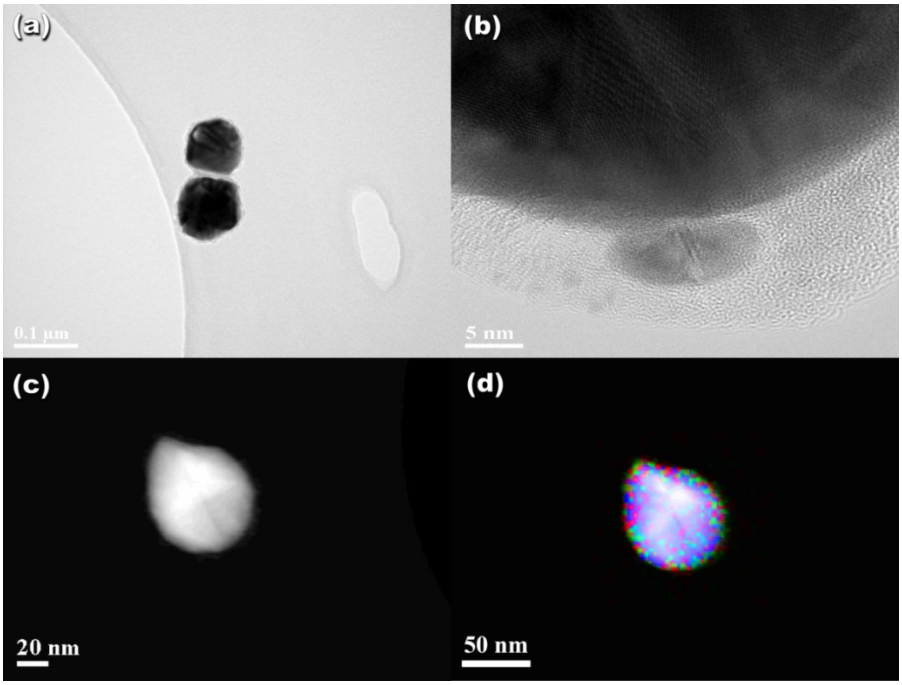

Figure 8.2: Images of as-synthesized AST nanoparticles in (a) conventional TEM, (b) HRTEM, (c) STEM, and (d) superimposed STEM-EDX (blue – Ag, red – Si, green – Ti). Reproduced with permission from [16].

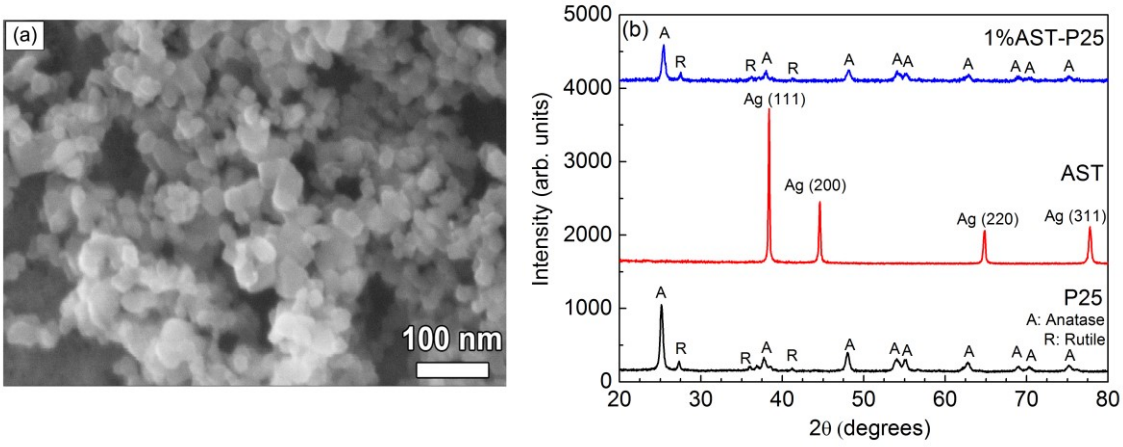

Figure 8.3: (a) SEM image and (B) XRD spectra of AST-P25 composite. Reproduced with permission from [16].

8.3.2 SS304 cyclic potentiodynamic polarization

SS304 was tested under cyclic polarization in 0.5 M NaCl solution with N_2 as seen in Fig. 8.4. The breakdown potential, E_b, is when pitting and crevices can propagate [16–18]. The E_b for the SS304 sample is around 0.4 V_{SCE} and there is an increase in current density as the potential is increased to more positive values. Anodic reactions (corrosion) occur at high current densities. The anodization polarization scan was reversed once the current reached 20 mA cm^{-2}. Under the reverse scan, the repassivation potential, E_{prot}, the potential in which the current intersects the forward scan, was reached at 0.1 V_{SCE},.

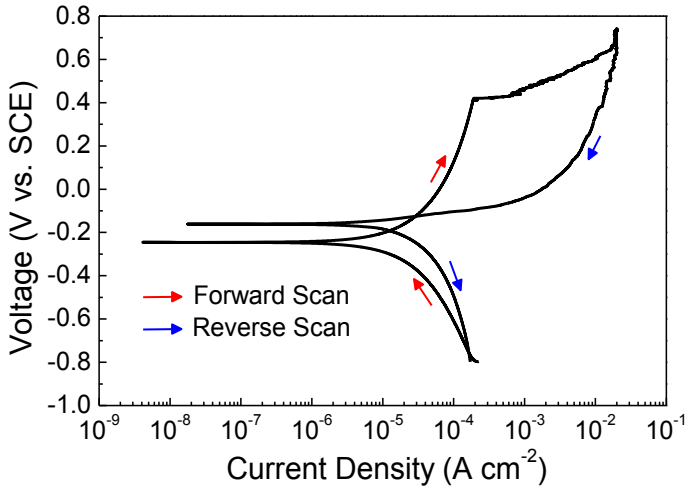

Figure 8.4: The cyclic potentiodynamic polarization test for SS304 in 0.5 M NaCl solution. Reproduced with permission from [16].

8.3.3 Photoelectrochemical properties of AST-P25 electrodes

8.3.3.1 Photocurrent densities under unfiltered and filtered lamp illumination

In Fig.8.5, the photocurrent density under unfiltered and filtered (< 400 nm cutoff) intermittent illumination was measured on P25 and AST-P25 electrodes. The photocurrent density of P25 and AST-P25 is 41 μm cm^{-2} and 84 μm cm^{-2}, respectively. Under filtered light (visible light), the photocurrent density of AST-P25 is 28 times the photocurrent density of P25. The use of Ag in TiO_2 improves the photocatalytic efficiency of TiO_2 under visible light due to the surface plasmons in Ag NPs [19–21]. The surface plasmonic peak of Ag NPs is around 420 nm for synthesized NPs (Fig. E1) so the absorption peak coincides with the bandgap of TiO_2 allowing for visible light to generate photocurrent.

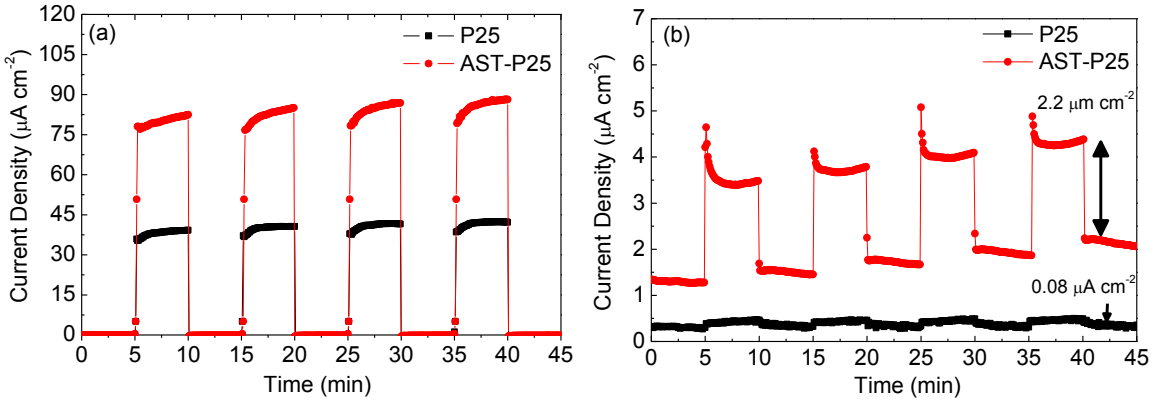

Figure 8.5: Photocurrent density tests using P25 and AST-P25 electrodes under (a) xenon lamp illumination and (b) filtered (400 nm cutoff filter) xenon lamp illumination in 1 M KOH solution. Reproduced with permission from [16].

8.3.3.2 Photocurrent densities as a function of glucose concentration

Glucose is used as a hole scavenger to reduce the recombination as seen in **Chapter 4** [22–24]. Glucose will adsorb onto the surface of TiO_2 and will decompose via hole or hydroxyl attack at the interface under illumination (Fig. E2). The photocurrent densities as a function of the glucose concentration was plotted and the curve corresponds to Langmuir kinetic models (Fig. 8.6). At lower concentrations, the process was limited by mass transfer. At higher concentrations, the photocurrent densities level off and the reaction rate was limited to interfacial reactions. The maximum photocurrent density was 620 μA cm^{-2} (50 mM glucose), 7.2 times the photocurrent density of 1 M KOH solution due to oxidation reactions occurring.

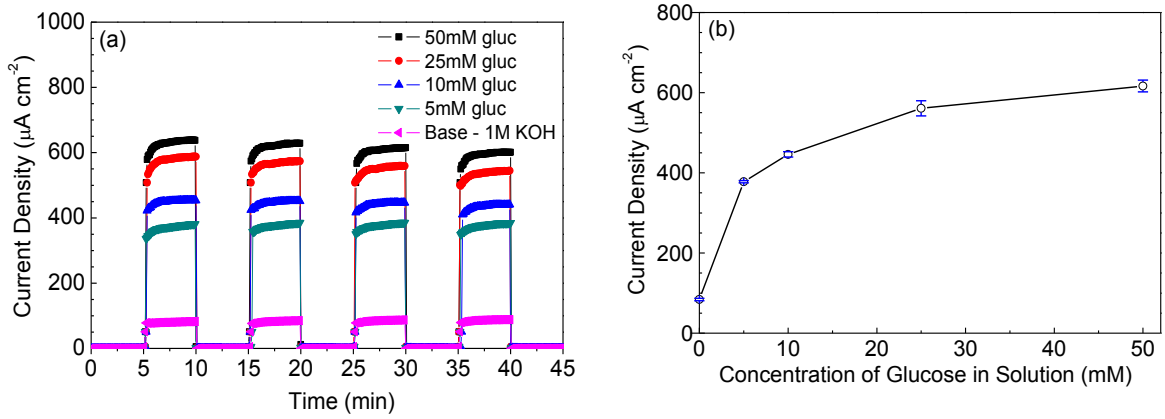

Figure 8.6: (a) Photocurrent density of AST-P25 electrodes in 1 M KOH electrolyte + glucose under intermittent illumination; (b) Photocurrent density as a function of glucose concentration in solution. Reproduced with permission from [16] .

8.3.4 Photocathodic protection of SS304 using AST-P25 photoanodes

The cathodic and anodic reaction processes will tend to equilibrium conditions. If electrons are withdrawn from metal, the rate of the anodic reaction will increase to compensate and iron dissolution will increase, while the cathodic reaction will decrease. If electrons are supplied from an external source, such as a semiconductor photoanode under UV illumination (Fig. 8.7a), the anodic reactions will decrease to reduce corrosion and cathodic reaction will increase. This is known as cathodic protection and is depicted in the anodic and cathodic curves of the Evan's diagram (Fig 8.7b). The corrosion current, I_{corr}, and the corrosion potential, E_{corr}, occur at the point of intersection of the anodic and cathodic curves (equilibrium). If electrons are injected into the metal, anodic (oxidation) of iron is decreased to a potential E_{corr}' and the rate of the anodic current decreases to I_{corr}' due to increase in the cathodic current.

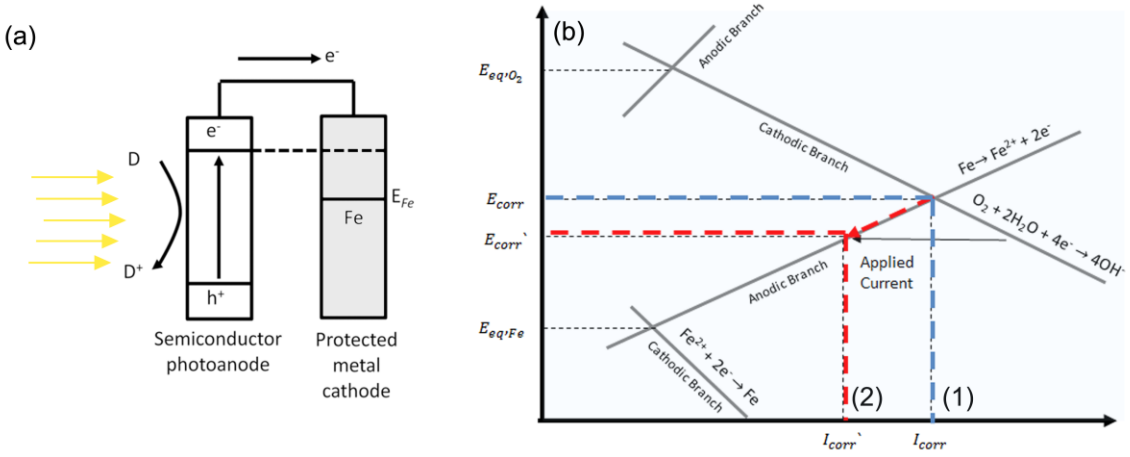

Figure 8.7: Schematic of (a) coupled photoanode and steel cathode and (b) Evan's diagram and application of current via photocathodic protection.

Electroimpedance spectroscopy (Fig. E3) and potentiodynamic polarization (Fig. E4) was conducted with and without coupling with TiO_2 photoanodes in 5 wt % NaCl solution corrosion cell and and 0.2 M KOH PEC cell under UV illumination. The corrosion potential of SS304 base metal (-0.258 V_{SCE}) was shifted to more negative potentials when SS304 was coupled with TiO_2 photoanode in the dark (-0.510 V_{SCE}) and under illumination (-0.970 V_{SCE}). The corrosion current (I_{corr}) increases when coupled under illumination, which may be attributed to enhanced of electrochemical reaction at the interface arising from photogenerated electrons

injected into the SS304 metal. The increased electrochemical reaction was measured using electrochemical impedance spectroscopy to investigate the surface and interface state of SS304 with and without coupling with TiO_2 photoanodes. It was observed in Nyquist plots that the diameter of the impedance arcs of SS304 coupled with TiO_2 was much smaller than that of SS304 base metal with and without UV illumination due to the increase in photoelectrons at the interface of SS304.

8.3.4.1 The effect of hole scavengers

Hole scavengers are useful in inhibiting recombination of photogenerated electron-hole pairs. Water can be considered a hole scavenger, however they perform poorly in terms of limiting electron-hole recombination compared to other inorganic and organic sources [25]. An organic hole scavenger, glucose, and an inorganic hole scavenger, sodium sulfide (Na_2S), was used to test the OCP of SS304 connected to an AST-P25 photoanode.

Inorganic Hole Scavenger

Fig. 8.8 shows the OCP vs. time of SS304 in a 0.5 M NaCl solution that is dearated with N_2 bubbling. The potential of SS304 shifts to more negative values over time and finally stays at a fairly steady-state value of about -0.19 V. Coupling the SS304 with the AST-P25 photoanode, immersed in a cell containing 0.2 M KOH and an inorganic hole scavenger (0.1 M Na_2S), the steel is protected from corrosion via the injection of photo-electrons. Under intermittent light, the steel is at a potential of -0.69 V_{SCE} in the dark; when light is applied, there is an overvoltage, η, of -0.21 V that decreases the potential to -0.90 V_{SCE}.. At both these potentials, the SS304 is protected from anodic corrosion reactions.

The inorganic hole scavenger, disodium sulfide (Na_2S) is dissociated into Na^+ and S^{2-} ions in aqueous solution. At the photoanode-electrolyte interface the following reaction occurs [26]:

$$S^{2-} + 2h^+ \rightarrow S. \qquad \text{Eq. 8.1}$$

The S^{2-} ions in this reaction are sacrificial donors so the photocatalytic efficiency will decay over time. Ideally, in order to obtain a regenerative redox couple, a second element is needed to couple S^{2-}, and in most studies, sulfur is often added to form a polysulfide (S^{2-}/S_x^{2-}) redox couple [26]. This regenerative couple allows the photocatalysis process to undergo optimally for long periods.

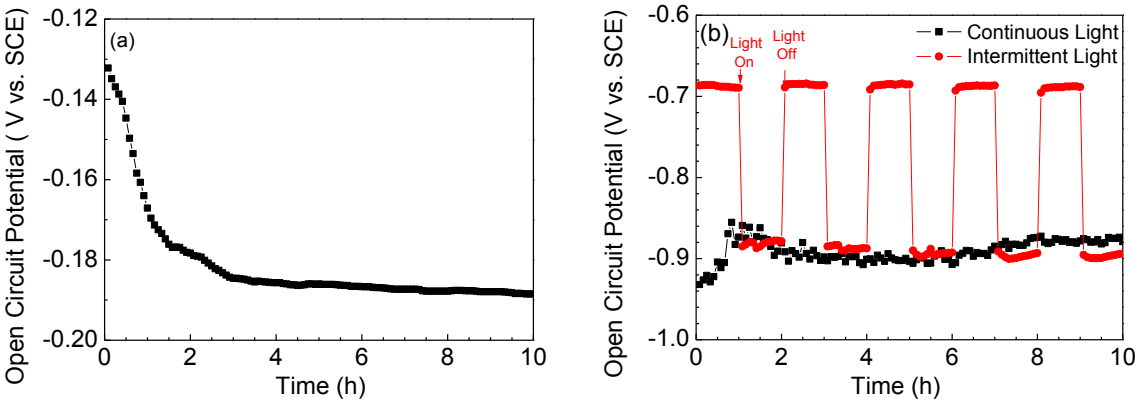

Figure 8.8: The OCP as a function of time of (a) uncoupled SS304 electrode in a 0.5 M NaCl electrolyte (corrosion cell) and (b) SS304 electrode coupled with a AST-P25 electrode in 0.5 M NaCl (corrosion cell) /1 M KCl (electrolyte bridge)/ 0.2 M KOH + 0.1 M Na_2S (photoanode cell).

Organic Hole Scavenger

Organic hole scavengers – alcohols, formate, acetate, citrate, and oxalate – have been previously compared to determine their efficacy [25]. Organic compounds, such as glucose will oxidize into intermediate compounds under the TiO_2/UV AOP process (see Section E2 and Fig. E2 in Appendix E). The effect of glucose on the photocathode protection of SS304 is demonstrated in Fig. 8.9a. The OCP shifts to more negative values and the magnitude of the shift is greater with the addition of glucose. Under intermittent light conditions and the addition of glucose, the SS304 is initially at an OCP of -0.25 V_{SCE} in the dark; when light is applied, there is an η of -0.68 V that decreases the coupled potential to -0.98 V_{SCE}. When light is removed, the potential of the coupled electrodes increases to -0.51 V_{SCE}; this suggests that SS304 is still partially protected from anodic reactions. The potential under dark conditions eventually decays to equilibrium conditions as the dark period is increased. After several intermittent light cycles, the η decreases in each cycle (1 h each under the dark and under illumination) demonstrating in Fig. 8.9b.

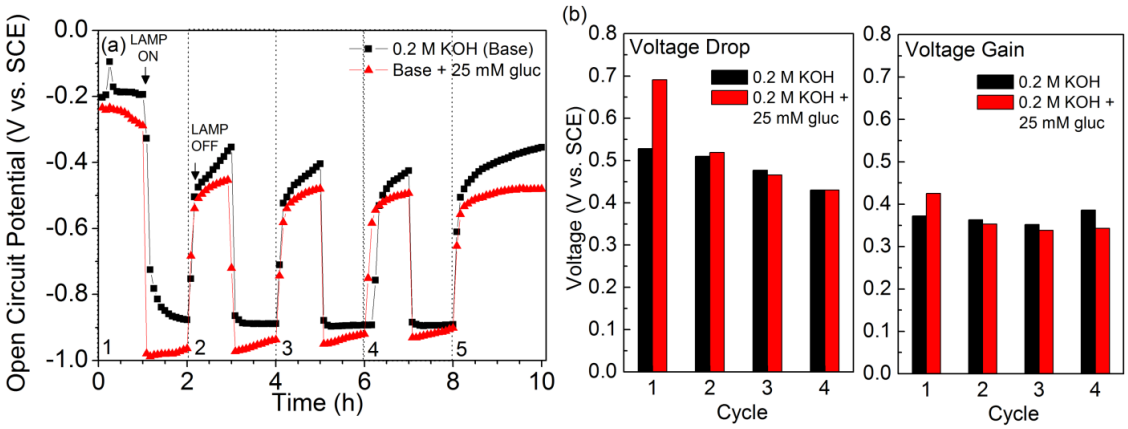

Figure 8.9: SS304 electrode coupled with an AST-P25 photoanode under intermittent light conditions using an electrolyte couple containing 0.5 M NaCl (corrosion cell) /1 M KCl (electrolyte bridge)/ 0.2 M KOH + 25 mM glucose (photoanode cell).

During the photocathodic process, the glucose will scavenge holes generated by the illuminated photoanode and oxidize over time (Fig. 8.10). Over 40 % and 75 % of glucose is oxidized into its constituents under dark and solar irradiation, respectively. The oxidation of glucose under illumination matches well with the η decay after each intermittent cycle in Fig. 8.9b, indicating the η is partially dependent on the glucose concentration in solution. In other words, photocathodic protection and organic degradation occur concurrently and the organic hole scavenger source must be replenished to maintain higher η than the base solution.

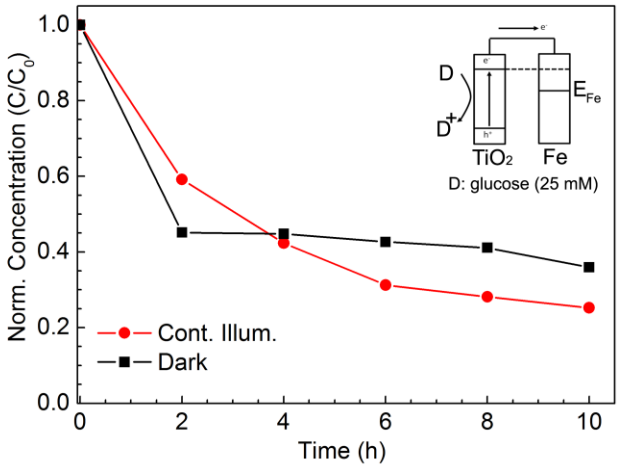

Figure 8.10: Glucose concentration as a function of time using coupled AST-P25 photoanode and SS304 under illumination and dark conditionscontaing 0.5 M NaCl (corrosion cell)/ 1M KCl (electrolyte bridge)/ 0.2 M KOH + 25 mM glucose.

8.3.5 Reduction of mass loss using corrosion-prone martensitic steel

Mass loss analysis was done on 22MNB5 base metal samples in 5 % NaCl for 48 h with and without photocathodic protection (Fig. 8.11a). 22MNB5 steel was used instead of SS304 in order to increase the corrosion rate for quick mass loss analysis in which detectable mass loss occurs is several orders of magnitude lower. The mass loss of 22MNB5 base metal over 48 h was 0.03 % when no cathodic protection was used. Under cathodic protection, the mass loss was negligible. When the metal is uncoupled from the photoanode, the OCP fluctuates from -0.71 to -0.72 V_{SCE}, which has a higher magnitude OCP than SS304 indicating that the metal is more prone to anodic reactions. The coupled OCP decreases to -1.15 V_{SCE} when 22MNB5 is coupled to the photoanode under UV illumination. The TiO_2 photoanode has a higher negative potential under illumination, which indicates that the photoanode supplies electrons via semiconductor photocatalysis to the 22MNB5 base metal to prevent anodic reactions. The prevention of anodic reactions is observed visually in the negligible mass loss and mirror-like finish of the base metal coupon in Fig. 8.11a. The negligible mass loss was also observed under Raman spectra analysis (Fig. 8.11b), which demonstrate lack of iron oxide peaks under cathodic protection and formation of iron oxide crystalline peaks under no protection producing iron oxide products and a more porous surface (Fig. E5b).

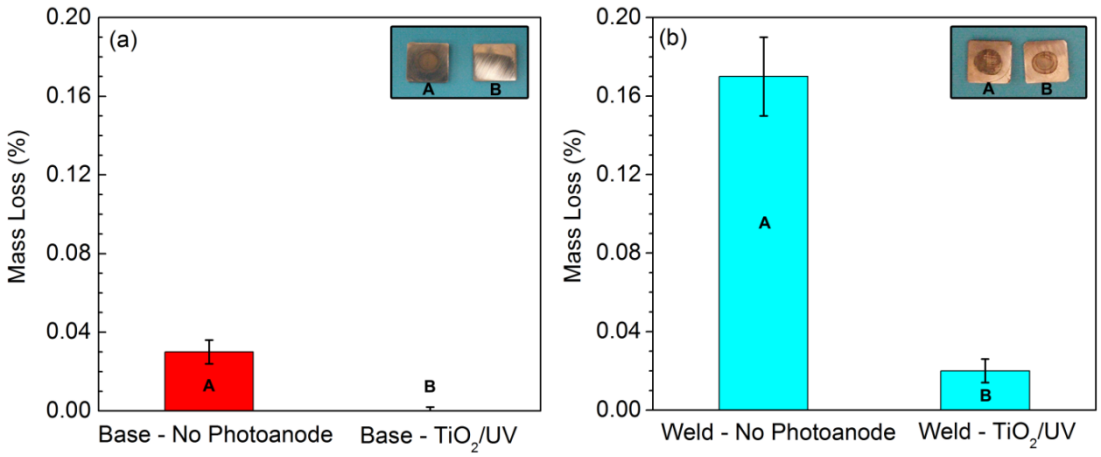

Figure 8.11: Percentage mass loss of 22MNB5 steel of (a) base metal and (b) welded samples with and without TiO_2 photoanode under illumination after 48 h in 5 % NaCl.

Welding of similar and dissimilar metals is required for water treatment infrastructure so it is necessary to test how welded metals behave under photocathodic systems. The welding process changes the composition of the base metal [27] so there are galvanic couples formed from heterogeneous metal compositions, which will preferentially corrode the higher negative potential regions in the weld, heat-affected zone, and base metal(s) [28]. In this study, a centre laser-

welded 22MNB5 samples were used to test the corrosion performance under OCP (Fig. 8.12a). Introducing a weld onto the steel increased the mass loss of the uncoupled metal to 0.17 % and a mass loss of 0.02 % when coupling with the photoanode under UV illumination (Fig. 8.12b). The OCP behaviour with and without coupling of 22MNB5 welded samples was similar to the base metal because only a small region of the metal coupon was affected and the metal is predominantly base metal composition. There are still iron oxides present on the surface under photocathodic protection for 22MNB5 welded samples, but it is mitigated significantly when compared to uncoupled case.

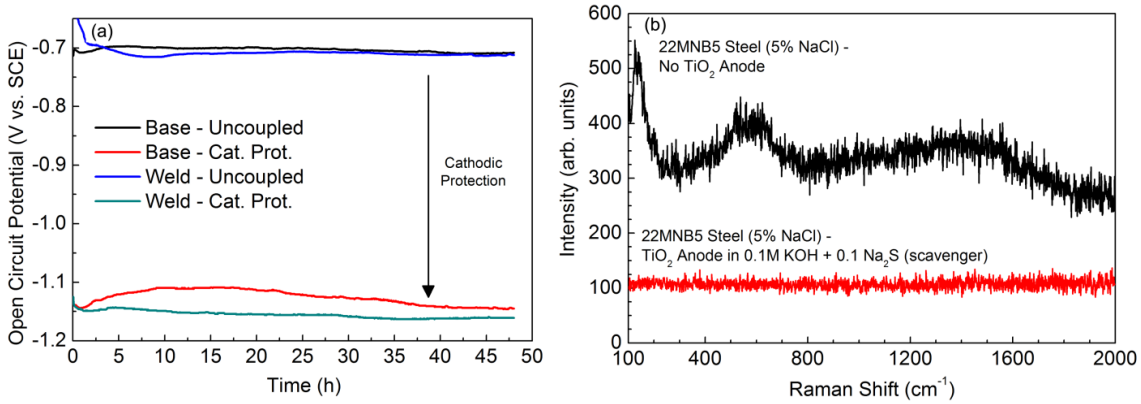

Figure 8.12: (a) Open circuit potential and (b) Raman spectra of 22MNB5 steel with and without TiO_2/UV photocathodic protection.

8.4 Conclusions

Conventional cathode protection requires periodic replacement of sacrificial anodes or a constant supply of external power. AST-P25 NPs were synthesized and demonstrated higher visible light photoactivity than commercial P25 alone. It was shown that:

(1) AST-P25 NPs had higher photocurrents under both unfiltered and filtered (< 400 nm cutoff) xenon lamp irradiation.

(2) Inorganic and organic hole scavengers can be used to limit recombination and increase photocurrent density supplied to the metal being protected.

(3) Using organic hole scavengers, such as glucose, imparted dual functionality to the photocathodic system in that organic compounds can be oxidized at the TiO_2 photoanode simultaneously as photoelectrons are injected to the metal cathode, SS304, to prevent anodic reactions and electron-hole recombination processes.

(4) Welded 22MNB5 samples corroded at a faster rate than base metal 22MNB5 samples and using photocathodic protection the mass loss from corrosion processes and surface oxides produced were minimized.

9.0 Conclusions and Future Work

Overview

In this thesis, the effect of pulsed and continuous light was explored on various TiO_2 nanomaterials. Various TiO_2 synthesis methods were used for these methods that aimed to increase photonic efficiency, including 1-D TiO_2, metal-semiconductor (Ag-TiO_2), and doped TiO_2 nanomaterials. Applications in emerging contaminants, membrane filtration, and corrosion protection were explored. This chapter contains the major conclusions from this work and recommendations for future avenues of research and development.

9.1 Conclusions

9.1.1 TiO_2 nanobelts – material, photoelectrochemical, and photochemical properties

TiO_2 nanobelts (TNB) were synthesized from a hydrothermal method and studied for its photoelectrochemical and photochemical properties. TNB decreased the grain boundary defects of TiO_2 nanoparticle aggregates limiting recombination. The photoelectrocatalytic efficiency of TNB photoanodes can be improved with the use of holes scavengers and applied potential. The photochemical degradation efficiency of pollutants, such as theophylline, can be improved using high reaction temperature, alkaline (high pH) conditions, and low pollutant concentration.

9.1.2 Ag-TiO_2 nanobelts under UV-LED controlled periodic illumination

Ag-TNB nanomaterials were synthesized using a hydrothermal synthesis method and compared with TNB and P25 in a slurry batch reactor. Controlled periodic illumination (CPI) was conducted using various duty cycles and frequencies and evaluated on the basis of apparent kinetic rate and energy requirements in the formation of 2-hydroxyterephthalic acid (HTPA) from the degradation of terephthalic acid. Ag-TNB reduces the recombination and increases the HTPA formation rate from Schottky junctions. Ag-TNB experiments demonstrate detrimental performance when lowering the duty cycle due to lower recombination rates. P25 shows a slight increase in HTPA formation rate when the frequency is increased, whereas TNB shows no change in formation rate because it is a prone to aggregation. The energy per order of magnitude was lowest for Ag-TNB under a high frequency CPI condition compared to TNB and P25.

9.1.3 Degradation of pharmaceuticals using UV-LED/TiO_2 pulse width modulation

A water matrix containing 21 pharmaceuticals and personal care products (PPCPs) was tested using UV/TiO_2 substrate under continuous illumination and CPI. The net charge at the

experimental pH was the main factor in determining the kinetic rate of a specific PPCP degradation. The compounds degrade via power law starting from negatively charged compounds first due to electrostatic attraction of the positively charged TiO_2 substrate at experimental pH = 5. Other factors such as solubility and molecular weight explain the variations in the kinetic rate using a multiple regression model.

Under CPI conditions, the duty cycle and frequency was varied. The electrical energy that is required to reduce the concentration per order of magnitude is lower at lower duty cycles (τ <50%) than under continuous illumination. Alternating frequency profiles of 0.05 Hz and 25 Hz lowered the electrical energy compared to single frequency profiles and continuous illumination, without changing the duty cycle. Overall, CPI is a feasible method from an operational standpoint to lower energy costs of light sources using immobilized TiO_2 due to inherent mass transport limitations.

9.1.4 Doped TiO_2-quartz fiber membranes in a photocatalytic membrane reactor

Photocatalytic quartz fiber filters (QFF) were synthesized using sol-gel and dip-coating processes. The filters were placed in a photocatalytic membrane reactor (PMR) that coupled adsorption, photowetting, photocatalysis, and membrane filtration processes. Adding a TiO_2 coating on quartz fiber filter (TQFF) increased the flux and improved the removal rate of dissolved organic matter compared to uncoated QFF due to the photowetting effect. Switching the UVA radiation source off during filtration did not immediately drop the flux. Nitrogen doped QFF (NTQFF) and TQFF demonstrated increased permeate flux using DI water and acid orange 7 (AO7) under UV illumination; whereas the flux in boron-doped TQFF (BTQFF) and QFF did not improve after UV irradiation was introduced. Higher doping concentrations generally produced better membrane removal properties than the lowest dopant concentration used. The percentage removal of AO7 exposed was greater in UV conditions than in dark conditions for NTQFF samples, but not for TQFF and BTQFF.

9.1.5 Concurrent Photocatalytic Degradation of Organic Contaminants and Photocathodic Protection of Steel

Conventional cathode protection requires periodic replacement of sacrificial anodes or a constant supply of external power. Introducing a TiO_2 photoanode allows for the combination of cathodic protection of photocatalytic degradation of organic pollutants. Silver core – silica-titania shell (AST) - P25 NPs were synthesized for higher photocatalytic activity in the visible light range compared to P25. Introducing organic hole scavengers, or organic pollutant, limits

recombination and increases the photocurrent density supplied to the metal being protected. Furthermore, using organic hole scavengers also adds an additional functionality to the photocathodic system in that organic compounds can be oxidized at the TiO_2 photoanode simultaneously as photoelectrons are injected to the metal cathode, SS304, to prevent anodic reactions and electron-hole recombination processes. It was also shown that mass loss from corrosion processes and surface oxides produced can be minimized for both welded and pristine 22MNB5 steel.

9.2 Recommendations and Future Work

9.2.1 Emerging contaminants

Emerging contaminants are an issue due to the uncertainty of the impact they may present to aquatic ecosystems. This work focused on PPCPs, but there are other contaminants that present not only problems to aquatic ecosystems, but also human health. Two types of emerging contaminants are of interest, especially in North America: (i) cyanobacteria toxins and (ii) naphthenic acids in oil sands process water (OSPW), which is a complex solution containing clays and dissolved organic compounds, trace heavy metals, bitumen residual, and solvents.

One major issue facing Canada is the prevalence of cyanobacteria, which produce algal toxins when stressed that is detrimental to the health of humans and aquatic ecosystems. It was found that microcystin, a class of toxins produced by cyanobacteria, was found in 246 water bodies across Canada, and in every province, often exceeding maximum guidelines for potable water and recreational water quality [1]. The occurrence of potentially hazardous algae blooms has been increasing around the globe and may become more common with the effects of climate change and continued release of nutrients into the environment. The factors that result in the release of toxin are still not well understood. More studies into TiO_2 photocatalysis may be conducted on these classes of toxins.

Extraction methods for bitumen mining in Canadian oil sands generate large volumes of OSPW and accumulate in tailing ponds. This solution is both toxic to many forms of life [2]. TiO_2 photocatalysis combined with solar irradiation may offer a treatment step, to decompose components of OSPW, such as naphthenic acids.

9.2.2 Controlled periodic illumination

UV-LED CPI was shown to reduce the energy per order of magnitude removal of a mixture of pollutants, especially in immobilized TiO_2 membrane reactors in **Chapter 6**. Further studies using the CPI UV/TiO_2 process should be conducted with complex water matrices,

containing microorganisms or natural organic matter, to understand its effects and varying treatment outcomes compared to continuous illumination. Furthermore, more studies should be conducted to determine whether dual frequencies are able to improve degradation rates in complex mixtures and elucidate its mechanism via computational studies. Using higher pulse frequencies in the 100 Hz – 1 kHz range should be attempted and compared to the highest frequency, 25 Hz, used in this work.

9.2.3 Photocatalytic membrane reactor

Improvements to the PMR design and implementation may be explored in the following ways: (i) using doped-TiO_2 and utilizing a UV/visible light sources such as xenon lamp irradiation or sunlight, (ii) operating the PMR under cross-flow conditions, and (iii) lowering PMR system footprint. **Chapter 7** discussed doped TiO_2 under UVA irradiation only and further studies on the effect of sunlight, or a visible light source, is useful in further determining the efficacy of doped-membranes in PMR. The PMR in this work was operating under dead-end filtration where membrane fouling was likely to occur. The rate of photocatalytic degradation may be much lower than the rate of fouling at high pollutant concentrations, so operating the PMR under cross-flow conditions would reduce the membrane fouling [3, 4]. Further improvements can be made by decreasing the PMR system footprint by incorporation of optical fiber bundles that can be used to transmit low power UV-LEDs into the membrane module and irradiate the membrane surface. Side-glowing optical fiber can be inserted into a membrane module to make the PMR compact.

9.2.4 Photocathodic protection

Photocathodic protection was combined with the organic degradation of glucose in a coupled galvanic and photoelectrochemical cell (**Chapter 8**). The same principle can be used in the form of coating TiO_2 on metals, which provide a barrier effect and photocathodic protection to prevent corrosion of metal. Another avenue of research is applying photocathodic protection to a solar PMR system. Solar PMR alone is costly, but adding corrosion protection may make it justifiable to use. A proposed system includes a flow-through photocatalytic reactor cell that degrades organic contaminants and produces photogenerated electrons that can be used to protect buried steel structures. A technical issue with this setup is that it requires a charging source to discharge during dark periods when there is no solar radiation. This problem can be alleviated using capacitors or materials with capacitive behaviour that can be added into TiO_2 [5].

Letters of Copyright Permission

This Agreement between University of Waterloo -- Robert Liang ("You") and Springer ("Springer") consists of your license details and the terms and conditions provided by Springer and Copyright Clearance Center.

License Number	4055100848207
Licensed Content Publisher	Springer
Licensed Content Publication	Journal of Nanoparticle Research
Licensed Content Title	Enhanced degradation of persistent pharmaceuticals found in wastewater treatment effluents using TiO2 nanobelt photocatalysts
Licensed Content Author	Robert Liang
Licensed Content Date	Jan 1, 2013
Licensed Content Volume	15
Licensed Content Issue	10
Type of Use	Thesis/Dissertation
Portion	Full text
Number of figures/tables/illustrations	
Number of copies	1
Author of this Springer article	Yes and you are the sole author of the new work
Order reference number	
Title of your thesis / dissertation	TiO2 Nanomaterials: Fundamentals of Photocatalysis and Multifunctional Water Treatment Applications
Expected completion date	Apr 2017
Estimated size(pages)	200
Requestor Location	University of Waterloo 200 University Ave.West Waterloo, ON N2L3G1 Canada

This Agreement between University of Waterloo -- Robert Liang ("You") and Springer ("Springer") consists of your license details and the terms and conditions provided by Springer and Copyright Clearance Center.

License Number	4055101040989
License date	
Licensed Content Publisher	Springer
Licensed Content Publication	Journal of Nanoparticle Research
Licensed Content Title	Enhanced degradation of persistent pharmaceuticals found in wastewater treatment effluents using TiO2 nanobelt photocatalysts
Licensed Content Author	Robert Liang
Licensed Content Date	Jan 1, 2013
Licensed Content Volume	15
Licensed Content Issue	10
Type of Use	Thesis/Dissertation
Portion	Figures/tables/illustrations
Number of figures/tables/illustrations	10
Author of this Springer article	Yes and you are the sole author of the new work
Order reference number	
Original figure numbers	Figures 1 to 10
Title of your thesis / dissertation	TiO2 Nanomaterials: Fundamentals of Photocatalysis and Multifunctional Water Treatment Applications
Expected completion date	Apr 2017
Estimated size(pages)	200
Requestor Location	University of Waterloo 200 University Ave.West Waterloo, ON N2L3G1 Canada

This Agreement between University of Waterloo -- Robert Liang ("You") and Springer ("Springer") consists of your license details and the terms and conditions provided by Springer and Copyright Clearance Center.

License Number	4055371385252
License date	
Licensed Content Publisher	Springer
Licensed Content Publication	Springer eBook
Licensed Content Title	Photoinduced charge transfer processes at semiconductor electrodes and particles
Licensed Content Author	Rüdiger Memming
Licensed Content Date	Jan 1, 1994
Type of Use	Thesis/Dissertation
Portion	Figures/tables/illustrations
Number of figures/tables/illustrations	1
Author of this Springer article	No
Order reference number	
Original figure numbers	9
Title of your thesis / dissertation	TiO2 Nanomaterials: Fundamentals of Photocatalysis and Multifunctional Water Treatment Applications
Expected completion date	Apr 2017
Estimated size(pages)	200
Requestor Location	University of Waterloo 200 University Ave.West Waterloo, ON N2L3G1 Canada

This Agreement between University of Waterloo -- Robert Liang ("You") and Elsevier ("Elsevier") consists of your license details and the terms and conditions provided by Elsevier and Copyright Clearance Center.

License Number	4055381425394
Licensed Content Publisher	Elsevier
Licensed Content Publication	Journal of Membrane Science
Licensed Content Title	TiO2 nanowire membrane for concurrent filtration and photocatalytic oxidation of humic acid in water
Licensed Content Author	Xiwang Zhang,Alan Jianhong Du,Peifung Lee,Darren Delai Sun,James O. Leckie
Licensed Content Date	10 April 2008
Licensed Content Volume	313
Licensed Content Issue	1-2
Licensed Content Pages	8
Start Page	44
End Page	51
Type of Use	reuse in a thesis/dissertation
Intended publisher of new work	other
Portion	figures/tables/illustrations
Number of figures/tables/illustrations	1
Format	both print and electronic
Are you the author of this Elsevier article?	No
Will you be translating?	No
Order reference number	
Original figure numbers	figure 8
Title of your thesis/dissertation	TiO2 Nanomaterials: Fundamentals of Photocatalysis and Multifunctional Water Treatment Applications
Elsevier VAT number	GB 494 6272 12
Requestor Location	University of Waterloo 200 University Ave.West Waterloo, ON N2L3G1

This Agreement between University of Waterloo -- Robert Liang ("You") and John Wiley and Sons ("John Wiley and Sons") consists of your license details and the terms and conditions provided by John Wiley and Sons and Copyright Clearance Center.

License Number	4055390448496
Licensed Content Publisher	John Wiley and Sons
Licensed Content Publication	Wiley oBooks
Licensed Content Title	Internal Corrosion of Water Conduits
Licensed Content Author	John C. Crittenden,R. Rhodes Trussell,David W. Hand,Kerry J. Howe,George Tchobanoglous
Licensed Content Date	Mar 21, 2012
Licensed Content Pages	105
Type of use	Dissertation/Thesis
Requestor type	University/Academic
Format	Print and electronic
Portion	Figure/table
Number of figures/tables	2
Original Wiley figure/table number(s)	Figure 22-5 Figure 22-4
Will you be translating?	No
Title of your thesis / dissertation	TiO2 Nanomaterials: Fundamentals of Photocatalysis and Multifunctional Water Treatment Applications
Expected completion date	Apr 2017
Expected size (number of pages)	200
Requestor Location	University of Waterloo 200 University Ave.West Waterloo, ON N2L3G1 Canada

This Agreement between University of Waterloo -- Robert Liang ("You") and Elsevier ("Elsevier") consists of your license details and the terms and conditions provided by Elsevier and Copyright Clearance Center.

License Number	4055380238213
Licensed Content Publisher	Elsevier
Licensed Content Publication	Applied Catalysis B: Environmental
Licensed Content Title	Photocatalysis fundamentals revisited to avoid several misconceptions
Licensed Content Author	Jean-Marie Herrmann
Licensed Content Date	9 September 2010
Licensed Content Volume	99
Licensed Content Issue	3-4
Licensed Content Pages	8
Start Page	461
End Page	468
Type of Use	reuse in a thesis/dissertation
Intended publisher of new work	other
Portion	figures/tables/illustrations
Number of figures/tables/illustrations	1
Format	both print and electronic
Original figure numbers	figure 3
Title of your thesis/dissertation	TiO2 Nanomaterials: Fundamentals of Photocatalysis and Multifunctional Water Treatment Applications
Expected completion date	Apr 2017
Estimated size (number of pages)	200
Elsevier VAT number	GB 494 6272 12
Requestor Location	University of Waterloo 200 University Ave.West Waterloo, ON N2L3G1 Canada

This Agreement between University of Waterloo -- Robert Liang ("You") and Elsevier ("Elsevier") consists of your license details and the terms and conditions provided by Elsevier and Copyright Clearance Center.

License Number	4055380882206
Licensed Content Publisher	Elsevier
Licensed Content Publication	Journal of Hazardous Materials
Licensed Content Title	Hydrothermal growth of free standing TiO2 nanowire membranes for photocatalytic degradation of pharmaceuticals
Licensed Content Author	Anming Hu,Xu Zhang,Ken D. Oakes,Peng Peng,Y. Norman Zhou,Mark R. Servos
Licensed Content Date	15 May 2011
Licensed Content Volume	189
Licensed Content Issue	1-2
Licensed Content Pages	8
Start Page	278
End Page	285
Type of Use	reuse in a thesis/dissertation
Intended publisher of new work	other
Portion	figures/tables/illustrations
Number of figures/tables/illustrations	1
Format	both print and electronic
Original figure numbers	table 1
Title of your thesis/dissertation	TiO2 Nanomaterials: Fundamentals of Photocatalysis and Multifunctional Water Treatment Applications
Expected completion date	Apr 2017
Estimated size (number of pages)	200
Elsevier VAT number	GB 494 6272 12
Requestor Location	University of Waterloo 200 University Ave.West Waterloo, ON N2L3G1 Canada

This Agreement between University of Waterloo -- Robert Liang ("You") and Elsevier ("Elsevier") consists of your license details and the terms and conditions provided by Elsevier and Copyright Clearance Center.

License Number	4055381009162
Licensed Content Publisher	Elsevier
Licensed Content Publication	Water Research
Licensed Content Title	Photocatalytic oxidation of DBP precursors using UV with suspended and fixed TiO2
Licensed Content Author	Fraser C. Kent,Krysta R. Montreuil,Ryan M. Brookman,Robbie Sanderson,Jeff R. Dahn,Graham A. Gagnon
Licensed Content Date	15 November 2011
Licensed Content Volume	45
Licensed Content Issue	18
Licensed Content Pages	8
Start Page	6173
End Page	6180
Type of Use	reuse in a thesis/dissertation
Intended publisher of new work	other
Portion	figures/tables/illustrations
Number of figures/tables/illustrations	1
Format	both print and electronic
Original figure numbers	figure 4
Title of your thesis/dissertation	TiO2 Nanomaterials: Fundamentals of Photocatalysis and Multifunctional Water Treatment Applications
Expected completion date	Apr 2017
Estimated size (number of pages)	200
Elsevier VAT number	GB 494 6272 12
Requestor Location	University of Waterloo 200 University Ave.West Waterloo, ON N2L3G1 Canada

This Agreement between University of Waterloo -- Robert Liang ("You") and Elsevier ("Elsevier") consists of your license details and the terms and conditions provided by Elsevier and Copyright Clearance Center.

License Number	4055381314857
Licensed Content Publisher	Elsevier
Licensed Content Publication	Water Research
Licensed Content Title	Concurrent filtration and solar photocatalytic disinfection/degradation using high-performance Ag/TiO2 nanofiber membrane
Licensed Content Author	Lei Liu,Zhaoyang Liu,Hongwei Bai,Darren Delai Sun
Licensed Content Date	15 March 2012
Licensed Content Volume	46
Licensed Content Issue	4
Licensed Content Pages	12
Start Page	1101
End Page	1112
Type of Use	reuse in a thesis/dissertation
Intended publisher of new work	other
Portion	figures/tables/illustrations
Number of figures/tables/illustrations	1
Format	both print and electronic
Order reference number	
Original figure numbers	figure 7
Title of your thesis/dissertation	TiO2 Nanomaterials: Fundamentals of Photocatalysis and Multifunctional Water Treatment Applications
Expected completion date	Apr 2017
Estimated size (number of pages)	200
Elsevier VAT number	GB 494 6272 12
Requestor Location	University of Waterloo 200 University Ave.West Waterloo, ON N2L3G1, Canada

Nanotechnology for Water Treatment and Purification

Order detail ID:	70388175
ISBN	:9783319374703
Publication Type:	Book
Publisher:	Springer
Permission type:	Republish or display content
Type of use:	Thesis/Dissertation
License Number:	4091690250405
Requestor type	Academic institution
Format	Electronic
Portion	chapter/article
Number of pages in chapter/article	77
Title or numeric reference of the portion(s)	Chapter 1: Fundamentals on Adsorption, Membrane Filtration, and Advanced Oxidation Processes for Water Treatment; and Chapter 2: Development of TiO2 Nanowires for Membrane Filtration Applications.
Author of portion(s)	Robert Liang, Melisa Hatat Fraile, Anming Hu, Y. Norman Zhou
Page range of portion	Chapters 1 and 2
Publication date of portion	2014
Rights for	Main product
Duration of use	Life of current edition
With minor editing privileges	yes
For distribution to	Canada
In the following language(s)	Original language of publication
The requesting person/organization	Robert Liang/University of Waterloo
Author/Editor	Robert Liang
The standard identifier of New Work	TiO2 Nanomaterials: Fundamentals of Photocatalysis and Multifunctional Water Treatment Applications
Title of New Work	TiO2 Nanomaterials: Fundamentals of Photocatalysis and Multifunctional Water Treatment Applications
Publisher of New Work	University of Waterloo
Expected publication date	Apr 2017
Estimated size (pages)	220

References

Chapter 1

[1] J. S. Ings, M. M. Vijayan, and M. R. Servos, "Tissue-specific metabolic changes in response to an acute handling disturbance in juvenile rainbow trout exposed to municipal wastewater effluent," *Aquat. Toxicol.*, vol. 108, pp. 53–59, 2012.

[2] O. P. Togunde, K. D. Oakes, M. R. Servos, and J. Pawliszyn, "Determination of Pharmaceutical Residues in Fish Bile by Solid-Phase Microextraction Couple with Liquid Chromatography-Tandem Mass Spectrometry (LC/MS/MS)," *Environ. Sci. Technol.*, vol. 46, no. 10, pp. 5302–5309, 2012.

[3] G. R. Tetreault, C. J. Bennett, C. Cheng, M. R. Servos, and M. E. McMaster, "Reproductive and histopathological effects in wild fish inhabiting an effluent-dominated stream, Wascana Creek, SK, Canada," *Aquat. Toxicol.*, vol. 110, pp. 149–161, 2012.

[4] V. Belgiorno, V. Naddeo, and L. Rizzo, *Water, wastewater and soil treatment by advanced oxidation processes.* 2011.

[5] K. Nakata and A. Fujishima, "TiO2 photocatalysis: Design and applications," *J. Photochem. Photobiol. C Photochem. Rev.*, vol. 13, no. 3, pp. 169–189, 2012.

[6] A. Fujishima and K. Honda, "Electrochemical Photolysis of Water at a Semiconductor Electrode," *Nature*, vol. 238, no. 5358, pp. 37–38, 1972.

[7] B. O'Regan and M. Grätzel, "A low-cost, high-efficiency solar cell based on dye-sensitized colloidal TiO2 films," *Nature*, vol. 353, no. 6346, pp. 737–740, 1991.

Chapter 2

[1] A. Fujishima, T. N. Rao, and D. A. Tryk, "Titanium dioxide photocatalysis," *J. Photochem. Photobiol. C Photochem. Rev.*, vol. 1, no. 1, pp. 1–21, 2000.

[2] A. R. Gandhe, S. P. Naik, and J. B. Fernandes, "Selective synthesis of N-doped mesoporous TiO2 phases having enhanced photocatalytic activity," *Microporous Mesoporous Mater.*, vol. 87, no. 2, pp. 103–109, 2005.

[3] R. Liang, A. Hu, M. Hatat-Fraile, and N. Zhou, (a) "Fundamentals on adsorption, membrane filtration, and advanced oxidation processes for water treatment," and, (b) Development of TiO2 nanowires for membrane filtration applications" in *Nanotechnology for Water treatment and Purification*, Springer, pp. 1-77, 2014.

[4] A. J. Dekker, *Solid State Physics*. Englewood Cliffs, NJ: Prentice-Hall, 1957.

[5] V. Augugliaro, V. Loddo, M. Pagliaro, G. Palmisano, L. Palmisano, and L. Palmisano, *Clean by Light Irradiation*. Cambridge: Royal Society of Chemistry, 2010.

[6] H. Gerischer, *Physical Chemistry, An Advanced Treatise Vol. IX*. New York: Academic Press, 1970.

[7] F. Lohmann, "Fermi-Niveau und Flachbandpotential von Molekulkristallen aromatischer Kohlenwasserstoffe," *Z. Naturforschg*, vol. 22, no. a, pp. 843–844, 1967.

[8] Y. V. Pleskov and Y. Y. Gurevich, *Semiconductor Photoelectrochemistry*. New York: Consultants Bureau, 1986.

[9] S. Litch, A. J. Bard, and M. Stratmann, *Encyclopedia of Electrochemistry, Vol. 6*. Weinheim, Germany, 2002.

[10] R. Memming, "Photoinduced charge transfer processes at semiconductor electrodes and particles," *Top. Curr. Chem.*, vol. 169, pp. 105–181, 1994.

[11] H. Zhang and J. F. Banfield, "Understanding Polymorphic Phase Transformation Behavior during Growth of Nanocrystalline Aggregates: Insights from TiO2," *J. Phys. Chem. B*, 2000, vol., no.104 (15), pp 3481–3487, 2000.

[12] A. Fujishima, X. Zhang, and D. A. Tryk, "TiO2 photocatalysis and related surface phenomena," *Surf. Sci. Rep.*, vol. 63, no. 12, pp. 515–582, 2008.

[13] R. W. G. Wycoff, *Crystal Structures, Vol. 1*. New York: Wiley, 1963.

[14] C. Hermann, O. Lohrmann, and H. Philipp, *Strukturbericht Band II 1928-1932*. Leipzig: Akademische Verlagsgesellschaft MBH, 1937.

[15] M. Horn, C. F. Schwerdtfeger, and E. P. Meagher, "Refinement of the structure of anatase at several temperatures *," vol. 136, pp. 273–281, 1972.

[16] M. R. Hoffmann, S. T. Martin, W. Choi, D. W. Bahnemannt, and W. M. Keck, "Environmental Applications of Semiconductor Photocatalysis," *Chem. Rev*, vol. 95, pp. 69–96, 1995.

[17] R. Asahi, T. Morikawa, T. Ohwaki, K. Aoki, and Y. Taga, "Visible-Light Photocatalysis in Nitrogen-Doped Titanium Oxides," *Science (80-.).*, vol. 293, no. 5528, 2001.

[18] H. Irie, Y. Watanabe, and K. Hashimoto, "Nitrogen-Concentration Dependence on Photocatalytic Activity of TiO 2 - x N x Powders," *J. Phys. Chem. B*, vol. 107, no. 23, pp. 5483–5486, Jun. 2003.

[19] P. Meriaudeau and J. C. Vedrine, "Electron paramagnetic resonance investigation of oxygen photoadsorption and its reactivity with carbon monoxide on titanium dioxide: the O 3? 3 species," *J. Chem. Soc. Faraday Trans. 2*, vol. 72, p. 472, 1976.

[20] W. R. Murphy, T. F. Veerkamp, and T. W. Leland, "Effect of ultraviolet radiation on zinc oxide catalysts," *J. Catal.*, vol. 43, no. 1, pp. 304–321, 1976.

[21] N. Sakai, R. Wang, A. Fujishima, T. Watanabe, and K. Hashimoto, "Effect of Ultrasonic Treatment on Highly Hydrophilic TiO 2 Surfaces," *Langmuir*, vol. 14, no. 20, pp. 5918–5920, 1998.

[22] R. Wang, N. Sakai, A. Fujishima, T. Watanabe, and K. Hashimoto, "Studies of Surface Wettability Conversion on TiO2 Single-Crystal Surfaces," *J. Phys. Chem. B*, vol. 103, no. 12, pp. 2188–2194, 1999.

[23] W.C. Wu, L.F. Liao, J.S. Shiu, and J.L. Lin, "FTIR study of interactions of ethyl iodide with powdered TiO2," *Phys. Chem. Chem. Phys.*, vol. 2, no. 19, pp. 4441–4446, 2000.

[24] A. Emeline, A. Salinaro, V. K. Ryabchuk, and N. Serpone, "Photo-induced processes in heterogeneous nanosystems. From photoexcitation to interfacial chemical transformations," *Int. J. Photoenergy*, vol. 3, no. 1, pp. 1–16, 2001.

[25] V. Ryabchuk, "Photophysical processes related to photoadsorption and photocatalysis on wide band gap solids: A review," *Int. J. Photoenergy*, vol. 6, no. 3, pp. 95–113, 2004.

[26] G. Palmisano, V. Loddo, V. Augugliaro, L. Palmisano, and S. Yurdakal, "Photocatalytic oxidation of nitrobenzene and phenylamine: Pathways and kinetics," *AIChE J.*, vol. 53, no. 4, pp. 961–968, 2007.

[27] A. Gora, B. Toepfer, V. Puddu, and G. Li Puma, "Photocatalytic oxidation of herbicides in

single-component and multicomponent systems: Reaction kinetics analysis," *Appl. Catal. B Environ.*, vol. 65, no. 1, pp. 1–10, 2006.

[28] H. de Lasa, B. Serrano, and M. Salaices, *Photocatalytic Reaction Engineering*. Boston, MA: Springer US, 2005.

[29] H. Ibrahim and H. de Lasa, "Kinetic modeling of the photocatalytic degradation of air-borne pollutants," *AIChE J.*, vol. 50, no. 5, pp. 1017–1027, 2004.

[30] J. M. Herrmann, "Photocatalysis fundamentals revisited to avoid several misconceptions," *Appl. Catal. B Environ.*, vol. 99, no. 3, pp. 461–468, 2010.

[31] A. K. Horváth, M. Dolnik, A. P. Muñuzuri, A. M. Zhabotinsky, and I. R. Epstein, "Control of Turing Structures by Periodic Illumination," *Phys. Rev. Lett.*, vol. 83, no. 15, pp. 2950–2952, 1999.

[32] R. Emerson and W. Arnold, " A Separation of the reactions in photosynthesis by means of intermittent light," *J. Gen. Physiol.*, vol. 15, no. 4, 1932.

[33] P. Xiong and J. Hu, "Inactivation/reactivation of antibiotic-resistant bacteria by a novel UVA/LED/TiO2 system," *Water Res.*, vol. 47, no. 13, pp. 4547–4555, 2013.

[34] H. Tada, F. Suzuki, S. Ito, T. Akita, K. Tanaka, T. Kawahara, and H. Kobayashi, "Au-Core/Pt-Shell Bimetallic Cluster-Loaded TiO2. 1. Adsorption of Organosulfur Compound," *J. Phys. Chem. B*, vol. 106, no. 34, pp 8714–8720, 2002.

[35] P. Pichat, Ed., *Photocatalysis and Water Purification*. Weinheim, Germany: Wiley-VCH Verlag GmbH & Co. KGaA, 2013.

[36] R. Alexandrescu, F. Dumitrache, I. Morjan, I. Sandu, …,. and R. Piticescu, "TiO_2 nanosized powders by $TiCl_4$ laser pyrolysis," *Nanotechnology*, vol. 15, no. 5, pp. 537–545, 2004.

[37] H. Maskrot, N. Herlin-Boime, Y. Leconte, K. Jursikova, C. Reynaud, and J. Vicens, "Blue TiO_{2-x} /SiO2 nanoparticles by laser pyrolysis," *J. Nanoparticle Res.*, vol. 8, no. 3–4, pp. 351–360, 2006.

[38] G. Ma, X. Zhao and J. Zhu, "Microwave Hydrothermal Synthesis of Rutile TiO_2 nanorods," *Int. J. Mod. Phys. B*, vol. 19, no. 15n17, pp. 2763–2768, 2005.

[39] S. Komarneni, R. K. Rajha, and H. Katsuki, "Microwave-hydrothermal processing of titanium dioxide," *Mater. Chem. Phys.*, vol. 61, no. 1, pp. 50–54, 1999.

[40] A. B. Corradi, F. Bondioli, B. Focher, A. M. Ferrari, C. Grippo, E. Mariani, and C. Villa, "Conventional and Microwave-Hydrothermal Synthesis of TiO2 Nanopowders," *J. Am. Ceram. Soc.*, vol. 88, no. 9, pp. 2639–2641, 2005.

[41] H. G. Yang, G. Liu, S. Z. Qiao, C. H. Sun, Y. G. Jin, S. C. Smith, J. Zou, H. M. Cheng, and G. Q. (Max) Lu, "Solvothermal Synthesis and Photoreactivity of Anatase TiO_2 Nanosheets with Dominant {001} Facets," *J. Am. Chem. Soc.*, vol. 131, no. 11, pp. 4078–4083, 2009.

[42] B.M. Wen, C.Y. Liu, Y. Liu, J. Hu, …, H. Herrmann, and M. R. Hoffmann, "Solvothermal synthesis of ultralong single-crystalline TiO2 nanowires," *New J. Chem.*, vol. 29, no. 7, pp. 969–971, 2005.

[43] Z. Jiang, F. Yang, N. Luo, B. T. T. Chu, D. Sun, H. Shi, T. Xiao, and P. P. Edwards, "Solvothermal synthesis of N-doped TiO2 nanotubes for visible-light-responsive photocatalysis," *Chem. Commun.*, vol. 0, no. 47, p. 6372, 2008.

[44] H. K. Kammler, L. Mädler, and S. E. Pratsinis, "Flame Synthesis of Nanoparticles,"

Chem. Eng. Technol., vol. 24, no. 6, pp. 583–596, 2001.

[45] R. N. Grass, S. Tsantilis, and S. E. Pratsinis, "Design of high-temperature, gas-phase synthesis of hard or soft TiO2 agglomerates," *AIChE J.*, vol. 52, no. 4, pp. 1318–1325, 2006.

[46] R. Liang, A. Hu, W. Li, and Y. N. Zhou, "Enhanced degradation of persistent pharmaceuticals found in wastewater treatment effluents using TiO2 nanobelt photocatalysts," *J. Nanoparticle Res.*, vol. 15, no. 10, p. 1990, 2013.

[47] A. Hu, X. Zhang, D. Luong, K. D. Oakes, M. R. Servos, R. Liang, S. Kurdi, P. Peng, and Y. Zhou, "Adsorption and Photocatalytic Degradation Kinetics of Pharmaceuticals by TiO2 Nanowires During Water Treatment," *Waste and Biomass Valorization*, vol. 3, no. 4, pp. 443–449, 2012.

[48] C. C. T. and and H. Teng*, "Structural Features of Nanotubes Synthesized from NaOH Treatment on TiO2 with Different Post-Treatments," *Chem. Mater.*, vol. 18, no. 2, pp. 367–373, 2006.

[49] Z. Yanqing, S. Erwei, C. Zhizhan, L. Wenjun,…, and Z.W. Yin, "Influence of solution concentration on the hydrothermal preparation of titania crystallites," *J. Mater. Chem.*, vol. 11, no. 5, pp. 1547–1551, 2001.

[50] D. Robert and J. V. Weber, "Titanium Dioxide Synthesis by Sol Gel Methods and Evaluation of Their Photocatalytic Activity," *J. Mater. Sci. Lett.*, vol. 18, no. 2, pp. 97–98, 1999.

[51] R. Campostrini, G. Carturan, L. Palmisano, M. Schiavello, and A. Sclafani, "Sol-gel derived anatase TiO2: morphology and photoactivity," *Mater. Chem. Phys.*, vol. 38, no. 3, pp. 277–283, 1994.

[52] M. Ischia, R. Campostrini, L. Lutterotti, E. Garcia-Lopez, L. Palmisano, M. Schiavello, F. Pirillo, and R. Molinari, "Synthesis, Characterization and Photocatalytic Activity of TiO2 Powders Prepared Under Different Gelling and Pressure Conditions," *J. Sol-Gel Sci. Technol.*, vol. 33, no. 2, pp. 201–213, Feb. 2005.

[53] M. S. Lee, S.-S. Hong, and M. Mohseni, "Synthesis of photocatalytic nanosized TiO2–Ag particles with sol–gel method using reduction agent," *J. Mol. Catal. A Chem.*, vol. 242, no. 1, pp. 135–140, 2005.

[54] X. Z. Li and F. B. Li, "Study of Au/Au3+-TiO2 photocatalysts toward visible photooxidation for water and wastewater treatment," *Environ. Sci. Technol.*, vol. 35, no. 11, pp. 2381–2387, 2001.

[55] J. O. Carneiro, V. Teixeira, A. Portinha, L. Dupák, A. Magalhães, and P. Coutinho, "Study of the deposition parameters and Fe-dopant effect in the photocatalytic activity of TiO2 films prepared by dc reactive magnetron sputtering," *Vacuum*, vol. 78, no. 1, pp. 37–46, 2005.

[56] F. B. Li and X. Z. Li, "The enhancement of photodegradation efficiency using Pt–TiO2 catalyst," *Chemosphere*, vol. 48, no. 10, pp. 1103–1111, 2002.

[57] R. Liang, A. Hu, J. Persic, and Y. Zhou, "Palladium Nanoparticles Loaded on Carbon Modified TiO2 Nanobelts for Enhanced Methanol Electrooxidation," *Nano-Micro Lett*, vol. 5, no. 3, pp. 202–212, 2013.

[58] S. Sato and J. M. White, "Photodecomposition of water over Pt/TiO2 catalysts," *Chem. Phys. Lett.*, vol. 72, no. 1, pp. 83–86, 1980.

[59] A. Zaleska, J. W. Sobczak, E. Grabowska, and J. Hupka, “Preparation and photocatalytic activity of boron-modified TiO2 under UV and visible light,” *Appl. Catal. B Environ.*, vol. 78, no. 1–2, pp. 92–100, 2008.

[60] S. Y. Treschev, P.-W. Chou, Y.-H. Tseng, J.-B. Wang, E. V. Perevedentseva, and C.-L. Cheng, “Photoactivities of the visible-light-activated mixed-phase carbon-containing titanium dioxide: The effect of carbon incorporation,” *Appl. Catal. B Environ.*, vol. 79, no. 1, pp. 8–16, 2008.

[61] L. Kőrösi and I. Dékány, “Preparation and investigation of structural and photocatalytic properties of phosphate modified titanium dioxide,” *Colloids Surfaces A Physicochem. Eng. Asp.*, vol. 280, no. 1, pp. 146–154, 2006.

[62] Z. Wu, F. Dong, W. Zhao, and S. Guo, “Visible light induced electron transfer process over nitrogen doped TiO2 nanocrystals prepared by oxidation of titanium nitride,” *J. Hazard. Mater.*, vol. 157, no. 1, pp. 57–63, 2008.

[63] K. Takeshita, A. Yamakata, T. Ishibashi, H. Onishi, K. Nishijima, and T. Ohno, “Transient IR absorption study of charge carriers photogenerated in sulfur-doped TiO2,” *J. Photochem. Photobiol. A Chem.*, vol. 177, no. 2, pp. 269–275, 2006.

[64] a. Hu, R. Liang, X. Zhang, S. Kurdi, D. Luong, H. Huang, P. Peng, E. Marzbanrad, K. D. Oakes, Y. Zhou, and M. R. Servos, “Enhanced photocatalytic degradation of dyes by TiO2 nanobelts with hierarchical structures,” *J. Photochem. Photobiol. A Chem.*, vol. 256, pp. 7–15, 2013.

[65] L. D. Landau and B. G. Levich, “Dragging of a liquid by a moving plate,” *Acta Physicochim. URSS*, vol. 17, pp. 42–54, 1942.

[66] T. E. Cloete, M. D. Kwaadsteniet, M. Botes, and J. M. Lopez-Romero, *Nanotechnology in Water Treatment Applications*. Norfolk: Caister Academic Press, 2010.

[67] D. Li and Y. Xia, “Electrospinning of Nanofibers: Reinventing the Wheel?,” *Adv. Mater.*, vol. 16, no. 14, pp. 1151–1170, 2004.

[68] S. Ramakrishna, K. Fujihara, W.-E. Teo, T. Yong, Z. Ma, and R. Ramaseshan, “Electrospun nanofibers: solving global issues,” *Mater. Today*, vol. 9, no. 3, pp. 40–50, 2006.

[69] M. R. Narayan and A. Raturi, “Deposition and characterisation of titanium dioxide films formed by electrophoretic deposition,” *Int. J. Mater. Eng. Innov.*, vol. 3, no. 1, pp. 17–31, 2012.

[70] P. Sarkar, D. De, T. Uchikochi, and L. Besra, “Electrophoretic Deposition (EPD): Fundamentals and Novel Applications in Fabrication of Advanced Ceramic Microstructures,” in *Electrophoretic Deposition of Nanomaterials*, Springer New York, 2012, pp. 181–215.

[71] M. Kawakita, T. Uchikoshi, J. Kawakita, and Y. Sakka, “Preparation of Crystalline-Oriented Titania Photoelectrodes on ITO Glasses from a 2-Propanol-2,4-Pentanedione Solvent by Electrophoretic Deposition in a Strong Magnetic Field,” *J. Am. Ceram. Soc.*, vol. 92, no. 5, pp. 984–989, 2009.

[72] Y. Lin, G. S. Wu, X. Y. Yuan, T. Xie, …, and F. S. S. Yuan Z H, “Fabrication and optical properties of TiO_2 nanowire arrays made by sol gel electrophoresis deposition into anodic alumina membranes,” *J. Phys. Condens. Matter*, vol. 15, no. 17, pp. 2917–2922, 2003.

[73] M. Shiojiri, “Crystallization of Amorphous Titanium Dioxide Films Prepared by Vacuum-

Evaporation," *J. Phys. Soc. Japan*, vol. 21, no. 2, pp. 335–345, Feb. 1966.

[74] K. N. Rao and S. Mohan, "Optical properties of electron-beam evaporated TiO_2 films deposited in an ionized oxygen medium," *J. Vac. Sci. Technol. A Vacuum, Surfaces, Film.*, vol. 8, no. 4, pp. 3260–3264, 1990.

[75] M. H. Suhail, G. M. Rao, and S. Mohan, "dc reactive magnetron sputtering of titanium-structural and optical characterization of TiO_2 films," *J. Appl. Phys.*, vol. 71, no. 3, pp. 1421–1427, 1992.

[76] X. Wang, H. Masumoto, Y. Someno, and T. Hirai, "Helicon plasma deposition of a TiO2/SiO2 multilayer optical filter with graded refractive index profiles," *Appl. Phys. Lett.*, vol. 72, no. 25, pp. 3264–3266, 1998.

[77] H. H. Nguyen, W. Prellier, J. Sakai, and A. Ruyter, "Substrate effects on the room-temperature ferromagnetism in Co-doped TiO2 thin films grown by pulsed laser deposition," *J. Appl. Phys.*, vol. 95, no. 11, pp. 7378–7380, 2004.

[78] K. L. Siefering and G. L. Griffin, "Kinetics of Low-Pressure Chemical Vapor Deposition of TiO[sub 2] from Titanium Tetraisopropoxide," *J. Electrochem. Soc.*, vol. 137, no. 3, pp. 814–818, 1990.

[79] P. Evans, M E. Pemble, and D.W. Sheel, "Precursor-Directed Control of Crystalline Type in Atmospheric Pressure CVD Growth of TiO2 on Stainless Steel," *Chem. Mater.*, vol. 18, no. 24, pp. 5750–5755, 2006.

[80] M. Ueda, R. Matsunaga, M. Ikeda, and M. Ogawa, "Hydrothermal Crystallization of TiO 2 Gel Films on Ti Substrates and Formability of Hydroxyapatite," *Mater. Trans.*, vol. 49, no. 7, pp. 1706–1709, 2008.

[81] X. F. Cheng, W. H. Leng, D. P. Liu, Y. M. Xu, J. Q. Zhang, and C. N. Cao, "Electrochemical Preparation and Characterization of Surface-Fluorinated TiO_2 Nanoporous Film and Its Enhanced Photoelectrochemical and Photocatalytic Properties," *J. Phys. Chem. C*, vol. 112, no. 23, pp. 8725–8734, 2008.

[82] M. Paulose, H. E. Prakasam, O. K. Varghese, L. Peng, K. C. Popat, G. K. Mor, and T. A. Desai, and C. A. Grimes, "TiO2 Nanotube Arrays of 1000 μm Length by Anodization of Titanium Foil: Phenol Red Diffusion," *J. Phys. Chem.*, vol. 111, no. 41, pp. 14992–14997, 2007.

[83] Q. Cai, M. Paulose, O. K. Varghese, and C. A. Grimes, "The Effect of Electrolyte Composition on the Fabrication of Self-Organized Titanium Oxide Nanotube Arrays by Anodic Oxidation," *J. Mater. Res.*, vol. 20, no. 1, pp. 230–236, Jan. 2005.

[84] W. Schmickler and E. Santos, *Interfacial Electrochemistry, Vol. 134*. New York: Oxford University Press, 1996.

[85] V. Naddeo, L. Rizzo, and V. Belgiorno, *Water, Wastewater and Soil Treatment by Advance Oxidation Processes*. Fisciano, Italy: SEED, 2011.

[86] S. A. Snyder, P. Westerhoff, Y. Yoon, and D. L. Sedlak, "Pharmaceuticals, Personal Care Products, and Endocrine Disruptors in Water: Implications for the Water Industry," *Environ. Eng. Sci.*, vol. 20, no. 5, pp. 449–469, 2003.

[87] R. J. Bull, "Health effects of drinking water disinfectants and disinfectant by-products," *Environ. Sci. Technol.*, vol. 16, no. 10, p. 554A–559A, 1982.

[88] S. Malato, J. Blanco, A. Vidal, P. Fernández, J. Cáceres, P. Trincado, J. . Oliveira, and M. Vincent, "New large solar photocatalytic plant: set-up and preliminary results,"

Chemosphere, vol. 47, no. 3, pp. 235–240, 2002.

[89] J. Blanco, S. Malato, P. Fernández, D. Alarcón, W. Gernjak, and M. I. Maldonado, "Solar energy and feasible applications to water processes," in *5th European Thermal-Sciences Conference,* 2008, pp. 978–90.

[90] A. Hu, X. Zhang, K. D. Oakes, P. Peng, Y. N. Zhou, and M. R. Servos, "Hydrothermal growth of free standing TiO2 nanowire membranes for photocatalytic degradation of pharmaceuticals," *J. Hazard. Mater.*, vol. 189, no. 1, pp. 278–285, 2011.

[91] C. D. Metcalfe, B. G. Koenig, D. T. Bennie, M. Servos, T. A. Ternes, and R. Hirsch, "Occurrence of neutral and acidic drugs in the effluents of Canadian sewage treatment plants," *Environ. Toxicol. Chem.*, vol. 22, no. 12, pp. 2872–2889, 2003.

[92] M. J. Benotti, R. A. Trenholm, B. J. Vanderford, J. C. Holady, B. D. Stanford, and S. A. Snyder, "Pharmaceuticals and Endocrine Disrupting Compounds in U.S. Drinking Water," *Environ. Sci. Technol.*, vol. 43, no. 3, pp. 597–603, 2009.

[93] M. J. Arlos, R. Liang, M. M. Hatat-Fraile, L. M. Bragg, N. Y. Zhou, M. R. Servos, and S. A. Andrews, "Photocatalytic decomposition of selected estrogens and their estrogenic activity by UV-LED irradiated TiO2 immobilized on porous titanium sheets via thermal-chemical oxidation," *J. Hazard. Mater.*, vol. 318, no. July, pp. 541–550, 2016.

[94] F. C. Kent, K. R. Montreuil, R. M. Brookman, R. Sanderson, J. R. Dahn, and G. A. Gagnon, "Photocatalytic oxidation of DBP precursors using UV with suspended and fixed TiO2," *Water Res.*, vol. 45, no. 18, pp. 6173–6180, 2011.

[95] S. Liu, M. Lim, R. Fabris, C. Chow, M. Drikas, and R. Amal, "TiO $_2$ Photocatalysis of Natural Organic Matter in Surface Water: Impact on Trihalomethane and Haloacetic Acid Formation Potential," *Environ. Sci. Technol.*, vol. 42, no. 16, pp. 6218–6223, Aug. 2008.

[96] K. K. Philippe, C. Hans, J. MacAdam, B. Jefferson, J. Hart, and S. A. Parsons, "Photocatalytic oxidation of natural organic matter surrogates and the impact on trihalomethane formation potential," *Chemosphere*, vol. 81, no. 11, pp. 1509–1516, 2010.

[97] H. M. Coleman, E. J. Routledge, J. P. Sumpter, B. R. Eggins, and J. A. Byrne, "Rapid loss of estrogenicity of steroid estrogens by UVA photolysis and photocatalysis over an immobilised titanium dioxide catalyst," *Water Res.*, vol. 38, no. 14, pp. 3233–3240, 2004.

[98] Z. Pan, E. A. Stemmler, H. J. Cho, W. Fan, L. A. LeBlanc, H. H. Patterson, and A. Amirbahman, "Photocatalytic degradation of 17α-ethinylestradiol (EE2) in the presence of TiO2-doped zeolite," *J. Hazard. Mater.*, vol. 279, pp. 17–25, 2014.

[99] K. MITAMURA, H. NARUKAWA, T. MIZUGUCHI, and K. SHIMADA, "Degradation of Estrogen Conjugates Using Titanium Dioxide as a Photocatalyst," *Anal. Sci.*, vol. 20, no. 1, pp. 3–4, 2004.

[100] T. Nakashima, Y. Ohko, Y. Kubota, and A. Fujishima, "Photocatalytic decomposition of estrogens in aquatic environment by reciprocating immersion of TiO2-modified polytetrafluoroethylene mesh sheets," *J. Photochem. Photobiol. A Chem.*, vol. 160, no. 1, pp. 115–120, 2003.

[101] R. Wang, D. Ren, S. Xia, Y. Zhang, and J. Zhao, "Photocatalytic degradation of Bisphenol A (BPA) using immobilized TiO2 and UV illumination in a horizontal circulating bed photocatalytic reactor (HCBPR)," *J. Hazard. Mater.*, vol. 169, no. 1, pp. 926–932, 2009.

[102] V. M. Daskalaki, Z. Frontistis, D. Mantzavinos, and A. Katsaounis, "Solar light-induced degradation of bisphenol-A with TiO2 immobilized on Ti," *Catal. Today*, vol. 161, no. 1,

pp. 110–114, 2011.
[103] K. Li, *Ceramic Membranes for Separation and Reaction*. Chichester, UK: John Wiley & Sons, Ltd, 2007.
[104] H. D. Mansilla, a. Mora, C. Pincheira, M. a. Mondaca, P. D. Marcato, N. Durán, and J. Freer, "New photocatalytic reactor with TiO2 coating on sintered glass cylinders," *Appl. Catal. B Environ.*, vol. 76, no. 1–2, pp. 57–63, Oct. 2007.
[105] P. Pucher, M. Benmami, R. Azouani, G. Krammer, K. Chhor, J.-F. Bocquet, and a. V. Kanaev, "Nano-TiO2 sols immobilized on porous silica as new efficient photocatalyst," *Appl. Catal. A Gen.*, vol. 332, no. 2, pp. 297–303, Nov. 2007.
[106] M. Huang, C. Xu, Z. Wu, Y. Huang, J. Lin, and J. Wu, "Photocatalytic discolorization of methyl orange solution by Pt modified TiO2 loaded on natural zeolite," *Dye. Pigment.*, vol. 77, no. 2, pp. 327–334, 2008.
[107] G. Li Puma, A. Bono, D. Krishnaiah, and J. G. Collin, "Preparation of titanium dioxide photocatalyst loaded onto activated carbon support using chemical vapor deposition: A review paper," *J. Hazard. Mater.*, vol. 157, no. 2, pp. 209–219, 2008.
[108] J.-W. Shi, H.-J. Cui, J.-W. Chen, M.-L. Fu, B. Xu, H.-Y. Luo, and Z.-L. Ye, "TiO2/activated carbon fibers photocatalyst: effects of coating procedures on the microstructure, adhesion property, and photocatalytic ability.," *J. Colloid Interface Sci.*, vol. 388, no. 1, pp. 201–8, Dec. 2012.
[109] L. Liu, Z. Liu, H. Bai, and D. D. Sun, "Concurrent filtration and solar photocatalytic disinfection/degradation using high-performance Ag/TiO2 nanofiber membrane," *Water Res.*, vol. 46, no. 4, pp. 1101–1112, 2012.
[110] X. Zhang, A. J. Du, P. Lee, D. D. Sun, and J. O. Leckie, "TiO2 nanowire membrane for concurrent filtration and photocatalytic oxidation of humic acid in water," *J. Memb. Sci.*, vol. 313, no. 1–2, pp. 44–51, Apr. 2008.
[111] H. H. Uhlig, *Uhlig's Corrosion Handbook, Vol. 51*. Hoboken, NJ, USA: John Wiley & Sons, Inc., 2011.
[112] G. H. Koch, M. P. H. Brongers, N. G. Thompson, Y. P. Virmani, and J. H. Payer, "Chapter 1 – Cost of corrosion in the United States," in *Handbook of Environmental Degradation of Materials*, 2005, pp. 3–24.
[113] J. C. Crittenden, R. R. Trussell, D. W. Hand, K. J. Howe, and G. Tchobanoglous, *MWH's Water Treatment*. Hoboken, NJ, USA: John Wiley & Sons, Inc., 2012.
[114] † Hyunwoong Park, ‡ and Kyoo Young Kim, and † Wonyong Choi*, "Photoelectrochemical Approach for Metal Corrosion Prevention Using a Semiconductor Photoanode," *J. Phys. Chem. B*, vol. 106, no. 18, pp. 4775–4781, 2002.
[115] H. Y. Ha and M. A. Anderson, "Photocatalytic Degradation of Formic Acid via Metal-Supported Titania," *J. Environ. Eng.*, vol. 122, no. 3, pp. 217–221, Mar. 1996.
[116] J. Yuan and S. Tsujikawa, "Characterization of Sol-Gel-Derived TiO[sub 2] Coatings and Their Photoeffects on Copper Substrates," *J. Electrochem. Soc.*, vol. 142, no. 10, pp. 3444–3450, 1995.
[117] Y. Ohko, S. Saitoh, T. Tatsuma, and A. Fujishima, "Photoelectrochemical Anticorrosion and Self-Cleaning Effects of a TiO2 Coating for Type 304 Stainless Steel," *J. Electrochem. Soc.*, vol. 148, no. 1, p. B24, Jan. 2001.
[118] Z.Q. Lin, Y.K. Lai, R.G. Hu, J. Li, R.G. Du, and C.J. Lin, "A highly efficient

ZnS/CdS@TiO2 photoelectrode for photogenerated cathodic protection of metals," *Electrochim. Acta*, vol. 55, no. 28, pp. 8717–8723, 2010.

[119] T. Tatsuma, S. Saitoh, Y. Ohko, and A. Fujishima, "TiO2−WO3 Photoelectrochemical Anticorrosion System with an Energy Storage Ability," *Chem. Mater.*, vol. 13, no. 9, pp. 2838–2842, 2001.

[120] Y. Ohko, S. Saitoh, T. Tatsuma, and A. Fujishima, "Photoelectrochemical Anticorrosion and Self-Cleaning Effects of a TiO[sub 2] Coating for Type 304 Stainless Steel," *J. Electrochem. Soc.*, vol. 148, no. 1, p. B24, 2001.

[121] G. X. Shen, Y. C. Chen, and C. J. Lin, "Corrosion protection of 316 L stainless steel by a TiO2 nanoparticle coating prepared by sol–gel method," *Thin Solid Films*, vol. 489, no. 1, pp. 130–136, 2005.

[122] H. Park, K. Y. Kim, W.Choi, "Photoelectrochemical Approach for Metal Corrosion Prevention Using a Semiconductor Photoanode," 2002.

Chapter 3

[1] J. Tauc, R. Grigorovici, and A. Vancu, "Optical Properties and Electronic Structure of Amorphous Germanium," *Phys. status solidi*, vol. 15, no. 2, pp. 627–637, 1966.

[2] M. J. Arlos, R. Liang, M. M. Hatat-Fraile, L. M. Bragg, N. Y. Zhou, M. R. Servos, and S. A. Andrews, "Photocatalytic decomposition of selected estrogens and their estrogenic activity by UV-LED irradiated TiO2 immobilized on porous titanium sheets via thermal-chemical oxidation," *J. Hazard. Mater.*, vol. 318, no. July, pp. 541–550, 2016.

[3] A. D. Eaton, M. A. H. Franson, American Public Health Association., American Water Works Association., and Water Environment Federation., *Standard methods for the examination of water & wastewater*. American Public Health Association, 2005.

[4] B. J. Vanderford and S. A. Snyder, "Analysis of Pharmaceuticals in Water by Isotope Dilution Liquid Chromatography/Tandem Mass Spectrometry†," *Environ. Sci. Technol.*, vol. 40, no. 23, pp. 7312–7320, 2006.

[5] S. Wang, K. D. Oakes, L. M. Bragg, J. Pawliszyn, G. Dixon, and M. R. Servos, "Validation and use of in vivo solid phase micro-extraction (SPME) for the detection of emerging contaminants in fish," *Chemosphere*, vol. 85, no. 9, pp. 1472–1480, 2011.

[6] C. S. Turchi and D. F. Ollis, "Photocatalytic degradation of organic water contaminants: Mechanisms involving hydroxyl radical attack," *J. Catal.*, vol. 122, no. 1, pp. 178–192, 1990.

Chapter 4

[1] T. L. Thompson and J. T. Yates, "Monitoring Hole Trapping in Photoexcited TiO2(110) Using a Surface Photoreaction," *J. Phys. Chem.*, vol. 109, no. 39, pp. 18230–18236, 2005.

[2] P. J. Boddy, "Oxygen Evolution on Semiconducting TiO[sub 2]," *J. Electrochem. Soc.*, vol. 115, no. 2, pp. 199–203, 1968.

[3] B. O'Regan and M. Grätzel, "A low-cost, high-efficiency solar cell based on dye-sensitized colloidal TiO2 films," *Nature*, vol. 353, no. 6346, pp. 737–740, Oct. 1991.

[4] F. A. Deorsola and D. Vallauri, "Synthesis of TiO2 nanoparticles through the Gel Combustion process," *J. Mater. Sci.*, vol. 43, no. 9, pp. 3274–3278, 2008.

[5] A. H. Sun, P. J. Guo, Z. X. Li, Y.Li, and P. Cui, "Low temperature synthesis of anatase

and rutile titania nanopowders by hydrolysis of TiCl4 using ammonia gas," *J. Alloys Compd.*, vol. 481, no. 1, pp. 605–609, 2009.

[6] E. Figgemeier, W. Kylberg, E. Constable, M. Scarisoreanu, R. Alexandrescu, I. Morjan, I. Soare, R. Birjega, E. Popovici, C. Fleaca, L. Gavrila-Florescu, and G. Prodan, "Titanium dioxide nanoparticles prepared by laser pyrolysis: Synthesis and photocatalytic properties," *Appl. Surf. Sci.*, vol. 254, no. 4, pp. 1037–1041, 2007.

[7] P. E. Meskin, A. I. Gavrilov, V. D. Maksimov, V. K. Ivanov, and B. P. Churagulov, "Hydrothermal/microwave and hydrothermal/ultrasonic synthesis of nanocrystalline titania, zirconia, and hafnia," *Russ. J. Inorg. Chem.*, vol. 52, no. 11, pp. 1648–1656, 2007.

[8] B. Liu and E. S. Aydil, "Growth of Oriented Single-Crystalline Rutile TiO_2 Nanorods on Transparent Conducting Substrates for Dye-Sensitized Solar Cells," *J. Am. Chem. Soc.*, vol. 131, no. 11, pp. 3985–3990, 2009.

[9] Y. X. Zhang, G. H. Li, Y. X. Jin, Y. Zhang, J. Zhang, and L. D. Zhang, "Hydrothermal synthesis and photoluminescence of TiO2 nanowires," *Chem. Phys. Lett.*, vol. 365, no. 3-4, pp. 300-304, 2002.

[10] A. R. Armstrong, G. Armstrong, J. Canales, R. García, and P. G. Bruce, "Lithium-Ion Intercalation into TiO_2 -B Nanowires," *Adv. Mater.*, vol. 17, no. 7, pp. 862–865, 2005.

[11] Z. Miao, D. Xu, J. Ouyang, G. Guo, X. Zhao, and Y. Tang, "Electrochemically Induced Sol−Gel Preparation of Single-Crystalline TiO2 Nanowires," *Nano Lett.*, vol. 2, no. 7, pp. 717–720, 2002.

[12] R. Liang, A. Hu, J. Persic, and Y. Norman Zhou, "Palladium nanoparticles loaded on carbon modified TiO2 nanobelts for enhanced methanol electrooxidation," *Nano-Micro Lett.*, vol. 5, no. 3, 2013.

[13] R. Liang, A. Hu, W. Li, and Y. N. Zhou, "Enhanced degradation of persistent pharmaceuticals found in wastewater treatment effluents using TiO2 nanobelt photocatalysts," *J. Nanoparticle Res.*, vol. 15, no. 10, p. 1990, 2013.

[14] F. Hu, F. Ding, S. Song, and P. K. Shen, "Pd electrocatalyst supported on carbonized TiO2 nanotube for ethanol oxidation," *J. Power Sources*, vol. 163, no. 1, pp. 415-419, 2006.

[15] X. Feng, K. Zhu, A. J. Frank, C. A. Grimes, and T. E. Mallouk, "Rapid Charge Transport in Dye-Sensitized Solar Cells Made from Vertically Aligned Single-Crystal Rutile TiO2 Nanowires," *Angew. Chemie*, vol. 124, no. 11, pp. 2781–2784, 2012.

[16] L. C. Sikuvhihulu, N. J. Coville, T. Ntho, and M. S. Scurrell, "Potassium Titanate: An Alternative Support for Gold Catalyzed Carbon Monoxide Oxidation?," *Catal. Letters*, vol. 123, no. 3, pp. 193–197, 2008.

[17] R. A. Zárate, S. Fuentes, J. P. Wiff, V. M. Fuenzalida, and A. L. Cabrera, "Chemical composition and phase identification of sodium titanate nanostructures grown from titania by hydrothermal processing," *J. Phys. Chem. Solids*, vol. 68, no. 4, pp. 628–637, 2007.

[18] Q. Li, B. Liu, L. Wang, D. Li, R. Liu, B. Zou, T. Cui, G. Zou, Y. Meng, H. Mao, Z. Liu, J. Liu, and J. Li, "Pressure-Induced Amorphization and Polyamorphism in One-Dimensional Single-Crystal TiO_2 Nanomaterials," *J. Phys. Chem. Lett.*, vol. 1, no. 1, pp. 309–314, 2010.

[19] T. Mazza, E. Barborini, P. Piseri, P. Milani, D. Cattaneo, A. Li Bassi, C. E. Bottani, and C. Ducati, "Raman spectroscopy characterization of Ti O 2 rutile nanocrystals," *Phys.*

Rev. B, vol. 75, no. 4, p. 45416, 2007.

[20] W. Li, C. Liu, Y. Zhou, Y. Bai, X. Feng, Z. Yang, L. Lu, X. Lu, and K.-Y. Chan, "Enhanced Photocatalytic Activity in Anatase/TiO $_2$ (B) Core−Shell Nanofiber," *J. Phys. Chem. C*, vol. 112, no. 51, pp. 20539–20545, 2008.

[21] R. Liang, A. Hu, W. Li, and Y. N. Zhou, "Enhanced degradation of persistent pharmaceuticals found in wastewater treatment effluents using TiO2 nanobelt photocatalysts," *J. Nanoparticle Res.*, vol. 15, no. 10, p. 1990, 2013.

[22] A. Di Paola, M. Bellardita, and L. Palmisano, "Brookite, the Least Known TiO2 Photocatalyst," *Catalysts*, vol. 3, no. 1, pp. 36–73, 2013.

[23] Y. Chimupala, P. Junploy, T. Hardcastle, A. Westwood, A. Scott, B. Johnson, and R. Brydson, "Universal synthesis method for mixed phase TiO $_2$ (B)/anatase TiO $_2$ thin films on substrates via a modified low pressure chemical vapour deposition (LPCVD) route," *J. Mater. Chem. A*, vol. 4, no. 15, pp. 5685–5699, 2016.

[24] P. Pichat, Ed., *Photocatalysis and Water Purification*. Weinheim, Germany: Wiley-VCH Verlag GmbH & Co. KGaA, 2013.

[25] R. Liang, M. Hatat-Fraile, M. Arlos, M. Servos, and Y. N. Zhou, "TiO<inf>2</inf> nanowires membranes for the use in photocatalytic filtration processes," in *14th IEEE International Conference on Nanotechnology, IEEE-NANO 2014*, 2014.

[26] J. H. Bang and P. V. Kamat, "Solar Cells by Design: Photoelectrochemistry of TiO2 Nanorod Arrays Decorated with CdSe," *Adv. Funct. Mater.*, vol. 20, no. 12, pp. 1970–1976, 2010.

[27] H. Liu, S. Cheng, M. Wu, H. Wu, J. Zhang, W. Li, and C. Cao, "Photoelectrocatalytic Degradation of Sulfosalicylic Acid and Its Electrochemical Impedance Spectroscopy Investigation," *J. Phys. Chem. A*, vol. 104, no. 30, pp. 7016–7020, 2000.

[28] X. Fu, J. Long, X. Wang, D. Y. C. Leung, Z. Ding, L. Wu, Z. Zhang, Z. Li, and X. Fu, "Photocatalytic reforming of biomass: A systematic study of hydrogen evolution from glucose solution," *Int. J. Hydrogen Energy*, vol. 33, no. 22, pp. 6484–6491, 2008.

[29] G. Balducci, "The adsorption of glucose at the surface of anatase: A computational study," *Chem. Phys. Lett.*, vol. 494, no. 1, pp. 54–59, 2010.

[30] M.-H. Du, J. Feng, and S. B. Zhang, "Photo-Oxidation of Polyhydroxyl Molecules on TiO 2 Surfaces: From Hole Scavenging to Light-Induced Self-Assembly of TiO 2 -Cyclodextrin Wires," *Phys. Rev. Lett.*, vol. 98, no. 6, p. 66102, 2007.

[31] M. C. Li and J. N. Shen, "Photoelectrochemical oxidation behavior of organic substances on TiO2 thin-film electrodes," *J. Solid State Electrochem.*, vol. 10, no. 12, pp. 980–986, 2006.

[32] P. Schmuki, L. E. Erickson, and D. J. Lockwood, "Light Emitting Micropatterns of Porous Si Created at Surface Defects," *Phys. Rev. Lett.*, vol. 80, no. 18, pp. 4060–4063, 1998.

[33] X. F. Cheng, W. H. Leng, D. P. Liu, Y. M. Xu, J. Q. Zhang, and C. N. Cao, "Electrochemical Preparation and Characterization of Surface-Fluorinated TiO $_2$ Nanoporous Film and Its Enhanced Photoelectrochemical and Photocatalytic Properties," *J. Phys. Chem. C*, vol. 112, no. 23, pp. 8725–8734, 2008.

[34] W. H. Leng, Z. Zhang, J. Q. Zhang, and C. N. Cao, "Investigation of the Kinetics of a TiO2 Photoelectrocatalytic Reaction Involving Charge Transfer and Recombination through Surface States by Electrochemical Impedance Spectroscopy," *J. Phys. Chem. B*,

vol. 109, no. 31, pp. 15008–15023, 2005.

[35] R. Amadelli and L. Samiolo, "Photoelectrocatalysis for Water Purification," in *Photocatalysis and Water Purification*, Weinheim, Germany: Wiley-VCH Verlag GmbH & Co. KGaA, 2013, pp. 241–270.

[36] a. Hu, X. Zhang, D. Luong, K. D. Oakes, M. R. Servos, R. Liang, S. Kurdi, P. Peng, and Y. Zhou, "Adsorption and Photocatalytic Degradation Kinetics of Pharmaceuticals by TiO2 Nanowires During Water Treatment," *Waste and Biomass Valorization*, vol. 3, no. 4, pp. 443–449, 2012.

[37] W.-Q. Wu, B.-X. Lei, H.-S. Rao, Y.-F. Xu, Y.-F. Wang, C.-Y. Su, and D.-B. Kuang, "Hydrothermal Fabrication of Hierarchically Anatase TiO2 Nanowire arrays on FTO Glass for Dye-sensitized Solar Cells," *Sci. Rep.*, vol. 3, p. 1352, 2013.

[38] Z. Zheng, H. Liu, J. Ye, J. Zhao, E. R. Waclawik, and H. Zhu, "Structure and contribution to photocatalytic activity of the interfaces in nanofibers with mixed anatase and TiO2(B) phases," *J. Mol. Catal. A Chem.*, vol. 316, no. 1, pp. 75–82, 2010.

[39] D. Yang, H. Liu, Z. Zheng, Y. Yuan, J. Zhao, E. R. Waclawik, X. Ke, and H. Zhu, "An Efficient Photocatalyst Structure: TiO_2 (B) Nanofibers with a Shell of Anatase Nanocrystals," *J. Am. Chem. Soc.*, vol. 131, no. 49, pp. 17885–17893, 2009.

[40] R. R. Giri, H. Ozaki, S. Ota, R. Takanami, and S. Taniguchi, "Degradation of common pharmaceuticals and personal care products in mixed solutions by advanced oxidation techniques," *Int. J. Environ. Sci. Technol.*, vol. 7, no. 2, pp. 251–260, 2010.

[41] I. Kim and H. Tanaka, "Photodegradation characteristics of PPCPs in water with UV treatment.," *Environ. Int.*, vol. 35, no. 5, pp. 793–802, Jul. 2009.

[42] W. Zhou, H. Liu, J. Wang, D. Liu, G. Du, S. Han, J. Lin, and R. Wang, "Interface dominated high photocatalytic properties of electrostatic self-assembled Ag2O/TiO2 heterostructure," *Phys. Chem. Chem. Phys.*, vol. 12, no. 45, pp. 15119–15123, 2010.

[43] W. F. Yao, X. H. Xu, H. Wang, J. T. Zhou, X. N. Yang, Y. Zhang, S. X. Shang, and B. B. Huang, "Photocatalytic property of perovskite bismuth titanate," *Appl. Catal. B Environ.*, vol. 52, no. 2, pp. 109–116, 2004.

[44] J. He, W. Ma, W. Song, J. Zhao, X. Qian, S. Zhang, and J. C. Yu, "Photoreaction of aromatic compounds at α-FeOOH/H2O interface in the presence of H2O2: evidence for organic-goethite surface complex formation," *Water Res.*, vol. 39, no. 1, pp. 119–128, 2005.

[45] S. Al-Qaradawi and S. R. Salman, "Photocatalytic degradation of methyl orange as a model compound," *J. Photochem. Photobiol. A Chem.*, vol. 148, no. 1, pp. 161–168, 2002.

[46] D. Bahnemann, D. Bockelmann, and R. Goslich, "Mechanistic studies of water detoxification in illuminated TiO2 suspensions," *Sol. Energy Mater.*, vol. 24, no. 1, pp. 564–583, 1991.

[47] A. Houas, H. Lachheb, M. Ksibi, E. Elaloui, C. Guillard, and J.-M. Herrmann, "Photocatalytic degradation pathway of methylene blue in water," *Appl. Catal. B Environ.*, vol. 31, no. 2, pp. 145–157, 2001.

[48] J. A. Rengifo-Herrera, L. R. Pizzio, M. N. Blanco, C. Roussel, and C. Pulgarin, "Photocatalytic discoloration of aqueous malachite green solutions by UV-illuminated TiO2 nanoparticles under air and nitrogen atmospheres: effects of counter-ions and pH.," *Photochem. Photobiol. Sci.*, vol. 10, no. 1, pp. 29–34, 2011.

[49] A. Maoz and B. Chefetz, “Sorption of the pharmaceuticals carbamazepine and naproxen to dissolved organic matter: Role of structural fractions,” *Water Res.*, vol. 44, no. 3, pp. 981–989, 2010.
[50] X. Zhang, D. D. Sun, G. Li, and Y. Wang, “Investigation of the roles of active oxygen species in photodegradation of azo dye AO7 in TiO2 photocatalysis illuminated by microwave electrodeless lamp,” *J. Photochem. Photobiol. A Chem.*, vol. 199, no. 2, pp. 311–315, 2008.
[51] C. Arrouvel, M. Digne, M. Breysse, H. Toulhoat, and P. Raybaud, “Effects of morphology on surface hydroxyl concentration: a DFT comparison of anatase–TiO2 and γ-alumina catalytic supports,” *J. Catal.*, vol. 222, no. 1, pp. 152–166, 2004.
[52] C. H. Cho, M. H. Han, D. H. Kim, and D. K. Kim, “Morphology evolution of anatase TiO2 nanocrystals under a hydrothermal condition (pH=9.5) and their ultra-high photo-catalytic activity,” *Mater. Chem. Phys.*, vol. 92, no. 1, pp. 104–111, 2005.
[53] K. Ishibashi, A. Fujishima, T. Watanabe, and K. Hashimoto, “Quantum yields of active oxidative species formed on TiO2 photocatalyst,” *J. Photochem. Photobiol. A Chem.*, vol. 134, no. 1, pp. 139–142, 2000.
[54] D. Lapenna, S. D.e gioia, A. Mezzetti, G. Ciofani, D. Festi, and F. Cuccurullo, “Aminophylline: could it act as an antioxidant in vivo?,” *Eur. J. Clin. Invest.*, vol. 25, no. 7, pp. 464–470, 1995.
[55] Q. Sun and L. Yang, “The adsorption of basic dyes from aqueous solution on modified peat–resin particle,” *Water Res.*, vol. 37, no. 7, pp. 1535–1544, 2003.
[56] L. Lin, Y. Chai, B. Zhao, W. Wei, D. He, B. He, and Q. Tang, “Photocatalytic oxidation for degradation of VOCs,” *Open J. Inorg. Chem.*, vol. 3, no. 1, pp. 14–25, 2013.
[57] N. Barka, S. Qourzal, A. Assabbane, A. Nounah, and Y. Ait-Ichou, “Factors influencing the photocatalytic degradation of Rhodamine B by TiO2-coated non-woven paper,” *J. Photochem. Photobiol. A Chem.*, vol. 195, no. 2, pp. 346–351, 2008.
[58] I. Bouzaida, C. Ferronato, J. M. Chovelon, M. E. Rammah, and J. M. Herrmann, “Heterogeneous photocatalytic degradation of the anthraquinonic dye, Acid Blue 25 (AB25): a kinetic approach,” *J. Photochem. Photobiol. A Chem.*, vol. 168, no. 1, pp. 23–30, 2004.

Chapter 5

[1] A. Fujishima, T. N. Rao, and D. A. Tryk, “Titanium dioxide photocatalysis,” *J. Photochem. Photobiol. C Photochem. Rev.*, vol. 1, no. 1, pp. 1–21, 2000.
[2] H. Dong, G. Zeng, L. Tang, C. Fan, C. Zhang, X. He, and Y. He, “An overview on limitations of TiO2-based particles for photocatalytic degradation of organic pollutants and the corresponding countermeasures,” *Water Res.*, vol. 79, pp. 128–146, 2015.
[3] F. B. Li and X. Z. Li, “The enhancement of photodegradation efficiency using Pt–TiO2 catalyst,” *Chemosphere*, vol. 48, no. 10, pp. 1103–1111, 2002.
[4] X. Z. Li and F. B. Li, “Study of Au/Au3+-TiO2 Photocatalysts toward Visible Photooxidation for Water and Wastewater Treatment,” 2001.
[5] R. Asahi, T. Morikawa, T. Ohwaki, K. Aoki, and Y. Taga, “Visible-Light Photocatalysis in Nitrogen-Doped Titanium Oxides,” *Science (80-.).*, vol. 293, no. 5528, 2001.
[6] A. Zaleska, J. W. Sobczak, E. Grabowska, and J. Hupka, “Preparation and photocatalytic

activity of boron-modified TiO2 under UV and visible light," *Appl. Catal. B Environ.*, vol. 78, no. 1–2, pp. 92–100, 2008.

[7] N. Shi, X. Li, T. Fan, H. Zhou, J. Ding, D. Zhang, and H. Zhu, "Biogenic N-I-codoped TiO 2 photocatalyst derived from kelp for efficient dye degradation," *Energy Environ. Sci.*, vol. 4, no. 1, pp. 172–180, 2011.

[8] W. Ho, J. C. Yu, and S. Lee, "Low-temperature hydrothermal synthesis of S-doped TiO2 with visible light photocatalytic activity," *J. Solid State Chem.*, vol. 179, no. 4, pp. 1171–1176, 2006.

[9] W. Wang, J. Zhang, F. Chen, D. He, and M. Anpo, "Preparation and photocatalytic properties of Fe3+-doped Ag@TiO2 core-shell nanoparticles.," *J. Colloid Interface Sci.*, vol. 323, no. 1, pp. 182–6, 2008.

[10] W. Zhou, G. Du, P. Hu, G. Li, D. Wang, H. Liu, J. Wang, R. I. Boughton, D. Liu, and H. Jiang, "Nanoheterostructures on TiO2 nanobelts achieved by acid hydrothermal method with enhanced photocatalytic and gas sensitive performance," *J. Mater. Chem.*, vol. 21, no. 22, p. 7937, 2011.

[11] T. Hirakawa and P. V Kamat, "Charge separation and catalytic activity of Ag@TiO2 core-shell composite clusters under UV-irradiation.," *J. Am. Chem. Soc.*, vol. 127, no. 11, pp. 3928–34, 2005.

[12] K. Awazu, M. Fujimaki, C. Rockstuhl, J. Tominaga, H. Murakami, Y. Ohki, N. Yoshida, and T. Watanabe, "A plasmonic photocatalyst consisting of silver nanoparticles embedded in titanium dioxide.," *J. Am. Chem. Soc.*, vol. 130, no. 5, pp. 1676–80, 2008.

[13] J.-C. Xu, M. Lu, X.-Y. Guo, and H.-L. Li, "Zinc ions surface-doped titanium dioxide nanotubes and its photocatalysis activity for degradation of methyl orange in water," *J. Mol. Catal. A Chem.*, vol. 226, no. 1, pp. 123–127, 2005.

[14] Z. Jiang, F. Yang, N. Luo, B. T. T. Chu, D. Sun, H. Shi, T. Xiao, and P. P. Edwards, "Solvothermal synthesis of N-doped TiO2 nanotubes for visible-light-responsive photocatalysis," *Chem. Commun.*, vol. 0, no. 47, p. 6372, 2008.

[15] Z. Xiong and X. S. Zhao, "Nitrogen-doped titanate-anatase core-shell nanobelts with exposed {101} anatase facets and enhanced visible light photocatalytic activity.," *J. Am. Chem. Soc.*, vol. 134, no. 13, pp. 5754–7, 2012.

[16] G. Ma, X. Zhao, and J. Zhu, "Microwave hydrothermal synthesis of rutile TiO_2 nanorods," *Int. J. Mod. Phys. B*, vol. 19, no. 15n17, pp. 2763–2768, 2005.

[17] J.-M. Herrmann, "Photocatalysis fundamentals revisited to avoid several misconceptions," *Appl. Catal. B Environ.*, vol. 99, no. 3, pp. 461–468, 2010.

[18] C. Höfl, G. Sigl, O. Specht, I. Wurdack, and D. Wabner, "Oxidative degradation of aox and cod by different advanced oxidation processes: A comparative study with two samples of a pharmaceutical wastewater," *Water Sci. Technol.*, vol. 35, no. 4, pp. 257–264, 1997.

[19] C. Martínez, M. Canle L., M. I. Fernández, J. A. Santaballa, and J. Faria, "Aqueous degradation of diclofenac by heterogeneous photocatalysis using nanostructured materials," *Appl. Catal. B Environ.*, vol. 107, no. 1, pp. 110–118, 2011.

[20] D. H. Quiñones, A. Rey, P. M. Álvarez, F. J. Beltrán, and G. Li Puma, "Boron doped TiO2 catalysts for photocatalytic ozonation of aqueous mixtures of common pesticides: Diuron, o-phenylphenol, MCPA and terbuthylazine," *Appl. Catal. B Environ.*, 2014.

[21] W. H. Glaze, J. Kang, and H. Douglas, "Ozone : Science & Engineering : The Journal of

the International Ozone Association The Chemistry of Water Treatment Processes Involving Ozone , Hydrogen Peroxide and Ultraviolet Radiation," no. February 2013, pp. 335–352, 2008.

[22] S. Irmak, O. Erbatur, and A. Akgerman, "Degradation of 17β-estradiol and bisphenol A in aqueous medium by using ozone and ozone/UV techniques," *J. Hazard. Mater.*, vol. 126, no. 1, pp. 54–62, 2005.

[23] M. R. Hoffmann, S. T. Martin, W. Choi, D. W. Bahnemannt, and W. M. Keck, "Environmental Applications of Semiconductor Photocatalysis," *Chem. Rev*, vol. 95, pp. 69–96, 1995.

[24] J. M. Herrmann, "Photocatalysis fundamentals revisited to avoid several misconceptions," *Appl. Catal. B Environ.*, vol. 99, no. 3–4, pp. 461–468, 2010.

[25] I. Kim and H. Tanaka, "Photodegradation characteristics of PPCPs in water with UV treatment.," *Environ. Int.*, vol. 35, no. 5, pp. 793–802, 2009.

[26] K. Tanaka, K. Abe, and T. Hisanaga, "Photocatalytic water treatment on immobilized TiO2 combined with ozonation," *J. Photochem. Photobiol. A Chem.*, vol. 101, no. 1, pp. 85–87, 1996.

[27] K. Song, M. Mohseni, and F. Taghipour, "Application of ultraviolet light-emitting diodes (UV-LEDs) for water disinfection: A review," *Water Res.*, vol. 94, pp. 341–349, 2016.

[28] P. Xiong and J. Hu, "Decomposition of acetaminophen (Ace) using TiO2/UVA/LED system," *Catal. Today*, vol. 282, pp. 48–56, 2017.

[29] S. Malato, J. Blanco, A. Vidal, P. Fernández, J. Cáceres, P. Trincado, J. . Oliveira, and M. Vincent, "New large solar photocatalytic plant: set-up and preliminary results," *Chemosphere*, vol. 47, no. 3, pp. 235–240, 2002.

[30] S. Malato, P. Fernández-Ibáñez, M. I. Maldonado, J. Blanco, and W. Gernjak, "Decontamination and disinfection of water by solar photocatalysis: Recent overview and trends," *Catal. Today*, vol. 147, no. 1, pp. 1–59, 2009.

[31] V. Augugliaro, V. Loddo, M. Pagliaro, G. Palmisano, L. Palmisano, and L. Palmisano, *Clean by Light Irradiation*. Cambridge: Royal Society of Chemistry, 2010.

[32] K. J. Buechler, C. H. Nam, and T. M. Zawistowski, "Design and Evaluation of a Novel-Controlled Periodic Illumination Reactor To Study Photocatalysis," *Ind. Eng. Chem. Res.*, vol. 38, no. 4, pp. 1258–1263, 1999.

[33] E. Kowalska, R. Abe, B. Ohtani, R. Asashi, …, and K. P. Vijayamohanan, "Visible light-induced photocatalytic reaction of gold-modified titanium(iv) oxide particles: action spectrum analysis," *Chem. Commun.*, vol. 293, no. 2, pp. 241–243, 2009.

[34] S. Kim, S.-J. Hwang, and W. Choi, "Visible Light Active Platinum-Ion-Doped TiO2 Photocatalyst," *J. Phys. Chem. B*, 109 (51), pp 24260–24267, 2005.

[35] R. Liang, A. Hu, J. Persic, and Y. Norman Zhou, "Palladium nanoparticles loaded on carbon modified TiO2 nanobelts for enhanced methanol electrooxidation," *Nano-Micro Lett.*, vol. 5, no. 3, 2013.

[36] M. S. Lee, S.-S. Hong, and M. Mohseni, "Synthesis of photocatalytic nanosized TiO2–Ag particles with sol–gel method using reduction agent," *J. Mol. Catal. A Chem.*, vol. 242, no. 1, pp. 135–140, 2005.

[37] F. Zhang, Z. Cheng, L. Cui, T. Duan, A. Anan, C. Zhang, and L. Kang, "Controllable synthesis of Ag@TiO $_2$ heterostructures with enhanced photocatalytic activities under UV

and visible excitation," *RSC Adv.*, vol. 6, no. 3, pp. 1844–1850, 2016.

[38] X. Zhang, Y. L. Chen, R.-S. Liu, and D. P. Tsai, "Plasmonic photocatalysis.," *Rep. Prog. Phys.*, vol. 76, no. 4, p. 46401, 2013.

[39] R. B. Thurman, C. P. Gerba, and G. Bitton, "The molecular mechanisms of copper and silver ion disinfection of bacteria and viruses," *Crit. Rev. Environ. Control*, vol. 18, no. 4, pp. 295–315, 1989.

[40] H. Eom, J.-Y. Jung, Y. Shin, S. Kim, …, and A. Fujishima, "Strong localized surface plasmon resonance effects of Ag/TiO $_2$ core–shell nanowire arrays in UV and visible light for photocatalytic activity," *Nanoscale*, vol. 6, no. 1, pp. 226–234, 2014.

[41] R. Liang, A. Hu, W. Li, and Y. N. Zhou, "Enhanced degradation of persistent pharmaceuticals found in wastewater treatment effluents using TiO2 nanobelt photocatalysts," *J. Nanoparticle Res.*, vol. 15, no. 10, p. 1990, 2013.

[42] S. W. Bennett, D. Zhou, R. Mielke, A. A. Keller, …, and U. Vierl, "Photoinduced Disaggregation of TiO2 Nanoparticles Enables Transdermal Penetration," *PLoS One*, vol. 7, no. 11, p. e48719, 2012.

[43] C. S. Turchi and D. F. Ollis, "Photocatalytic degradation of organic water contaminants: Mechanisms involving hydroxyl radical attack," *J. Catal.*, vol. 122, no. 1, pp. 178–192, 1990.

[44] M. J. Arlos, R. Liang, M. M. Hatat-Fraile, L. M. Bragg, N. Y. Zhou, M. R. Servos, and S. A. Andrews, "Photocatalytic decomposition of selected estrogens and their estrogenic activity by UV-LED irradiated TiO2 immobilized on porous titanium sheets via thermal-chemical oxidation," *J. Hazard. Mater.*, vol. 318, no. July, pp. 541–550, 2016.

[45] U. Černigoj, M. Kete, and U. L. Štangar, "Development of a fluorescence-based method for evaluation of self-cleaning properties of photocatalytic layers," *Catal. Today*, vol. 151, no. 1, pp. 46–52, 2010.

[46] R. Liang, A. Hu, W. Li, and Y. N. Zhou, "Enhanced degradation of persistent pharmaceuticals found in wastewater treatment effluents using TiO2 nanobelt photocatalysts," *J. Nanoparticle Res.*, vol. 15, no. 10, p. 1990, Sep. 2013.

[47] A. Hu, R. Liang, X. Zhang, S. Kurdi, D. Luong, H. Huang, P. Peng, E. Marzbanrad, K. D. Oakes, Y. Zhou, and M. R. Servos, "Enhanced photocatalytic degradation of dyes by TiO2 nanobelts with hierarchical structures," *J. Photochem. Photobiol. A Chem.*, vol. 256, pp. 7–15, 2013.

[48] W.-Q. Wu, H.-S. Rao, Y.-F. Xu, Y.-F. Wang, …, and T. Peng, "Hierarchical Oriented Anatase TiO2 Nanostructure arrays on Flexible Substrate for Efficient Dye-sensitized Solar Cells," *Sci. Rep.*, vol. 3, pp. 737–740, May 2013.

[49] Z. Zheng, H. Liu, J. Ye, J. Zhao, E. R. Waclawik, and H. Zhu, "Structure and contribution to photocatalytic activity of the interfaces in nanofibers with mixed anatase and TiO2(B) phases," *J. Mol. Catal. A Chem.*, vol. 316, no. 1, pp. 75–82, 2010.

[50] A. Zaban, M. Greenshtein, and J. Bisquert, "Determination of the Electron Lifetime in Nanocrystalline Dye Solar Cells by Open-Circuit Voltage Decay Measurements," *ChemPhysChem*, vol. 4, no. 8, pp. 859–864, 2003.

[51] J. H. Bang and P. V. Kamat, "Solar Cells by Design: Photoelectrochemistry of TiO2 Nanorod Arrays Decorated with CdSe," *Adv. Funct. Mater.*, vol. 20, no. 12, pp. 1970–1976, 2010.

[52] J. Bisquert, A. Zaban, M. Greenshtein, and I. Mora-Seró, "Determination of Rate Constants for Charge Transfer and the Distribution of Semiconductor and Electrolyte Electronic Energy Levels in Dye-Sensitized Solar Cells by Open-Circuit Photovoltage Decay Method," *J. Am. Chem. Soc.*, vol. 126, no. 41, pp 13550–13559, 2004.

[53] S. U. and and D. F. Ollis, "Simple Photocatalysis Model for Photoefficiency Enhancement via Controlled, Periodic Illumination," *J. Phys. Chem. B*, vol. 101, no. 14, pp 2625–2631, 1997.

[54] O. Tokode, R. Prabhu, L. A. Lawton, and P. K. J. Robertson, "Controlled periodic illumination in semiconductor photocatalysis," *J. Photochem. Photobiol. A Chem.*, vol. 319–320, pp. 96–106, 2016.

[55] S. Litch, A. J. Bard, and M. Stratmann, *Encyclopedia of Electrochemistry, Vol. 6*. Weinheim, Germany, 2002.

[56] D. B. Ingram and S. Linic, "Water Splitting on Composite Plasmonic-Metal/Semiconductor Photoelectrodes: Evidence for Selective Plasmon-Induced Formation of Charge Carriers near the Semiconductor Surface," *J. Am. Chem. Soc.*, vol. 133, no. 14, pp. 5202–5205, 2011.

[57] I. Lee, J. Y. Park, K. Hong, J. H. Son, …, and J.-M. Nunzi, "The effect of localized surface plasmon resonance on the emission color change in organic light emitting diodes," *Nanoscale*, vol. 8, no. 12, pp. 6463–6467, 2016.

[58] R. Sellappan, M. G. Nielsen, F. González-Posada, P. C. K. Vesborg, I. Chorkendorff, and D. Chakarov, "Effects of plasmon excitation on photocatalytic activity of Ag/TiO2 and Au/TiO2 nanocomposites," *J. Catal.*, vol. 307, pp. 214–221, 2013.

[59] C. J. G. Cornu, A. J. Colussi, and M. R. Hoffmann, "Quantum Yields of the Photocatalytic Oxidation of Formate in Aqueous TiO2 Suspensions under Continuous and Periodic Illumination," *J. Phys. Chem. B*, vol. 105, no. 7, pp 1351–1354, 2001.

[60] C. Y. Wang, R. Pagel, J. K. Dohrmann, and D. W. Bahnemann, "Antenna mechanism and deaggregation concept: novel mechanistic principles for photocatalysis," *Comptes Rendus Chim.*, vol. 9, no. 5–6, pp. 761–773, 2006.

[61] J. G. Sczechowski, C. A. Koval, and R. D. Noble, "A Taylor vortex reactor for heterogeneous photocatalysis," *Chem. Eng. Sci.*, vol. 50, no. 20, pp. 3163–3173, 1995.

[62] C.-Y. Wang, R. Pagel, D. W. Bahnemann, and J. K. Dohrmann, "Quantum yield of formaldehyde formation in the presence of colloidal TiO 2-based photocatalysts: Effect of intermittent illumination, platinization, and deoxygenation," *J. Phys. Chem. B*, vol. 108, no. 37, pp. 14082–14092, 2004.

[63] C.-Y. Wang, R. Pagel, D. W. Bahnemann, and J. K. Dohrmann, "Quantum Yield of Formaldehyde Formation in the Presence of Colloidal TiO2-Based Photocatalysts: Effect of Intermittent Illumination, Platinization, and Deoxygenation," *J. Phys. Chem. B*, vol. 108, no. 37, pp 14082–14092, 2004.

[64] D. Zhou, S. W. Bennett, A. A. Keller, M. Wiesner,…, and A. Keller, "Increased Mobility of Metal Oxide Nanoparticles Due to Photo and Thermal Induced Disagglomeration," *PLoS One*, vol. 7, no. 5, p. e37363, 2012.

[65] E. M. Hotze, T. Phenrat, and G. V Lowry, "Nanoparticle aggregation: challenges to understanding transport and reactivity in the environment.," *J. Environ. Qual.*, vol. 39, no. 6, pp. 1909–24, 2010.

[66] M. A. Behnajady, B. Vahid, N. Modirshahla, and M. Shokri, “Evaluation of electrical energy per order (E EO) with kinetic modeling on the removal of Malachite Green by US / UV / H 2 O 2 process,” *Des*, vol. 249, no. 1, pp. 99–103, 2009.

[67] Y. Ku, S. J. Shiu, and H. C. Wu, “Decomposition of dimethyl phthalate in aqueous solution by UV–LED/TiO2 process under periodic illumination,” *J. Photochem. Photobiol. A Chem.*, vol. 332, pp. 299–305, 2017.

Chapter 6

[1] M. Klavarioti, D. Mantzavinos, and D. Kassinos, “Removal of residual pharmaceuticals from aqueous systems by advanced oxidation processes.,” *Environ. Int.*, vol. 35, no. 2, pp. 402–17, 2009.

[2] J. M. Poyatos, M. M. Muñio, M. C. Almecija, J. C. Torres, E. Hontoria, and F. Osorio, “Advanced Oxidation Processes for Wastewater Treatment: State of the Art,” *Water. Air. Soil Pollut.*, vol. 205, no. 1–4, pp. 187–204, 2010.

[3] R. L. Fernández, J. A. McDonald, S. J. Khan, and P. Le-Clech, “Removal of pharmaceuticals and endocrine disrupting chemicals by a submerged membrane photocatalysis reactor (MPR),” *Sep. Purif. Technol.*, vol. 127, pp. 131–139, 2014.

[4] R. Rosal, A. Rodríguez, J. A. Perdigón-Melón, A. Petre, E. García-Calvo, M. J. Gómez, A. Agüera, and A. R. Fernández-Alba, “Occurrence of emerging pollutants in urban wastewater and their removal through biological treatment followed by ozonation.,” *Water Res.*, vol. 44, no. 2, pp. 578–88, 2010.

[5] S. Esplugas, D. M. Bila, L. G. T. Krause, and M. Dezotti, “Ozonation and advanced oxidation technologies to remove endocrine disrupting chemicals (EDCs) and pharmaceuticals and personal care products (PPCPs) in water effluents,” *J. Hazard. Mater.*, vol. 149, no. 3, pp. 631–642, 2007.

[6] L. Rizzo, S. Meric, M. Guida, D. Kassinos, and V. Belgiorno, “Heterogenous photocatalytic degradation kinetics and detoxification of an urban wastewater treatment plant effluent contaminated with pharmaceuticals.,” *Water Res.*, vol. 43, no. 16, pp. 4070–8, 2009.

[7] R. Liang, A. Hu, W. Li, and Y. N. Zhou, “Enhanced degradation of persistent pharmaceuticals found in wastewater treatment effluents using TiO2 nanobelt photocatalysts,” *J. Nanoparticle Res.*, vol. 15, no. 10, p. 1990, Sep. 2013.

[8] C. Martínez, M. Canle L., M. I. Fernández, J. A. Santaballa, and J. Faria, “Aqueous degradation of diclofenac by heterogeneous photocatalysis using nanostructured materials,” *Appl. Catal. B Environ.*, vol. 107, no. 1, pp. 110–118, 2011.

[9] M. J. Arlos, M. M. Hatat-Fraile, R. Liang, L. M. Bragg, N. Y. Zhou, S. A. Andrews, and M. R. Servos, “Photocatalytic decomposition of organic micropollutants using immobilized TiO2 having different isoelectric points,” *Water Res.*, vol. 101, pp. 351–361, 2016.

[10] M. J. Arlos, R. Liang, M. M. Hatat-Fraile, L. M. Bragg, N. Y. Zhou, M. R. Servos, and S. A. Andrews, “Photocatalytic decomposition of selected estrogens and their estrogenic activity by UV-LED irradiated TiO2 immobilized on porous titanium sheets via thermal-chemical oxidation,” *J. Hazard. Mater.*, vol. 318, no. July, pp. 541–550, 2016.

[11] O. Tokode, R. Prabhu, L. A. Lawton, and P. K. J. Robertson, "Controlled periodic illumination in semiconductor photocatalysis," *J. Photochem. Photobiol. A Chem.*, vol. 319–320, pp. 96–106, 2016.

[12] J. M. Herrmann, "Photocatalysis fundamentals revisited to avoid several misconceptions," *Appl. Catal. B Environ.*, vol. 99, no. 3–4, pp. 461–468, 2010.

[13] W. Ho, J. C. Yu, and S. Lee, "Low-temperature hydrothermal synthesis of S-doped TiO2 with visible light photocatalytic activity," *J. Solid State Chem.*, vol. 179, no. 4, pp. 1171–1176, 2006.

[14] R. Azouani, A. Michau, K. Hassouni, K. Chhor, J.-F. Bocquet, J.-L. Vignes, and A. Kanaev, "Elaboration of pure and doped TiO2 nanoparticles in sol–gel reactor with turbulent micromixing: Application to nanocoatings and photocatalysis," *Chem. Eng. Res. Des.*, vol. 88, no. 9, pp. 1123–1130, 2010.

[15] Z. Xiong and X. S. Zhao, "Nitrogen-doped titanate-anatase core-shell nanobelts with exposed {101} anatase facets and enhanced visible light photocatalytic activity.," *J. Am. Chem. Soc.*, vol. 134, no. 13, pp. 5754–7, 2012.

[16] M. Pelaez, N. T. Nolan, S. C. Pillai, M. K. Seery, P. Falaras, A. G. Kontos, P. S. M. Dunlop, J. W. J. Hamilton, J. A. Byrne, K. O'Shea, M. H. Entezari, and D. D. Dionysiou, "A review on the visible light active titanium dioxide photocatalysts for environmental applications," *Appl. Catal. B Environ.*, vol. 125, pp. 331–349, 2012.

[17] R. Asahi, T. Morikawa, T. Ohwaki, K. Aoki, and Y. Taga, "Visible-Light Photocatalysis in Nitrogen-Doped Titanium Oxides," *Science (80-.).*, vol. 293, no. 5528, 2001.

[18] M. N. Chong, B. Jin, C. W. K. Chow, and C. Saint, "Recent developments in photocatalytic water treatment technology: a review.," *Water Res.*, vol. 44, no. 10, pp. 2997–3027, 2010.

[19] S. Malato, P. Fernández-Ibáñez, M. I. Maldonado, J. Blanco, and W. Gernjak, "Decontamination and disinfection of water by solar photocatalysis: Recent overview and trends," *Catal. Today*, vol. 147, no. 1, pp. 1–59, 2009.

[20] J. G. Sczechowski, C. A. Koval, and R. D. Noble, "Evidence of critical illumination and dark recovery times for increasing the photoefficiency of aqueous heterogeneous photocatalysis," *J. Photochem. Photobiol. A Chem.*, vol. 74, no. 2, pp. 273–278, 1993.

[21] K. J. Buechler, C. H. Nam, and T. M. Zawistowski, "Design and Evaluation of a Novel-Controlled Periodic Illumination Reactor To Study Photocatalysis," *Ind. Eng. Chem. Res.*, vol. 38, no. 4, pp. 1258–1263, 1999.

[22] S. Vilhunen, H. Särkkä, and M. Sillanpää, "Ultraviolet light-emitting diodes in water disinfection," *Environ. Sci. Pollut. Res.*, vol. 16, no. 4, pp. 439–442, 2009.

[23] K. Song, M. Mohseni, and F. Taghipour, "Application of ultraviolet light-emitting diodes (UV-LEDs) for water disinfection: A review," *Water Res.*, vol. 94, pp. 341–349, 2016.

[24] M. A. Würtele, T. Kolbe, M. Lipsz, A. Külberg, M. Weyers, M. Kneissl, and M. Jekel, "Application of GaN-based ultraviolet-C light emitting diodes – UV LEDs – for water disinfection," *Water Res.*, vol. 45, no. 3, pp. 1481–1489, 2011.

[25] D. C. Osipovitch, C. Barratt, P. M. Schwartz, R. F. Ludlow, …, and U. J. Quaade, "Systems chemistry and Parrondo's paradox: computational models of thermal cycling," *New J. Chem.*, vol. 33, no. 10, p. 2022, 2009.

[26] H. Tada, F. Suzuki, S. Ito, T. Akita, K Tanaka, T. Kawahara, and H. Kobayashi, "Au-

Core/Pt-Shell Bimetallic Cluster-Loaded TiO2. 1. Adsorption of Organosulfur Compound," *J. Phys. Chem. B*, vol. 106, no. 34, pp 8714–8720, 2002.

[27] P. Xiong and J. Hu, "Decomposition of acetaminophen (Ace) using TiO2/UVA/LED system," *Catal. Today*, vol. 282, pp. 48–56, 2017.

[28] E. Korovin, D. Selishchev, A. Besov, and D. Kozlov, "UV-LED TiO2 photocatalytic oxidation of acetone vapor: Effect of high frequency controlled periodic illumination," *Appl. Catal. B Environ.*, vol. 163, pp. 143–149, 2015.

[29] Y. Ku, S. J. Shiu, and H. C. Wu, "Decomposition of dimethyl phthalate in aqueous solution by UV–LED/TiO2 process under periodic illumination," *J. Photochem. Photobiol. A Chem.*, vol. 332, pp. 299–305, 2017.

[30] H. W. Chen, Y. Ku, and A. Irawan, "Photodecomposition of o-cresol by UV-LED/TiO2 process with controlled periodic illumination," *Chemosphere*, vol. 69, no. 2, pp. 184–190, 2007.

[31] K. Noguera-Oviedo and D. S. Aga, "Lessons learned from more than two decades of research on emerging contaminants in the environment," *J. Hazard. Mater.*, vol. 316, pp. 242–251, 2016.

[32] P. A. Bahamonde, M. L. Fuzzen, C. J. Bennett, G. R. Tetreault, M. E. McMaster, M. R. Servos, C. J. Martyniuk, and K. R. Munkittrick, "Whole organism responses and intersex severity in rainbow darter (Etheostoma caeruleum) following exposures to municipal wastewater in the Grand River basin, ON, Canada. Part A," *Aquat. Toxicol.*, vol. 159, pp. 290–301, 2015.

[33] J. Lu, J. Wu, P. J. Stoffella, and P. C. Wilson, "Uptake and distribution of bisphenol A and nonylphenol in vegetable crops irrigated with reclaimed water," *J. Hazard. Mater.*, vol. 283, pp. 865–870, 2015.

[34] V. S. Thomaidi, A. S. Stasinakis, V. L. Borova, and N. S. Thomaidis, "Is there a risk for the aquatic environment due to the existence of emerging organic contaminants in treated domestic wastewater? Greece as a case-study," *J. Hazard. Mater.*, vol. 283, pp. 740–747, 2015.

[35] A. Tong, "TiO2-assisted photodegradation of pharmaceuticals — a review," *Cent. Eur. J. Chem.*, vol. 10, no. 4, 2012.

[36] S. Kleywegt, V. Pileggi, P. Yang, C. Hao, X. Zhao, C. Rocks, S. Thach, P. Cheung, and B. Whitehead, "Pharmaceuticals, hormones and bisphenol A in untreated source and finished drinking water in Ontario, Canada — Occurrence and treatment efficiency," *Sci. Total Environ.*, vol. 409, no. 8, pp. 1481–1488, 2011.

[37] D. R. Helsel and R. M. Hirsch, "Statistical Methods in Water Resources."

[38] J. C. Crittenden, R. R. Trussell, D. W. Hand, K. J. Howe, and G. Tchobanoglous, "Adsorption," in *MWH's Water Treatment*, Hoboken, NJ, USA: John Wiley & Sons, Inc., 2012, pp. 1117–1262.

[39] C. S. Turchi and D. F. Ollis, "Photocatalytic degradation of organic water contaminants: Mechanisms involving hydroxyl radical attack," *J. Catal.*, vol. 122, no. 1, pp. 178–192, 1990.

[40] R. Memming, "Photoinduced charge transfer processes at semiconductor electrodes and particles," *Top. Curr. Chem.*, vol. 169, pp. 105–181, 1994.

[41] J. G. Sczechowski, C. A. Koval, and R. D. Noble, "A Taylor vortex reactor for

heterogeneous photocatalysis," *Chem. Eng. Sci.*, vol. 50, no. 20, pp. 3163–3173, 1995.
[42] M. A. Behnajady, B. Vahid, N. Modirshahla, and M. Shokri, "Evaluation of electrical energy per order (E EO) with kinetic modeling on the removal of Malachite Green by US / UV / H2O2 process," *Des*, vol. 249, no. 1, pp. 99–103, 2009.

Chapter 7

[1] C. A. K. Gouvêa, F. Wypych, S. G. Moraes, N. Durán, N. Nagata, and P. Peralta-Zamora, "Semiconductor-assisted photocatalytic degradation of reactive dyes in aqueous solution," *Chemosphere*, vol. 40, no. 4, pp. 433–440, 2000.
[2] P. Cooper, "Removing colour from dyehouse waste waters—a critical review of technology available," *J. Soc. Dye. Colour.*, 1993.
[3] A. L. Ahmad, M. R. Othman, and H. Mukhtar, "H2 separation from binary gas mixture using coated alumina – titania membrane by sol – gel technique at high-temperature region," *Int. J. Hydrogen Energy*, vol. 29, pp. 817–828, 2004.
[4] I. Voigt, G. Fischer, P. Puhlfu, M. Schleifenheimer, and M. Stahn, "TiO 2 -NF-membranes on capillary supports," *Sep. Purif. Technol.*, vol. 32, pp. 87–91, 2003.
[5] R. J. Davis, J. L. Gainer, G. O. Neal, I. Wu, and J. Davis, "decolorization Photocatalytic of wastewater dyes," *Water Environ. …*, vol. 66, pp. 50–53, 2011.
[6] M. Oturan, N. Oturan, and M. Edelahi, "Oxidative degradation of herbicide diuron in aqueous medium by Fenton's reaction based advanced oxidation processes," *Chem. Eng.J.*, vol. 171, no. 1, pp. 127-135, 2011.
[7] M. Hussain, R. Ceccarelli, D. L. Marchisio, D. Fino, N. Russo, and F. Geobaldo, "Synthesis, characterization, and photocatalytic application of novel TiO2 nanoparticles," *Chem. Eng. J.*, vol. 157, pp. 45–51, 2010.
[8] A. Mills and S. Le Hunte, "An overview of semiconductor photocatalysis," *J. Photochem. Photobiol. A Chem.*, vol. 108, pp. 1–35, 1997.
[9] M. A. Henderson, "A surface science perspective on photocatalysis," *Surf. Sci. Rep.*, vol. 66, pp. 185–297, 2011.
[10] M. Faisal, M. Abu, A. Khan, K. Umar, and M. Muneer, "Photochemical reactions of 2,4-dichloroaniline and 4-nitroanisole in aqueous suspension of titanium dioxide," *Sci. Adv. Mater.*, vol. 3, p. 269–275 ST–Photochemical reactions of 2,4–dichl, 2011.
[11] R. Liang, A. Hu, W. Li, and Y. N. Zhou, "Enhanced degradation of persistent pharmaceuticals found in wastewater treatment effluents using TiO2 nanobelt photocatalysts," *J. Nanoparticle Res.*, vol. 15, no. 10, p. 1990, 2013.
[12] K. Tennakone, C. T. K. Tilakaratne, and I. R. M. Kottegoda, "Photocatalytic degradation of organic contaminants in water with TiO2 supported on polythene films," *J. Photochem. Photobiol. A Chem.*, vol. 87, pp. 177–179, 1995.
[13] M. G. Antoniou, P. a. Nicolaou, J. A.. Shoemaker, A. A.. de la Cruz, and D. D. Dionysiou, "Impact of the morphological properties of thin TiO2 photocatalytic films on the detoxification of water contaminated with the cyanotoxin, microcystin-LR," *Appl. Catal. B Environ.*, vol. 91, pp. 165–173, 2009.
[14] H. Choi, E. Stathatos, and D. D. Dionysiou, "Photocatalytic TiO2 films and membranes for the development of efficient wastewater treatment and reuse systems," *Desalination*,

vol. 202, no. 1–3, pp. 199–206, 2007.

[15] R. Azouani, A. Michau, K. Hassouni, K. Chhor, J.-F. Bocquet, J.-L. Vignes, and A. Kanaev, "Elaboration of pure and doped TiO2 nanoparticles in sol–gel reactor with turbulent micromixing: Application to nanocoatings and photocatalysis," *Chem. Eng. Res. Des.*, vol. 88, no. 9, pp. 1123–1130, 2010.

[16] P. Pucher, M. Benmami, R. Azouani, G. Krammer, K. Chhor, J.-F. Bocquet, and a. V. Kanaev, "Nano-TiO2 sols immobilized on porous silica as new efficient photocatalyst," *Appl. Catal. A Gen.*, vol. 332, no. 2, pp. 297–303, 2007.

[17] R. Molinari, A. Caruso, and T. Poerio, "Direct benzene conversion to phenol in a hybrid photocatalytic membrane reactor," *Catal. Today*, vol. 144, no. 1–2, pp. 81–86, 2009.

[18] H. Zhang, X. Quan, S. Chen, H. Zhao, and Y. Zhao, "Fabrication of photocatalytic membrane and evaluation its efficiency in removal of organic pollutants from water," *Sep. Purif. Technol.*, vol. 50, no. 2, pp. 147–155, 2006.

[19] M. Benmami, K. Chhor, and A. V. Kanaev, "High photocatalytic activity of monolayer nanocoatings prepared from non-crystalline titanium oxide sol nanoparticles," *Chem. Phys. Lett.*, vol. 422, no. 4–6, pp. 552–557, 2006.

[20] A. Fernández, G. Lassaletta, V. M. Jiménez, A. Justo, A. R. González-Elipe, J.-M. Herrmann, H. Tahiri, and Y. Ait-Ichou, "Preparation and characterization of TiO2 photocatalysts supported on various rigid supports (glass, quartz and stainless steel). Comparative studies of photocatalytic activity in water purification," *Appl. Catal. B Environ.*, vol. 7, no. 1–2, pp. 49–63, 1995.

[21] N. Takeda, N. Iwata, T. Torimoto, and H. Yoneyama, "Influence of carbon black as an adsorbent used in TiO2 photocatalyst films on photodegradation behaviors of propyzamide," *J. Catal.*, vol. 177, no. 2, pp. 240–246, 1998.

[22] R. Molinari, M. Mungari, E. Drioli, A. Di Paola, V. Loddo, L. Palmisano, and M. Schiavello, "Study on a photocatalytic membrane reactor for water purification," *Catal. Today*, vol. 55, no. 1–2, pp. 71–78, 2000.

[23] N. Ma, X. Quan, Y. Zhang, S. Chen, and H. Zhao, "Integration of separation and photocatalysis using an inorganic membrane modified with Si-doped TiO2 for water purification," *J. Memb. Sci.*, vol. 335, no. 1–2, pp. 58–67, 2009.

[24] M. Hatat-Fraile, J. Mendret, M. Rivallin, and S. Brosillon, "Effect of hydrodynamics during sol–gel synthesis of TiO2 nanoparticles: From morphology to photocatalytic properties," *Chem. Eng. Res. Des.*, vol. 91, no. 12, pp. 2389–2400, 2013.

[25] S. Adjimi, N. Sergent, J.-C. Roux, F. Delpech, M. Pera-Titus, K. Chhor, A. Kanaev, and P.-X. Thivel, "Photocatalytic paper based on sol–gel titania nanoparticles immobilized on porous silica for VOC abatement," *Appl. Catal. B Environ.*, vol. 154–155, pp. 123–133, 2014.

[26] M. M. H. Fraile, "Etude des méthodes d'élaboration et de la mise en oeuvre de photocatalyseurs pour le traitement de la micro pollution bio-réfractaire dans l'eau," Montpellier 2, 2013.

[27] C. J. Brinker and G. W. Scherer, *Sol-Gel Science: The Physics and Chemistry of Sol-Gel Processing*. Elsevier Science, 2013.

[28] M. Rivallin, M. Benmami, A. Kanaev, and A. Gaunand, "Sol–Gel Reactor With Rapid Micromixing," *Chem. Eng. Res. Des.*, vol. 83, no. 1, pp. 67–74, 2005.

[29] A. Fujishima, X. Zhang, and D. Tryk, “TiO2 photocatalysis and related surface phenomena,” *Surf. Sci. Rep.*, vol. 63, no. 12, pp. 515–582, 2008.

[30] M. Pelaez, P. Falaras, V. Likodimos, A. G. Kontos, A. A. de la Cruz, K. O’shea, and D. D. Dionysiou, “Synthesis, structural characterization and evaluation of sol–gel-based NF-TiO2 films with visible light-photoactivation for the removal of microcystin-LR,” *Appl. Catal. B Environ.*, vol. 99, no. 3–4, pp. 378–387, 2010.

[31] M. Pelaez, N. T. Nolan, S. C. Pillai, M. K. Seery, P. Falaras, A. G. Kontos, P. S. M. Dunlop, J. W. J. Hamilton, J. A. Byrne, K. O’Shea, M. H. Entezari, and D. D. Dionysiou, “A review on the visible light active titanium dioxide photocatalysts for environmental applications,” *Appl. Catal. B Environ.*, vol. 125, pp. 331–349, 2012.

[32] H. Irie, Y. Watanabe, and K. Hashimoto, “Nitrogen-Concentration Dependence on Photocatalytic Activity of TiO 2 - x N x Powders,” *J. Phys. Chem. B*, vol. 107, no. 23, pp. 5483–5486, 2003.

[33] Y. Park, W. Kim, H. Park, T. Tachikawa, T. Majima, and W. Choi, “Carbon-doped TiO2 photocatalyst synthesized without using an external carbon precursor and the visible light activity,” *Appl. Catal. B Environ.*, vol. 91, no. 1–2, pp. 355–361, 2009.

[34] N. Sakai, R. Wang, A. Fujishima, T. Watanabe, and K. Hashimoto, “Effect of Ultrasonic Treatment on Highly Hydrophilic TiO 2 Surfaces,” *Langmuir*, vol. 14, no. 20, pp. 5918–5920, 1998.

[35] W. Choi, A. Termin, and M. R. Hoffmann, “The Role of Metal Ion Dopants in Quantum-Sized TiO2: Correlation between Photoreactivity and Charge Carrier Recombination Dynamics,” *J. Phys. Chem.*, vol. 98, no. 51, pp. 13669–13679, 1994.

[36] X. Chen and S. S. Mao, “Titanium dioxide nanomaterials: synthesis, properties, modifications, and applications.,” *Chem. Rev.*, vol. 107, no. 7, pp. 2891–959, 2007.

[37] J.-C. Xu, M. Lu, X.-Y. Guo, and H.-L. Li, “Zinc ions surface-doped titanium dioxide nanotubes and its photocatalysis activity for degradation of methyl orange in water,” *J. Mol. Catal. A Chem.*, vol. 226, no. 1, pp. 123–127, 2005.

[38] R. Janes, “Structural and spectroscopic studies of iron (III) doped titania powders prepared by sol-gel synthesis and hydrothermal processing,” *Dye. Pigment.*, vol. 62, no. 3, pp. 199–212, 2004.

[39] F. Peng, L. Cai, H. Yu, H. Wang, and J. Yang, “Synthesis and characterization of substitutional and interstitial nitrogen-doped titanium dioxides with visible light photocatalytic activity,” *J. Solid State Chem.*, vol. 181, no. 1, pp. 130–136, 2008.

[40] N. Lu, H. Zhao, J. Li, X. Quan, and S. Chen, “Characterization of boron-doped TiO2 nanotube arrays prepared by electrochemical method and its visible light activity,” *Sep. Purif. Technol.*, vol. 62, no. 3, pp. 668–673, 2008.

[41] W. Ho, J. C. Yu, and S. Lee, “Low-temperature hydrothermal synthesis of S-doped TiO2 with visible light photocatalytic activity,” *J. Solid State Chem.*, vol. 179, no. 4, pp. 1171–1176, 2006.

[42] Y. Ao, J. Xu, D. Fu, and C. Yuan, “A simple method to prepare N-doped titania hollow spheres with high photocatalytic activity under visible light.,” *J. Hazard. Mater.*, vol. 167, no. 1–3, pp. 413–7, 2009.

[43] F. Peng, L. Cai, L. Huang, H. Yu, and H. Wang, “Preparation of nitrogen-doped titanium dioxide with visible-light photocatalytic activity using a facile hydrothermal method,” *J.*

Phys. Chem. Solids, vol. 69, no. 7, pp. 1657–1664, 2008.

[44] P. Silija, Z. Yaakob, M. A. Yarmo, S. Sugunan, and N. N. Binitha, "Visible light active anion codoped sol gel titania photocatalyst for pollutant degradation," *J. Sol-Gel Sci. Technol.*, vol. 59, no. 2, pp. 252–259, 2011.

[45] J. Yu, M. Zhou, B. Cheng, and X. Zhao, "Preparation, characterization and photocatalytic activity of in situ N,S-codoped TiO2 powders," *J. Mol. Catal. A Chem.*, vol. 246, no. 1–2, pp. 176–184, 2006.

[46] T. C. Jagadale, S. P. Takale, R. S. Sonawane, H. M. Joshi, S. I. Patil, B. B. Kale, and S. B. Ogale, "N-Doped TiO 2 Nanoparticle Based Visible Light Photocatalyst by Modified Peroxide Sol−Gel Method," *J. Phys. Chem. C*, vol. 112, no. 37, pp. 14595–14602, 2008.

[47] M. Hatat-Fraile, J. Mendret, M. Rivallin, and S. Brosillon, "Photocatalytic Membranes for the Treatment of Refractory Organic Pollutants," *Procedia Eng.*, vol. 44, pp. 440–442, 2012.

[48] A. N. Kadam, R. S. Dhabbe, M. R. Kokate, Y. B. Gaikwad, and K. M. Garadkar, "Preparation of N doped TiO2 via microwave-assisted method and its photocatalytic activity for degradation of Malathion," *Spectrochim. Acta Part A Mol. Biomol. Spectrosc.*, vol. 133, pp. 669–676, 2014.

[49] J. Tauc, R. Grigorovici, and A. Vancu, "Optical Properties and Electronic Structure of Amorphous Germanium," *Phys. status solidi*, vol. 15, no. 2, pp. 627–637, 1966.

[50] H. Lin, C. Huang, W. Li, C. Ni, S. Shah, and Y. Tseng,"Size dependency of nanocrystalline TiO2 on its optical property and photocatalytic reactivity exemplified by 2-chlorophenol," *Appl. Catal. B Environ.*, vol. 68, no. 1–2, pp. 1–11, 2006.

[51] A. Galenda, L. Crociani, N. El Habra, M. Favaro, M. M. Natile, and G. Rossetto, "Effect of reaction conditions on methyl red degradation mediated by boron and nitrogen doped TiO2," *Appl. Surf. Sci.*, vol. 314, pp. 919–930, 2014.

[52] Y. Cong, J. Zhang, F. Chen, and M. Anpo, "Synthesis and Characterization of Nitrogen-Doped TiO2 Nanophotocatalyst with High Visible Light Activity," *J. Phys. Chem. C*, vol. 111, no. 19, pp. 6976–6982, 2007.

[53] R. R. Bhosale, S. R. Pujari, G. G. Muley, S. H. Patil, K. R. Patil, M. F. Shaikh, and A. B. Gambhire, "Solar photocatalytic degradation of methylene blue using doped TiO2 nanoparticles," *Sol. Energy*, vol. 103, pp. 473–479, 2014.

[54] L. Li, Y. Yang, X. Liu, R. Fan, Y. Shi, S. Li, L. Zhang, X. Fan, P. Tang, R. Xu, W. Zhang, Y. Wang, and L. Ma, "A direct synthesis of B-doped TiO2 and its photocatalytic performance on degradation of RhB," *Appl. Surf. Sci.*, vol. 265, pp. 36–40, 2013.

[55] D. H. Quiñones, A. Rey, P. M. Álvarez, F. J. Beltrán, and G. Li Puma, "Boron doped TiO2 catalysts for photocatalytic ozonation of aqueous mixtures of common pesticides: Diuron, o-phenylphenol, MCPA and terbuthylazine," *Appl. Catal. B Environ.*, 2014.

[56] Y. Huang, W. Ho, Z. Ai, X. Song, L. Zhang, and S. Lee, "Aerosol-assisted flow synthesis of B-doped, Ni-doped and B–Ni-codoped TiO2 solid and hollow microspheres for photocatalytic removal of NO," *Appl. Catal. B Environ.*, vol. 89, no. 3–4, pp. 398–405, 2009.

[57] Z. Xiong and X. S. Zhao, "Nitrogen-doped titanate-anatase core-shell nanobelts with exposed {101} anatase facets and enhanced visible light photocatalytic activity.," *J. Am. Chem. Soc.*, vol. 134, no. 13, pp. 5754–7, 2012.

[58] R. P. Cavalcante, R. F. Dantas, B. Bayarri, O. González, J. Giménez, S. Esplugas, and A. Machulek, "Synthesis and characterization of B-doped TiO2 and their performance for the degradation of metoprolol," *Catal. Today*, vol. 252, pp. 27–34, 2015.

[59] "Introduction to Membrane Science and Technology." [Online]. Available: http://www.wiley-vch.de/publish/en/AreaOfInterestCG00/availableTitles/3-527-32451-8/?sID=b72uu95nh8skhcmra24ef1cde1. [Accessed: 22-Feb-2016].

[60] N. Stevens, C. I. Priest, and R. Sedev, and J. Ralston, "Wettability of Photoresponsive Titanium Dioxide Surfaces," 2003.

[61] M. Miyauchi, A. Nakajima, A. Fujishima, and K. Hashimoto, and T. Watanabe, "Photoinduced Surface Reactions on TiO2 and SrTiO3 Films: Photocatalytic Oxidation and Photoinduced Hydrophilicity," *Chem. Mater.*, 12 (1), pp 3–5, 1999.

[62] R. Wang, K. Hashimoto, A. Fujishima, M. Chikuni, E. Kojima, A. Kitamura, M. Shimohigoshi, and T. Watanabe, "Light-induced amphiphilic surfaces," vol. 388, no. 6641, pp. 431–432, 1997.

[63] R. Wang, K. Hashimoto, A. Fujishima, M. Chikuni, E. Kojima, A. Kitamura, M. Shimohigoshi, and T. Watanabe, "Photogeneration of Highly Amphiphilic TiO2 Surfaces," *Adv. Mater.*, vol. 10, no. 2, pp. 135–138, 1998.

[64] V. Gekas and B. Hallström, "Microfiltration membranes, cross-flow transport mechanisms and fouling studies," *Desalination*, vol. 77, pp. 195–218, 1990.

[65] P. Ramesh Babu and V. G. Gaikar, "Membrane characteristics as determinant in fouling of UF membranes," *Sep. Purif. Technol.*, vol. 24, no. 1–2, pp. 23–34, 2001.

[66] H. Y. Lee, Y. H. Park, and K. H. Ko, "Correlation between Surface Morphology and Hydrophilic/Hydrophobic Conversion of MOCVD−TiO 2 Films," *Langmuir*, vol. 16, no. 18, pp. 7289–7293, 2000.

[67] N. P. Xekoukoulotakis, D. Mantzavinos, R. Dillert, and D. Bahnemann, "Synthesis and photocatalytic activity of boron-doped TiO(2) in aqueous suspensions under UV-A irradiation.," *Water Sci. Technol.*, vol. 61, no. 10, pp. 2501–6, 2010.

[68] A. Zaleska, J. W. Sobczak, E. Grabowska, and J. Hupka, "Preparation and photocatalytic activity of boron-modified TiO2 under UV and visible light," *Appl. Catal. B Environ.*, vol. 78, no. 1–2, pp. 92–100, 2008.

Chapter 8

[1] M. Kraljić, Z. Mandić, and L. Duić, "Inhibition of steel corrosion by polyaniline coatings," *Corros. Sci.*, vol. 45, no. 1, pp. 181–198, 2003.

[2] G. X. Shen, Y. C. Chen, L. Lin, C. J. Lin, and D. Scantlebury, "Study on a hydrophobic nano-TiO2 coating and its properties for corrosion protection of metals," *Electrochim. Acta*, vol. 50, no. 25, pp. 5083–5089, 2005.

[3] J. Gallardo, P. Galliano, and A. Durán, "Bioactive and Protective Sol-Gel Coatings on Metals for Orthopaedic Prostheses," *J. Sol-Gel Sci. Technol.*, vol. 21, no. 1/2, pp. 65–74, 2001.

[4] A. Yağan, N. Özçiçek Pekmez, and A. Yıldız, "Poly(N-ethylaniline) coatings on 304 stainless steel for corrosion protection in aqueous HCl and NaCl solutions," *Electrochim. Acta*, vol. 53, no. 5, pp. 2474–2482, 2008.

[5] D. A. Jones, *Principles and prevention of corrosion*. Prentice Hall, 1996.

[6] J. Yuan and S. Tsujikawa, “Characterization of Sol-Gel-Derived TiO[sub 2] Coatings and Their Photoeffects on Copper Substrates,” *J. Electrochem. Soc.*, vol. 142, no. 10, p. 3444, 1995.

[7] Y. Ohko, S. Saitoh, T. Tatsuma, and A. Fujishima, “Photoelectrochemical Anticorrosion and Self-Cleaning Effects of a TiO[sub 2] Coating for Type 304 Stainless Steel,” *J. Electrochem. Soc.*, vol. 148, no. 1, p. B24, 2001.

[8] T. Tatsuma, S. Saitoh, Y. Ohko, and A. Fujishima, “TiO2−WO3 Photoelectrochemical Anticorrosion System with an Energy Storage Ability,” *Chem. Mater.*, vol. 13, no. 9, pp. 2838–2842, 2001.

[9] T. Hirakawa and P. V. Kamat, “Charge Separation and Catalytic Activity of Ag@TiO2 Core−Shell Composite Clusters under UV−Irradiation,” *J. Am. Chem. Soc.*, vol. 127, no. 11, pp. 3928–3934, 2005.

[10] J. Yu, L. Qi, and M. Jaroniec, “Hydrogen Production by Photocatalytic Water Splitting over Pt/TiO $_2$ Nanosheets with Exposed (001) Facets,” *J. Phys. Chem. C*, vol. 114, no. 30, pp. 13118–13125, 2010.

[11] H. Li, Z. Bian, J. Zhu, Y. Huo, H. Li, and Y. Lu, “Mesoporous Au/TiO2 Nanocomposites with Enhanced Photocatalytic Activity,” *J. Am. Chem. Soc.*, vol. 129, no. 15, pp. 4538–4539, 2007.

[12] R. Liang, A. Hu, J. Persic, and Y. Norman Zhou, “Palladium Nanoparticles Loaded on Carbon Modified TiO2 Nanobelts for Enhanced Methanol Electrooxidation,” *Nano-Micro Lett.*, vol. 5, no. 3, pp. 202–212, 2013.

[13] M. A. Butkus, M. P. Labare, J. A. Starke, K. Moon, and M. Talbot, “Use of aqueous silver enhance inactivation of coliphage MS-2 by UV disinfection.,” *Appl. Environ. Microbiol.*, vol. 70, no. 5, pp. 2848–53, 2004.

[14] K. Awazu, M. Fujimaki, C. Rockstuhl, J. Tominaga, H. Murakami, Y. Ohki, N. Yoshida, and T. Watanabe, “A Plasmonic Photocatalyst Consisting of Silver Nanoparticles Embedded in Titanium Dioxide,” *J. Am. Chem. Soc.*, vol. 130, no. 5, pp. 1676–1680, 2008.

[15] M. K. Kumar, S. Krishnamoorthy, L. K. Tan, S. Y. Chiam, S. Tripathy, and H. Gao, “Field Effects in Plasmonic Photocatalyst by Precise SiO $_2$ Thickness Control Using Atomic Layer Deposition,” *ACS Catal.*, vol. 1, no. 4, pp. 300–308, 2011.

[16] R. Liang, M. Hatat-Fraile, H. He, M. Arlos, M. R. Servos, and Y. N. Zhou, “TiO2 membranes for concurrent photocatalytic organic degradation and corrosion protection,” in *SPIE Nanoscience + Engineering*, p. 95450M, 2015..

[17] A. Neville and T. Hodgkiess, “An assessment of the corrosion behaviour of high-grade alloys in seawater at elevated temperature and under a high velocity impinging flow,” *Corros. Sci.*, vol. 38, no. 6, pp. 927–956, 1996.

[18] G. Salvago and G. Fumagalli, “Application of Breakdown Potential Distribution in Corrosion Comparisons of Stainless Steels,” *Corrosion*, vol. 52, no. 10, pp. 760–767, 1996.

[19] M. Pelaez, N. T. Nolan, S. C. Pillai, M. K. Seery, P. Falaras, A. G. Kontos, P. S. M. Dunlop, J. W. J. Hamilton, J. A. Byrne, K. O’Shea, M. H. Entezari, and D. D. Dionysiou, “A review on the visible light active titanium dioxide photocatalysts for environmental applications,” *Appl. Catal. B Environ.*, vol. 125, pp. 331–349, 2012.

[20] D. Behar and J. Rabani, "Kinetics of Hydrogen Production upon Reduction of Aqueous TiO2 Nanoparticles Catalyzed by Pd0, Pt0, or Au0 Coatings and an Unusual Hydrogen Abstraction; Steady State and Pulse Radiolysis Study," *J. Phys. Chem. B*, vol. 110, no. 17, pp. 8750–8755, 2006.

[21] W. Wang, J. Zhang, F. Chen, D. He, and M. Anpo, "Preparation and photocatalytic properties of Fe3+-doped Ag@TiO2 core–shell nanoparticles," *J. Colloid Interface Sci.*, vol. 323, no. 1, pp. 182–186, 2008.

[22] M.-H. Du, J. Feng, and S. B. Zhang, "Photo-Oxidation of Polyhydroxyl Molecules on TiO 2 Surfaces: From Hole Scavenging to Light-Induced Self-Assembly of TiO 2 -Cyclodextrin Wires," *Phys. Rev. Lett.*, vol. 98, no. 6, p. 66102, 2007.

[23] G. Balducci, "The adsorption of glucose at the surface of anatase: A computational study," *Chem. Phys. Lett.*, vol. 494, no. 1, pp. 54–59, 2010.

[24] X. Fu, J. Long, X. Wang, D. Y. C. Leung, Z. Ding, L. Wu, Z. Zhang, Z. Li, and X. Fu, "Photocatalytic reforming of biomass: A systematic study of hydrogen evolution from glucose solution," *Int. J. Hydrogen Energy*, vol. 33, no. 22, pp. 6484–6491, 2008.

[25] H. Park, and K. Y.Kim, and W. Choi, "Photoelectrochemical Approach for Metal Corrosion Prevention Using a Semiconductor Photoanode," *J. Phys. Chem. B*, 106 (18), pp 4775–4781, 2002.

[26] H. K. Jun, M. A. Careem, and A. K. Arof, "A Suitable Polysulfide Electrolyte for CdSe Quantum Dot-Sensitized Solar Cells," *Int. J. Photoenergy*, vol. 2013, pp. 1–10, 2013.

[27] T. G. Gooch, "Corrosion Behavior of Welded Stainless Steel," *Weld. Res.*, 1996.

[28] S. Bakour, A. Guenbour, A. Bellaouchou, C. Escrivà-Cerdán, R. Sánchez-Tovar, R. Leiva-García, and J. García-Antón, "Effect of Welding on The Corrosion Behaviour of a Highly Alloyed Austenitic Stainless Steel UNS N06027 in Polluted Phosphoric Acid Media," *Int. J. Electrochem. Sci*, vol. 7, pp. 10530–10543, 2012.

Chapter 9

[1] D. M. Orihel, D. F. Bird, M. Brylinsky, H. Chen,…, and R. E. H. Smith, "High microcystin concentrations occur only at low nitrogen-to-phosphorus ratios in nutrient-rich Canadian lakes," *Can. J. Fish. Aquat. Sci.*, vol. 69, no. 9, pp. 1457–1462, 2012.

[2] T. Leshuk, T. Wong, S. Linley, K. M. Peru, J. V Headley, and F. Gu, "Solar photocatalytic degradation of naphthenic acids in oil sands process-affected water.," *Chemosphere*, vol. 144, pp. 1854–61, 2016.

[3] S. Mozia, "Photocatalytic membrane reactors (PMRs) in water and wastewater treatment. A review," *Sep. Purif. Technol.*, vol. 73, no. 2, pp. 71–91, 2010.

[4] R. Liang, A. Hu, M. Hatat-Fraile, and N. Zhou, "Fundamentals on adsorption, membrane filtration, and advanced oxidation processes for water treatment," in *Nanotechnology for Water treatment and Purification*, Springer, pp. 1-45, 2014.

[5] K. Vinodgopal, Idriss Bedja, and Prashant V. Kamat, "Nanostructured Semiconductor Films for Photocatalysis. Photoelectrochemical Behavior of SnO2/TiO2 Composite Systems and Its Role in Photocatalytic Degradation of a Textile Azo Dye," 1996.

Appendix A

[1] R. Liang, A. Hu, W. Li, and Y. N. Zhou, "Enhanced degradation of persistent

pharmaceuticals found in wastewater treatment effluents using TiO2 nanobelt photocatalysts," *J. Nanoparticle Res.*, vol. 15, no. 10, p. 1990, 2013.

Appendix B

[1] S. W. Bennett, D. Zhou, R. Mielke, A. A. Keller, …, and U. Vierl, "Photoinduced Disaggregation of TiO2 Nanoparticles Enables Transdermal Penetration," *PLoS One*, vol. 7, no. 11, p. e48719, 2012.

[2] D. Zhou, Z. Ji, X. Jiang, D. R. Dunphy, J. Brinker, and A. A. Keller, "Influence of Material Properties on TiO2 Nanoparticle Agglomeration," *PLoS One*, vol. 8, no. 11, p. e81239, 2013.

Appendix E

[1] X. Zhang, Y. Zhu, X. Yang, S. Wang, J. Shen, B. Lin, and C. Li, "Enhanced visible light photocatalytic activity of interlayer-isolated triplex Ag@SiO2@TiO2 core–shell nanoparticles," *Nanoscale*, vol. 5, no. 8, p. 3359, 2013.

[2] L. Lękawska-Andrinopoulou, E. G. Vasiliou, D. G. Georgakopoulos, C. P. Yialouris, and C. A. Georgiou, "Rapid enzymatic method for pectin methyl esters determination.," *J. Anal. Methods Chem.*, vol. 2013, p. 854763, 2013.

[3] A. D. Eaton and M. A. H. Franson, *Standard Methods for the Examination of Water & Wastewater*. American Public Health Association, 2005.

Appendix A: Supplementary Information for Chapter 4

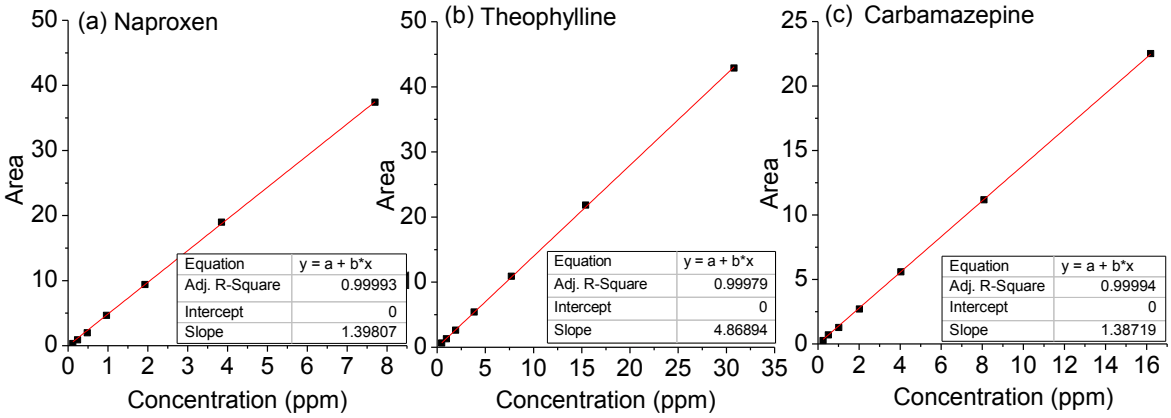

Figure A1: Calibration curves of a) naproxen, b) theophylline, and c) theophylline. Reproduced with permission from [1]

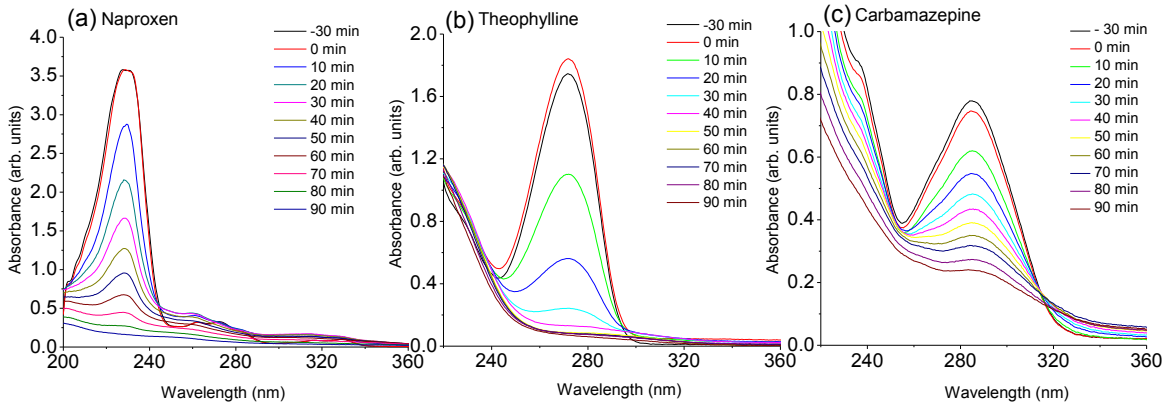

Figure A2: UV-Visible spectra of three pharmaceuticals (15 ppm) – naproxen, theophylline, and carbamazepine – undergoing photocatalytic degradation. Reproduced with permission from [1]

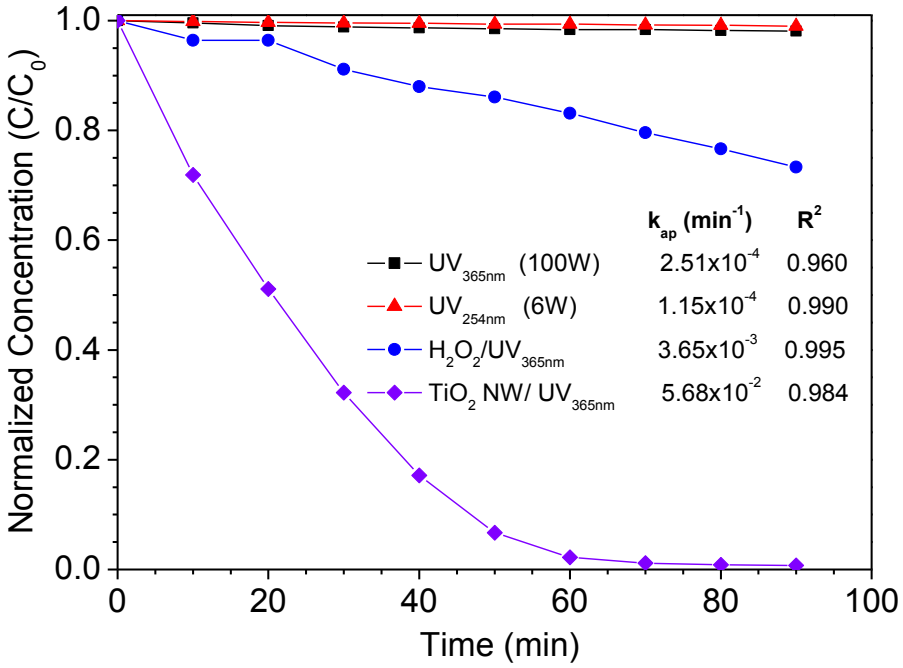

Figure A3: Theophylline (15 ppm) under four degradation processes: UV_{365nm} at 100W, UV_{254nm} at 6W, 10 mM H_2O_2/UV_{365nm}, and 0.2 g L^{-1} TiO_2/ UV_{365nm}. Reproduced with permission from [1]

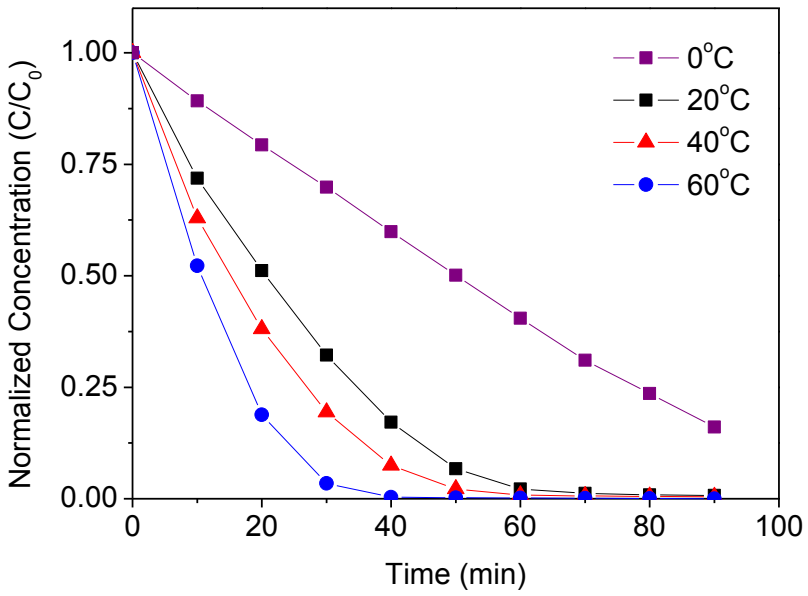

Figure A4: Normalized Concentration of theophylline over time at temperatures of 4 °C, 20 °C, 40 °C, and 60 °C. Reproduced with permission from [1]

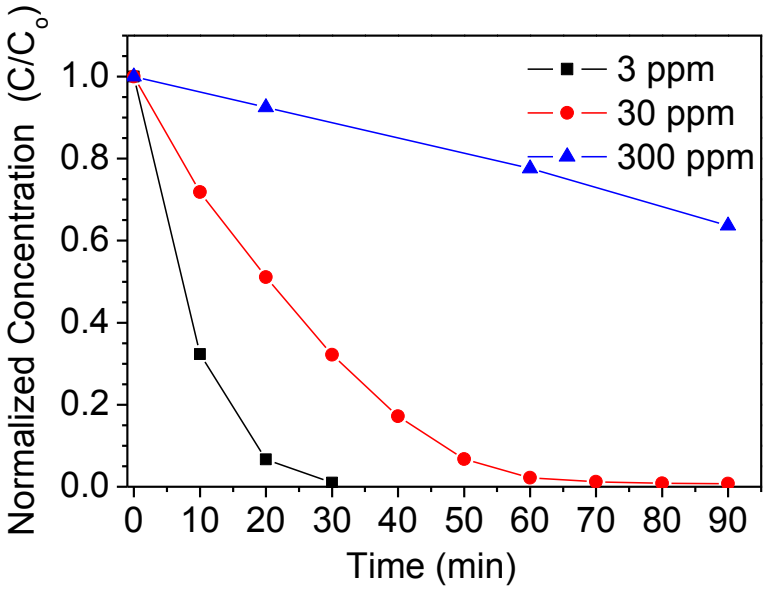

Figure A5: Photocatalytic degradation of theophylline at concentrations of 3 ppm, 30 ppm, and 300 ppm. Reproduced with permission from [1]

Appendix B: Supplementary Information for Chapter 5

B1: Pulse-width modulation script

Pulsed width modulation (PWM) was used to control the UV-LED. Digital control is used to create a square wave, a signal switched between on and off states. This on-off pattern can simulate voltages in between full on (5 volts) and off (0 volts) by changing the portion of the time the signal spends on versus the time it spends off. The duration of the "on time" is called the pulse width. An Arduino Uno connected to a LED Current Driver (LEDSEEDUINO) and a high power UV-LED (LED Engin, 1 A, λ = 365 nm) was used. Each time the *digitalWrite* function is used, it needs to be followed with a delay function. The desired duty cycle and pulse frequency was acquired by changing the time on and time off. Based on this, a PWM program was coded into the Arduino microcontroller using the following script:

```
int ledPin = 9;              // LED connected to digital pin 9
int  timeON = x              // initializes x value of time that LED  is ON
int timeOFF = y              // initializes y value of time that LED is OFF

void setup()
{
  pinMode(ledPin, OUTPUT);      // sets the digital pin as output
}

void loop()
{
  digitalWrite(ledPin, HIGH);   // sets the LED on
  delay(timeON);                // waits for x milliseconds
  digitalWrite(ledPin, LOW);    // sets the LED off
  delay(timeOFF);               // waits for y milliseconds
}.
```

B2: TiO_2 Electrodeposition Method

P25/FTO and TNB/FTO glass photoanodes were used as working electrodes and fabricated via electrodeposition. All chemicals required for electrodeposition was acquired from Sigma-Aldrich. TiO_2 nanomaterials (0.5 g) were dispersed in a solution containing 250 mL of ethanol, 15 mL acetylacetone, 4 mL acetone, and 2 mL H_2O. Iodine (27 mg) was added to increase dispensability. For TNB/FTO samples, polydimethyl ammonium chloride (0.1 mL) was

added to increase adhesion on the FTO electrode. The solution was sonicated for 30 min and stirred for an hour prior to deposition. The deposition process was conducted using a two electrode setup in which a titanium sheet (2.54 cm x 7.62 cm) was used as the anode and FTO glass (2.54 cm x 7.62 cm) was used as the cathode. The cathode and anode were placed upright and separated by 1 cm and connected with a DC voltage power supply using alligator clips with the conductive side of the FTO glass facing the titanium plate. Electrochemical tape (2.54 cm x 2.54 cm) was taped in the middle to prevent contact with the solution at the air/liquid interface and expose two ends with an area 2.54 cm x 2.54 cm area – one exposed end in the solution and the other in contact with the negative terminal. Half of the electrode area was immersed in a solution bath. The electrophoretic deposition was conducted at a constant voltage of 30 V for a period of 30 s for P25 and 60 s for TNB due to differing deposition rates. The resulting electrode was dried upright under 80^{o}C for an hour and heat treatment at 450^{o}C to remove organics and improved adhesion without affecting the FTO/glass.

B3: Photoelectrochemical experiments

Photoelectrochemical experiments were performed using a Gamry potentiostat (Series 300) using a three electrode setup with 1M KOH solution as an electrolyte. TiO_2/FTO glass photoanodes were used as the working electrode, Pt wire was used as the counter electrode, and a Ag/AgCl (satureated KCl) electrode was used as the reference electrode. A 4.1 W UV-LED (LED Engin) with a 2.54 cm diameter collimating column was used a light source with an incident light intensity of 8 mW cm^{-2} detected from 10 cm from the light source. Electron lifetime tests were conducted under open circuit potential, V_{oc}.

B4: Energy absorption and DLVO calculations

Particle energy absorption

To estimate the amount of light energy absorbed by each particle the number of TiO_2 molecules per particle was calculated. Using a density 3.78 g cm^{-3}, the number of TiO_2 molecules per particle was estimated at 2.94x10^{5}. The total number of molecules in the system was 7.70x10^{14} .
100 mg L^{-1} TiO_2 sample containing 30 mg of TiO_2 in 300 mL ultrapure water. Assuming a monodisperse sample and 100% light absorption, the energy available is sufficient to dislodge a TiO_2 nanoparticle from the secondary minimum.

DLVO theory calculations

Two interparticle interactions, electrostatic repulsion and van der Waals attraction are considered in DLVO theory [1, 2]. Assuming low surface charge, spherical particles of equal size, and thin double layers compared to particle size, the electrostatic repulsion, G_{EL}, is given by:

$$G_{EL} = \frac{64 n_0 k_B T \gamma_o^2 \exp(-\kappa D)}{\kappa} \quad \text{Eqn. B1}$$

$$\gamma_0 = \tanh\left(\frac{Ze\phi_o}{4kT}\right) \quad \text{Eqn. B2}$$

where k is Boltzmann constant (J K^{-1})
T is the temperature (K),
γ_0 is the particle surface potential (V),
Z is the ion charge,
e is the elementary charge (C),
D is the separation distance between two particles (m).

The inverse Debye length, κ, can be obtained by:

$$\kappa = \sqrt{\left(\frac{2(ze)^2 N_A c}{\epsilon k_B T}\right)} \quad \text{Eqn. B3}$$

where N_A is Avogadro's constant,
c is the ion concentration,
γ_0 is the particle surface potential (V),

Under the assumptions that particles are spherical and of equal size, and separation is small compared to particle size, the van der Waals attraction force can be calculation by the following equation:

$$G_{LW} = -\frac{A_{121}}{12\pi D^2}$$

where A_{121} is the Hamaker constant (J)

The total energy is the summation of the two interactions:

$$G_T = G_{EL} + G_{LW}$$

The following values were used for this case was given by Bennett et al. [1]: $A_{121} = 9.1 \times 10^{-20}$, of ϕ_o (mV) = 30.97, D = 27 nm, T = 298 K, and c = 1×10^{-3} M.

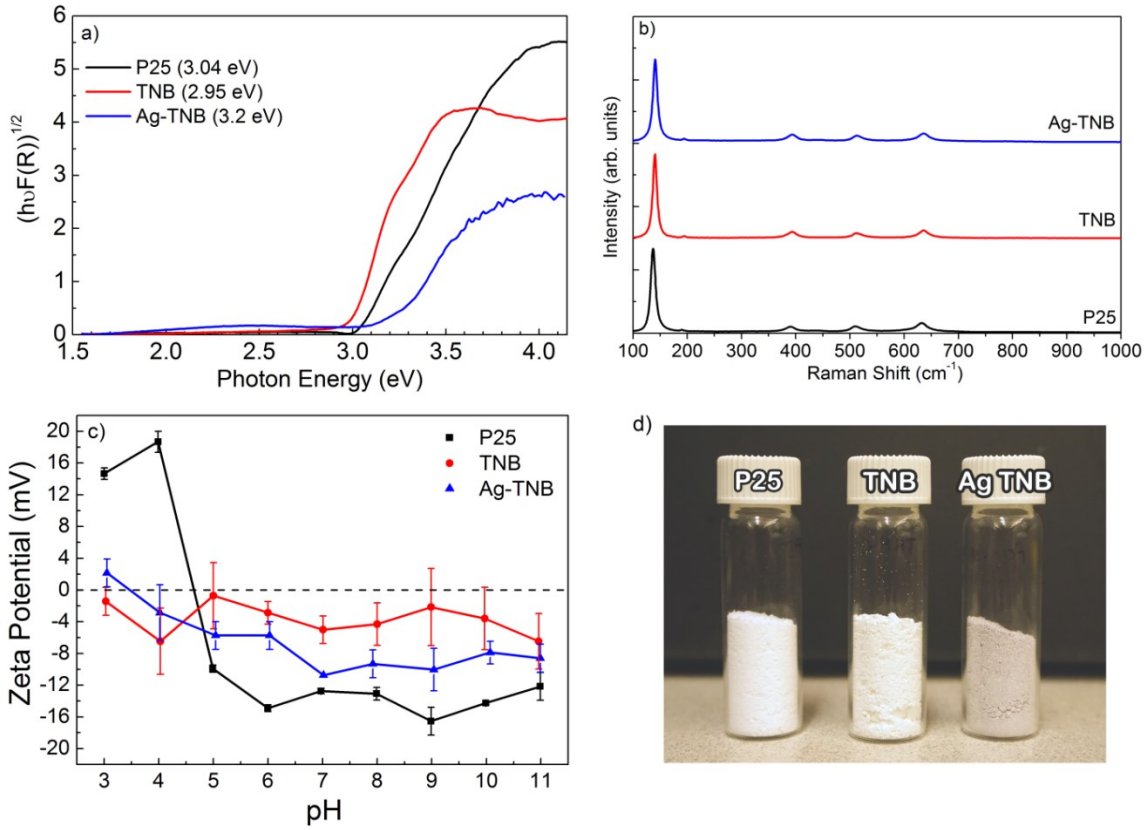

Figure B1: The (a) Tauc plot, (b) Raman spectra, (c) zeta potential vs. pH and (d) powder sample images of P25, TNB, and Ag-TNB nanomaterials

Table B1-A: P25 - Individual LED apparent kinetic rates as a function of duty cycle

Duty Cycle (%)	LED_1		LED_2		LED_3		AVERAGE			
	k_1 ($x10^{-1}$ min^{-1})	k_2 ($x10^{-3}$ min^{-1})	k_1 ($x10^{-1}$ min^{-1})	k_2 ($x10^{-3}$ min^{-1})	k_1 ($x10^{-1}$ min^{-1})	k_2 ($x10^{-3}$ min^{-1})	k_1 ($x10^{-1}$ min^{-1})	Std ($x10^{-1}$ min^{-1})	k_2 ($x10^{-3}$ min^{-1})	Std ($x10^{-3}$ min^{-1})
10	-1.23	3.47	-1.35	3.90	-0.90	2.02	-1.16	0.23	3.13	0.10
25	-2.06	4.33	-2.19	4.81	-2.01	4.40	-2.09	0.09	4.51	0.26
50	-4.00	8.08	-4.74	9.46	-3.41	6.51	-4.05	0.67	8.02	1.48
75	-4.89	9.89	-5.09	10.3	-5.00	10.21	-4.99	0.10	10.1	0.22
100	-6.74	13.02	-6.91	13.36	-5.94	11.65	-6.53	0.51	12.68	0.91

Table B1-B: TNB - Individual LED apparent kinetic rates as a function of duty cycle

Duty Cycle (%)	LED_1		LED_2		LED_3		AVERAGE			
	k_1 ($x10^{-1}$ min^{-1})	k_2 ($x10^{-3}$ min^{-1})	k_1 ($x10^{-1}$ min^{-1})	k_2 ($x10^{-3}$ min^{-1})	k_1 ($x10^{-1}$ min^{-1})	k_2 ($x10^{-3}$ min^{-1})	k_1 ($x10^{-1}$ min^{-1})	Std ($x10^{-1}$ min^{-1})	k_2 ($x10^{-3}$ min^{-1})	Std ($x10^{-3}$ min^{-1})
10	-1.73	3.28	-1.85	2.82	-1.66	3.89	-1.75	0.096	3.33	0.54
25	-2.34	5.86	-2.39	6.54	-2.22	6.68	-2.32	0.087	6.36	0.44
50	-5.52	10.04	-8.27	14.61	-5.74	10.83	-6.51	1.53	11.83	2.44
75	-7.68	13.62	-11.64	20.19	-6.67	12.84	-8.66	2.63	15.55	4.04
100	-13.55	24.12	-14.96	26.68	-9.65	17.15	-12.72	2.75	22.65	4.93

Table B1-C: Ag-TNB – Individual LED apparent kinetic rates as a function of duty cycle

Duty Cycle (%)	LED_1		LED_2		LED_3		AVERAGE			
	k_1 ($x10^{-1}$ min^{-1})	k_2 ($x10^{-3}$ min^{-1})	k_1 ($x10^{-1}$ min^{-1})	k_2 ($x10^{-3}$ min^{-1})	k_1 ($x10^{-1}$ min^{-1})	k_2 ($x10^{-3}$ min^{-1})	k_1 ($x10^{-1}$ min^{-1})	Std ($x10^{-1}$ min^{-1})	k_2 ($x10^{-3}$ min^{-1})	Std ($x10^{-3}$ min^{-1})
10	1.23	4.01	-1.25	3.71	-1.07	3.25	-0.36	1.38	3.66	0.38
25	-2.99	4.31	-3.85	6.19	-2.75	3.93	-3.20	0.58	4.81	1.21
50	-7.41	13.06	-8.51	15.03	-6.08	10.82	-7.33	1.22	12.97	2.11
75	-11.71	20.29	-13.81	23.26	-10.80	18.91	-12.11	1.54	20.82	2.22
100	-18.32	32.58	-17.29	30.46	-15.21	26.37	-16.94	1.58	29.80	3.16

Table B2-A: Material comparison experiments under continuous illumination of p-values using one-way ANOVA tests (OriginLab, α=0.05). Post-hoc tests (multiples comparisons) were conducted when a statistical difference was detected using Holm-Sidak method with overall statistical levels.

Material Comparison	HTPA formation			MG degradation		
	***p*-value**	***α***	**Sign.**	***p*-value**	***α***	**Sign.**
P25 vs. Ag-TNB	<0.0000	0.0170	YES	0.0132	0.0170	YES
TNB vs. Ag-TNB	<0.0000	0.0253	YES	0.0313	0.0253	NO
P25 vs. TNB	<0.0000	0.0500	YES	0.5201	0.0500	NO

Table B2-B: Duty Cycle experiments of p-values using one-way ANOVA tests (OriginLab, α=0.05). Post-hoc tests (multiples comparisons) were conducted when a statistical difference was detected using Holm-Sidak method with overall statistical levels.

Duty Cycle Comparison	P25			TNB			Ag-TNB		
	***p*-value**	***α***	**Sign.**	***p*-value**	***α***	**Sign.**	***p*-value**	***α***	**Sign.**
25% vs. 10%	1.685×10^{-2}	0.05	YES	7.114×10^{-1}	0.05	NO	1.685×10^{-2}	0.05	YES
50% vs. 10%	4.435×10^{-6}	0.0085	YES	9.800×10^{-3}	0.0102	YES	4.435×10^{-6}	0.0085	YES
50% vs. 25%	1.208×10^{-4}	0.0127	YES	1.879×10^{-2}	0.0127	NO	1.208×10^{-4}	0.0127	YES
75% vs. 10%	3.298×10^{-7}	0.0064	YES	9.522×10^{-4}	0.0064	YES	3.299×10^{-7}	0.0064	YES
75% vs. 25%	4.212×10^{-6}	0.0073	YES	1.720×10^{-3}	0.0073	YES	4.212×10^{-6}	0.0073	YES
75% vs. 50%	1.543×10^{-2}	0.0253	YES	1.801×10^{-1}	0.0253	NO	1.543×10^{-2}	0.0253	YES
100% vs. 10%	1.319×10^{-8}	0.0051	YES	2.518×10^{-5}	0.0051	YES	1.320×10^{-8}	0.0051	YES
100% vs. 25%	8.150×10^{-8}	0.0057	YES	3.960×10^{-5}	0.0057	YES	8.150×10^{-8}	0.0057	YES
100% vs. 50%	1.712×10^{-5}	0.0102	YES	1.990×10^{-3}	0.0085	YES	1.712×10^{-5}	0.0102	YES
100% vs. 75%	7.818×10^{-4}	0.0170	YES	2.197×10^{-2}	0.0170	NO	7.818×10^{-4}	0.0170	YES

Table B2-C: Pulse frequency experiments of p-values using one-way ANOVA tests (OriginLab, α=0.05). Post-hoc tests (multiples comparisons) were conducted when a statistical difference was detected using Holm-Sidak method with overall statistical levels. Green highlighted values represents α=0.05 significance and yellow highlighted values represent α=0.1 significance.

Pulse Frequency Comparison	P25			TNB			Ag-TNB		
	***p*-value**	***α***	**Sign.**	***p*-value**	***α***	**Sign.**	***p*-value**	***α***	**Sign.**
5 Hz vs. 0.05 Hz	0.0002	0.0085	YES	0.3815	0.0102	NO	0.6769	0.0500	NO
25 Hz vs. 0.05 Hz	0.0006	0.0102	YES	0.7250	0.0170	NO	0.0194	0.0085	NO
0.5 Hz vs. 0.05 Hz	0.0018	0.0127	YES	0.2845	0.0085	NO	0.4350	0.0253	NO
5 Hz vs. 0.5 Hz	0.1044	0.0170	NO	0.8306	0.0253	NO	0.2452	0.0170	NO
25 Hz vs. 5 Hz	0.3777	0.0253	NO	0.8895	0.0500	NO	0.1348	0.0127	NO
25 Hz vs. 0.5 Hz	0.3957	0.0500	NO	0.4564	0.0127	NO	0.0694	0.0102	NO

Appendix C: Supplementary Information for Chapter 6

C1: Pulsed Width Modulation Setup

Pulse width modulation (PWM) was used to control the UV-LED. Digital control is used to create a square wave, a signal switched between on and off states. This on-off pattern can simulate voltages in between full on (5 volts) and off (0 volts) by changing the portion of the time the signal spends on versus the time it spends off. The duration of the "on time" is called the pulse width. An Arduino Uno connected to a LED Current Driver (LEDSEEDUINO) and a high power UV-LED (LED Engin, 1 A, λ = 365 nm) was used. A PWM program was coded into the Arduino microcontroller using the following script:

```
int ledPin = 9;              // LED connected to digital pin 9
int  timeON = x              // initializes x value of time that LED  is ON
int timeOFF = y              // initializes y value of time that LED is OFF

void setup()
{
 pinMode(ledPin, OUTPUT);      // sets the digital pin as output
}

void loop()
{
 digitalWrite(ledPin, HIGH);   // sets the LED on
 delay(timeON);                // waits for x milliseconds
 digitalWrite(ledPin, LOW);    // sets the LED off
 delay(timeOFF);               // waits for x milliseconds
}.
```

Table C1. Optimized MS/MS parameters and detection limits for the analysis of target compounds (regular standards).

Compound	IDL* (µg/L)	Q1	Q3	Polarity	DP	EP	CEP	CE	CXP
Pharmaceuticals									
Carbamazepine	1	216.2	174.3	+	55	4.9	14.3	51	2.7
Venlafaxine	1	278.3	58.1	+	38.2	2.9	21.00	42	8
Fluoxetine	3	310.3	44.3	+	48	2.9	12.08	44	7
Atenolol	2	267.2	145.1	+	51	3	30.00	36	5
Sulfamethoxazole	1	254.1	156.2	+	41	3	9.00	22.1	3
Ibuprofen	2	204.9	160.9	−	-41	-2.6	-19.24	-11	-0.5
Atorvastatin	8	559.3	440.2	+	83	5.9	18.91	32	22
Naproxen	3	229.0	170.0	−	-29	-1.9	-20.13	-25	-3.8
Atrazine	1	216.0	174.3	+	66.9	3.8	13.5	27.0	2.4
Diclofenac	1	293.9	250.0	−	-46.0	-2.5	-22.53	-15.0	-1.7
Gemfibrozil	1	249.1	121.1	−	-55.0	-2.0	-20.87	-17.0	-3.0
Trimethoprim	0.5	291.1	261.2	+	59.0	4.0	12.00	32.0	3.0
Caffeine	1	195.2	123	+	8.8	8.8	41	41	5
Estrogen Compounds									
Ethinylestradiol	10	295.1	144.9	−	-71.8	-7	-10	-54	-3
Bisphenol A	10	227	211.9	−	-53	-10	-20.055	-28	-5
Personal care products									
Triclosan	10	286.9	35.0	−	-33	-2	-7	-30	-3
Triclocarban	4	314.8	161.6	−	-50	-3	-12	-20	-13
Metabolites									
10,11 epoxide carbamazepine	1	253.2	180.3	+	26	3.5	20	34	5
Norfluoxetine	10	296.1	134.1	+	23	3	9.5	9	5
p-hydroxy atorvastatin	10	575.2	440.3	+	64	4	19	32	5
o-hydroxy atorvastatin	10	575.2	440.3	+	64	4	19	32	5

*the samples were consequently concentrated via solvent evaporation and reconstruction on the IDLs (concentration factor = 25)

Table C2. Optimized MS/MS parameters used for the analysis of target compounds (deuterated standards).

Deuterated standards	Q1	Q3	Polarity	DP	EP	CEP	CE	CXP
carbamazepine- d_5	247.200	204.400	+	60.9	4.3	17.07	28.0	3.3
venlafaxine- d_6	284.271	64.100	+	44.8	3.3	18.22	45.0	2.4
fluoxetine- d_5	315.200	44.200	+	50.0	4.0	18.97	38.2	3.1
atenolol- d_7	274.300	145.200	+	49.8	3.7	41.40	35.6	3.7
sulfamethoxazole- d_4	258.122	160.100	+	54.0	4.0	25.00	37.0	3.0
ibuprofen- d_3	207.900	164.100	−	-24.1	-7.6	-19.35	-10.0	-3.0
atorvastatin- d_5	564.300	445.300	+	45.6	4.0	25.94	30.0	16.0
naproxen- d_3	233.000	16.900	−	-36.8	-2.0	-20.28	-25.7	-1.0
triclosan- d_3	289.900	35.000	−	-28.5	-2.0	-11.31	-25.3	-2.3
triclocarban- d_4	316.900	159.900	−	-50.0	-2.5	-23.38	-18.0	-2.0
10,11 epoxide carbamazepine - d_{10}	263.200	190.300	+	53.0	3.5	20.00	34.0	5.0
norfluoxetine- d_5	301.200	139.200	+	23.0	3.0	10.00	9.0	5.0
p-hydroxtatorvastatin- d_5	580.200	445.200	+	64.0	4.0	19.00	32.0	5.0
o-hydroxtatorvastatin- d_5	580.200	445.200	+	64.0	4.0	19.00	32.0	5.0
ethinylestradiol- d_4	299.100	146.900	−	-72.9	-5	-28.23	-51.8	-15.1
emfibrozil- d_6	255	120.7	−	-46.5	-11	-21.091	-19.2	-2
bisphenol A- d_{16}	241	142	−	-50	-10	-20.573	-50	-3
norfluoxetine- d_5	301.2	139.2	+	10	10	9	9	5
diclofenac- d_4	298.2	253.8	−	-25.8	-6.9	-22.689	-16.9	-6.1
trimethoprim- d_3	294.2	230.3	+	22	22	31	31	6
caffeine- d_3	198.2	123.1	+	15	15	42	42	4

Table C3. Chromatographic and ionization parameters used for LC-MS/MS analysis for target analytes.

Ionization conditions	**Positive**	**Negative**
Curtain Gas (psig)	30	10
Collision Gas (psig)	Low	Low
Ion Spray Voltage	5500	-4500
Temperature (^{o}C)	750	750
Ion Source Gas 1	50	60
Ion Source Gas 2	30	40
Chromatographic conditions		
Injection volume (μL)	20	
Solvent A	5 mM ammonium acetate in water	
Solvent B	methanol	
Flow rate (mL/min)	0.8	

Mobile Phase Gradient

For pharmaceuticals in positive mode, the mobile phase gradient began at 80% B and was ramped to 100% B over a 4.5 min period where it was held constant for 1 min. The initial negative mobile phase for pharmaceuticals gradient was 60% B which was then increased to 100% B over an 8 min period where it was held constant for 0.5 min. Column re-equilbration was done for 8 min at the end of the run.

Table C4: Pseudo-first order kinetics for dark, photolysis, and continuous experiments

Compound	Dark			Photolysis			Continuous UV		
	k_{app} ($x10^{-2}$ min^{-1})	Std. Dev.	R^2	k_{app} ($x10^{-2}$ min^{-1})	Std. Dev.	R^2	k_{app} ($x10^{-2}$ min^{-1})	Std. Dev.	R^2
IBU	-0.019	0.046	0.04	-0.099	0.053	0.48	-0.497	0.120	0.99
BPA	-0.173	0.317	0.43	0.022	0.137	0.15	-0.497	0.423	0.45
NPX	0.038	0.093	0.50	0.016	0.054	0.00	-1.495	0.289	0.99
GFZ	-0.096	0.048	0.60	-0.014	0.047	0.06	-0.551	0.086	0.99
DCF	-0.033	0.041	0.15	0.002	0.079	0.36	-1.750	0.232	0.98
EE2	-0.223	0.261	0.35	-0.293	0.280	0.48	-0.422	0.108	0.77
TCS	0.008	0.091	0.40	-0.182	0.169	0.74	-0.299	0.045	0.99
TCCB	-0.053	0.167	0.36	-0.322	0.134	0.98	-0.113	0.016	0.97
ATRZ	0.004	0.158	0.37	0.111	0.272	0.65	0.013	0.030	0.11
CBZ	-0.055	0.027	0.35	-0.035	0.056	0.21	-0.065	0.007	0.83
FLX	-0.094	0.020	0.66	-0.110	0.028	0.56	0.030	0.024	0.01
ATOR	-0.553	0.545	0.63	-1.195	0.102	0.88	-1.652	0.117	1.00
VEN	0.028	0.032	0.20	-0.032	0.054	0.28	-0.014	0.014	-0.04
SULF	0.056	0.050	0.14	-0.017	0.043	-0.09	-0.435	0.036	1.00
TRIM	0.039	0.121	0.37	-0.046	0.056	0.14	-0.132	0.035	0.93
NFLX	-0.054	0.161	0.46	-0.152	0.085	0.59	0.049	0.056	0.23
ATEN	0.014	0.026	-0.10	0.020	0.027	0.05	0.007	0.023	0.00
CAFF	0.028	0.013	-0.12	0.149	0.129	0.37	-0.077	0.085	0.22
e-CBZ	0.008	0.216	0.47	-0.112	0.163	0.55	-0.033	0.041	0.46
p-ATOR	-0.553	0.532	0.76	-0.975	0.248	0.93	-1.846	0.772	0.57
o-ATOR	-0.386	0.237	0.73	-0.793	0.209	0.88	-2.195	0.125	0.97

*negative kinetic rates are compound decomposition rates, whereas positive kinetic rates are due to LC-MS/MS detection variance since the initial concentration should not be less than subsequent concentration at time *t*

Table C5: ANOVA results for a multiple regression analysis (OriginPro)

	DF	Sum of Squares	Mean Square	F value	p
Model	3	9.436	3.145	45.630	<0.000
Error	17	1.172	0.069		
Total	20	10.608			

Table C6-A: Duty cycle experiments table (total PPCP parent compound concentration) of *p*-values for One-Way ANOVA tests (OriginPro, α=0.05). Post-hoc tests (multiple comparisons) were conducted when a statistical significance was detected using Tukey method with overall statistical significance level of 0.05. Green highlighted values represents α = 0.05 significance and yellow highlighted values represent that the comparison passes α = 0.1 significance threshold.

Duty Cycle Comparison	*p-value*	Significance
10% 0%	0.000	Yes
25% 0%	0.024	Yes
25% 10%	0.270	No
50% 0%	0.002	Yes
50% 10%	0.945	No
50% 25%	0.720	No
75% 0%	0.004	Yes
75% 10%	0.808	No
75% 25%	0.894	No
75% 50%	0.999	No
100% 0%	0.000	Yes
100% 10%	0.948	No
100% 25%	0.070	No (Yes at α =0.1)
100% 50%	0.533	No
100% 75%	0.344	No

Table C6-B: Duty cycle experiments using one-way ANOVA OriginPro, α=0.05). Post-hoc tests were conducted (Tukey method). Green and yellow represent α = 0.05 and α = 0.1 significance.

PPCP	Duty Cycle Comparisons									
	25% vs 10%	**50% vs 10%**	**50% vs 25%**	**75% vs 10%**	**75% vs 25%**	**75% vs 50%**	**100% vs 10%**	**100% vs 25%**	**100% vs 50%**	**100% vs 75%**
IBU	No	No	No	No	No	No	No	No	No	No
p-value	0.707	0.601	1.000	0.620	1.000	1.000	0.423	0.983	0.997	0.996
BPA	No	No	No	No	No	No	No	No	No	No
p-value	0.845	0.879	1.000	0.921	1.000	1.000	0.989	0.601	0.646	0.712
EE2	No	No	No	No	No	No	No	No	No	No
p-value	1.000	1.000	1.000	0.781	0.754	0.851	0.704	0.675	0.782	1.000
TCS	No	No	No	No	No	No	**Yes**	No	No	No
p-value	0.446	0.517	1.000	0.949	0.829	0.886	0.048	0.547	0.475	0.141
TCCB	No	No	No	No	No	No	No	No	No	No
p-value	1.000	0.992	0.979	0.999	0.996	1.000	0.605	0.530	0.831	0.729
ATRZ	No	No	No	No	No	No	No	No	No	No
p-value	0.456	0.690	0.992	0.992	0.692	0.896	0.817	0.960	0.999	0.964
ATN	No	No	No	No	No	No	No	No	No	No
p-value	0.828	0.756	1.000	0.996	0.951	0.909	0.981	0.984	0.962	1.000
CBZ	No	No	No	No	No	No	No	**No**	No	No
p-value	0.505	1.000	0.425	1.000	0.586	0.998	0.469	0.045	0.553	0.396
SULF	No	No	No	No	No	No	No	**No**	No	No
p-value	0.929	0.863	0.448	0.918	0.526	1.000	0.180	0.055	0.597	0.516
e-CBZ	No	No	No	No	No	No	No	No	No	No
p-value	0.922	0.841	0.999	0.997	0.988	0.956	0.975	0.999	0.991	0.999
VEN	No	No	No	No	No	No	No	No	**No**	**Yes**
p-value	0.958	0.600	0.274	0.305	0.117	0.973	0.622	0.936	0.090	0.036
FLX	No	No	No	No	No	No	No	No	No	No
p-value	0.426	0.366	1.000	0.469	1.000	0.999	0.281	0.997	1.000	0.993
NFLX	No	No	No	No	**No**	No	No	No	No	No
p-value	0.135	0.999	0.185	0.993	0.071	0.966	0.996	0.223	1.000	0.935
CAF	No	No	No	No	No	No	No	No	No	No
p-value	0.978	0.809	0.982	0.833	0.988	1.000	0.594	0.880	0.994	0.990
p-ATOR	No	No	No	No	No	No	No	No	No	No
p-value	0.980	0.991	1.000	0.993	1.000	1.000	0.929	0.999	0.997	0.995
o-ATOR	No	No	No	No	No	No	No	No	No	No
p-value	0.945	1.000	0.894	0.960	0.644	0.985	0.696	0.976	0.604	0.345
ATOR	No	No	No	No	No	No	No	No	No	No
p-value	0.707	0.702	1.000	0.910	0.991	0.991	0.333	0.948	0.950	0.777
TRIM	No	No	No	No	No	No	No	No	No	No
p-value	0.974	0.999	0.997	0.952	1.000	0.991	0.300	0.590	0.413	0.655
NPX	No	No	No	No	No	No	No	No	No	No
p-value	0.986	0.984	0.869	0.928	0.751	0.998	0.638	0.451	0.891	0.968
GFZ	No	No	No	No	No	No	No	No	No	No
p-value	1.000	0.921	0.949	0.866	0.904	1.000	0.489	0.543	0.904	0.949
DCF	No	No	No	No	No	No	No	No	No	No
p-value	0.966	1.000	0.991	0.898	0.577	0.813	0.833	0.994	0.913	0.369

Table C7-A: Frequency experiments table (total PPCP parent compound concentration) of *p*-values for One-Way ANOVA tests (OriginPro, α=0.05). Post-hoc tests (multiple comparisons) were conducted when a statistical significance was detected using Tukey method with overall statistical significance level of 0.05. Green highlighted values represents α = 0.05 significance and yellow highlighted values represent that the comparison passes α = 0.1 significance threshold.

Frequency Comparison	*p-value*	Significance
25 Hz vs. 0.05 Hz	0.677	No
Dual Freq. vs. 0.05 Hz	0.050	Yes
Dual Freq. vs. 25 Hz	0.246	No
Cont. vs. 0.05 Hz	0.013	Yes
Cont. vs. 25 Hz	0.062	No
Cont. vs. Dual Freq.	0.758	No

Table C7-B: Frequency experiments table (individual PPCP compound) of *p*-values for One-Way ANOVA tests (OriginPro, α=0.05). Post-hoc tests (multiple comparisons) were conducted when a statistical significance was detected using Holm-Sidak method with overall statistical significance level of 0.05. Green highlighted values represents α = 0.05 significance and yellow highlighted values represent that the comparison passes α = 0.1 significance threshold.

PPCP	Frequency Comparisons					
	Cont. vs. Dual Freq.	**Cont. vs. 25 Hz**	**Cont. vs. 0.05 Hz**	**Dual Freq. vs. 25 Hz**	**Dual Freq. vs. 0.05 Hz**	**25 Hz vs. 0.05 Hz**
IBU	No	No	No	No	No	No
p-value	0.898	0.252	0.671	0.563	0.965	0.814
BPA	No	No	No	No	No	No
p-value	0.927	0.429	0.402	0.757	0.727	1.000
EE2	No	No	No	No	No	No
p-value	0.334	0.125	0.124	0.878	0.876	1.000
TCS	**No**	**Yes**	**Yes**	No	No	No
p-value	0.072	0.008	0.003	0.411	0.134	0.823
TCCB	**Yes**	**Yes**	**Yes**	No	No	No
p-value	0.023	0.004	0.003	0.261	0.219	0.903
ATRZ	No	No	No	No	No	No
p-value	0.995	0.998	0.653	1.000	0.521	0.552
ATN	No	No	No	No	No	No
p-value	0.650	0.841	0.227	0.798	0.427	0.303
CBZ	No	**Yes**	**Yes**	No	No	No
p-value	0.116	0.010	0.027	0.342	0.737	0.869
SULF	No	No	No	No	No	No
p-value	0.939	0.705	0.299	0.951	0.568	0.847
e-CBZ	No	No	No	No	No	No
p-value	0.983	0.975	1.000	0.864	0.975	0.983
VEN	No	No	No	No	No	No
p-value	1.000	0.705	1.000	0.705	1.000	0.637
FLX	No	No	No	No	No	No
p-value	0.469	0.273	0.996	0.967	0.586	0.359
NFLX	**No**	No	No	**No**	No	No
p-value	0.086	0.984	0.185	0.053	0.944	0.114
CAF	No	No	No	No	No	No
p-value	0.977	0.361	0.923	0.217	0.744	0.683
p-ATOR	No	No	No	No	No	No
p-value	0.996	0.976	0.901	0.920	0.804	0.996
o-ATOR	No	No	No	No	No	No
p-value	0.964	0.326	0.723	0.552	0.932	0.863
ATOR	No	No	No	No	No	No
p-value	0.394	0.128	0.560	0.825	0.987	0.651
TRIM	No	**Yes**	**Yes**	No	No	No
p-value	0.116	0.031	0.017	0.786	0.550	0.972
NPX	No	No	No	No	No	No
p-value	0.998	0.234	0.899	0.297	0.956	0.530
GFZ	No	No	No	**Yes**	**No**	No
p-value	0.578	0.132	0.522	0.021	0.096	0.702
DCF	No	No	No	No	No	No
p-value	0.901	0.352	0.631	0.705	0.947	0.944

.

Appendix D: Supplementary Information for Chapter 7

Table D1: The properties of acid orange 7

Formula:	$C_{16}O_4H_{11}N_2Na$
Charge:	Negative
Molecular weight:	350.32 g mol^{-1}
Solubility limit	116 g L^{-1}
λ_{max} :	485 nm
Molar extinction coefficient:	ε = 21,400 L mol^{-1} cm^{-1} at 485 nm
pKa:	pKa_1 = 1.1, pKa_2 = 11

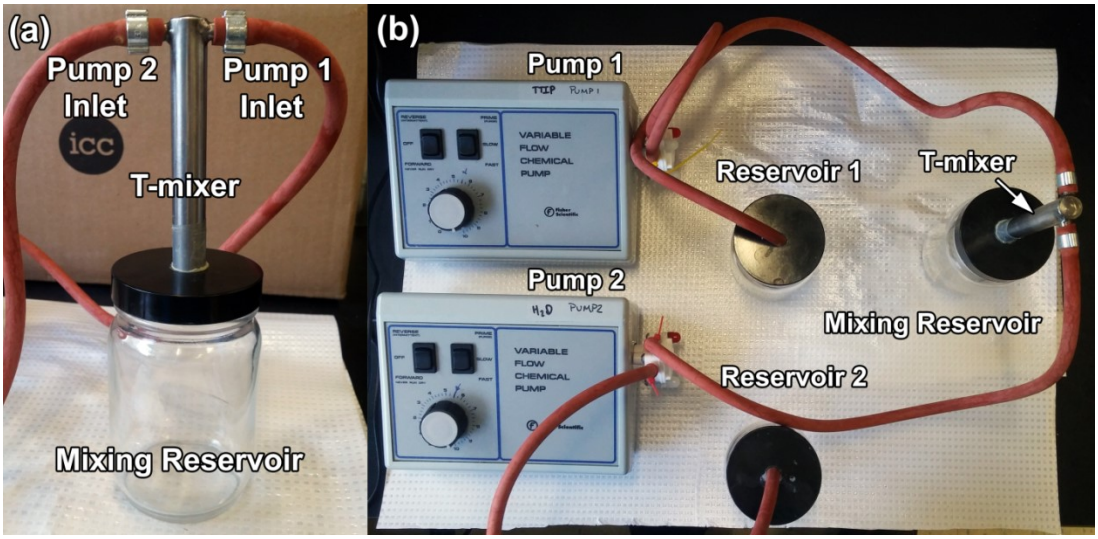

Figure D1: (a) Close-up image of T-mixer unit and (b) T-mixer sol-gel setup containing two peristaltic pumps (Pump 1 and 2) and reservoirs (Reservoir 1 and 2) that deliver solution into a mixing reservoir via a T-mixer

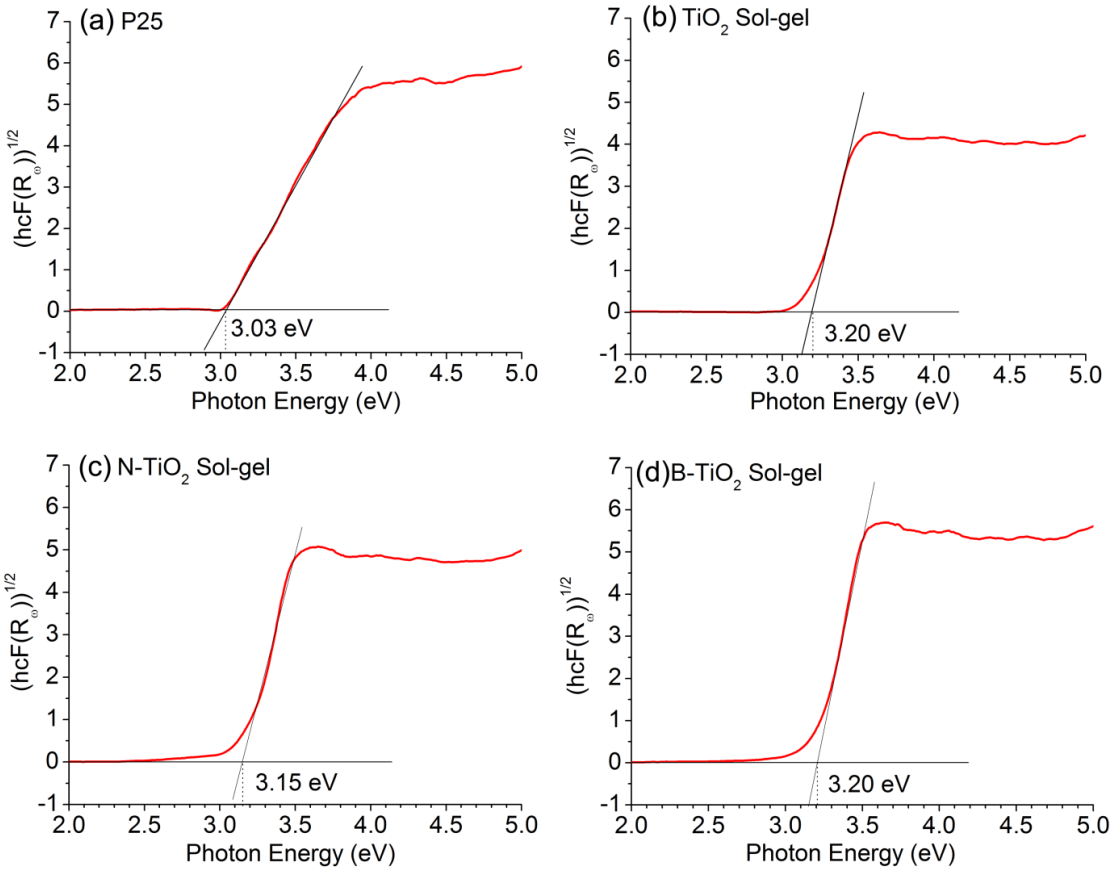

Figure D2: Diffuse reflectance spectra of (a) uncoated quartz fiber filter (QFF), (b) TiO_2/QFF, (c) N-doped TiO_2/QFF, and (d) B-doped TiO_2/QFF

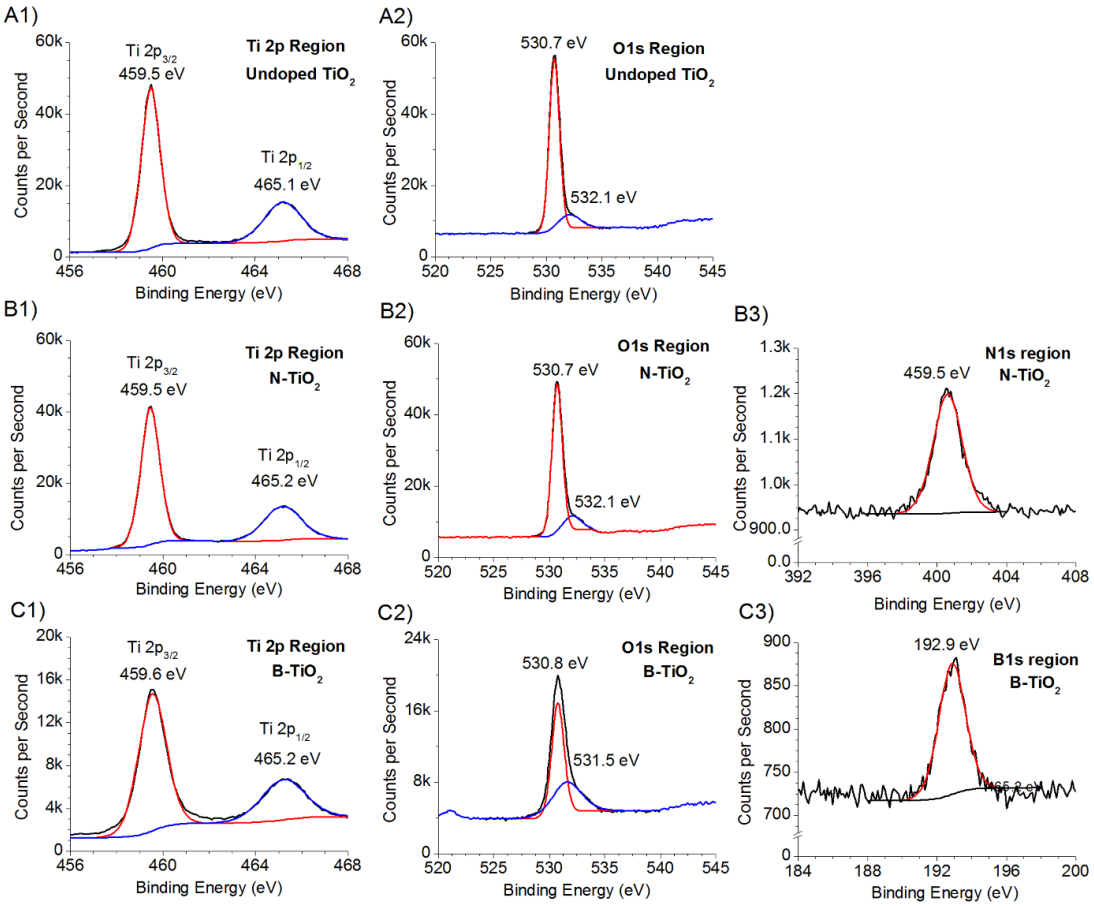

Figure D3: XPS spectra of A) Undoped TiO_2, B) N-TiO_2, and C) B-TiO_2; and their 1) Ti 2p, 2) O1s, and 3) dopant (N, B) 1s regions.

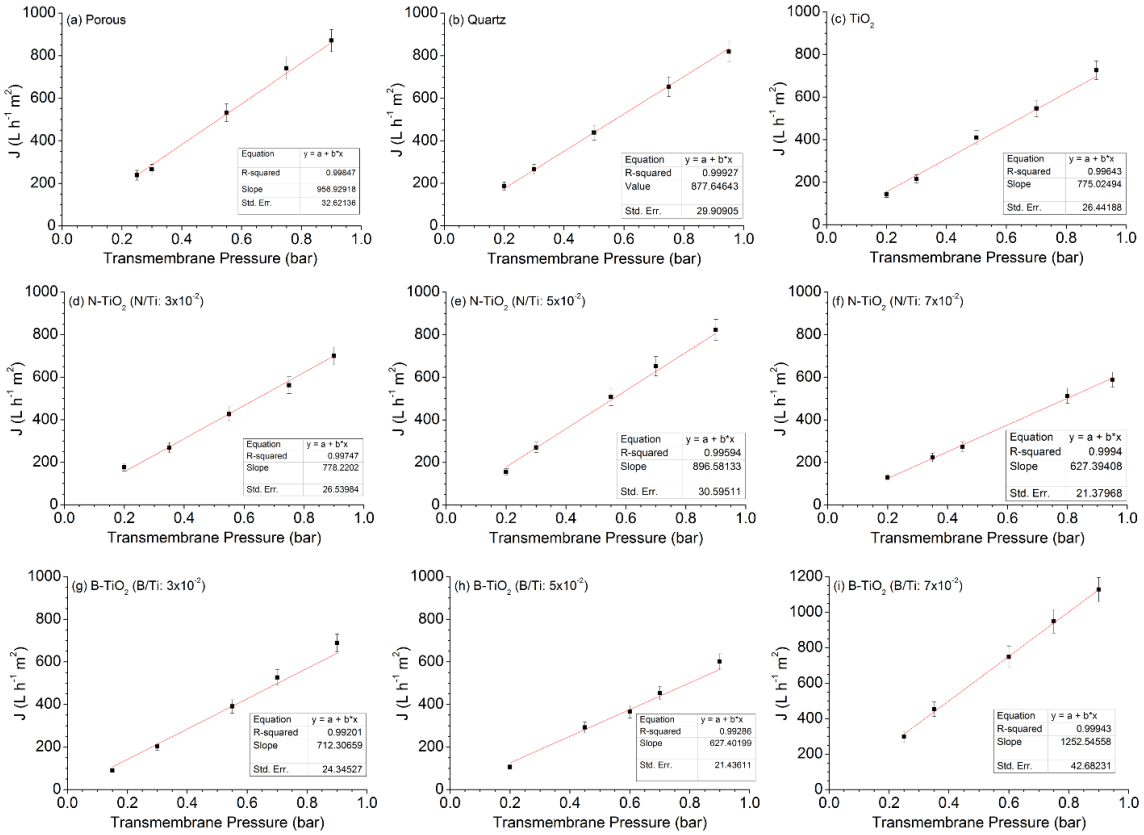

Figure D4: Permeate flux as a function of transmembrane pressure for (a) porous support; (b) quartz fiber filter (QFF); and quartz fiber filter deposited with (c) TiO_2 (d-f) N-TiO_2 (N/Ti: 3, 5, and 7x10^{-2}), and (g-i) B-TiO_2 (B/Ti: 3, 5, and 7x 10^{-2})

Appendix E: Supplementary Information for Chapter 7

E.1: Synthesis of Ag@SiO_2-TiO_2 (AST) nanoparticles

Materials

3-Aminopropyltrimethoxysilane (APTMS), titanium tetraisopropoxide (TTIP), polyvinylpyrrolidone (PVP K30) and P25 Aeroxide^{TM} were purchased from Sigma-Aldrich Chemicals Co. Silver nitrate and tetra orthosilicate (TEOS) were purchased from Alfa-Aesar.

Synthesis

Ag NPs were synthesized using 1.0 g $AgNO_3$ and 5.0 g of PVP dissolved in 400 mL ethylene glycol. The mixture was heated to 130 ^oC and held for 0.5 h under 600 rpm. The temperature was further held for 1 h without stirring. The Ag NPs were separated from ethylene glycol by the addition of 800 mL acetone, followed by sonication and centrifugation. The Ag NPs were redispersed in 100 mL of ethanol to obtain a concentration of about 6.0 g L^{-1}.

The Ag@SiO_2 NPs were formed using a procedure described elsewhere [1]. In a typical synthesis of Ag@SiO_2, 50 mL of Ag NPs/ethanol solution (6.0 g L^{-1}) obtained from the aforementioned method was dissolved in 120 mL ethanol and stirred for 0.5 h at 600 rpm at room temperature. Subsequently, 40 mL of deionized water , 2.4 mL ammonia aqueous solution (28 wt%) were added to the mixture. 50 uL TEOS in 10 mL ethanol was introduced to the mixture dropwise under continuous stirring and the reaction was continued for 10 h. The Ag@SiO_2 core-shell NPs were washed with deionized water and ethanol 3 times and redispersed in 50 mL ethanol.

50 mL of Ag@SiO_2 NPs was dispersed in 70 mL of ethanol and 200 uL APTMS was refluxed at 85 ^oC for 6 h. The as-synthesized APTMS-modified Ag@SiO_2 was washed with ethanol 3 times and redispersed in 200 mL of ethanol. 200 uL of TTIP in 40 mL ethanol was added dropwise to the APTMS-modified Ag@SiO_2 dispersion under stirring, followed by refluxing at 85 ^oC for 3 h. The resultant Ag@SiO_2-TiO_2 NPs (AST) were centrifuged, washed with deionized water, and dried overnight at 60 ^oC.

E.2: Glucose oxidation via TiO_2/UV process

E.2.1 Experimental Method

Photocatalytic degradation experiment

A 0.4 g L^{-1} TiO_2 nanobelt slurry containing 600 mL (50 ppm, 0.278 mM) at room temperature was prepared. Initial adsorption profiles were conducted for 60 min under magnetic stirring, followed by photocatalytic degradation. A medium pressure mercury lamp was used as the UV light source.

Glucose detection - spectrophotometric analysis

Glucose spectrophotometric detection was determined using a protocol developed elsewhere [2]. In short, glucose is oxidized to β-D-glucose in the presence of glucose oxidase (GOX):

$$\beta\text{-D-glucose} + O_2 + H_2O \rightarrow \delta\text{-D-gluconolactone} + H_2O_2 \qquad \text{Eq. E.1}$$

The measure the glucose concentration via the production of H_2O_2 is coupled to the enzyme horse radish peroxidase (HRP):

$$2\ H_2O_2 + \text{phenol} + \text{4-aminoantipyrine} \rightarrow \qquad \text{Eq. E.2}$$
$$\text{4-N-(}p\text{-benzoquinoeimine)-antipyrine} + 4\ H_2O$$

The reaction product exhibits an absorption maximum at 505 nm and a molecular extinction coefficient of 1.27×10^4 M^{-1} cm^{-1} [2]. The glucose standards and unknowns were incubated at 30 ^oC for 10 min and absorbance values were measured. A glucose calibration curve was also prepared.

Total Organic Carbon Determination

Total organic carbon (TOC) was measured using an Aurora 1030c TOC Analyzer. The TOC concentration of a sample is determined by converting the organically bound carbon into CO_2. The method is based on the Standard Method 531- D: Wet Oxidation method [3]. In short, the sample is acidified to pH 2 or below to convert inorganic carbon species to CO_2, purged to remove the inorganic carbon, then oxidized with persulfate in an autoclave at temperatures between 116 ^oC to 130 ^oC. The CO_2 produced from the sample is then quantified by infrared spectrometry.

E.2.2 Results of glucose oxidation using TiO_2/UV arc lamp process

Glucose oxidation was conducted using TiO_2/UV arc lamp process using synthesized TNB. The TNB degraded 50 % of the parent glucose compound within 90 min after the UV light was turned on (Fig. E2a).The mineralization of glucose using TNB/UV_{365nm} occurred according to the TOC degradation profile (Fig. E2b); the organic carbon degradation had a half-life of around 68 min. It was also shown that UV light had no effect on the degradation of glucose

.

Table E1: Chemistry of 22MNB5 Usibor® steel

Element	Weight (%)
C	0.221
Mn	1.17
P	0.012
S	0.003
Si	0.252
Cu	0.038
Ni	0.017
Cr	0.179
Sn	0.003
Al_{sol}	0.037
Al_{total}	0.038
Ca	0.0013
Nb	0.002
Mo	0.005
V	0.006
Zr	0.002
Ti	0.026
B	0.0025
N	0.0064

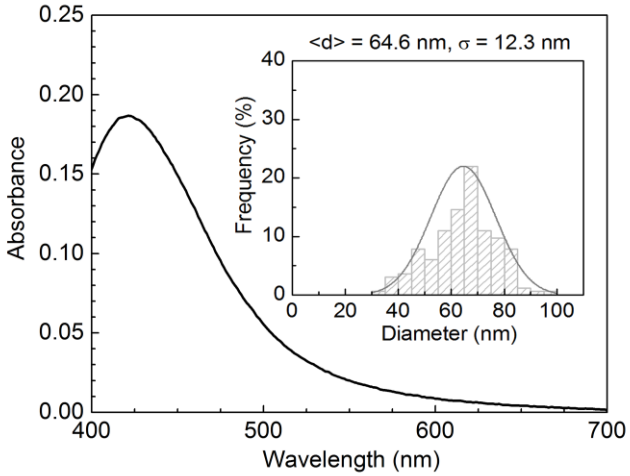

Figure E1: Ag nanoparticle absorption spectra and size distribution curve (inset graph)

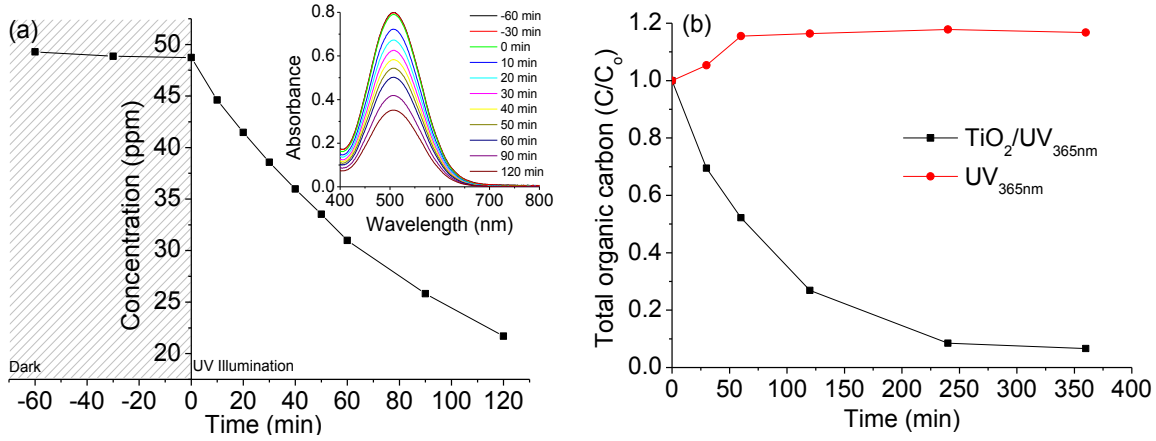

Figure E2: (a) Glucose concentration as a function of time using anatase TNB under UV_{365nm} illumination and (b) total organic carbon content through time under UV_{365} illumination with and without anatase TiO_2.

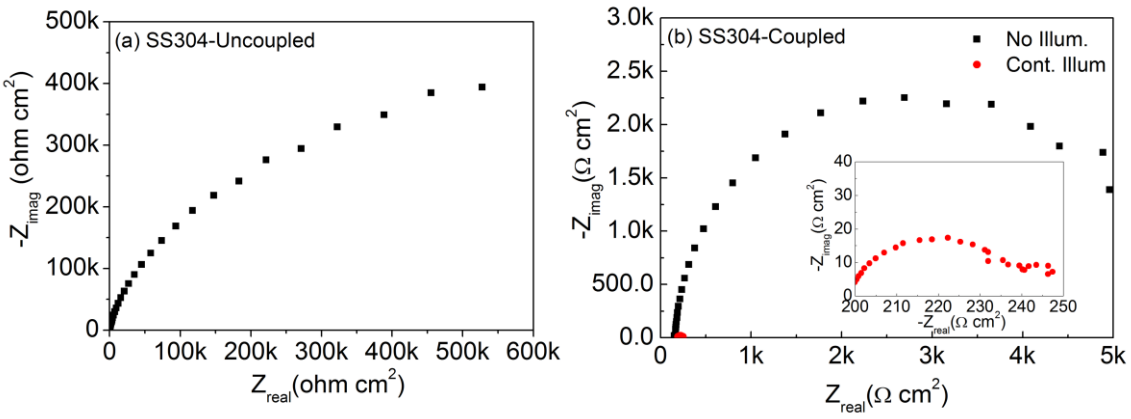

Figure E3: EIS spectra of SS304 (a) uncoupled and (b) coupled with TiO_2 photoanode under (i) illumination and (ii) no illumination

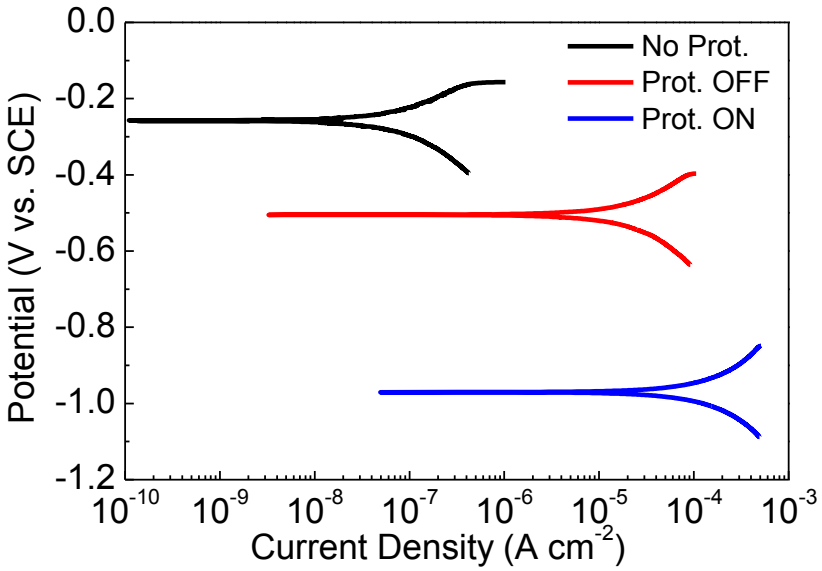

Figure E4: Polarization curves of SS304 uncoupled and coupled with TiO_2 photoanode under (i) illumination and (ii) no illumination

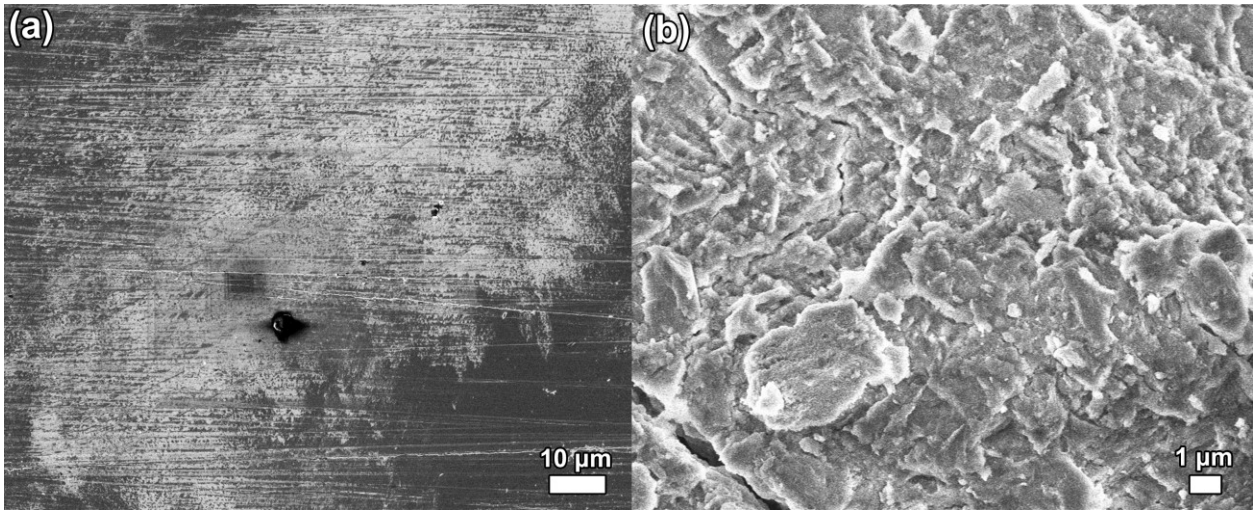

Figure E5: (a) Unprotected and (b) photocathodic protected 22MNB5 base metal after 48 h of immersion in 5 wt % NaCl